Study and realization of shear wave mode solidly mounted film bulk acoustic resonators (FBAR) made of c-axis inclined zinc oxide (ZnO) thin films: application as gravimetric sensors in liquid environments.

Mathias Link

Faculté des Sciences et Techniques
U.F.R. Sciences et Techniques de la Matière et des Procédés
École Doctorale EMMA

Thèse

présentée pour l'obtention du titre de

Docteur de l'Université Henri Poincaré, Nancy I

Spécialité: Plasmas, Optique, Opto-Électronique et Micro-nanosystèmes

par

Mathias Link
Ingénieur en microtechnique diplômé
Ecole Polytechnique Fédérale de Lausanne

Étude et réalisation de résonateurs à ondes acoustiques de volume (FBAR) montés sur miroir acoustique et exploitant le mode de cisaillement dans les couches minces d'oxyde de zinc (ZnO) à axe c incliné : application aux capteurs gravimétriques en milieux liquides.

Study and realization of shear wave mode solidly mounted film bulk acoustic resonators (FBAR) made of c-axis inclined zinc oxide (ZnO) thin films: application as gravimetric sensors in liquid environments.

Soutenue publiquement le 14 septembre 2006 devant la commission d'examen

Président :	Dr. S. Ballandras	Directeur de recherches CNRS, FEMTO-ST, Besançon (F)
Rapporteurs :	Dr. R. J. Jiménez Riobóo	Chercheur, ICMM, CSIC, Madrid (E)
	Prof. Dr. C. Wagner	Professeur, Université de la Sarre, Saarebruck (D)
Examinateurs :	Prof. Dr. P. Alnot	Professeur, UHP, Nancy I (directeur de thèse)
	Prof. Dr. O. Elmazria	Professeur, UHP, Nancy I (co-directeur de thèse)
Invités :	Dipl.-Ing. M. Schreiter	Ingénieur de recherche, Siemens CT, Munich (D)
	Dipl.-Phys. W. Wersing	Chercheur (en retraite), Siemens CT, Munich (D)

Laboratoire de Physique des Milieux Ionisés et Applications
Faculté des Sciences et Techniques, UHP, BP 239 - 54506 Vandoeuvre-lès-Nancy Cedex

A Martine

A mes parents et mes frères

Le travail décrit dans cette thèse a été réalisé en grande partie dans les laboratoires de la centrale de recherche de Siemens à Munich. S'agissant d'une **thèse européenne**, elle a été rédigée majoritairement en Anglais. L'introduction et la conclusion de la thèse ainsi qu'un résumé de chaque chapitre sont également donnés en Français.

REMERCIEMENTS
ACKNOWLEDGEMENTS

Cette thèse a été effectuée en collaboration avec le ***Laboratoire de Physique des Milieux Ionisés et Applications*** *(LPMIA) de l'Université Henri Poincaré (UHP) à Nancy. Je remercie Prof. Dr. Patrick ALNOT, Professeur au LPMIA et Vice-Président du Conseil Scientifique de l'UHP, ainsi que Prof. Dr. Omar ELMAZRIA, Professeur au LPMIA, d'avoir accepté d'encadrer cette thèse et de m'avoir conseillé judicieusement au cours de ce travail. J'adresse mes vifs remerciements à Dr. Badreddine ASSOUAR, chercheur CNRS au LPMIA, pour m'avoir soutenu d'un point de vue scientifique et organisationnel, ainsi que pour sa disponibilité permanente et les bons moments passés ensemble. Je tiens également à remercier Dr. Bernard WEBER, directeur de recherches CNRS et directeur du LPMIA, de m'avoir accepté en temps que doctorant externe dans son laboratoire.*

Most of the work realized during this thesis was done at the Materials and Microsystems department (MM2) of **Siemens Corporate Technology** (CT) in Munich. I would like to thank Dr. Wolfgang ROSSNER, head of the Ceramics division of CT MM2, for having accepted me into his division, and I am grateful that Siemens AG Corporate Technology financed this work.

I would like to express my gratitude to Dr. Reinhard GABL and Matthias SCHREITER, project leaders of the Ferroelectric materials group within Siemens CT MM2, for giving me the opportunity to work in such a fascinating field and for supervising my thesis. Their encouragement, advice and enthusiasm made this thesis an inspiring and enjoyable experience. I'm especially grateful to Matthias SCHREITER for his excellent, precise guidance on thin film sputtering and many other topics, for the long discussions we had concerning the c-axis inclined ZnO process developments and for his acceptance to be part of my jury.

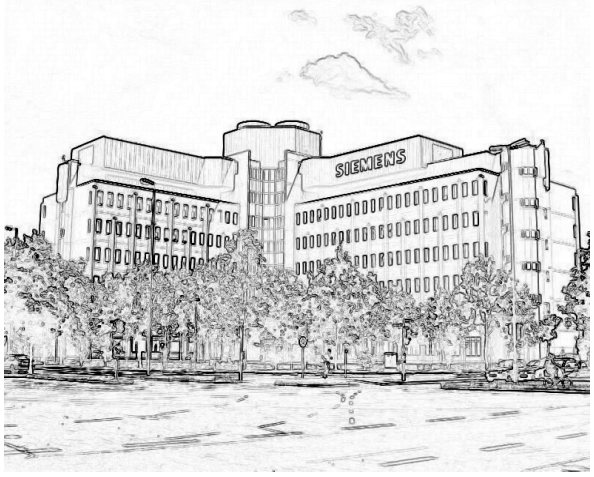

I would also like to show my appreciation to all other permanent members of the Ferroelectric materials group within Siemens CT MM2 for all the scientific discussions as well as for the excellent atmosphere. I would like to thank Jan WEBER, PhD student and my

desk neighbour, for all the interesting discussions and scientific experiments, especially the biochemical testing of FBARs. I am in debt to Robert PRIMIG, project engineer, for his support in the clean-room processing and for the pleasant initiation to the "Munich-life-style", and to Dana PITZER, project engineer, for her support in various aspects of the thesis, especially the SEM pictures. I would like to thank Anett HEBOLD, team assistant, for ensuring that my administrative affairs did not become major issues. I would like to acknowledge Wolfram WERSING, retired senior research engineer and invited member of my jury, for many inspiring discussions, and for reviewing and commenting on this thesis.

J'exprime également mes sincères remerciements à Dr. Rafael J. JIMÉNEZ RIOBÓO, chercheur à l'ICMM du CSCI à Madrid, et à Prof. Dr. Christian WAGNER, Professeur à l'Université de la Sarre, pour avoir accepté d'être les rapporteurs de ma thèse et d'y avoir porté un grand intérêt ; ainsi qu'à Dr. Sylvain BALLANDRAS, directeur de recherches CNRS à l'institut FEMTO-ST à Besançon, pour avoir accepté de présider mon jury de thèse et d'avoir examiné mon travail.

Special thanks go also to the great students who contributed in this work: Alex WINTERBURN, the "master of the network analyzer", for numerous measurement series and excellent company; Alain PHOMMAHAXAY and Marina SCHMIDT, for measurements in liquids with different viscosities and laborious over-modes analyses; and Max AMBERGER for helping with the ZnO process development.

My thanks go to the PhD-students and other members of Siemens CT MM, for their support, good company and many discussions, not only professional ones: Katrin BENKERT, Francois BAMIÈRE, Christian SCHRÖTER, Daniel SICKERT, Stefan DENNELER, Aurélie CARDIN, Thomas RICHTER, Jürgen ZIMMERMANN, Dr. Nils VAN DER LAAG, Dr. Willi METZGER, Dr. Roman KARMAZIN, Dr. Mahmoud AL-AHMAD, Dr. Uwe RETTIG, Dr. Stefan LAMPENSCHERF, Dr. Thorsten STEINKOPFF, Dr. Berit WESSLER, and all the others.

Je remercie également : Philippe KIRSCH, sans qui je n'aurais probablement pas abouti au LPMIA et qui m'a montré les différentes facettes de Nancy, notamment gastronomiques; Félicidade MOREIRA, Pascal NICOLAY et Denis BEYSSEN, entre autres pour leur bonne compagnie à Paris, Barcelone et Rotterdam; ainsi que Dr. Laurent LEBRIZOUAL, Laurent BOUVOT, Dr. Brice VINCENT, Dr. Frédéric SARRY, Dr. Didier ROUXEL, Prof. Dr. Mohammed BELMAHI et tous les autres membres du LPMIA pour leur gentillesse et les bons moments partagés durant cette période. Mes remerciements vont également à Dr. Coriolan TIUSAN du LPM de l'UHP, pour ses mesures AFM, ainsi qu'aux membres du LCM3B de l'UHP, pour plusieurs mesures DRX intéressantes.

I would also like to acknowledge Ms Barbara JOBST from Siemens CT MM7 for the XRD measurements. My appreciation goes also to Professor Dr. Dieter BÄUERLE and Dr. Johannes PEDARNIG from the Institute of Applied Physics of the JKU in Linz (Austria) for accepting me as a temporary member in their group, and especially Dr. Martin PERUZZI for his help with the XRD measurements and the nice impressions of Linz.

Finalement, je remercie chaleureusement mes parents MARIE-CLAIRE et JOACHIM pour leur support inconditionnel durant ces trois dernières années et toutes les années précédentes, ainsi que mes frères INGMAR, ALEXANDER et FREDERIK, pour leurs conseils et bonne compagnie. J'exprime ma plus profonde reconnaissance à MARTINE, pour ses encouragements, sa patience et tous les moments extraordinaires passés ensemble durant ces années pleines de hauts et de bas.

Munich et Nancy, Septembre 2006

Mathias LINK [mathias.link@a3.epfl.ch]

Table des matières

Introduction (English)

It is not because things are difficult that we do not dare,
it is because we do not dare that they are difficult.
[Seneca, epistulae morales 104, 26]

Ever improving and more cost-efficient medical diagnostics are among the challenges of future health care. With the decentralization of the point of care there is increasing demand for **easy-to-use, fast, reliable, miniaturized and inexpensive diagnostic devices**, e.g. for early detection and monitoring of cancer.

In this context, the **aim** of this thesis is to exploit micro-electromechanical systems (MEMS) used in high-frequency electronics applications, as bio-chemical sensors for the medical diagnostic market. More precisely, the objective is to **simulate, realize and characterize shear mode solidly mounted film bulk acoustic resonators**, and demonstrate their ability to function as **gravimetric sensors in liquid environments.** Since these goals may sound obscure, the following lines will briefly explain them and show how they were tackled in this work.

The **medical diagnostic market** encompasses the products needed for the detection and monitoring of disease by laboratory techniques. The systems are envisioned to be used in hospitals, in physician's offices and other point-of-care sites, as well as for testing at home. Today, the majority of clinical tests are performed in large independent clinical laboratories with advanced automated analytical equipment. In the shift towards the decentralization of the point of care and better cost-efficiency, bio-chemical MEMS (**BioMEMS**) and **miniaturized sensors** have much to offer. MEMS refer to devices with some of their dimensions in the micrometer range. They were introduced more than 20 years ago by combining sensors, actuators, and processing units. In the early years, this discipline was almost exclusively based on thin and thick film processes and materials borrowed from micro-electronics fabrication labs for mechanical applications such as pressure sensors, accelerometers and inkjet printer heads. Later MEMS applications broadened, with new manufacturing techniques and materials (like piezoelectric or biological materials) being added. The biological application field of MEMS is referred to as BioMEMS. It includes systems as diverse as disposable diagnostic sensors, micro-fluidic structures, systems speeding up medicine discovery or smart pills improving drug delivery.

In 2002, the Materials & Microsystems Group (MM2) of **Siemens** AG Corporate Technology (CT) in Munich started to work on BioMEMS sensors for the diagnostic market in collaboration with different

All references throughout this document will be given in the footnotes, in the form:
Author, *Journal Abbreviation* **Volume**, page number (year).

partners from all over **Europe**. The general objectives are the combination of microelectronics, life sciences and thin film sensor technologies for the **development of novel and inexpensive bio-chemical sensor arrays**. In particular, these sensors are to be applied for the **detection of cancer**. One of the main aims is to develop the core sensing element of the bio-chemical sensor. This task is partly treated within this thesis with the development of suitable **film bulk acoustic resonators (FBAR)**.

An FBAR consists of a piezoelectric thin film (such as ZnO, AlN or PZT) sandwiched between two metal electrodes and fabricated directly onto a carrier substrate (such as Si). By applying an electrical field to the electrodes, acoustic waves are excited in the piezoelectric film. If the film is acoustically isolated from its environment, the waves exist only in the bulk of the film and a standing wave pattern is developed in resonance. Such an FBAR is therefore similar to the well-established quartz crystal resonators with the difference that the thicknesses of the layers used for the FBAR are much thinner, between 100 nm and a few µm, and allow resonance frequencies at several GHz, whereas a typical quartz vibrates at around 10 MHz. FBARs have mainly been considered for radio-frequency (RF) applications and have been under development for over 40 years. But only recently, significant advances in integrated circuit processing have been obtained, permitting to reach microwave frequencies and practical manufacturing for high-volume applications. FBARs are suitable for front-end filters for global positioning system receivers and RF components such as filters, duplexers and oscillators.

In the same way as quartz resonators are applied as quartz crystal microbalances (QCM), FBARs can be used for physical, chemical and bio-chemical sensors. In the latter case, **the mass adsorbed or deposited on the FBAR surface induces a frequency change that can be measured**. The surface of the FBAR is functionalized with a bio-chemical receptor coating, which is able to selectively adsorb target molecules. When the target species interacts or binds with the surface bound probe molecules, the mass load of the resonator is increased and the resonant frequency proportionally decreased. The use of FBARs for bio-chemical sensing applications appeared only recently, CT MM2 being one of the first groups to publish the idea in 2003.[1]

FBARs have several **advantages** over other sensing principles. First, there is the **label-free** detection common to all gravimetric sensing principles. Traditional methods for bio-chemical detection require chemical labelling or the use of fluorescent tags, which can compromise the bio-chemical activity. The label-free detection also gives the possibility of a **quantitative time-dependent measurement** of the reaction. For FBARs operating at a few GHz, the **mass sensitivity can be 1000 times larger than that of a QCM** whose working resonance is in the MHz range. Limits of detection are expected to be of the same order of magnitude than for the QCMs. Moreover, since the device uses standing waves in the direction perpendicular to the substrate surface and standard micro-technologies are used to structure the resonator, the lateral sensor dimensions can be downscaled to $10\,\mu m \times 10\,\mu m$. They can be integrated together with CMOS on silicon substrates. Due to their small size, they can be **mass produced to yield inexpensive sensors**, and **arrayed** for the simultaneous analysis of multiple targets.

[1] R. Gabl, M. Schreiter, E. Green, H.-D. Feucht, H. Zeininger, J. Runck, W. Reichl, R. Primig, D. Pitzer, G. Eckstein, W. Wersing, *Proc. IEEE Sensors*, Toronto, 1184 (2003).

In a gaseous environment, FBARs operating in the longitudinal wave mode are appropriate, since there is no loss of energy to the environment. However, FBARs using the longitudinal wave mode are drastically affected when used for sensing in liquid phase environments. In fact, displacements normal to the surface generate compressional waves dissipating into the liquid. The resulting energy losses reduce the mass resolution substantially. In contrast, the **shear wave mode**, with a deflection parallel to the surface, allows an operation in liquids with only minor damping effects due to viscous loading. The excitation of shear waves requires a certain orientation of the exciting electric field with respect to the crystallographic orientation of the material. FBARs have fixed electrodes on the top and bottom of the film resulting in an electric field perpendicular to the substrate surface. For materials like ZnO, it was shown that shear wave-modes can be excited when the **c-axis of the ZnO is inclined with respect to the surface normal**.[2] But ZnO thin films grow preferentially with their crystallographic c-axis perpendicular to the substrate, allowing only longitudinal mode excitation. One of the main tasks of this work is thus to develop a suitable process for the deposition of c-axis inclined ZnO.

An FBAR also requires interfaces that confine waves to a finite volume in an efficient manner. Ideally, both interfaces are solid-to-air interfaces. Most quartz resonators come very close to this condition. There are several techniques for FBARs to prevent energy dissipation into the substrate and to keep the wave confined within a desired volume. In this work, the solidly mounted option is chosen. Here, the acoustic isolation from the substrate is obtained by means of an acoustic mirror that is composed of several pairs of quarter-wavelength layers with a high acoustic impedance contrast. Such **solidly mounted FBARs (SMR)** are favourable for integration and can be fabricated on a wide variety of substrates. It is a planar technology, with a simple fabrication and mechanical robustness. The latter is important in respect that chips have to undergo coating steps as well as packaging.

Contents

The **organization and content** of this thesis are shaped by the large number of interdisciplinary fields which have an influence on the device operation. The various subjects encompass among others piezoelectric properties of thin films, high-frequency electronics, clean room manufacturing techniques or measurements in liquid environments. Since it was mainly carried out in an industrial applied research laboratory, the goal was to obtain results in the fastest and most cost-efficient way and to confirm concepts. Both the realization and the characterization of structures were bound to economic and timely restrictions. After a review of the basics, the report will follow a straightforward path, depicted on Figure Ie. Based on the information given in the above lines, the subjects that were treated in this thesis are structured into five distinct chapters:

Chapter 1 gives the basics and state of the art of this work. An overview on biological micro-electromechanical systems (BioMEMS) and modern sensors with different sensing mechanisms is shown. It describes different resonant devices, including FBARs. It will also give the basics of piezoelectricity, possible materials and thin film deposition methods. Moreover, the projects in which this thesis is situated

[2] N. F. Foster, G. A. Coquin, G. A. Rozgonyi, F. A. Vannatta, IEEE Trans. Sonics Ultrason., **SU-15**, 28 (1968).

are described more precisely.

Chapter 2 deals with the theoretical calculations, the modelling of FBARs for numerical simulations and the main characterization methods. Since the FBARs use c-axis inclined ZnO films, the obtained models are complex, and models like the Mason Model or the Butterworth-Van Dyke need to be adapted. Characterization tools, which permit to extract the main parameters of the sputtered ZnO films or the solidly mounted FBARs, are described.

Chapter 3 describes the development of suitable c-axis inclined ZnO deposition processes. After a review of the basics of sputtering and thin film growth, different process possibilities are presented. Then three processes developed in this work and building on each other are presented in detail, with respective explanations for inclined ZnO growth mechanisms and results of the electrical characterization.

Chapter 4 describes the realization, characterization and optimization of solidly mounted FBARs. Simulations tools are used to find the correct dimensions prior to the fabrication of the devices, which are then characterized in air using the methods derived in Chapter 2. Parameters such as the resonance frequencies, the coupling coefficients and the Q-factors are extracted and expected sensing characteristics are presented.

Chapter 5 shows the characterization of SMRs in different liquid environments. This includes the study in liquids with different viscosities to see the influence on the resonance frequencies and the quality factors. First bio-chemical experiments, which have been performed together with partners from EU projects, are shown at the end of this chapter.

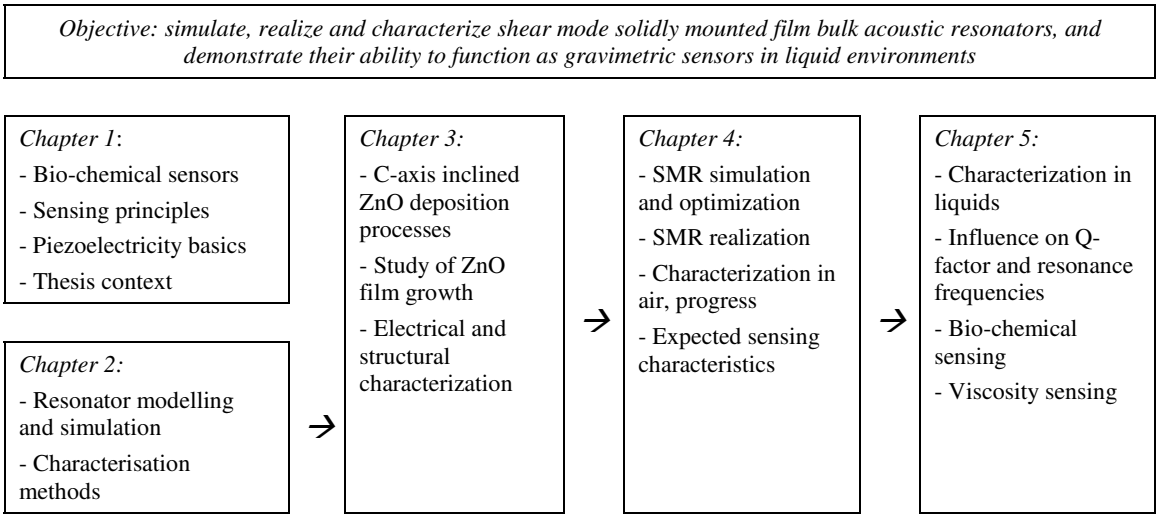

Figure Ie: Structure of the thesis.

Introduction (Français)

Ce n'est pas parce que les choses sont difficiles que nous n'osons pas,
c'est parce que nous n'osons pas qu'elles sont difficiles.
[Sénèque, epistulae morales 104, 26]

Pouvoir réaliser des **diagnostics médicaux de plus en plus rapides et efficaces, tout en minimisant les coûts**, tels sont les défis majeurs du futur système de la santé publique. Avec la décentralisation des points de traitement, la demande en **systèmes de diagnostic faciles à utiliser, rapides, fiables, miniaturisés et bon marché est croissante**, p.ex. pour le dépistage et l'observation du cancer.

Dans ce contexte, le **but** de cette thèse est d'exploiter des systèmes micro-électromécaniques (MEMS), qui sont utilisés dans des applications d'électronique hautes fréquences, comme capteurs biochimiques pour le marché croissant du diagnostic médical. Plus précisément, l'objectif est de **simuler, réaliser et caractériser des résonateurs à ondes acoustiques de volume à base de couches minces, vibrant en mode de cisaillement et montés sur miroir acoustique,** et de démontrer leur capacité à fonctionner comme **capteurs gravimétriques en milieux liquides**. Cette description pouvant paraître compliquée, les lignes qui suivent donnent de brèves explications et montrent comment ce travail a été abordé.

Le **marché du diagnostic médical** comprend les produits nécessaires pour la détection et le suivi de maladies avec des techniques de laboratoire. Il est envisagé d'utiliser les systèmes en question dans des hôpitaux, dans des cabinets médicaux et dans d'autres points de traitement ainsi que pour des tests à domicile. Aujourd'hui la majorité des tests cliniques sont effectués dans de grands laboratoires indépendants avec un équipement analytique avancé et automatisé. Les MEMS biochimiques (**BioMEMS**) et les **capteurs miniaturisés** peuvent jouer un rôle important pour la décentralisation du point de traitement et une meilleure gestion des coûts. Les MEMS sont des systèmes avec au moins une dimension micrométrique. Ils ont été introduits il y a plus de 20 ans en combinant capteurs, actionneurs et unités de traitement de l'information. Au début, cette discipline était presque exclusivement basée sur des procédés de couches minces et épaisses, ainsi que sur des matériaux empruntés aux laboratoires de fabrication microélectronique, pour des applications telles que capteurs de pression, accéléromètres et têtes d'imprimantes à jet d'encre. Ensuite, d'autres applications ont vu le jour, avec l'avènement des nouvelles techniques de fabrication et un choix de matériaux plus large. Le champ d'application biochimique des MEMS est connu sous le nom de BioMEMS. Ceux-ci incluent des systèmes tels que les capteurs pour le diagnostic médical, les structures microfluidiques,

---

Les références de ce document sont données dans les notes en bas de page, sous la forme:
Auteur*, Abréviation du Journal* **Volume**, numéro de la page (année).

les systèmes pour la recherche médicale ou encore les pilules intelligentes pour la médication.

En 2002, le groupe de matériaux et microsystèmes (MM2) des laboratoires de la centrale de recherche de **Siemens** (CT) à Munich a commencé à travailler sur des BioMEMS pour le marché du diagnostic médical en collaboration avec différents partenaires **européens**. Ces coopérations ont comme objectifs la combinaison de la microélectronique, des sciences de la vie et des technologies de dépôt et de structuration de couches minces pour le développement de matrices de capteurs biochimiques intégrés et bon marché. En particulier, ces capteurs devraient permettre la détection de différents types de cancers. Un des buts principaux est de développer le système de détection central du capteur biochimique. Cette tâche est en partie traitée dans cette thèse avec l'étude de **résonateurs à ondes acoustiques de volume à base de couches minces (FBAR)**.

Un FBAR est constitué d'une couche mince piézoélectrique (p.ex. ZnO, AlN ou PZT) intercalée entre deux électrodes métalliques et fabriquée directement sur un substrat porteur (p.ex. du Si). En appliquant un champ électrique entre les deux électrodes, des ondes acoustiques sont excitées dans la couche piézoélectrique. Si la couche est isolée de son environnement, les ondes sont excitées uniquement dans le volume du matériau et un profil d'onde stationnaire est développé en résonance. Un FBAR est donc similaire aux résonateurs à quartz avec la différence que les épaisseurs des couches utilisées pour les FBARs sont beaucoup plus faibles, entre 100 nm et quelques µm. Ceci permet d'atteindre des fréquences de résonance de quelques GHz, tandis qu'un quartz typique vibre aux alentours de 10 MHz. Depuis plus de 40 ans, les FBARs ont été étudiés pour des applications électroniques de radiofréquences (RF). Mais c'est seulement récemment que des avancées significatives dans la fabrication de circuits intégrés ont permis d'atteindre ces fréquences et d'arriver à de grands volumes de production. Les FBARs peuvent être utilisés comme filtres pour les systèmes de réception GPS et dans des composants électroniques RF (p.ex. des oscillateurs).

Tout comme les résonateurs à quartz peuvent être appliqués comme microbalances à quartz (QCM), les FBARs peuvent être utilisés comme capteurs physiques, chimiques ou biochimiques. Dans ce cas, **la masse adsorbée ou déposée à la surface du FBAR induit un changement de la fréquence de résonance qui peut être mesuré**. La surface du FBAR est fonctionnalisée avec une couche réceptrice biochimique, capable d'adsorber sélectivement les molécules à détecter. Quand la molécule interagit ou se lie à la surface, la masse attachée au résonateur augmente et la fréquence de résonance décroît proportionnellement. L'utilisation de FBARs pour des applications de détection biochimique n'est apparue que récemment, CT MM2 étant un des premiers groupes à publier cette idée en 2003.[1]

Les FBARs ont plusieurs **avantages** par rapport à d'autres principes de détection. Premièrement, la détection se fait **sans marquage physique supplémentaire**, ce qui vaut pour tous les systèmes gravimétriques. D'autres méthodes de détection biochimique nécessitent des marqueurs chimiques ou fluorescents, qui peuvent compromettre l'activité biochimique. En outre, la détection sans marqueurs donne la possibilité d'une mesure quantitative en fonction du temps. Pour des FBARs opérant à des fréquences de plusieurs GHz, la sensibilité massique peut être 1000 fois plus élevée que celle des QCM, pour lesquels les fréquences de résonance se situent dans le domaine des MHz. Les résolutions sont estimées être du même ordre de

[1] R. Gabl, M. Schreiter, E. Green, H.-D. Feucht, H. Zeininger, J. Runck, W. Reichl, R. Primig, D. Pitzer, G. Eckstein, W. Wersing, *Proc. IEEE Sensors*, Toronto, 1184 (2003).

grandeur que pour les QCMs. De plus, comme le résonateur utilise des ondes stationnaires dans la direction perpendiculaire à la surface du substrat et que des microtechnologies standard sont utilisées pour structurer le résonateur, les dimensions latérales du capteur peuvent être réduites à $10\,\mu m \times 10\,\mu m$. Les FBARs peuvent être intégrés avec de l'électronique CMOS sur des substrats en silicium. De part de leur faible taille, les FBARs peuvent être fabriqués en grande série, ce qui permet d'obtenir des capteurs bon marché, et des matrices de capteurs pour l'analyse simultanée de molécules différentes.

En milieu gazeux, les FBARs vibrant en mode longitudinal sont appropriés, puisqu'il n'y a pas de pertes d'énergie vers l'environnement. Toutefois, les FBARs utilisant le mode longitudinal sont drastiquement affectés quand ils sont utilisés en milieu liquide. En effet, des déplacements normaux à la surface génèrent des ondes se propageant dans le liquide. Ces pertes d'énergie réduisent substantiellement la résolution. En revanche, le **mode de cisaillement**, avec une déflection parallèle à la surface, permet un fonctionnement en milieu liquide avec uniquement de faibles pertes dues à la viscosité. L'excitation du mode de cisaillement requiert une certaine direction du champ électrique par rapport à l'orientation cristallographique du matériau piézoélectrique. Les FBARs possèdent des électrodes au-dessus et au-dessous de la couche piézoélectrique, ce qui donne un champ électrique perpendiculaire à sa surface. Pour des matériaux comme le ZnO, il a été montré que le cisaillement ne peut être excité que **si l'axe c du ZnO est incliné par rapport à la normale de la surface**.[2] Malheureusement, les couches minces de ZnO croissent de préférence avec leur axe c perpendiculaire à la surface, ce qui n'autorise que l'excitation du mode longitudinal. Une des difficultés majeures de cette thèse a donc été de développer un procédé de dépôt de ZnO à axe c incliné.

Un FBAR a également besoin d'interfaces confinant les ondes dans un volume fini d'une manière effective. Idéalement, celles-ci sont des interfaces air-solide. Les résonateurs à quartz satisfont généralement cette condition. Pour les FBARs, il existe plusieurs techniques permettant d'éviter la dissipation d'énergie dans le substrat et de garder les ondes dans un certain volume. Dans ce travail, c'est celle du miroir acoustique qui a été choisie. L'isolation acoustique du substrat est obtenue en utilisant plusieurs paires de couches minces d'une épaisseur d'un quart de longueur d'onde possédant un grand contraste d'impédance acoustique. Ces **FBARs sur miroir acoustique (SMR)** sont faciles à intégrer et peuvent être fabriqués sur un grand nombre de substrats différents. Il s'agit d'une technologie planaire avec une bonne robustesse mécanique. Ceci est très important puisqu'en général les capteurs subissent différents traitements de surface et de packaging.

Contenu

L'organisation et le contenu de cette thèse reflètent l'interdisciplinarité que demandent la réalisation et la caractérisation des FBARs. Les sujets traités comprennent entre autres les propriétés piézoélectriques de couches minces, l'électronique hautes fréquences, les techniques de réalisation en salle blanche, et les mesures en milieux liquides. Comme la thèse a surtout été réalisée dans un laboratoire industriel de recherche appliquée, l'objectif était d'obtenir des résultats d'une manière rapide et peu coûteuse, et de confirmer des concepts. La réalisation et la caractérisation des structures étaient liées à des restrictions temporelles et économiques. Après un rappel des bases, ce rapport de thèse va suivre une voie logique, montrée à la Figure If. Les sujets traités dans cette thèse sont structurés en 5 chapitres :

[2] N. F. Foster, G. A. Coquin, G. A. Rozgonyi, F. A. Vannatta, IEEE Trans. Sonics Ultrason., **SU-15**, 28 (1968).

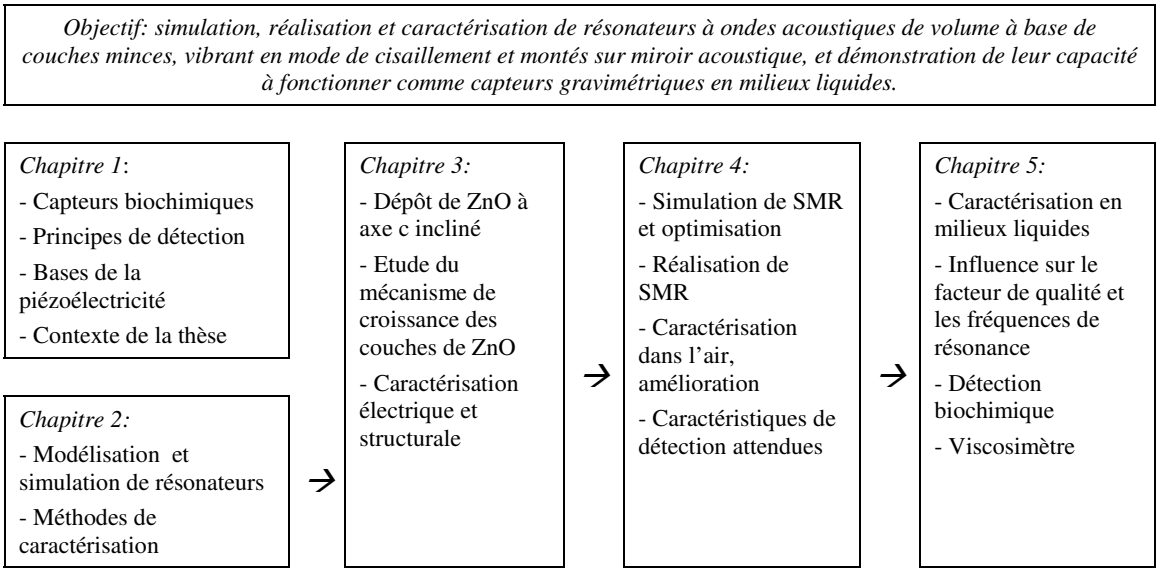

Figure If: Structure de la thèse.

Le **Chapitre 1** expose les bases et l'état de l'art de ce domaine de recherche. Une vue d'ensemble des BioMEMS et de capteurs biochimiques modernes utilisant différents principes de détection est présentée. Y sont également décrits différents systèmes résonants, dont les FBARs. Les bases de la piézoélectricité sont brièvement expliquées, avec les matériaux et les méthodes de dépôt de couches minces. De plus, les projets dans le cadre desquels s'inscrit cette thèse, sont décrits plus précisément.

Le **Chapitre 2** présente les développements théoriques, la modélisation de FBARs pour des simulations numériques et les principales méthodes de caractérisation. Comme les FBARs utilisent des couches minces de ZnO à axe c incliné, les modèles obtenus sont complexes et des modèles comme ceux de Mason ou de Butterworth-Van Dyke doivent être adaptés. Les outils de caractérisation, permettant d'extraire les principaux paramètres des couches minces de ZnO ou des FBARs sur miroir acoustique, sont décrits.

Le **Chapitre 3** décrit le développement de procédés de dépôt de couches minces de ZnO à axe c incliné. Les bases de la pulvérisation et de la croissance de couches minces sont exposées et les différentes possibilités de dépôt sont présentées. Ensuite, les trois procédés développés successivement dans ce travail sont présentés en détail, avec les explications respectives pour les mécanismes de croissance du ZnO et les résultats de la caractérisation électrique.

Le **Chapitre 4** présente la réalisation, la caractérisation et l'optimisation de SMRs. Des simulations sont utilisées pour trouver les épaisseurs correctes avant la réalisation. Les SMRs sont caractérisés à l'air et les principaux paramètres comme la fréquence de résonance, les coefficients de couplage et les facteurs de qualité sont extraits. Les caractéristiques de détection attendues sont présentées.

Le **Chapitre 5** traite de la caractérisation des SMRs dans différents milieux liquides et de l'influence de la viscosité sur la fréquence de résonance et sur le facteur de qualité. Les résultats des premières expériences biochimiques effectuées avec des partenaires des projets européens sont présentés en fin de ce chapitre.

1. State of the art and basics

Etat de l'art et concepts de base — *Résumé*: Ce chapitre donne une vue d'ensemble des différents thèmes traités dans ce travail ainsi qu'un bref aperçu de l'état de l'art. Les **FBARs**, résonateurs à ondes acoustiques de volume à base de couches minces, ont traditionnellement été utilisés pour réaliser des filtres et des oscillateurs à hautes fréquences. Dans le contexte de cette thèse, les FBARs sont utilisés comme **capteurs biochimiques pour le diagnostic médical**. Pour cette raison, un aperçu du marché du diagnostic médical et des microsystèmes électromécaniques biochimiques (BioMEMS) est donné. Les caractéristiques d'un capteur biochimique sont brièvement analysées, les plus importantes étant sa **sensibilité, sa résolution et sa spécificité**. Une comparaison des différents principes physiques servant à transformer l'information biochimique en information physique est présentée. Les avantages des FBARs utilisés comme capteurs acoustiques gravimétriques résident dans une **détection sans marquage physique supplémentaire, quantitative et dépendante du temps, possédant une bonne résolution et une haute sensibilité, et alliant une réalisation bon marché et une intégration possible en matrices de capteurs avec de l'électronique CMOS**. Puisque ces capteurs sont basés sur des couches minces piézoélectriques telles que le ZnO, la piézoélectricité, les matériaux utilisés et les méthodes de dépôt sont brièvement expliqués. Enfin, les objectifs de ce travail et son rôle dans deux projets européens sont exposés. L'utilisation des FBARs comme capteurs gravimétriques et le **fonctionnement en mode de cisaillement** requis pour les applications en milieu liquide sont également présentés.

1.1. Introduction

This chapter gives an overview of the different parts treated in this thesis. First, in paragraph **1.2**, we introduce the context of this thesis. The developed system aims to address the medical diagnostic market, of which a brief overview is given. It belongs to biochemical electromechanical systems (BioMEMS) used as sensors, of which the functioning and general structure are explained. Secondly, in paragraph **1.3**, the different technologies used for sensors are compared, particularly acoustic gravimetric sensors. Then, the basics of piezoelectricity, possible materials and thin film deposition methods are detailed in paragraph **1.4**. Finally, in paragraph **1.5**, the system developed in this thesis is shown, along with the concept of a complete bio-chemical sensor envisioned in the framework of two European projects.

1.2. Bio-chemical sensors for the medical diagnostic market

1.2.1. Miniaturization in the medical diagnostic market

At the beginning of this thesis, the European average per capita annual expenditure for health care was about 1700 € and the total world health market was about 1700 billion €.[1] Research associated with it can grossly be divided into three domains: (a) diagnostics (e.g. diabetic tests), (b) treatment of medical data (e.g.

[1] Figures for 2002 in: M. J. Madou, *Fundamentals of Microfabrication*, CRC Press, Bacaraton, FL (2002).

information systems) and (c) image-giving techniques (e.g. computer tomography).[2] The work of this thesis has been done in the context of two international research projects of the European Union. Both aim at developing solutions for the diagnostics market, which is about 1.7 billion € and is projected to grow with a rate of up to 20 % in the next years.[3] It encompasses the instruments and solutions used for the screening, diagnostics, monitoring, or detection of disease by laboratory techniques. The products are envisioned to be used in hospitals and private laboratories, in physician's offices and other point-of-care sites (e.g. intensive care units or nursing homes) as well as for tests performed at home (e.g. diabetic glucose or pregnancy tests). In contrast, today the majority of clinical tests are performed in large independent clinical laboratories with advanced automated, analytical equipment. As the amount of resources spent on health care increases, there is a growing pressure for the decentralization of the point of care. Easy-to-use, fast, miniaturized and inexpensive diagnostic devices are increasingly demanded. In this shift, bio-chemical micro-systems and miniaturized sensors have much to offer. Judging by the number of scientific publications, research in this area has steadily grown in the last decade (Figure 1.1).[4]

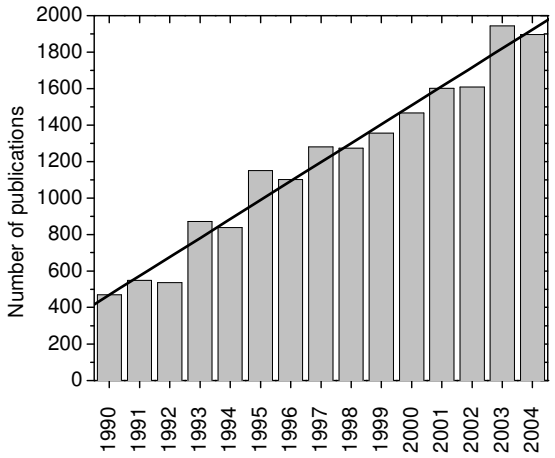

Figure 1.1 : Number of publications addressing bio-chemical sensors in the INSPEC Database.[4]

1.2.2. Biological Micro-electromechanical systems (BioMEMS)

Micro-electromechanical systems (MEMS) refer to devices with some of their dimensions in the micrometer range. They were introduced more than 20 years ago by combining sensors, actuators, and processing units. In the early years, this discipline was almost exclusively based on thin and thick film processes and materials borrowed from integrated-circuit (IC) fabrication labs (like lithography and single-crystal and polycrystalline Si) for mechanical applications such as pressure sensors, accelerometers and inkjet printer heads. In the 1990s MEMS applications broadened, with microphones, radio frequency (RF) MEMS and optical MEMS.

[2] Personal communication from J. Weber, Molekulare Medizin Conference, Erlangen (2005).
[3] Web-Site: http://www.chemlin.de/news/nov04/2004111202.htm; November 2005.
[4] *INSPEC database*, keywords "Sensor or sensing" and "chemical or biological or bio or medical", October 2005.

Emphasis shifted to a wider view of manufacturing methods. New techniques such as micro-molding, laser machining or ion- and electron-beam machining were introduced. A multitude of IC-distant materials (like piezoelectric or biological materials) was added to make new applications possible. Recently, nano electro-mechanical systems (NEMS) with dimensions in the nanometer range have made their apparition,[5] e.g. systems using carbon nano tubes.[6] Optimistic predictions of 2004 show that the total MEMS and NEMS market will reach around 800 billion $ in 2015, up from around 100 billion $ in 2000.[7] In 2004, 2059 publications referring to MEMS and NEMS were registered in the INSPEC database, up from only 45 in 1994.[8]

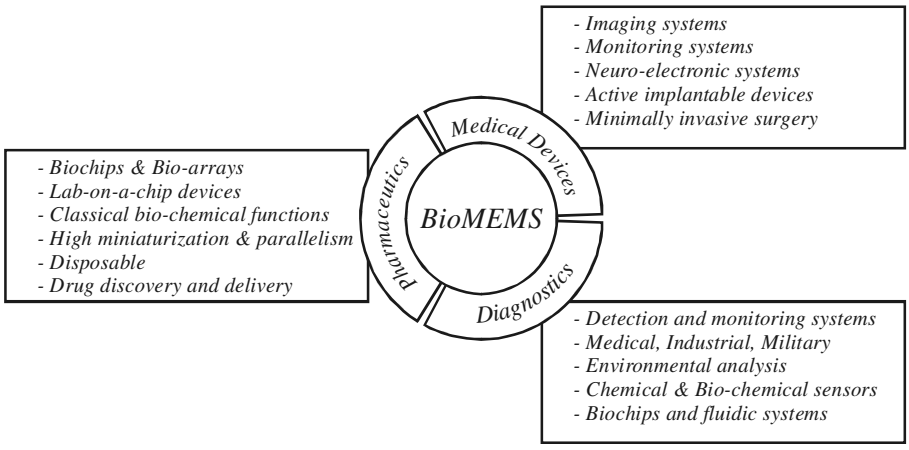

Figure 1.2 : BioMEMS markets and applications.[9]

The biological application field of MEMS is often referred to as BioMEMS. It includes systems as diverse as disposable diagnostic sensors, micro-fluidic structures, systems speeding up medicine discovery or smart pills improving drug delivery. As shown in Figure 1.2, BioMEMS can generally be divided in three markets with different applications:[9]

Pharmaceutical: Bio-chips, bio-arrays and lab-on-a-chip devices belong to this category. They feature classical biological experiments, but at a high miniaturization (thus lower volumes) and high parallelism. The devices are mostly disposable and aim at drug discovery and delivery. They include micro-fluidic dispensing systems and screening possibilities.

Medical Devices: Interface and communication devices for medical applications can be situated here. This includes imaging systems, electronic monitoring systems, neuro-electronic systems or active implantable devices (e.g. electronics cell). Some systems aim at minimally invasive surgery.

---

[5] S. E. Lyshevski, *MEMS and NEMS : systems, devices, and structures*, CRC Press (2002).
[6] D. Sickert, S. Taeger, A. Neumann, O. Jost, G. Eckstein, M. Mertig, W. Pompe, *AIP Conf. Proc.* **786**, 271 (2005).
[7] *Small wonders, A survey of nanotechnology*, The Economist, London (2005).
[8] Research in the *INSPEC database*, Keywords "MEMS" and "NEMS", November 2005.
[9] Classification based on: Nexus [www.nexus-mems.com]; M. J. Madou, *Fundamentals of Microfabrication*, CRC Press, Bacaraton, FL (2002).

Diagnostics: This category includes detection systems for (a) medical diagnostic, (b) control of industrial processes, e.g. chemical, pharmaceutical and food industry, (c) environmental monitoring and (d) military applications. These systems allow doing a complete analysis in a device of only a few mm^2; biochips, fluidic systems and bio-chemical sensors belong to this category.

This work is concerned with bio-chemical sensors for medical diagnostics. Low cost, highly integrated, fast and sensitive sensors and sensor arrays are key components for this growing market. Depending on the application, bio-chemical sensors can also be referred to as electronic noses or tongues. Other popular denominations are Micro-total-analysis systems (μ-TAS) or BioChemLab-on-a-chip.[10]

1.2.3. Modern bio-chemical sensors

Modern bio-chemical sensors developed with advanced micro-fabrication technologies and signal processing techniques use a broad range of sensing mechanisms such as electrochemical, optical and acoustic, which will be treated in more detail in paragraph 1.3. The miniaturization of classical measurement techniques has led to the realization of complex analytical systems. A conceptual model of a modern bio-chemical sensor is shown in Figure 1.3.[11] This model presents a complete scheme in which, in addition to a sensing section of the sensor, microfluidic, signal processing and packaging units are included. Simultaneous design of all these elements is essential for the development of successful sensors. The principle of operation of such a sensor can be understood by following its sensing path (indicated by arrows in Figure 1.3).

A measurand is introduced to the sensor using a sample delivery system or by bringing the sensor to the patient, as with implantable sensor probes. Tumor markers for example, which can be specific to a particular type of cancer, can be found in the blood, serum, urine or body tissues of patients.[12] Micro-fluidic systems like pumps or channels help to bring the measurand to the sensing element. Next, it passes through a pre-processing section such as semi-permeable membrane which performs an initial selective screening of possible interfering factors.[13] After that the measurand is exposed to a biologically active substance, which is selective to the measurand of interest. This substance can be in the form of a thin film deposited on the sensor surface, or another molecule attaching to the measurand in liquid phase. Various bio-chemical mechanisms are used in this recognition step. The first group, called **catalytic biosensors**, uses **enzymes** (i.e. proteins that catalyze specific chemical reactions in our body) as their recognition element. A second group is based on an **immuno-chemical** reaction, i.e. a specific attachment between **antigens** (proteins that stimulate an immune response) and **antibodies** (proteins of our immune system), or **complementary DNA** strands.[14]An important issue here is how to immobilize the receptor layers on the sensor surface (e.g. self-assembling mono-layers of thiols or silanes, on respectively, gold and oxide surfaces).

---

[10] S. D. Gawad, PhD Thesis N°3011, EPFL, Lausanne (2004).
[11] Representation based on: G. L.Coté, R. M. Lec, M. V. Pishko, *IEEE Sensors J.* **3**, 251 (2003); R. M. Lec, *Proc. IEEE Int. Freq. Contr. Symp.*, 419 (2001); A. Campitelli, E. Parton, *Solid State Technology*, July, 87 (2002).
[12] P. W. Laird, *Nature Reviews* **3**, 253 (2003).
[13] R. M. Lec, *Proc. IEEE Int. Freq. Contr. Symp.*, 419 (2001).
[14] A. Campitelli, E. Parton, *Solid State Technology*, July, 87 (2002).

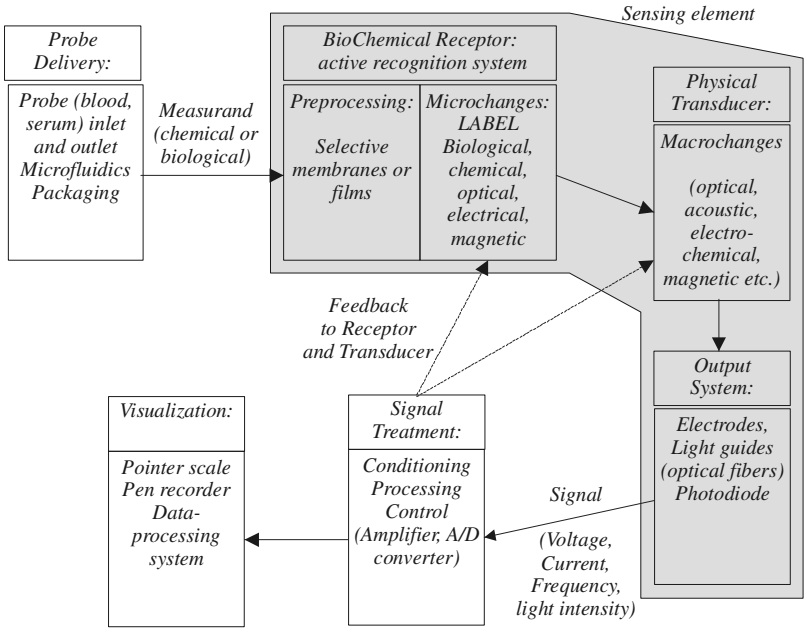

Figure 1.3 : General diagram of a modern biochemical sensor. The arrows show the sensing path. The sensor could also be an array that allows for simultaneous detection of multiple analytes.[11]

When the measurand interacts with the biologically active substance, microscopic physical, chemical, and/or biochemical changes are produced. Depending on the sensing principle, **labels** are needed to produce these changes. Examples of labels are fluorescent molecules or magnetic beads. A principle that in general is label-free is the gravimetric sensing principle. The microscopic changes cause macroscopic physical changes which are converted by a transducer into an output signal, usually voltage, current or frequency. The different physical methods that can be used for this conversion will be treated in paragraph 1.3. Finally, the output signal is conditioned, processed and displayed. The processing can implement important sensor features such as self-calibration, self-diagnostic and pattern recognition. All these elements are enclosed in a package that provides measurement integrity to the device.[15]

Today, most bio-chemical sensors involve sizable instruments. Only some of the components have been miniaturized. Microsystems of this type have a price similar to that of large instruments.[16] Examples of commercial products of bio-chemical sensors for diagnostic applications are Nanogen's NanoChip molecular biology workstation, Caliper's microfluidic LabChip systems, and Agilent's MicroGC.[17] The miniaturized components enable some improved functionality, but not yet a lower cost or a smaller, perhaps hand-held, instrument. Exceptions are Texas Instruments' portable surface plasmon resonance (SPR) sensor (Spreeta) and hand-held reader, i-STAT's hand-held automated blood analyzer and Siemens' Quicklab shown on Figure 1.4.

[15] A. Campitelli, C. Batric, J-M. Friedt, K. De Keersmaecker, W. Laureyn, L. Francis, F. Frederix, G. Reekmans, A. Angelova, J. Suls, K. Bonroy, R. De Palma, Z. Cheng, G. Borghs, *Proc. IEEE Cust. Integr. Circ. Conf.*, 505 (2003).
[16] M. J. Madou, *Fundamentals of Microfabrication*, CRC Press, Bacaraton, FL (2002).
[17] [www.nanogen.com], [www.caliperls.com]; [www.chem.agilent.com].

a) *b)* *c)*

Figure 1.4 : Examples of existing bio-chemical sensors for the medical diagnostic market. a) TI Spreeta SPR sensor, b) i-STAT's hand-held automated blood analyzer, c) Siemens Quicklab.[18]

1.2.4. Important characteristics of a sensor

The key features of bio-chemical sensors are defined in the following and will be used throughout this document. The most important features are specificity, sensitivity and limit of detection.[19] The **specificity** or **selectivity** of a sensor is its ability to pick out one parameter without interference of other parameters. It is an essential parameter since a sensor becomes useless if its response is linked to compounds other than that which have to be measured. It determines the accuracy of the measurement, which represents the agreement with the true content of the sample. Specificity is always limited, and bio-chemical sensors tend to report higher concentrations than a sample actually contains. It is mostly determined by the biological interface layer and the labels that attach to the measurand.

The (absolute) **sensitivity** of a sensor is its capability to measure changes in a given measurand. It describes how the output signal changes with changes of a certain measurand property like mass attachment:

$$S_a = \frac{\Delta \text{ Output Signal}}{\Delta \text{ Measurand Properties Change}} \tag{1.1}$$

The relative sensitivity has been normalized to the initial output. It can be used to compare different sensing principles and sensors within one category:

$$S_r = \frac{1}{\text{Initial Output}} S_a \tag{1.2}$$

The **limit of detection (LOD)** or **resolution** is reached when the output signal goes below three times the noise level, where the noise is quantified by the standard deviation σ_{noise} of the signal:[20]

$$LOD = \frac{1}{S_a} \cdot 3 \cdot \sigma_{noise} \tag{1.3}$$

At this low measurand property change, no quantitative measurements are possible and the sensor can only act as a probe to measure whether the measurand is present or not. At around three times the LOD, one can

[18] [http://www.ti.com/snc/products/sensors/spreeta.htm]; [www.i-stat.com]; [http://w4.siemens.de/ct/en/technologies/ps/beispiele/lab.html].
[19] G. L.Coté, R. M. Lec, *IEEE Sensors J.* **3**, 251 (2003).
[20] E. J. Uttenthaler, PhD Thesis, Universität der Bundeswehr, München (2002).

start to make quantitative measurements.[20] The LOD becomes often worse as the sensor ages.

The **dynamic response range** of a sensor is the range over which the sensor is usable. The broader the dynamic response range, the less important are dilution or enrichment steps during sample preparation. It is limited by the LOD at the lowest concentration end and by saturation effects at the highest levels. A good bio-chemical sensor should function over at least one or two concentration decades. The **response time** of a sensor is usually not defined in an exact way. It is the time interval over which a signal reaches a certain percentage (e.g. 90 %) of its final value. The particular percentage which is chosen represents a pragmatic decision, since most signal-time curves follow an exponential increase or decrease where the true final value is unknown. Specification in terms of the time constant is clearer. It corresponds to the time required for a signal to reach about 63 % of its final value and can be found without waiting for a final reading, by the slope of the curve signal against time.[21] Typical response times for bio-chemical sensors are in the range of seconds, but some sensors require several minutes to reach a final reading.[22]

There are two kinds of **reliability**. The first is comparable to specificity and is a measure of the accuracy of a result. The second is a function of the time during which the sensor performs satisfactorily without a breakdown or need for repair. This time can be remarkably great (in the range of years), as in the case of membrane electrodes. On the other hand, a bio-chemical sensor that depends upon a cascade of enzymes to produce a signal will usually have a short span of proper functioning (a few days only). Problems associated with insufficient lifetimes are best overcome with mass-produced miniaturized replacement sensors based on inexpensive materials. This also circumvents surface fouling, interfering layers of proteins, and certain drift and poisoning problems. **Other important features** of a bio-chemical sensor are: biocompatibility, robustness, small size and low cost. In addition, the sensor must have compatibility with the chemical, optoelectronic, or electronic IC processing technology.

1.3. Acoustic and other sensing technologies

In this paragraph, important features and basic working principles of acoustic and other sensing technologies are presented and compared concerning their **sensitivities, limits of detection, and qualitative advantages** and **disadvantages**. Bio-chemical sensors can be categorized either by the measurand, or the **transducer mechanism**. The latter method is chosen here. Currently, electrochemical, optical and acoustic wave sensing technologies have emerged as the most promising bio-chemical sensor technologies. Common to most optical and electrochemical principles is the requirement for a label, equipped with the physical information to stimulate the transducer, but increasing the complexity and thus the cost for analysis. Examples of labels are the coupling with an enzyme, a fluorescent molecule, a magnetic bead or a radioactive element.[23] A detection principle, which in general is **label-free**, is the **acoustic gravimetric principle**. A rather

[21] The signal against time curve generally follows a trend of the form: $A\times(1-e^{-kt})$. The time constant k defines the slope of the curve at the origin and at t=1/k, the curve has reached $(1-e^{-1})$ which corresponds to 63 %.
[22] T. Auth, Chemical and Biochemical Sensors, Siemens IRC Technology Report (2004).
[23] G.Asch, *Les capteurs en instrumentation industrielle*, Dunod, Paris, 1999.

comprehensive overview of sensing technologies for biochemical applications was given by Coté *et al.*[24]

1.3.1. Sensors based on acoustic principles

Acoustic sensors have benefited from the decades-long growth of radio-frequency (RF) telecommunication technologies. The piezoelectric elements, utilized in radars, cellular phones or electronic watches, have been well applied to sensors.[25] Since the late 1950s, it has been recognized that one can make sensitive high-resolution sensors by exploiting the effects of various bio-chemical and mechanical measurands (e.g. temperature, pressure, density, viscosity) on propagating or standing acoustic waves. Examples are the first study of a vibrating piezoelectric crystal in a chemical solution by King in 1964,[26] or the use of acoustic waves as pressure-sensors.[27] In bio-chemical sensing, the resonance frequency change due to a mass attachment on the sensor surface is of interest. One speaks of a **gravimetric** detection. It has been used to study physico-chemical properties of gases, liquids, and solids for decades.

Different types of acoustic sensing elements exist, varying in wave propagation and deflection type, and in the way they are excited. They can be classified into two categories: **bulk acoustic waves (BAW)** and **surface-generated acoustic waves (SGAW)**. Moreover they may employ longitudinal waves (with the deflection in the direction of propagation) or shear waves (with the deflection perpendicular to the direction of propagation). In order to minimize acoustic radiation into the medium of interest, the shear wave is used in most cases. The various types of acoustic waves are summarized in Figure 1.5 and will be treated individually in the following lines.[28]

To compare different gravimetric sensing devices, it is helpful to define the **relative mass sensitivity** S_r of a sensor. In this case, equation (1.2) can be written as:

$$S_r = \lim_{\Delta\mu \to 0} \frac{1}{f} \frac{\Delta f}{\Delta \mu} = \frac{1}{f} \frac{df}{d\mu} \tag{1.4}$$

Where $\Delta\mu$ is the mass/area ratio of the agglomerated film and f is the operating frequency of the device. Another important characterization is the sensor's **limit of detection** (LOD) or **mass resolution μ_r**. It can be derived from rearranging equation (1.4) as:

$$\mu_r = \frac{1}{S_r} \frac{\Delta f_{min}}{f} = \frac{\Delta f_{min}}{S_a} \tag{1.5}$$

where Δf_{min} is the minimum detectable frequency change defined as three times its standard deviation. It does not only depend on the acoustic device itself, but also on the electronic read-out circuit.

---

[24] L.Coté, R. M. Lec, M. V. Pishko, *IEEE Sensors J.* **3**, 251 (2003).
[25] R. M. Lec, *Proc. IEEE Int. Freq. Contr. Symp.*, 419 (2001).
[26] W. King, *Anal. Chem.* **36**, 1735 (1964).
[27] A. Talbi, F. Sarry, L. Le Brizoual, O. Elmazria, P. Alnot, *IEEE Trans. Ultrason., Ferroelec., Freq. Contr.* **51**, 1421 (2004); J. Weber, M. Link, R. Primig, D. Pitzer, M. Schreiter, *Proc. IEEE Ultrason. Symp.*, 1258 (2005).
[28] Representation and classification based on : E. J. Uttenthaler, PhD Thesis, Universität der Bundeswehr, München (2002).

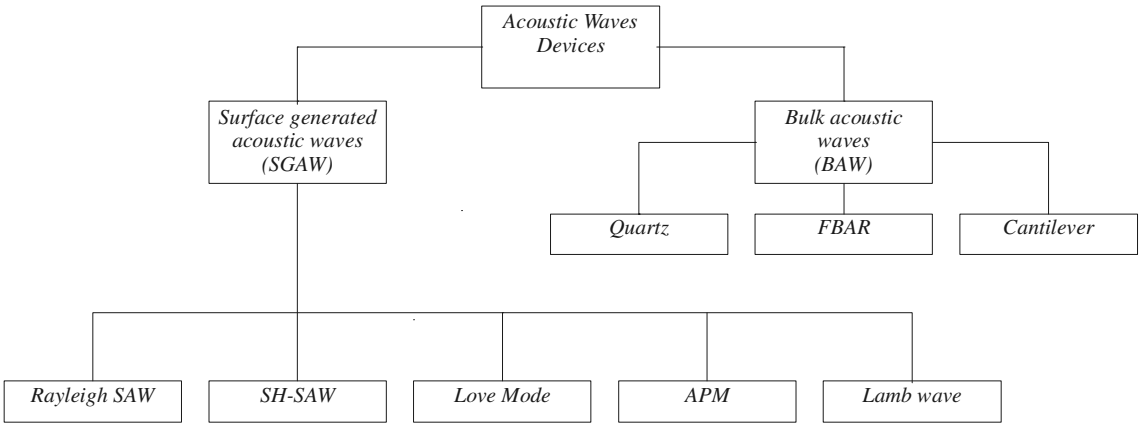

Figure 1.5 : Different types of acoustic sensing technologies.[28]

1.3.1.1. Bulk acoustic wave devices

Bulk acoustic wave (BAW) devices utilize waves travelling or standing in the bulk of the material. They are mostly excited through the piezoelectric or capacitive effects by using electrodes on which an alternative voltage is applied. Three important BAW devices are briefly discussed in the following: quartz crystal microbalances (QCM), film bulk acoustic resonators (FBAR) and cantilevers. Figure 1.6 shows their basic structure and typical dimensions.

In 1959, Sauerbrey was the first to relate the resonance frequency change of a piezoelectric quartz crystal plate to the mass attachment at its surface, thereby establishing the principle of **quartz crystal microbalances (QCM)**.[29] QCMs have been employed as mass sensors for monitoring film thickness in thin-film deposition systems and by researchers studying chemical interactions with thin films deposited on the crystals. A QCM has typical thicknesses of a few hundreds of µm yielding typical fundamental resonance frequencies in the 3-30 MHz range.[30] Acoustic waves are excited by a voltage applied to an electrode structure placed on both surfaces of the quartz (see Figure 1.6 a). For bio-chemical applications, the quartz surface is covered with a sensitive film, adsorbing the measurand. In the simplest case, considering a bulk wave and assuming the agglomerated material to have the same properties as the crystal, the frequency is dependent on the mass/area ratio µ of the agglomerated film: [29]

$$f(\mu) = \frac{v_{ac}}{2}\left(\frac{1}{h_0 + \mu/\rho}\right) \tag{1.6}$$

Where v_{ac} is the sound velocity in the piezoelectric material, ρ is its density and h_0 its thickness. When µ equals zero, equation (1.6) gives the fundamental resonance frequency of the quartz plate. The absolute sensitivity of such a QCM is found by using formulas (1.2), (1.4) and (1.6):[29]

$$S_a = \frac{\Delta f}{\Delta \mu} = -\frac{2}{\rho \cdot v_{ac}} f_0^2 \tag{1.7}$$

[29] G. Sauerbrey, *Zeitschrift für Physik* **155**, 206 (1959).
[30] R.M. White, *Proc. IEEE Int. Freq. Contr. Symp.*, 587 (1998); R. M. Lec, *Proc. IEEE Int. Freq. Contr. Symp.*, 419 (2001).

which is commonly known as the "**Sauerbrey relation**". The absolute sensitivity is directly proportional to the square of the resonance frequency. The relative sensitivity defined in equation (1.4) is proportional to the resonance frequency, which is approximately valid for all acoustic sensing devices:[31]

$$S_r = -\frac{2}{\rho \cdot v_{ac}} f_0 \qquad (1.8)$$

Many commercial systems are already on the market.[32] Absolute and relative sensitivities of a 30 MHz QCM reach 2 Hz·cm^2/ng and 72 cm^2/g respectively, with typical mass resolutions of around 10 ng/cm^2.[33] Lower mass resolutions down to 1 ng/cm^2 seem possible by ameliorating the electronic read-out circuitry. So far, commercial QCM systems are mostly based on single element sensors, or on multi-channel systems composed of several single element sensors.[34] They have been proved to be suitable for the detection of bio-chemical reactions.[35] For example, Uttenthaler *et al.* showed the detection of an immunoassay using a virus specific monoclonal antibody and a M13-Phage.[36] Nevertheless quartzes are expensive, their manufacturing is elaborate especially for high frequencies, and their application for sensor arrays suffers due to lack of integration ability. Moreover, since their resonance frequency is limited by the thickness to which the quartz crystals can be thinned down without breaking, the obtainable mass sensitivities show little potential for improvement.

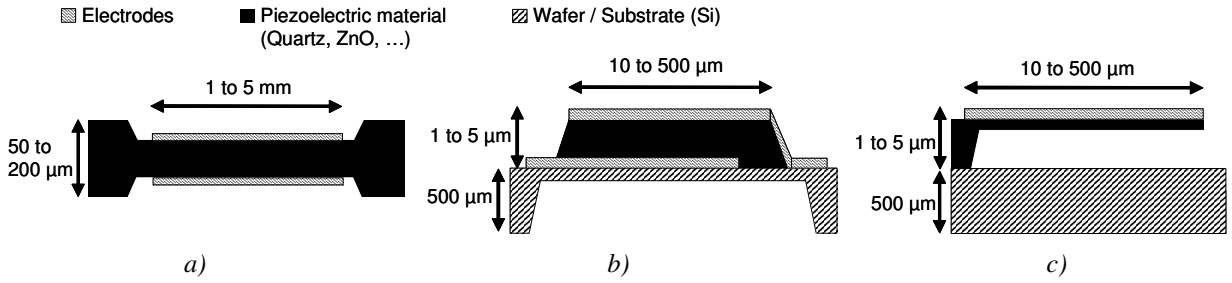

Figure 1.6 : Schematic pictures of the three main bulk acoustic wave devices with typical dimensions: a) Quartz, b) membrane FBAR and c) cantilever.

A typical **film bulk acoustic resonator (FBAR)** consists of a piezoelectric thin film (such as ZnO or AlN) sandwiched between two metal layers. In the past few years, FBARs on silicon substrates have been considered for filter applications in RF devices.[37] Gabl *et al.* were the first to considerer FBARs for gravimetric bio-chemical sensing applications.[38] **They basically function like QCMs. However, unlike**

[31] S. Rey-Mermet, R. Lanz, P. Muralt, *Proc. IEEE Ultrason. Symp.*, 1253 (2005).
[32] G. L.Coté, R. M. Lec, *IEEE Sensors J.* **3**, 251 (2003).
[33] Z. Lin, C. M. Yip, I. S. Joseph, M. D. Ward, *Anal. Chem.* **65**, 1546 (1993).
[34] T. Tatsuma, Y. Watanabe, N. Oyama, K. Kitakizaki, M. Haba, *Anal. Chem.* **71**, 3632 (1999).
[35] M. V. Voinova, M. Jonson, B. Kasemo, *Biosens. Bioelectron.* **17**, 835 (2002).
[36] E. Uttenthaler, M. Schräml, J. Mandel, S. Drost, *Biosens. Bioelectron.* **16**, 735 (2001).
[37] C. Vale, J. Rosenbaum, S. Horwitz, S. Krishnaswamy, R. Moore, *Proc. IEEE Ultrason. Symp.*,332 (1990).
[38] R. Gabl, M. Schreiter, E. Green, H.-D. Feucht, H. Zeininger, J. Runck, W. Reichl, R. Primig, D. Pitzer, G. Eckstein, W. Wersing, *Proc. IEEE Sensors*, Toronto, 1184 (2003).

QCMs, typical thicknesses for the piezoelectric thin film are between 100 nm and a few µm, allowing FBARs to easily attain resonance frequencies in the GHz range. Thus, according to equation (1.7), higher sensitivities than for QCMs can be reached. In Figure 1.6 b), a membrane based FBAR is shown, other FBAR types will be discussed in section 1.5.2. In this case, the piezoelectric film is supported by a membrane etched in a silicon wafer. Estimations reveal a relative mass sensitivity of 1000 cm^2/g for FBARs vibrating at 800 MHz, with mass resolutions in the range or even better than those of QCMs. But this sensitivity value can be increased without difficulty by using higher frequencies, obtained by depositing films with lower thicknesses. Moreover, since FBARs use standing waves in the direction perpendicular to the substrate surface and standard micro-technologies can be used to structure the resonator, the lateral sensor dimensions can be scaled down to 10 µm × 10 µm. They can be integrated into sensor arrays together with CMOS on silicon substrates. Due to their small size, low absolute measurand volumes are needed. Thus thin-film bulk acoustic resonators constitute good candidates for integrated gravimetric bio-chemical sensors, as will be seen in greater detail in paragraph 1.5.

A third kind of bulk acoustic wave device used for gravimetric sensing is the silicon-based **micro-cantilever** (Figure 1.6 c).[39] A beam with typical length of a few hundreds of µm is brought into resonance piezoelectrically or capacitively. Read-out of the deflection or resonance frequency can be done piezoelectrically or optically. Resonance frequencies of up to several tens of kHz are typically reached,[40] and mass sensitivities of 30 cm^2/g have been reported for a 15 kHz device.[41] As for other acoustic wave devices, the sensitivity increases with increasing frequency. For cantilevers with fundamental frequencies of up to 1 MHz, optimistic calculations have predicted mass resolutions down to the single-molecule level.[42] The devices are suitable for integrated sensors; however intrinsic stress problems and the sensitivity to mechanical damage might hinder reliable operation. Moreover, a utilization of this technology for bio-chemical sensors suffers from the fact that the vibrating mode is not suited for operation in liquids due to the high damping. Recently, Manilis *et al.* from MIT presented a hollow cantilever which includes the liquid sample to be tested, with the intention that the bio-chemical binding happens inside the beam.[43] This beam would thus not suffer from damping effects, but the fabrication technology is not straightforward.

1.3.1.2. Surface generated acoustic wave devices

Surface generated acoustic wave (SGAW) devices have gained enormous interest during the past three decades. The SGAW either travels directly along or near the surface, or travels in the bulk of the material or adjacent fluid. All wave types are excited using an interdigitated transducer (IDT) consisting of a metal electrodes pattern on a piezoelectric substrate or film. A spatially periodic electric field produces a corresponding periodic mechanical strain pattern. This causes acoustic waves propagating away from the IDT, in directions perpendicular to the electrode. The vibrations interfere constructively only if the distance

[39] Y. Tang, J. Fang, X. Yan, H.-F. Ji, *Sens. and Actuators B*, **97**, 109 (2004).
[40] J. Zhang, S. O'Shea, *Sens. and Actuators B*, **94**, 65 (2003).
[41] L. Fadel, I. Dufour, F. Lochon, O. Francais, *Proc. 203rd Meeting of the Electrochemical Society*, Paris (2003).
[42] M. Sepaniak, P. Datskos, N. Lavrik, C. Tipple, *Anal. Chem.*, 268 (2002).
[43] D. Rotman, *MIT Technology Review*, December/January, 82 (2005/2006).

between adjacent electrodes is equal to half of the wavelength. In a typical delay-line configuration, a second IDT, placed at a certain distance, permits to sense the acoustic wave after a certain time delay, explaining the name of the configuration (Figure 1.7 a). Typical substrate materials include quartz or lithium niobate ($LiNbO_3$). In 1979, Wohltjen first demonstrated that a gravimetric acoustic sensor could be made in the form of a SAW delay line operating at a few hundreds of MHz.[44] The sensing mechanism consists of a perturbation of the surface along which the waves propagate. In bio-chemical gravimetric sensing applications, the adsorption of molecules affects the propagation velocity and damping of the wave. Electric fields and physical properties of liquids, such as density and viscosity, can also change the properties of acoustic waves. A comprehensive overview of SGAW devices and their application as sensors has been given by Vellekoop.[45]

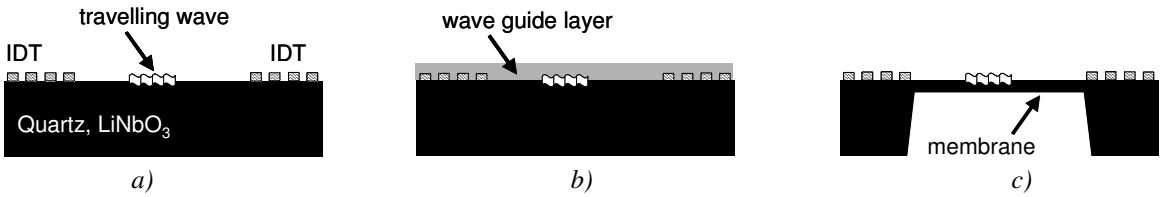

Figure 1.7 : Schematic view of surface generated acoustic wave (SGAW) devices.

Rayleigh surface acoustic waves were first described 1885 by Lord Rayleigh.[46] The deflection is perpendicular to the substrate surface. This is a problem for liquid operation, as the deflection component in direction of the substrate normal couples to the liquid, inducing energy losses and attenuation of the signal. Rayleigh waves are mostly used in high frequency filter techniques and gas-sensing. **Shear horizontal surface acoustic waves** (SH-SAW) have a deflection perpendicular to the propagation direction and parallel to the surface. They are horizontally polarized shear waves and thus adequate for sensing in liquids. For example, Berkenpas *et al.* used such a device for protein detection.[47] Another horizontally polarised wave form is the surface skimming bulk wave (SSBW), which is radiated in a small angle into the substrate and reaches the target-IDT before the waves reaches the substrate backside. When the surface is covered by metal or amorphous SiO_2 thin films with an acoustic velocity lower than that of the substrate, the SSBW can be converted into a guided SAW, in this case called a **Love Mode** (Figure 1.7 b). Love waves are especially sensitive and important for sensing applications. For example, Gizeli *et al.* demonstrated the detection of Immunoglobulin G to a protein modified surface.[48]

SGAW modes travelling in the bulk of the substrate are reflected at the substrate backside, and thus the front and the backside are vibrating, similar to the BAW devices presented above. **Shear horizontal acoustic plate modes** (SH-APM) are well suited for viscosity and bio-sensing in liquid, as the deflection is

[44] H. Wohltjen, R. Dessy, *Anal. Chem.* **51**, 1458 (1979).
[45] M. J. Vellekoop, *Ultrasonics* **36**, 7 (1998).
[46] J. WS. L. Rayleigh, *Proc. Lond. Math. Soc.* **17**, 4 (1885).
[47] E. Berkenpas, S. Bitla, P. Millard, M. Pereira da Cunha, *IEEE Trans. Ultrason. Ferroel. Frequ. Contr.* **51**, 1404 (2004).
[48] E. Gizeli, F. Bender, A. Rasmusson, K. Saha, F. Josse, R. Cernosek, *Biosens. Bioelectron.* **18**, 1399 (2003).

perpendicular to the propagation and parallel to the surface.[49] If the substrate thickness is strongly reduced to form a membrane, APM modes become **Lamb-modes**, consisting of a longitudinal wave and a flexural wave (Figure 1.7 c). This flexural plate wave is very sensitive and can also be employed for gravimetric sensing in liquids since its acoustic wave velocity is lower than that of longitudinal waves in water.

1.3.1.3. Comparison of acoustic sensing technologies

Table 1.1 gives an overview of the different acoustic sensing principles that can be used for gravimetric biochemical detection with their advantages and disadvantages, and examples of the sensitivity for particular devices. The mass resolution is not given, since it strongly depends on the resolution of the read-out circuit. Compared to other sensing technologies which will be presented in the next sections, acoustic sensing principles have one main common advantage: the label-free time-dependent detection.

TABLE 1.1
COMPARISON OF ACOUSTIC SENSING PRINCIPLES FOR BIO-CHEMICAL DETECTION

	Principle	Advantages	Disadvantages	Sensitivity [cm^2/g]
BAW	FBAR (800 MHz) [this work]	- Si integration - Low-cost - Low absolute measurand volumes needed - Operation in liquids difficult, but possible		> 1000
	QCM (30 MHz) [Lin-1993]	- Commercially available - Established principle - Operation in liquids	- No integration with CMOS possible - Elaborate manufacturing - Limited sensitivity due to frequency limitation	72
	Micro- Cantilever (15 kHz) [Fadel-2003]	- Si integration - Routinely fabricated using well-established batch processes	- No operation in liquids - Mechanically fragile - Intrinsic stress problems	30
SGAW	*Generally*	- Easy planar fabrication process - High sensitivity due to energy near surface	- Miniaturization limit due to length between IDTs - Difficult integration with electronics	
	Rayleigh (100 MHz)		- No operation in liquids - Requires piezoelectric crystal	100-200
	SH-SAW	- Operation in liquids	- Requires piezoelectric crystal	100-200
	Love mode (100-200 MHz)	- Operation in liquids	- Extra process step for wave guide film	150-500
	SH-APM	- Operation in liquids	- Requires piezoelectric crystal - Lower sensitivity due energy in bulk	20-40
	Lamb mode (5-20 MHz)	- Operation in liquids - Can use Si substrates - Integration with electronics possible	- Thin, fragile - Complex manufacturing	200-1000

Details of the BAW references can be found in the footnotes of the previous pages. Numbers for the SGAW devices are mostly from Vellekoop-1998.

SGAWs generally show high sensitivities as the acoustic wave has significant interaction with the surface of the device. Most require crystalline substrates and a certain propagation length between the IDTs, so they are difficult to be integrated into small arrays together with read-out circuitry. Moreover, the Q-factor of SGAW devices gets better when increasing the number of fingers, which in turn, increases the total surface. As has

[49] S. J. Martin, A. J. Ricco, T. M. Niemezyk, G. C. Frye, *Sens. Act.* **20**, 253 (1989).

already been mentioned, the well-established Rayleigh wave-mode cannot be used in liquid sensing applications.

BAW devices can generally be manufactured on smaller surfaces, and, in case of FBARs and cantilevers, can be integrated with electronics. QCM are commercially available and a well-established principle, but cannot be integrated into small arrays. Cantilevers lack the possibility of operation in liquids. FBARs are mechanically robust, and, as this work will show, can work in liquids and reach very high sensitivities. For a more complete comparison between BAW and SGAW sensor principles, the reader is referred to an article by Benes *et al.*[50]

1.3.2. Electrochemical sensing

Electrochemical sensing has been a subject of research for a number of decades already and is well-established. It uses reactions taking place at the interface of an electronic conductor and an ionic conductor. These devices can be operated in two modes: **potentiometric or amperometric**. The majority of bio-chemical sensors based on electrochemical principles consist of the association of an enzymatic preparation (mostly immobilized directly on an electrode) and an electrochemical sensor detecting a chemical species implicated in the enzymatic detection. Amperometric devices are the most prevalent and have seen commercialization for measurands such as glucose and lactic acid. For glucose detection, the enzyme glucose oxidase is immobilized on a membrane placed over a platinum electrode. Hydrogen peroxide is oxidized on the electrode, producing a current proportional to the amount of glucose.[51] Electrode arrays have been micro-fabricated. However, reference electrodes which are difficult to integrate are often required. The redox reaction can also be started by labels which attach to the adsorbed molecules after immobilization. This allows the detection of immunological and DNA reactions, but involves a further bio-chemical step and does not give time-dependent information.

Field Effect Transistors (FET) can also be used for electromechanical sensing. They are used in bio-chemical sensing after modifying their structure. By replacing the gate oxide (SiO_2) by other oxides, it is possible to change the FET response with the surrounding environment. For example, it can be possible to develop gas sensors using FETs with highly selective oxides. It is also possible to replace the channel of the transistor, which is usually made of low doped silicon under the gate oxide. By using a chemical compound sensible to certain molecules as the channel, it is possible to modulate the response with the environment. This is the principle of the **ISFET**, Ion Selective Field Effect Transistor. The ISFETs are also suited for measurements in conductive liquid environments when the current flowing between the source and the drain is generated by ions present in the liquid. Various applications such as flow sensors or liquid level detectors are possible.[52] ISFETs can be used for bio-chemical sensing when a sensitive coating is deposited on the surface; in that case, they are called ChemFETs or BioFETs.[53] ISFETs can be associated to enzymatic

[50] E. Benes, M. Gröschl, F. Seifert, A. Pohl, *Proc. IEEE Int. Freq. Contr. Symp.*, 5 (1997).
[51] G. L.Coté, R. M. Lec, *IEEE Sensors J.* **3**, 251 (2003).
[52] A. Poghossian, J. Schultze, M. Schöning, *Electrochimica Acta* **48**, 3289 (2003).
[53] A. Campitelli, E. Parton, *Solid State Technology*, July, 87 (2002).

reactions during which protons are produced or consumed.[54] Miniaturization is the main advantage of the FET sensors. They can be integrated into arrays, allowing multiple measurands to be detected with one device. They are manufactured by CMOS technology using silicon wafers as substrate material, making them very cheap. However, the ISFETs also need a reference potential sensing electrode to function properly, which is difficult to integrate close to the interface.

1.3.3. Optical sensing

Advances in optic and electronic technologies have lead to the research and development of many optical bio-chemical sensors. Today, they represent the most often used sensing technology in bio-medical applications. Mechanisms in optical sensing include interferometry, infrared absorption, scattering, luminescence and polarimetry. Optical sensors can be very sensitive, but tend to be quite expensive compared to other sensing technologies.[55]

Optical detection using **fluorescence** is one of the most sensitive sensing techniques.[56] Due to the availability of lasers and fluorescence markers, this optical detection has seen an impressive development in the last 20 years. The labels attach themselves to selected target molecules and a fluorescent light allows recognizing their presence and quantity. Although these sensors have very good sensitivities, their detection principle requires very complicated read out systems. This is one of the limiting factors of their integration with electronics in a simple device. Their use in high numbers will not be economically viable until all the optical parts can be integrated on a single chip.

Surface Plasmon Resonance (SPR) sensors detect changes in the refractive index of a layer by detecting the angle of minimum reflection intensity of a laser or LED pointed at the layer. After the bio-chemical reaction, this index changes, and so does the reflection angle. SPR sensors can be label free, but they require a light source. They are more easily integrable than fluorescent sensors but the optical parts are still problematic. They have been used for monitoring bio-specific interactions as well as gas absorption. Similar to the QCM, SPR has become known as a well established method suitable for the direct on-line detection of immunological reactions.[57] Commercialized Spreeta sensors with very high sensitivities are compatible with many receptor coatings.[58]

Optical-fibre sensors also have potential in the field of bio-chemical sensing. They can be divided in extrinsic sensors, where the fibre merely acts as a guide from the detector to the measurement region, and intrinsic sensors, where the fibre itself is part of the sensing principle. In the former case, the optical fibre is used to transport the light between the reaction site and the optical sensor or between a light source and the fluorescent or adsorbent layer. The reaction site or layers are situated at the end of the fibre.[59] Intrinsic optical-fibre sensors are based on absorbance, reflectance, Bragg gratings, fluorescence or bio-luminescence. On the interface between the core of the fibre and the cladding of the fibre, the necessary total internal

[54] W. Sant, M. Pourciel, J. Launay, T. D. Conto, A. Martinez, P. Temple-Boyer, *Sens. Act. B* **95**, 309 (2003).
[55] D. J. Webb, *MRS Bulletin*, May, 365 (2002).
[56] S. D. Gawad, PhD Thesis N°3011, EPFL, Lausanne (2004).
[57] C. Kößlinger, E. Uttenthaler, S. Drost, F. Aberl, H. Wolf, G. Brink, A. Stanglmaier, E. Sackmann, *Sens. Act. B* **24-25**, 107 (1995).
[58] [http://www.ti.com/snc/products/sensors/spreeta.htm].
[59] G.Asch, Les capteurs en instrumentation industrielle, Dunod, Paris, 1999.

reflection condition is not perfect and evanescent waves can appear. These waves are propagating parallel to the core/cladding interface and can for example be used to excite a fluorophore immobilized on the core's surface. This type of configuration is mainly used for the development of immunosensors. Interferometric devices can also be used, where one branch of the interferometer interacts with the bio-chemical coating. The SPR method can also be combined with fibre-optics.[60]

1.3.4. Calorimetric and magnetic sensing

The **calorimetric (thermal)** mode of detection is based on the principle that every reaction is accompanied by a variation of enthalpy that can be detected by calorimetry. The temperature variation depends on the number of moles that are reacting, the enthalpy variation and the calorific capacity of the system. The variation can be as low as 0.01°C, thus one needs temperature sensors that are very sensitive.[61] A thermistor is most often used, which is a type of resistor used to measure temperature changes, relying on the change in its resistance with changing temperature. Other thermal detection principles are for instance catalytic or heat conduction sensors. The problem with calorific sensing resides in the fact that one can only measure the global enthalpy change of the system and not only the change due to the enzymatic reaction. Thus these sensors lack sufficient selectivity. Another problem is the difficulty for integration with array structures, since heating sources must be employed.

Magnetic bio-chemical sensors are based on the measurement of paramagnetic nanoparticles by a (giant) magnetoresistance. The latter is made of materials able to lose or gain electrical resistance when an external magnetic field is applied to them. The magnetic nanoparticles are labels attaching to the measurand of interest, which can previously attach to a selective coating or functionalisation on the sensor surface. Since bio-chemical substances are hardly magnetic, the specificity of such devices can be very high.[62] These sensors can easily be integrated, but time-dependent measurements are not possible.

1.3.5. About the comparison of sensing principles

The comparison of the various sensing principles is not straightforward. Qualitatively, one can look at certain advantages like the ability to be integrated with CMOS, the mechanical stability or the requirement of a label. Quantitatively, the comparison is more complicated. The obvious way is to look at the sensitivities and detection limits. However these are measured differently for the various principles. For acoustic sensing devices, the sensitivities are given in cm^2/g, thus they can easily be compared (see section 1.3.1). For other techniques (electrochemical, optical) the sensitivities are most often given in units per volume, i.e. g/l or g/cm^3 or M. To compare all principles the area sensitivities have to be converted to volume sensitivities. In other words, for bio-chemical sensors, the yield of the bio-receptor coating has to be considered, to relate the concentration in liquid to the mass loading on the device surface. Lading *et al.* introduced a bio-chemical quantum efficiency to see how many molecules participate in the process recognized by the physical sensing

[60] J.-F. Masson, L. Obando, S. Beaudoin, K. Booksh, *Talanta* **62**, 865 (2004).
[61] G.Asch, Les capteurs en instrumentation industrielle, Dunod, Paris, 1999.
[62] Personal communication from M. Prins, Trends in Microsystems Congress, Munich (2006).

principle.[63] If a label is needed, its efficiency must also be considered. For the LOD one has the added difficulty that it depends on the utilized read-out circuit. For these reasons, an extensive sensing principle comparison would go beyond the scope of this work.

Most of the rival techniques to FBARs are established since many years, for example the electrochemical principles, the fluorescence method, or QCM and SPR techniques. Kösslinger compared SPR and QCM principles by performing the same immunological experiments on each sensor. Concerning sensitivity, he found no advantage for one particular system.[64] Therefore, if a performance comparable to the QCM is reached, the FBARs of this work will be acceptable considering sensitivity and LOD, even without considering the other qualitative advantages. Consequently, in this thesis, **the performance of the FBARs was mainly compared to the QCM**.

Acoustic devices are label-free, which allows a quantitative time-dependent detection. For principles where labels are involved, the actual quantitative measurement is only done after the bio-chemical recognition step. Moreover, labels can compromise the bio-chemical activity. SPR or coated optical fibre techniques can also be label-free. But the shortcomings of these methods are that they cannot be configured easily for high-throughput detection. What is also interesting for acoustic wave devices compared to other principles is the frequency output, which is easy to process. In addition to those advantages, FBARs can yield low-cost systems, which are miniaturized and integrated with CMOS electronics. Also, FBARs require only very small absolute measurand volumes. More details about FBARs used as bio-chemical sensors are given in paragraph 1.5.

1.4. Piezoelectricity: materials & thin film deposition

Most of the acoustic sensing devices presented in the previous paragraph are based on piezoelectric mono-crystals or thin films. This paragraph will therefore describe the basics of piezoelectricity, give a comparison of common piezoelectric thin film materials and briefly explain some methods used to deposit ZnO thin films, which are used in this work.

1.4.1. Basics of piezoelectricity

In 1880, Pierre and Paul-Jacques Curie discovered that external forces applied to single crystals of quartz and several other minerals generate a charge on the surface of these crystals. They found that the charge is roughly proportional to the applied mechanical stress.[65] This effect is called the **direct piezoelectric effect**, which is derived from the Greek *piezein*, meaning to squeeze or press. Piezoelectric materials also exhibit the **inverse effect** as well: an applied voltage generates a deformation of the crystal. The inverse effect was mathematically deduced from fundamental thermodynamic principles by Lippmann in 1881.[66] A simplified model of piezoelectricity involves the movement of anions and cations in opposite directions under the

[63] L. Lading, L. B. Nielsen, T. Sevel, Proc. IEEE Sensors, 229 (2002).
[64] C. Kößlinger, E. Uttenthaler, S. Drost, F. Aberl, H. Wolf, G. Brink, A. Stanglmaier, E. Sackmann, *Sens. Act. B* **24-25**, 107 (1995).
[65] M. Curie, P. Curie., *Bull. Soc. Min. Paris* **3**, 90 (1880).
[66] G. Lippmann, *Annales de Chimie et de Physique* **5**ème série, t. XXIV, 145 (1881).

influence of an electric field or a mechanical force.[67] The forces generated by this motion cause lattice deformation for **non-centrosymmetric** crystals. All piezoelectric materials are necessarily anisotropic; in case of central symmetry, an applied force does not yield an electric polarization.

A more detailed understanding of piezoelectricity is based on the piezoelectric equations describing the coupling between electric and mechanical strains in a piezoelectric material. Polarization and stress are vector and tensor properties, respectively, and components for each can be related via the piezoelectric effect. For this reason, piezoelectricity is a complicated property, and up to 18 constants may be required to specify it. One way to write the complete piezoelectric equations can be written as follows:

$$T_{ij} = c^{E}_{ijkl} S_{kl} - e_{kij} E_k \tag{1.9}$$

$$D_i = e_{ikl} S_{kl} + \varepsilon^{S}_{ij} E_j \tag{1.10}$$

In these equations, T_{ij} is the stress, S_{kl} is the strain, E_j is the electric field and D_i is the electric displacement. These are tensors, with 9, respectively 3 components. These tensors are related through the stiffness tensor c^{E}_{ijkl}, the piezoelectric tensor e_{kij} and the permittivity tensor ε^{S}_{ij}. The indices {i,j,k,l} are taken from {1,2,3} and the Einstein summation convention is applied.[68] These two equations provide one way of defining the direct and inverse piezoelectric effect. Another set of equations exists, where the strain and electric displacement are expressed as a function of stress and electrical field. Piezoelectricity will be explained in more detail in Chapter 2. Many useful applications exist, such as the production and detection of sound, motors and accelerometers, gas ignitors, precision positioning stages and micro-surgical tools.[67] Most important for this work are the sensing and frequency-control applications.

1.4.2. Piezoelectric materials

Crystalline materials are divided into 32 classes, or point groups, according to the number of rotational axes and reflection planes that leave the crystalline structure unchanged. Only 20 of the 32 crystal classes are piezoelectric. All 20 piezoelectric classes are non-centrosymmetric. Of these, 10 classes are polar[69] and exhibit the pyroelectric effect. Pyroelectricity can be defined as the ability to generate an electrical potential under a certain change of temperature. The 10 pyroelectric classes can be divided into ferroelectrics and non-ferroelectrics. Ferroelectric materials exhibit a spontaneous dipole moment, which can be reversed by the application of an electric field. Generally they also have high coupling coefficients,[70] but are less stable. An example of a ferroelectric class is the perovskite structure (e.g. lead zirconate titanate, PZT). The wurtzite structure (e.g. ZnO, AlN) belongs to the non-ferroelectric classes (6mm). Only a few of the piezoelectric materials have found widespread technical application. The most dominantly used piezoelectric single crystal

[67] M. J. Madou, *Fundamentals of Microfabrication*, CRC Press, Bacaraton, FL (2002).
[68] The Einstein summation convention is a notational convention useful when dealing with coordinate formulae. According to this convention, when an index variable appears twice, it implies that one sums over all of its possible values.
[69] All materials develop a dielectric polarization under influence of an electric field. But polar materials show a natural charge separation, and a polar axis, even in the absence of an electrical field.
[70] The electromechanical coupling coefficient is an important measure of the interchange of electrical and mechanical energy and is indicative of the ability of a material to both detect and generate mechanical vibrations. For the inverse piezoelectric effect, the ratio of the converted mechanical energy stored at any instant in a piezoelectric to the input electrical energy is defined as the square of the electromechanical coupling coefficient.

(bulk) material both in the sensor field as well as in the frequency-control field is **quartz**, due to its temperature stability, precision and low cost.[71] In both fields the oxide form of silicon plays the same dominating role as pure Si in the semiconductor industry. Depending on the required properties, different crystal cuts are used. When quartz is used for generating thickness shear wave modes, as for sensing applications in liquid environments, the AT cut is used. Other currently used bulk materials are lithium niobate ($LiNbO_3$) or gallium orthophosphate ($GaPO_4$). Some polymer materials like rubber, wool, or wood fibre can exhibit piezoelectricity to some extent. The ferroelectric polymer polyvinylidine difluoride (PVDF) exhibits piezoelectricity several times larger than quartz. However, of all the piezoelectric materials, only some have the ability to be deposited as thin films while conserving interesting properties. For micro-systems, three materials are particularly interesting and will be discussed in more detail: ZnO, PZT and AlN.

Zinc Oxide (ZnO) is one of the most used thin film piezoelectric material. It belongs to the hexagonal wurtzite crystal type, having 6mm symmetry. This structure can be considered as two inter-inserted hexagonal structures (zinc and oxygen) spaced by (3/8)c from each other (see Figure 1.8), where c is the main symmetry axis of the crystal. The stiffness and piezoelectric constants can be found in Table 3.1 on page 78. It is generally treated as a semiconductor as a result of excessive zinc. ZnO is very versatile and due to its high coupling coefficient, many applications exist, like SAW devices, BAW devices, cantilever-beam accelerometers, AFM sensors, gas sensors, infrared detectors, tactile sensor arrays, etc.[72] Chapter 3 will detail the ZnO sputtering processes developed in this work.

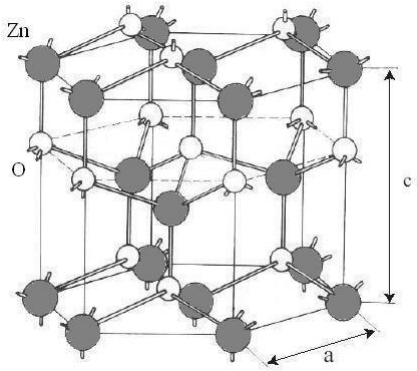

Figure 1.8 : Zinc Oxide (ZnO) in its wurtzite crystalline structure showing the hexagonal symmetry.

Aluminium Nitride (AlN) has the same crystalline structure than ZnO. It is a recommendable candidate material if the coupling coefficient determining the bandwidth in FBAR filters does not have to be very large. AlN-based FBAR devices have good acoustic wave properties that make them suitable for current front-end filters for global positioning system (GPS) receivers and RF components in personal communications systems, such as duplexer and voltage controlled oscillators.[73] AlN films feature a high acoustic velocity, a low acoustic attenuation and they are compatible with CMOS processing.[74]

---

[71] E. Benes, M. Gröschl, F. Seifert, A. Pohl, *Proc. IEEE Int. Freq. Contr. Symp.*, 5 (1997).
[72] Y. E. Lee, J. B. Lee, Y. J. Kim, H. K. Yang, J. C. Park, H. J. Kim, *J. Vac. Sci. Technol. A* **14**, 1943 (1996); M. J. Madou, *Fundamentals of Microfabrication*, CRC Press, Bacaraton, FL (2002).
[73] S.-H.Lee, K.H.Yoon, J.-K.Lee, *J.Appl.Phys.* **92**, 4062 (2002).
[74] M. B. Assouar, O. Elmazria, M. El Hakiki, P. Alnot, C. Tiusan, *Proc. IEEE Int. Freq. Contr. Symp.*, 43 (2004).

Lead Zirconate Titanate ($Pb[Zr_xTi_{1-x}]O_3$, or **PZT**) has a perovskite structure, i.e. a structure of the type ABO_3. Since it is ferroelectric, it must be poled to exhibit sufficient coupling coefficients, i.e. the dipoles in the compacted crystals must be aligned in the same direction by subjecting them to a strong electric field. Above the Curie point, the dipole directions in ferroelectric materials disappear. [75] PZT can be deposited in thin film form by sputtering and by the sol-gel process. Sputtered PZT films can also show a spontaneous polarity, eliminating the need of poling.[76] Despite the difficult fabrication process, PZT-based compounds are some of the most useful electro-ceramics. They are used to make ultrasound transducers and other sensors and actuators, as well as high-value ceramic capacitors and FRAM chips.

For **comparison**, Table 1.2 lists some of the main characteristics of AT-cut quartz, PZT, AlN and ZnO. For thin film resonator applications, one generally needs a high coupling coefficient and low attenuation of the acoustic wave. Concerning the acoustic velocity, two different aspects must be considered. A higher acoustic velocity results in thicker films for a particular resonance frequency. Since the piezoelectric properties of the film improve with film thickness,[77] a film as thick as possible is desirable for very high frequency applications. However, for lower frequency applications, were one is not in a critical range concerning the film thickness, a lower acoustic velocity is better, since the required thickness and thus the deposition time are reduced. **ZnO was chosen for the FBARs studied in this work**.

TABLE 1.2
MATERIAL PROPERTIES OF PIEZOELECTRIC MATERIALS FOR FBARS, AND COMPARISON WITH QUARTZ

Parameter Description[e]	Unit	AT-cut Quartz[a]	PZT[b]	AlN[f]	ZnO[c]
Relative dielectric constant	–	4.54	350	8.5	8.8
Density ρ	kg/m^3	2650	7480	3260	5665
Longitudinal mode coupling coefficient K	–	n.a.	0.45	0.25 [d]	0.27 [d]
Shear mode coupling coefficient K	–	0.07	n.a.	0.16 [d]	0.32 [d]
Longitudinal mode v_{ac}	m/s	5968	4500	11374 [d]	6330 [d]
Shear mode v_{ac}	m/s	3310	2200	6094 [d]	2883 [d]

[a] E. J. Uttenthaler, PhD Thesis, Universität der Bundeswehr, München (2002).
[b] Q.-X.Su *et al*., *IEEE Trans. Microwave Theory Tech.* **49**, 769 (2001).
[c] N. F. Foster *et al.*, IEEE Trans. Sonics Ultrason., **SU-15**, 28 (1968).
[d] The longitudinal mode parameters are given for 0° c-axis inclination. The shear mode parameters are given for 90° c-axis inclination.
[e] v_{ac} is the acoustic velocity. K is the electromechanical coupling coefficient.
[f] M. El Hakiki *et al*., *Diamond Rel. Mat.* **14**, 1175 (2005).

1.4.3. Deposition techniques for Zinc Oxide thin films

Various deposition techniques have been used for ZnO thin films. Two types are predominant: chemical vapour deposition (CVD) and physical vapour deposition (PVD). During **CVD**, the constituents of a vapour

[75] M. J. Madou, *Fundamentals of Microfabrication*, CRC Press, Bacaraton, FL (2002).
[76] M. Schreiter, R. Gabl, D. Pitzer, R. Primig, W. Wersing, *J. European Ceramic Soc.* **24**, 1589 (2004).
[77] F. Martin, P. Muralt, M.-A. Dubois, A. Pezous, *J. Vac. Sci. Technol. A* **22**, 361 (2004).

phase, often diluted with an inert carrier gas, react at a hot surface to form a solid film. The CVD method is very versatile and works at low or atmospheric pressure. Amorphous, polycrystalline and epitaxial films can be deposited with a high degree of purity, control and economy.[78] Deposition of ZnO thin films using chemical ways has been done by interaction of two or more gases, one containing Zn and the other containing O. After energy addition, mostly in form of heat, gases are dissociated and combine on the substrate to form ZnO. An advantage is the possibility to realize a crystalline thin film. The drawback of this method is the high temperature (around 700°C) which is incompatible with CMOS electronics.[79] Another chemical method is the **sol-gel** process, where solid particles and chemical precursors in a colloidal suspension in a liquid (sol) form a gelatinous network (gel). Upon removal of the solvent by heating, a wide variety of differently shaped glasses or ceramics result. The sol-gel technique is a low-temperature process and can be used to make ZnO films. A solution containing precursor compounds and an organic binder is spun onto the substrate and then heated to drive off the organic constituents and leave a densified film. Alcoholic solvents are often used to prepare sols; for instance, most sol-gel syntheses of undoped and doped ZnO use solvents such as methoxyethanol or ethanol/propanol.[80] The advantages of the sol-gel method are its low-cost and rapid fabrication, however very thin films of less than 1 µm are difficult to obtain and the crystallographic orientation is difficult to control.

Many different kinds of thin films in ICs and MEMS are deposited by evaporation and sputtering, both of which are examples of **PVD**. PVD processes for deposition of ZnO thin films use the generation of gaseous phase ZnO molecules from a solid ZnO target and the condensation of these molecules on a substrate. Another method is to take a pure Zn target with a gas containing oxygen to create ZnO (reactive process). **Thermal evaporation** represents one of the oldest of thin films deposition techniques. Evaporation is based on the boiling (or sublimating) of a heated material onto a substrate in a vacuum. During "resistive heating", a metal is usually evaporated by passing a high current through a highly refractory metal containment structure (e.g. a tungsten boat or filament). In industrial applications, resistive heating has been surpassed by electron-beam and induction evaporation. For depositing with **Pulsed Laser Deposition** (PLD) the ZnO target is irradiated with pulsed Laser. The ZnO evaporates due to the elevated temperature brought by the Laser and ZnO particles in gaseous phase recombine on the substrate. With this technique, high-quality ZnO films have been deposited from ZnO ceramic targets.[81] A reactive laser ablation process was also shown, where a Zn target is ablated in a reactive oxygen atmosphere.[82] The disadvantage with PLD is that the substrate size on which films can be deposited with a good homogeneity is very small. During **sputtering**, the target (Zn or ZnO) at a high negative potential, is bombarded with positive inert gas ions (mostly Ar) created in a plasma. The target material is sputtered away by momentum transfer and the ejected surface atoms are deposited (condensed) onto the substrate placed an anode. Sputtering is preferred over evaporation

[78] R. H. Wittstruck, X. Tong, N. W. Emanetoglu, P. Wu, Y. Chen, J. Zhu, S. Muthukumar, Y. Lu, A. Ballato, *IEEE Trans. Ultrason. Ferroel. Freq. Contr.* **50**, 1272 (2003).
[79] T. M. Barnes, S. Hand, J. Leaf, C. A. Wolden, *J. Vac. Sci. Technol. A* **22**, 2118 (2004).
[80] N.R.S. Farley, C.R. Staddon, L.X. Zhao, K.W. Edmonds, B.L. Gallagher, D.H. Gregory, *J. Mat. Chem.* **14**, 1087 (2004).
[81] S. J. Henley, M. N. R. Ashfold, D. Cherns, *Surf. Coat. Technol.* **177-178**, 271 (2004); M. Peruzzi, J. D. Pedarnig, D. Bäuerle, W. Schwinger, F. Schäffler, *Appl. Phys. A* **79**, 1873 (2004).
[82] P. Verardi, M. Dinescu, *Proc. IEEE Ultrason. Symp.*,1015 (1995).

in many applications due to a wider choice of materials to work with and better adhesion to the substrate.[83] Actually, sputtering is employed in laboratories and production settings. Most sputtered ZnO films are polycrystalline and grow preferentially with their crystallographic c-axis perpendicular to the substrate on any material.[84] **Sputtering will be described in more detail in Chapter 3 since it was used in this work for the deposition of ZnO films.**

1.5. FBAR as sensor in liquid environments and context of the thesis

1.5.1. Description of the planned bio-chemical sensor based on FBARs

This paragraph presents the bio-chemical sensor being developed in the Materials & Microsystems Ceramics Group of Siemens AG Corporate Technology (CT MM2) in collaboration with different partners from all over Europe. The development of this sensor received financial support through the European Union: first, in the years 2002 to 2004, through project IST-2001-33326 PISARRO (Piezoelectric sensing arrays for biomolecular interactions and gas monitoring); then, from August 2005 to 2008 in project FP6-016467 BIOGNOSIS (Integrated Biosensor system for label-free in-vitro DNA and protein diagnostics in health care applications). Table 1.3 shows some key facts of both projects.[85] The general objectives of both projects are the combination of microelectronics, life science and thin film sensor technologies for the development of novel and inexpensive bio-chemical sensor arrays. These sensors are applied in medical diagnostics, especially for the detection of cancer using DNA or protein based bio-markers.[86] This thesis started in the middle of the PISARRO project. The second half was done during the BIOGNOSIS project. One of the main work-packages of both projects was to develop the acoustic sensing element of the bio-chemical sensor. This task was partly treated within this thesis.

TABLE 1.3
KEY FACTS OF THESIS RELATED EUROPEAN RESEARCH PROJECTS

	Start Date	End Date	Project cost	Countries involved
Pisarro (Piezoelectric sensing arrays for biomolecular interactions and gas monitoring)	1.1.2002	31.12.2004	4.53 million €	Italy, Austria, Romania, Finland, United Kingdom, Germany
Biognosis (Integrated Biosensor system for label-free in-vitro DNA and protein diagnostics in health care applications)	1.8.2005	31.7.2008	6.12 million €	Sweden, United Kingdom, Austria, Finland, Germany

A simplified schematic cross-section of the integrated bio-chemical sensor array is shown in Figure 1.9. Each sensing element of the array consists of a molecular receptor coating which is attached to an FBAR processed on silicon substrates using thin film and micromachining techniques. The FBARs are used as gravimetric bio-chemical sensors as was explained in section 1.3.1. The sensor elements are prepared for the detection of different molecular species. All applied sensor processing steps are required to be compatible

[83] M. J. Madou, *Fundamentals of Microfabrication*, CRC Press, Bacaraton, FL (2002).
[84] J. G. E. Gardeniers, Z. M. Rittersma, G. J. Burger, *J. Appl. Phys.* **83**, 7844 (1998).
[85] [www.cordis.lu] (Cordis is the "Community Research and Development Information Service" of the European Union).
[86] J. A. Ludwig, J. N. Weinstein, *Nature Reviews* **5**, 845 (2005).

with semiconductor technology in order to make systems with many sensor elements and integrated readout circuits possible. With the FBAR as sensing element, there is the possibility for label-free electronic detection of bio-chemical reactions, which results in a reduced size and low cost of the measuring instrument. The system is able to measure more than one measurand simultaneously due to the use of arrays. This also gives the possibility of increasing the detection selectivity by using reference sensors. Extremely high sensitivities and low resolutions can be achieved due to the high resonance frequency. Time-dependent quantitative measurements with low absolute volumes can be performed and reaction dynamics can be observed. There is also the possibility of detection in liquids, as will be analyzed in this thesis.

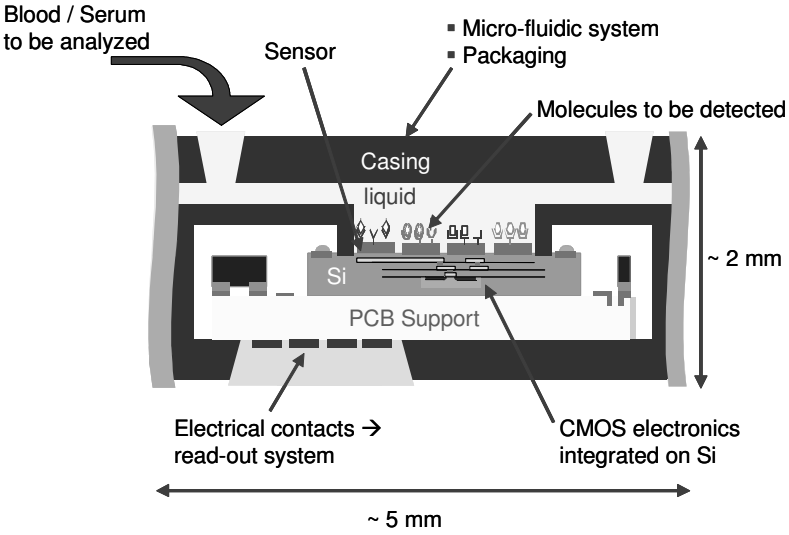

Figure 1.9 : Schematic view of the micro sensor array system and work package.

1.5.2. Film bulk acoustic resonators as gravimetric sensors

FBARs have been under development for over 40 years, but only recently significant advances in integrated circuit processing to reach microwave frequencies and practical manufacturing for high-volume applications have been obtained.[87] If FBAR devices of sufficient performance can be fabricated, they could replace the current ceramic or SAW devices due to their compactness and good compatibility with IC processing. For example, FBARs are suitable for current front-end filters for global positioning system (GPS) receivers and RF components such as filters, duplexers and VCOs.[88] Candidate piezoelectric materials for FBAR devices, including ZnO, AlN and PZT, have been presented in section 1.4.2.

Figure 1.10 shows a close-up view of the FBAR developed in this work. The chosen piezoelectric thin film is **ZnO**. It can be easily deposited using sputtering techniques. The main reason for choosing ZnO over AlN is its higher coupling coefficient and the availability of an oxygen atmosphere sputtering system at CT MM2. Moreover, ZnO is a well investigated piezoelectric material which has been proved to be suited to realize

[87] K.M.Lakin, *IEEE Trans. Ultrason., Ferroelec., Freq. Contr.* **52**, 707 (2005).
[88] Q.-X.Su, P.Kirby, E.Komuro, M.Imura, Q.Zhang, R.Whatmore, *IEEE Trans. Microwave Theory Tech.* **49**, 769 (2001).

FBARs with high quality factors.[89] In addition, the successful deposition of ZnO films possessing an in-plane orientation appropriate for shear mode excitation had already been reported,[90] and relatively high sputtering rates and low process temperatures were expected.

An FBAR vibrating in shear or longitudinal wave mode requires material interfaces that confine waves to a finite volume in an efficient manner. For ideal FBARs consisting of only a piezoelectric layer and very thin electrodes, both interfaces are solid-to-air interfaces. Most quartz resonators for example come very close to this condition. For real FBARs, one attempts to realize this ideal condition on a wafer. There are several techniques for FBARs to prevent energy dissipation into the substrate and to keep the wave confined within a desired volume.[91] In this work, the solidly mounted option was chosen. In this case the acoustic isolation from the substrate is obtained by means of a Bragg reflector that is composed of several pairs of quarter-wavelength layers with a high acoustic impedance contrast. This "**acoustic mirror**" is shown schematically on Figure 1.10. Its principle of operation is explained in detail in Chapter 4. Such **solidly mounted FBARs (SMR)** are favourable for integration and can be fabricated on a wide variety of substrates. It is a planar technology, with a simple fabrication and mechanical robustness. The latter is important in respect that chips have to undergo coating steps as well as packaging.

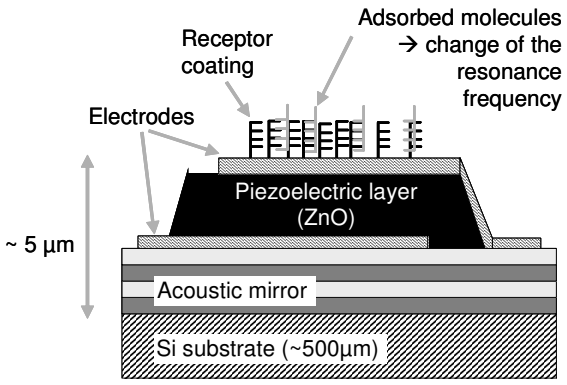

Figure 1.10 : Schematic view of the film bulk acoustic resonator, the sensing part of the bio-chemical sensor.

The other two methods for energy confinement take advantage of the low acoustic impedance of air or vacuum and need either bulk or surface micromachining in order to create an air gap between the substrate and the resonating film. Lakin and Wang were the first to report about such membrane based FBARs.[92] Figure 1.11 shows both types. For both methods, the fabrication is not easy and they are less robust than the SMR types.

[89] C. Vale, J. Rosenbaum, S. Horwitz, S. Krishnaswamy, R. Moore, *Proc. IEEE Ultrason. Symp*.,332 (1990).
[90] J. S. Wang, K. M. Lakin, *Proc. IEEE Ultrason. Symp.*, 480 (1982).
[91] S.-H.Lee, K.H.Yoon, J.-K.Lee, *J.Appl.Phys.* **92**, 4062 (2002).
[92] K. M. Lakin, J. S. Wang, *Appl. Phys. Lett*. **38**, 125 (1981).

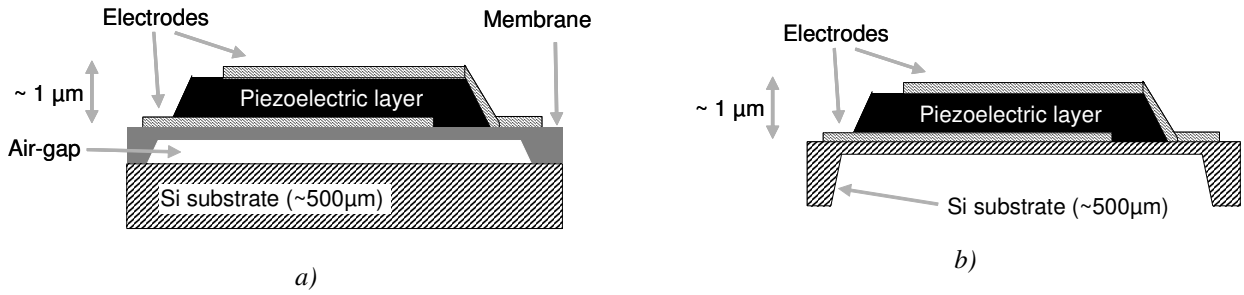

Figure 1.11 : 2 types of membrane-based FBARs using a) surface micro-machining and b) bulk micro-machining.

The resonance frequency of an FBAR is determined roughly by the total acoustic thickness of the resonance cavity defined by the piezolayer and the electrodes. Since this thickness is typically around 1 µm, resonance frequencies up to several GHz can easily be achieved. This is 50 to 100 times higher than the resonance frequencies of quartz resonators typically operating at around 10 to 20 MHz. This means that much higher **sensitivities** can be achieved as was seen in section 1.3.1. The mass resolution μ_r of bulk acoustic wave devices defined in formula (1.5) is inversely proportional to the quality factor Q of the device, times its sensitivity.[93] Since the quality factor is generally inversely proportional to the frequency and since the sensitivity increases with the frequency, the mass resolution stays in the same order of magnitude independently of the resonance frequency provided that the phase resolution of the measurement setup stays constant. This will be seen in more detail in Chapter 4. For QCMs, typical values for μ_r are around several ng/cm^2. For FBARs operated in air, Q-factors lie between 300 and 1000,[94] which is much lower than typical values for quartz resonators. Nevertheless, due to the much higher oscillation frequencies of FBARs, detection limits comparable to QCM systems can be achieved. A detailed theoretical description of the FBARs will be given in Chapter 2.

1.5.3. Operation in liquid environment: the need for shear wave mode

Usually FBARs operate in the longitudinal wave mode, which is appropriate in a gaseous environment. However, FBARs using the longitudinal wave mode are adversely affected when used for sensing in liquid phase environments. Displacements normal to the surface generate compressional waves dissipating into the liquid. Rayleigh waves for example, cannot efficiently be applied in liquids due to the high acoustic losses when immersed. The resulting decrease of quality factor Q increases the mass resolution substantially. Nevertheless some research groups have tried to use the longitudinal wave mode FBAR for measurements in liquids, with only limited success. Zhang *et al.* for example mention a membrane-based FBAR achieving a resonance frequency of 1 GHz with a Q-factor of 200 in air, which drops to about 10 in water.[95] They found that for the second harmonic resonance the Q-factor dropped only to 40, but still resulted in a mass resolution worse than typical values for QCMs. Another method to use longitudinal modes in liquid environment without damping of the resonance is to use a feedback loop. For example, the effective Q-factor of

[93] The quality factor Q definition will be seen in Chapter 2. It is a measure of the losses in the device and corresponds to the reciprocal of the lost energy.
[94] K. M. Lakin, G. R. Kline, K. T. McCarron, *IEEE Trans. Microwave Theo. Techn.*, **41**, 2139 (1993).
[95] H. Zhang, M. Marma, E. S. Kim, C. McKenna, M. Thompson, *IEEE Int. MEMS Conf.*, 347 (2004).

cantilevers in liquids was shown to increase from 20 to 19000 using such a method.[96] However, the closed-loop operation has a bad influence on the sensitivity, which deteriorates strongly for low initial Q-factors.[97]

In contrast, the **shear wave mode**, with a deflection parallel to the surface, allows an operation in liquids with only minor damping effects.[98] This was verified in numerous articles with AT-cut quartz resonators and SAW devices. The operation of shear mode AT-cut quartz devices in liquids has first been investigated rigorously by Kanazawa and Gordon in 1985.[99] There are some propagation losses due to viscous loading of the surface. Because of its viscosity, a thin liquid film becomes entrained with the shear wave movement of the substrate. The entrainment decays with the distance from the vibrating surface. The difference between the longitudinal and shear modes in liquids is shown schematically in Figure 1.12. Since the Q-factors in liquids are larger for shear-mode, better mass resolutions can be obtained.

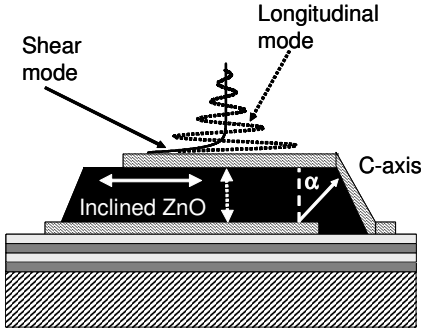

Figure 1.12 : Schematic figure showing the difference between shear mode and longitudinal mode for an FBAR with c-axis inclined ZnO during operation in liquid. The shear mode cannot propagate into the liquid.

The excitation of shear waves requires a certain orientation of the exciting electric field with respect to the crystallographic orientation of the material. This means that either the electrodes have to be positioned such as to orient the electric field. Or, when the position of the electrodes is fixed by the design of the device, the material orientation has to be adapted. For QCM devices, this problem is solved by using appropriate quartz cuts, such as the widely used AT-cut. For SGAW devices, one can chose an appropriate propagation method by choosing the substrate material and SGAW type (see section 1.3.1). For FBARs this is more complicated. FBARs have fixed electrodes on the top and bottom of the film resulting in an electric field perpendicular to the substrate surface. For 6mm crystal type materials like ZnO, AlN or CdS it was shown that shear wave-modes can be excited when the **c-axis of the material is inclined with respect to the surface normal**.[100] ZnO thin films grow preferentially with their crystallographic c-axis perpendicular to the substrate, allowing only longitudinal mode excitation. Although several articles describe this inclined film growth, it is nevertheless not fully understood and most articles only describe growth on substrates with limited size. One of the main tasks of this work was thus to develop a suitable process for this deposition (Chapter 3). Some of the articles also mention the realization of shear wave mode bulk acoustic wave devices, which first appeared

[96] Y. Li, C. Vancura, C. Hagleitner, J. Lichtenberg, O. Brand, and H. Baltes, *Proc. IEEE Sensors 2003*, 809 (2003).
[97] A. Phommahaxay, Diploma Thesis, Siemens/ESIEE (2004).
[98] M. J. Vellekoop, *Ultrasonics* **36**, 7 (1998).
[99] K. K. Kanazawa, J. G. Gordon, *Analytica Chimica Acta* **175**, 99 (1985).
[100] N. F. Foster, G. A. Coquin, G. A. Rozgonyi, F. A. Vannatta, *IEEE Trans. Sonics Ultrason.*, **SU-15**, 28 (1968).

around 30 years ago. However, these devices were meant for high-frequency applications and thus, they were never tested in liquid environment. Only very recently towards the end of this thesis, some research groups realized shear mode FBARs and applied them in liquids. The next section will give a short overview of these efforts.

1.5.4. State of the art: FBARs as bio-chemical sensors

In 2003, at the beginning of this thesis, Gabl *et al.* of CT MM2 were among the first to show the use of SMRs for gravimetric bio- and gas- measurements.[101] They showed the detection of both proteins and DNA hybridisation. The SMRs used c-axis oriented ZnO thin films to excite longitudinal wave mode vibrations at 2 GHz. Consequently, no satisfying operation in liquids was possible. However, mass attachments in liquid environment and subsequent drying of the samples permitted to determine a relative sensitivity of 1200 cm^2/g and a mass resolution of 25 ng/cm^2. Also in 2003, Brederlow *et al.* presented a SMR with AlN thin films vibrating at 1.8 GHz. They were able to detect the protein BSA (bovine serum albumin).[102] Since 2003, some other research groups have used FBARs as bio-chemical sensors. In 2004, Zhang *et al.* presented a longitudinal mode membrane ZnO FBAR vibrating at 1 GHz. They detected various chemical solutions inducing mass changes on the surface. They made no indication of the obtained sensitivity or the mass resolution.[103]

In 2005, the first shear mode ZnO SMR originating from this work was presented at Eurosensors XIX conference in Barcelona with first results for measurements in liquid environments.[104] Only a couple of months *later*, Wingquist *et al.* from Uppsala University presented the first membrane-based shear mode AlN FBARs operating at 1.2 GHz to be used for sensing applications at IEEE Ultrasonics conference in Rotterdam.[105] At this conference, we mentioned our first bio-chemical measurements with standard Avidin - Antiavidin bindings demonstrating a sensitivity of 946 cm^2/g and a detection limit of 3.5 ng/cm^2.[106] These measurements have later been published in a regular article by Weber *et al*.[107] Wingquist *et al.* presented measurements with different concentrations of Albumin, but did not give an indication of the obtained sensitivity or mass resolution. Also in 2005, Rey-Mermet *et al.* from EPFL presented longitudinal mode AlN SMRs vibrating at 8 GHz, and showed the detection of a self-assembled monolayer with a relative sensitivity of up to 10^4 cm/g.[108] As can be recognized, the interest in FBAR for use as bio-chemical sensors is high and received increasing attention in the last years.

---

[101] R. Gabl, M. Schreiter, E. Green, H.-D. Feucht, H. Zeininger, J. Runck, W. Reichl, R. Primig, D. Pitzer, G. Eckstein, W. Wersing, *Proc. IEEE Sensors*, Toronto, 1184 (2003); R. Gabl, H.-D. Feucht, H. Zeininger, G. Eckstein, M. Schreiter, R. Primig, D. Pitzer, W. Wersing, *Biosens. Bioelectron.* **19**, 615 (2004).
[102] R. Brederlow, S. Zauner, A. L. Scholtz, K. Aufinger, W. Simbürger, C. Paulus, A. Martin, M. Fritz, H.-J. Timme, H. Heiss, S. Marksteiner, L. Elbrecht, R. Aigner, R. Thewes, *Proc. IEEE Electron Devices Meeting*, 992 (2003).
[103] H. Zhang, M. Marma, E. S. Kim, C. McKenna, M. Thompson, *IEEE Int. MEMS Conf.*, 347 (2004).
[104] M. Link, M. Schmidt, J. Weber, R. Primig, D. Pitzer, R. Gabl, M. Schreiter, *Proc. Eurosensors XIX*, N° TB10 (2005).
[105] G. Wingqvist, J. Bjurström, I. Katardjiev, *Proc. IEEE Ultrason. Symp.*, 50 (2005).
[106] M. Link, M. Schreiter, J. Weber, D. Pitzer, R. Primig, M. B. Assouar, O. Elmazria, *Proc. IEEE Ultrason. Symp.*, 202 (2005).
[107] J. Weber, W. M. Albers, J. Tuppurainen, M. Link, R. Gabl, W. Wersing, M. Schreiter, *Sens. Act. A* **128**, 84 (2006).
[108] S. Rey-Mermet, R. Lanz, P. Muralt, *Proc. IEEE Ultrason. Symp.*, 1253 (2005).

1.6. Chapter conclusion

In this introductory chapter, an overview of the different topics addressed in this thesis was given. It aims at the modelling, realization and characterization of shear mode solidly mounted FBARs, and their testing in liquid environments in view of their application as bio-chemical sensing devices. This development is part of a broader effort to realize complete bio-chemical sensor arrays and micro electro-mechanical systems (BioMEMS) suitable for medical diagnostic applications. Therefore, a short introduction about the diagnostic market, the MEMS market and typical characteristics of modern bio-chemical sensors were given. The most important characteristics are specificity, sensitivity and resolution.

Then, a comparison of different existing sensing technologies was done, with a closer look at acoustic gravimetric technologies. The advantages of FBARs for gravimetric sensing were stressed, such as label free detection, quantitative and time-dependent detection, high detectivity, low-cost realization and Si-based full integration with CMOS electronics. Acoustic technologies use either bulk or surface generated acoustic waves which are mostly excited by using the piezoelectric effect. Consequently, this effect was briefly explained, together with typical materials for thin film applications. In this work, ZnO thin films are used, consequently the different techniques to deposit such films were mentioned in a few words.

The last paragraph of this chapter looked more closely at the projects within which this thesis was realized and at the use of FBARs as bio-chemical sensing devices. Most importantly, it was mentioned that the shear wave mode is needed for applications in liquid environments and that c-axis inclined ZnO is needed for the excitation of such waves in FBARs. The advantages of using shear mode FBARs for sensing applications in liquids has been recognized by other research groups, and some publications have emerged during the curse of this thesis.

2. Resonator modelling, simulation and characterization methods

Modélisation, simulation et méthodes de caractérisation de résonateurs — *Résumé*: Dans ce chapitre sont présentées la modélisation, la simulation et les méthodes de caractérisation des FBARs simples et composites. L'étude de la propagation des ondes acoustiques dans les solides piézoélectriques permet d'établir les équations de base pour un FBAR simple avec des électrodes d'une épaisseur infinitésimale et avec une couche mince de ZnO à axe c incliné. Les paramètres fondamentaux des résonateurs tels que les fréquences de résonance, le facteur de qualité et le coefficient de couplage sont introduits. Il est montré que, **selon l'inclinaison de l'axe c du ZnO** par rapport à la normale à la couche, des ondes à mode longitudinal ou de **cisaillement** peuvent être excitées avec différents coefficients de couplage. Pour une inclinaison de 13.6° les deux modes sont excités avec des coefficients comparables. Les équations de base sont ensuite étendues à des FBARs plus complexes, constitués de plusieurs couches successives. Le concept d'impédance mécanique est introduit et différents modèles sont établis, tels que le **modèle de Mason et de Butterworth-Van Dyke**. La caractérisation électrique des FBARs est expliquée, avec l'extraction du facteur de couplage K^2 et du facteur de qualité Q. Il en résulte que les formules standard pour l'extraction de ces paramètres sont uniquement valables pour des produits $K^2 \cdot Q$ élevés, tandis que des paramètres obtenus à l'aide du modèle BVD sont toujours admis. Finalement, les **FBARs à modes supérieurs** sont introduits. Ils permettent la reconnaissance du mode excité ainsi que l'extraction du coefficient de couplage électromécanique de la couche piézoélectrique. Les outils et modèles obtenus dans ce chapitre sont utilisés tout au long de ce travail. Ils sont utiles en amont de la réalisation des FBARs pour déterminer l'épaisseur des couches, et en aval, lors de leur caractérisation, pour en extraire les propriétés.

2.1. Introduction

This chapter analyzes the modelling, the simulation and the characterization of FBARs. Paragraph **2.2** begins with the fundamental equations needed to describe the elastic and piezoelectric domains. After that the propagation of elastic waves in piezoelectric solids is treated in linear approximation. Given that the solidly mounted FBARs aimed at in this work attempt to realize an ideal BAW resonator on a wafer, the working principle of a simple FBAR with infinitely small electrodes and c-axis inclined ZnO is detailed in paragraph **2.3**. In paragraph **2.4**, the obtained equations are generalized to composite FBARs with multiple layers. Among others, the concept of mechanical impedance is explained. Different models like the Butterworth-Van Dyke (BVD) and Mason Model are introduced. In paragraph **2.5**, the electrical characterization of the FBARs is explained, with the extraction of two fundamental parameters characterizing an FBAR: the coupling coefficient and the quality factor. Finally, in paragraph **2.6**, over-moded FBARs are explained. They permit to check which wave mode is excited and to extract the coupling coefficient of the thin films.

A rigorous one-dimensional mathematical description of a layered piezoelectric BAW-resonator with two

electrodes has been developed by Nowotny and Benes.[1] In this chapter, a simplified description, which suffices for our purpose, will be done. It is **based on own calculations**, but inspired by various sources. It is shown that shear waves can be excited with c-axis inclined ZnO. The most important hypothesis is that we deal with plane waves, i.e. 1D propagation. For the purpose of this work, this model is accurate enough, as lateral dimensions of the resonator exceed by far its thickness (e.g. $200\,\mu m \times 200\,\mu m$ for a thickness of 400 nm). Spurious modes arising because of the lateral limits of the FBAR can not be represented. The models derived in this chapter are needed a) prior to the fabrication of the FBARs for acoustic stack simulation and the determination of the correct thickness for a certain frequency, and b) after the fabrication of the FBAR for the determination of the parameters.

2.2. Acoustic wave propagation in piezoelectric materials

Subscript notation and a Cartesian coordinate system (x_1, x_2, x_3), shown on Figure 2.1 are used for the following derivations.

2.2.1. Strain and Stress

When a solid is subjected to mechanical stresses, its atoms are displaced. $u_i(x_i)$ represents the displacement of a point along an axis x_i with respect to its initial position. The relation between the displacement u_i and the strain S_{ij} is given by:[2]

$$S_{ij} = \frac{1}{2}\left(\frac{\partial u_i}{\partial x_j} + \frac{\partial u_j}{\partial x_i}\right) \tag{2.1}$$

Where {i,j} are taken from {1,2,3}. S_{ij} is called the strain tensor, which has no units and is of 2nd rank. The strain is linked to the stress tensor T_{ij} through Hooke's law:

$$T_{ij} = \sum_{k=1}^{3}\sum_{l=1}^{3} c_{ijkl} S_{kl} \tag{2.2}$$

The stress tensor components are represented on Figure 2.1. In the following, the Einstein summation convention will be applied.[3] With this, equation (2.2) becomes:

$$T_{ij} = c_{ijkl} S_{kl} \tag{2.3}$$

Or in terms of the strain tensor:

$$S_{ij} = s_{ijkl} T_{kl} \tag{2.4}$$

Where {i,j,k,l} are taken from {1,2,3}. c_{ijkl} represent the components of the stiffness tensor that has units of $[N.m^{-2}]$ or [Pa]. s_{ijkl} represent the components of the compliance tensor with units of $[m^2.N^{-1}]$. The tensors are of 4th rank and incorporate longitudinal and shear components. They include 3^4=81 components. However,

[1] H. Nowotny, E. Benes, *J. Acoust. Soc. Am.*, **82**, 513 (1987).
[2] Valid for small deformations: J. Rosenbaum, *Bulk Acoustic Wave Theory and Devices*, Artech House, Norwood, MA (1988).
[3] The Einstein summation convention is a notational convention useful when dealing with coordinate formulae. According to this convention, when an index variable appears twice, it implies that we are summing over all of its possible values.

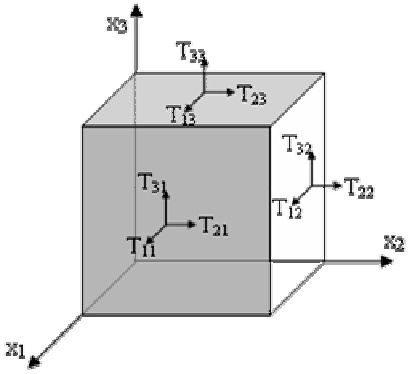

Figure 2.1 : Coordinate system with representation of the stresses T_{ij}.

due to the symmetry of the strain and stress tensors ($T_{ij}=T_{ji}$ and $S_{ij}=S_{ji}$) there are only 36 independent components that can be placed in a square 6x6 **matrix**. *Reduced* subscript notation can be used:

$$\begin{gathered}(ij)\rightarrow\alpha \text{ and } (k,l)\rightarrow\beta \\ (11)\rightarrow(1),\ (22)\rightarrow 2,\ (33)\rightarrow 3,\ (23)=(32)\rightarrow(4),\ (13)=(31)\rightarrow(5),\ (12)=(21)\rightarrow(6)\end{gathered} \tag{2.5}$$

For the stiffness tensor the correspondence to the stiffness matrix is simple:

$$c_{ijkl} \equiv c_{\alpha\beta} \tag{2.6}$$

Where $\{\alpha,\beta\}$ are taken from $\{1,2,3,4,5,6\}$. The stiffness and the compliance coefficients are linked through the following relation:

$$c_{\alpha\beta} \cdot s_{\beta\gamma} = \delta_{\alpha\gamma} \tag{2.7}$$

Where $\delta_{\alpha\gamma}$ is the Kronecker symbol: $\delta_{\alpha\gamma}=1$ if $\alpha=\gamma$, else $\delta_{\alpha\gamma} = 0$. Equation (2.3) can be rewritten as:

$$T_\alpha = c_{\alpha\beta} S_\beta \tag{2.8}$$

And equation (2.4) becomes:

$$S_\alpha = s_{\alpha\beta} T_\beta \tag{2.9}$$

Moreover, energy considerations[4] permit to reduce the number of independent coefficients to 21, i.e. only the upper triangular part of the matrix. This stiffness matrix represents the general case of a triclinic crystalline system without any particular symmetry. The coefficient $1/s_{11}$ is called the Young's modulus in the direction x_1. It varies from several tens of GPa for soft materials like aluminium to several TPa for hard materials like diamond.

Depending on the crystal symmetry certain coefficients of the $c_{\alpha\beta}$ and $s_{\alpha\beta}$ matrices become zero or interdependent, which further decreases the number of free elastic constants. For example, for isotropic materials, only two independent constants c_{11} and c_{12} exist. Their stiffness matrix can be written as:

[4] L. Valbin, PhD Thesis, Université Paris VII (2004): in a linear system in presence of small deformations, only reversible transformations are done. One can show that in case of an adiabatic transformation (no heat transfer between system and outside), the elastic constant c_{ijkl} is the second derivative of the internal energy with respect to the deformations S_{ij} and S_{kl}. In case of a isothermal transformation, the elastic constant c_{ijkl} is the second derivative of the free energy. Thus there is an invariance of the elastic constants when indices pairs ij (or a) and kl (or b) are permutated. The Maxwell relation of symmetry: $c_{ijkl}=c_{klij}$ results.

$$c_{\alpha\beta} = \begin{pmatrix} c_{11} & c_{12} & c_{12} & 0 & 0 & 0 \\ c_{12} & c_{11} & c_{12} & 0 & 0 & 0 \\ c_{12} & c_{12} & c_{11} & 0 & 0 & 0 \\ 0 & 0 & 0 & c_{44} & 0 & 0 \\ 0 & 0 & 0 & 0 & c_{44} & 0 \\ 0 & 0 & 0 & 0 & 0 & c_{44} \end{pmatrix} \quad \text{with } c_{44}=(c_{11}-c_{12})/2 \tag{2.10}$$

2.2.2. Piezoelectricity

As explained in paragraph 1.4, piezoelectricity is a reversible effect. The direct piezoelectric effect is the property of a material to generate an electrical displacement when subjected to mechanical stress. The inverse piezoelectric effect is the property of a material to distort itself under the influence of an electrical field. Hooke's law given by (2.3) and (2.4) is not sufficient to characterize the response of a piezoelectric solid to a stress. The equations characterizing this electromechanical coupling are:[5]

$$T_{ij} = c^{E}_{ijkl} S_{kl} - e_{kij} E_k \tag{2.11}$$

$$D_i = e_{ikl} S_{kl} + \varepsilon^{S}_{ij} E_j \tag{2.12}$$

E_j is the electrical field, i.e. the derivate of the electrical potential φ:

$$E_i = -\frac{\partial \varphi}{\partial x_i} \tag{2.13}$$

D_i is the electrical displacement, and c^{E}_{ijkl}, e_{kij}, ε^{S}_{ij} represent respectively the stiffness tensor at constant electric field E, the piezoelectric constant tensor (of rank 3) and the electrical permittivity tensor (of rank 2) at constant strain S. The units are respectively [N.m^{-2}], [C.m^{-2}] and [F.m^{-1}]. Similarly:

$$S_{ij} = s^{E}_{ijkl} T_{kl} + d_{kij} E_k \tag{2.14}$$

$$D_i = d_{ikl} T_{kl} + \varepsilon^{T}_{ij} E_j \tag{2.15}$$

Where s^{E}_{ijkl}, d_{ikl}, ε^{T}_{ij} represent respectively the compliance at constant electric field E, the piezoelectric constant tensor and the electrical permittivity tensor at constant stress T.

For non-piezoelectric materials, tensors d_{ikl} and e_{kij} are both zero, and tensors ε^{S}_{ij} and ε^{T}_{ij} are equal. Equations (2.11) and (2.14) reduce to (2.3) and (2.4) respectively. By applying the reduced subscript notation, both tensors can also be written in matrix form $e_{i\alpha}$ and $d_{i\alpha}$. For ZnO the constitutive matrixes are:

$$c^{E}_{\alpha\beta} = \begin{pmatrix} c^{E}_{11} & c^{E}_{12} & c^{E}_{13} & 0 & 0 & 0 \\ c^{E}_{12} & c^{E}_{11} & c^{E}_{13} & 0 & 0 & 0 \\ c^{E}_{13} & c^{E}_{13} & c^{E}_{33} & 0 & 0 & 0 \\ 0 & 0 & 0 & c^{E}_{55} & 0 & 0 \\ 0 & 0 & 0 & 0 & c^{E}_{55} & 0 \\ 0 & 0 & 0 & 0 & 0 & \frac{1}{2}\left(c^{E}_{11} - c^{E}_{12}\right) \end{pmatrix} \quad e_{i\alpha} = \begin{pmatrix} 0 & 0 & 0 & 0 & e_{15} & 0 \\ 0 & 0 & 0 & e_{15} & 0 & 0 \\ e_{31} & e_{31} & e_{33} & 0 & 0 & 0 \end{pmatrix} \quad \varepsilon^{S}_{ij} = \begin{pmatrix} \varepsilon^{S}_{11} & 0 & 0 \\ 0 & \varepsilon^{S}_{11} & 0 \\ 0 & 0 & \varepsilon^{S}_{33} \end{pmatrix} \tag{2.16}$$

The components values for ZnO are given in Table 3.1 on page 78.

[5] J. Rosenbaum, *Bulk Acoustic Wave Theory and Devices*, Artech House, Norwood, MA (1988).

2.2.3. Acoustic propagation and coupled wave equations

In the following paragraphs, electrostatics and the absence of mobile charge will be assumed. This is justified since at frequencies of hundreds of MHz, the dimensions of the analyzed structures are much smaller than the electromagnetic wavelength. The derivation of the propagation equation of acoustic waves in an unbounded solid permits to find the acoustic velocities and the polarization, i.e. the displacement direction, of the wave. The fundamental dynamic principle (Newton's law) can be written as follows:

$$\rho \frac{\partial^2 u_i}{\partial t^2} = \frac{\partial T_{ij}}{\partial x_j} \tag{2.17}$$

Assuming electrostatics and the absence of mobile charge, we have (Poisson's law):

$$\frac{\partial D_j}{\partial x_j} = 0 \tag{2.18}$$

By replacing the stress and the electrical displacement by their expressions of formulas (2.11) and (2.12), and considering formula (2.13) for the electric potential, formulas (2.17) and (2.18) become:

$$\rho \frac{\partial^2 u_i}{\partial t^2} = c^E_{ijkl} \frac{\partial S_{kl}}{\partial x_j} + e_{kij} \frac{\partial^2 \varphi}{\partial x_j \partial x_k} \tag{2.19}$$

$$e_{jkl} \frac{\partial S_{kl}}{\partial x_j} - \varepsilon^S_{jk} \frac{\partial^2 \varphi}{\partial x_j \partial x_k} = 0 \tag{2.20}$$

Or written solely as a function of the displacement:

$$\rho \frac{\partial^2 u_i}{\partial t^2} = c^E_{ijkl} \frac{\partial^2 u_l}{\partial x_j \partial x_k} + e_{kij} \frac{\partial^2 \varphi}{\partial x_j \partial x_k} \tag{2.21}$$

$$e_{jkl} \frac{\partial^2 u_l}{\partial x_j \partial x_k} - \varepsilon^S_{jk} \frac{\partial^2 \varphi}{\partial x_j \partial x_k} = 0 \tag{2.22}$$

The coupled piezoelectric field equations are given by these four partial differential equations of motion and electrostatic charge. They couple the electric potential to the mechanical displacement. In the absence of piezoelectricity, when e_{jkl}=0, the two equations separate, which uncouples acoustic and electrical responses.

For plane waves in the direction of a given unit vector $\vec{n}$ with components n_i, the combination of equations (2.21) and (2.22) produces an eigenvalue equation of the form:

$$\overline{\Gamma_{il}} u_i = \rho v_{ac}^2 u_l \tag{2.23}$$

Where v_{ac} is the phase velocity of the acoustic wave in the piezoelectric and $\overline{\Gamma_{il}}$ is a tensor depending on the propagation direction defined by n_i, and the stiffness, the piezoelectric constants and electrical permittivity of the material. It can be written as:

$$\overline{\Gamma_{il}} = \Gamma_{il} + \frac{\gamma_i \gamma_l}{\varepsilon_{ik} n_i n_k} \tag{2.24}$$

Where $\gamma_i = e_{ikl} n_l n_k$ and $\Gamma_{il} = c_{ijkl} n_j n_k$. Γ_{il} is called the Christoffel tensor.[6]

[6] More about this general solution in J. Rosenbaum, *Bulk Acoustic Wave Theory and Devices*, Artech House, Norwood, MA (1988).

The solutions of (2.23) have phase values equal to the eigenvalues of the Christoffel tensor, and polarization vectors equal to the eigenvectors of the Christoffel tensor. In the general case of a triclinic material, with propagation along an arbitrary direction, one will have coexistence of 3 plane waves with orthogonal polarization: a **quasi-longitudinal wave, a rapid quasi-shear wave and a slow quasi-shear wave**.

The term *quasi* refers to the fact that the deflection of a quasi-longitudinal wave, respectively a quasi-shear wave, is approximately parallel, respectively perpendicular, to the propagation direction. In an isotropic non-piezoelectric medium where only two independent constants c_{11} and c_{12} exist, there are 3 acoustic velocities corresponding to 3 plane waves. The velocities of the 3 modes are independent of the directions of propagation. The longitudinal mode corresponds to the eigenvalue c_{11} and has the phase velocity $v_{ac} = \sqrt{c_{1111}/\rho} = \sqrt{c_{11}/\rho}$. There are two shear wave modes with the same velocity for all directions of propagation; this situation is called shear wave mode degeneracy. The shear wave mode phase velocity is $v_{ac} = \sqrt{c_{44}/\rho} = \sqrt{c_{2323}/\rho}$. In section 2.3.1., equation (2.23) will be solved for c-axis inclined ZnO, where the c-axis is inclined at a certain angle with respect to the propagation direction x_3.

2.3. Simple FBAR with c-axis inclined ZnO

A thin film of hexagonal ZnO can generally excite both longitudinal and shear waves simultaneously, unless the film normal is directed along the c-axis, in which case only a longitudinal wave is excited, or when the film normal is perpendicular to the c-axis, in which case only a shear wave is excited. As will be shown later, if the elastic and piezoelectric constants of the resonator satisfy certain relationships, a single mode can also be excited when the c-axis is inclined at some other angle to the resonator normal. In this paragraph, equations (2.21) and (2.22) will be solved in the case of a resonator consisting of a thin c-axis inclined ZnO film. The derivation is comparable to the one done by Foster *et al.* in 1968, who did the calculation for a transducer using inclined ZnO and CdS.[7] It will be shown that depending on the inclination of the c-axis with respect to the resonator normal and depending at which frequency the resonator is excited, longitudinal or shear wave modes are predominately excited.

2.3.1. Resolution of the propagation equations for c-axis inclined ZnO

In this section, the propagation conditions for c-axis inclined ZnO are derived. In the next section, they will be used to derive the impedance characteristics of a simple resonator consisting of a thin c-axis inclined ZnO film, using the appropriate boundary conditions. Figure 2.2 illustrates the problem to be solved. Vectors $\vec{a}_1$ and $\vec{a}_3$ are the unit vectors in direction x_1 and x_3 respectively. The propagation of the wave is in direction x_3. We consider ZnO whose c-axis is inclined in the plane given by x_1 and x_3 by an angle χ with respect to x_3. ZnO is isotropic in the (x_1,x_2) plane (transverse isotropy of (6mm) class materials), therefore there is no loss of generality in assuming that the c-axis lies in the (x_1,x_3) plane. If this was not the case, one would have to consider the x_2 direction too, by doing an averaging of the tensor components around the c-axis. With the c-

[7] N. F. Foster, G. A. Coquin, G. A. Rozgonyi, F. A. Vannatta, IEEE Trans. Sonics Ultrason., **SU-15**, 28 (1968).

axis as shown in Figure 2.2, the u_2 mechanical displacement component is independent of the c-axis angle χ and will not be considered here, since in a typical FBAR using c-axis inclined ZnO, no wave with polarization in the x_2 direction will be excited.

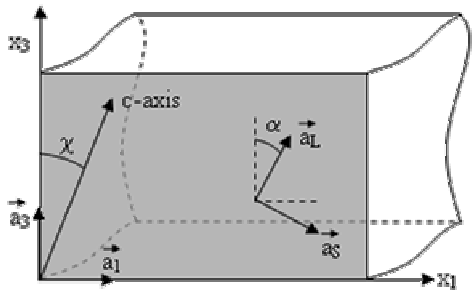

Figure 2.2 : Coordinate system for simple c-axis inclined ZnO.

The stiffness, piezoelectric and permittivity tensors must be expressed in the (x_1,x_3) referential. In this derivation, the c-axis is inclined by an angle χ to the normal. The coefficients (denoted with a prime) relevant for this derivation must be given in terms of the regular coefficients and the angle of rotation χ:[8]

$$\begin{aligned}
c'_{33} &= c^E_{33}\cos^4\chi + 2\left(c^E_{13}+2c^E_{55}\right)\sin^2\chi\cos^2\chi + c^E_{11}\sin^4\chi \\
c'_{55} &= c^E_{55}\left(\cos^4\chi+\sin^4\chi\right)+\left(c^E_{11}+c^E_{33}-2c^E_{13}-2c^E_{55}\right)\sin^2\chi\cos^2\chi \\
c'_{35} &= \sin\chi\cos\chi\left[\left(c^E_{11}-2c^E_{55}-c^E_{13}\right)\sin^2\chi+\left(c^E_{13}+2c^E_{55}-c^E_{33}\right)\cos^2\chi\right] \\
e'_{33} &= \cos\chi\left[\left(e_{31}+2e_{15}\right)\sin^2\chi+e_{33}\cos^2\chi\right] \\
e'_{35} &= -\sin\chi\left[e_{15}\sin^2\chi+\left(e_{33}-e_{31}-e_{15}\right)\cos^2\chi\right] \\
\varepsilon'_{33} &= \varepsilon^S_{11}\sin^2\chi+\varepsilon^S_{33}\cos^2\chi
\end{aligned} \tag{2.25}$$

Equations (2.21) and (2.22) governing the displacement components u_1 and u_3 and the electric potential φ become:

$$\rho\frac{\partial^2 u_1}{\partial t^2} = c'_{55}\frac{\partial^2 u_1}{\partial x_3^2}+c'_{35}\frac{\partial^2 u_3}{\partial x_3^2}+e'_{35}\frac{\partial^2\varphi}{\partial x_3^2} \tag{2.26}$$

$$\rho\frac{\partial^2 u_3}{\partial t^2} = c'_{35}\frac{\partial^2 u_1}{\partial x_3^2}+c'_{33}\frac{\partial^2 u_3}{\partial x_3^2}+e'_{33}\frac{\partial^2\varphi}{\partial x_3^2} \tag{2.27}$$

$$\varepsilon'_{33}\frac{\partial^2\varphi}{\partial x_3^2} = e'_{35}\frac{\partial^2 u_1}{\partial x_3^2}+e'_{33}\frac{\partial^2 u_3}{\partial x_3^2} \tag{2.28}$$

By substituting the potential φ of equation (2.28) into equations (2.26) and (2.27), one obtains:

$$\rho\frac{\partial^2 u_1}{\partial t^2} = c^*_{55}\frac{\partial^2 u_1}{\partial x_3^2}+c^*_{35}\frac{\partial^2 u_3}{\partial x_3^2} \tag{2.29}$$

$$\rho\frac{\partial^2 u_3}{\partial t^2} = c^*_{35}\frac{\partial^2 u_1}{\partial x_3^2}+c^*_{33}\frac{\partial^2 u_3}{\partial x_3^2} \tag{2.30}$$

In which:

[8] N. F. Foster, G. A. Coquin, G. A. Rozgonyi, F. A. Vannatta, IEEE Trans. Sonics Ultrason., **SU-15**, 28 (1968).

$$c_{55}^{*} = c'_{55} + \frac{e'^{2}_{35}}{\varepsilon'_{33}} \qquad c_{35}^{*} = c'_{35} + \frac{e'_{33}e'_{35}}{\varepsilon'_{33}} \qquad c_{33}^{*} = c'_{33} + \frac{e'^{2}_{33}}{\varepsilon'_{33}} \tag{2.31}$$

c_{55}^{*}, c_{35}^{*} and c_{33}^{*} are called the piezoelectrically stiffened elastic constants. If the crystal is not piezoelectric ($e_{i\alpha} = 0$), they reduce to the rotated stiffness constants c'_{55}, c'_{35} and c'_{33} given in equations (2.25). Equations (2.29) and (2.30) have the plane-wave solutions:

$$\vec{u}_L(x_3) = \underbrace{\mathrm{Re}\left[U_{L1}\exp\left(j\omega(t + x_3/v_L)\right) + U_{L2}\exp\left(j\omega(t - x_3/v_L)\right)\right]}_{u_{L0}(x_3)} \cdot \vec{a}_L \tag{2.32}$$

$$\vec{u}_S(x_3) = \underbrace{\mathrm{Re}\left[U_{S1}\exp\left(j\omega(t + x_3/v_S)\right) + U_{S2}\exp\left(j\omega(t - x_3/v_S)\right)\right]}_{u_{S0}(x_3)} \cdot \vec{a}_S \tag{2.33}$$

Where ω is the radial frequency and t is the time. $\vec{u}_L$ and $\vec{u}_S$ are the mechanical displacements of the quasi-longitudinal and quasi-shear waves, respectively. v_L and v_S are their respective velocities, given by:[9]

$$v_L = \left[\frac{c_{33}^{*} + c_{55}^{*}}{2\rho} + \sqrt{\left(\frac{c_{33}^{*} - c_{55}^{*}}{2\rho}\right)^2 + \left(\frac{c_{35}^{*}}{\rho}\right)^2}\right]^{1/2} \tag{2.34}$$

$$v_S = \left[\frac{c_{33}^{*} + c_{55}^{*}}{2\rho} - \sqrt{\left(\frac{c_{33}^{*} - c_{55}^{*}}{2\rho}\right)^2 + \left(\frac{c_{35}^{*}}{\rho}\right)^2}\right]^{1/2} \tag{2.35}$$

U_{L1}, U_{L2}, U_{S1} and U_{S2} are arbitrary amplitudes, and $\vec{a}_L$ and $\vec{a}_S$ are unit vectors expressed in terms of the unit vectors $\vec{a}_1$ and $\vec{a}_3$, as

$$\vec{a}_L = \vec{a}_1 \sin\alpha + \vec{a}_3 \cos\alpha \tag{2.36}$$

$$\vec{a}_S = \vec{a}_1 \cos\alpha - \vec{a}_3 \sin\alpha \tag{2.37}$$

In which α is the angle between $\vec{a}_L$ and the x_3 axis and is given by:

$$\tan\alpha = \frac{2c_{35}^{*}}{c_{33}^{*} - c_{55}^{*}} \tag{2.38}$$

This angle shows that the displacement $\vec{u}_L$ is inclined with respect to the propagation direction. The polarization $\vec{u}_S$ is also not exactly perpendicular to the propagation direction, but inclined by an angle α. In general, the displacement of the particles is thus neither pure shear nor pure longitudinal wave mode. For this reason they are called quasi-longitudinal and quasi-shear mode respectively. Figure 2.3 shows the velocities v_L and v_S and the polarization angle α as a function of the inclination angle χ (calculation in MATLAB[10]).

[9] N. F. Foster, G. A. Coquin, G. A. Rozgonyi, F. A. Vannatta, IEEE Trans. Sonics Ultrason., **SU-15**, 28 (1968).

[10] MATLAB is a high-level technical computing language and interactive environment for algorithm development, data visualization, data analysis, and numeric computation. [see www.matlab.com].

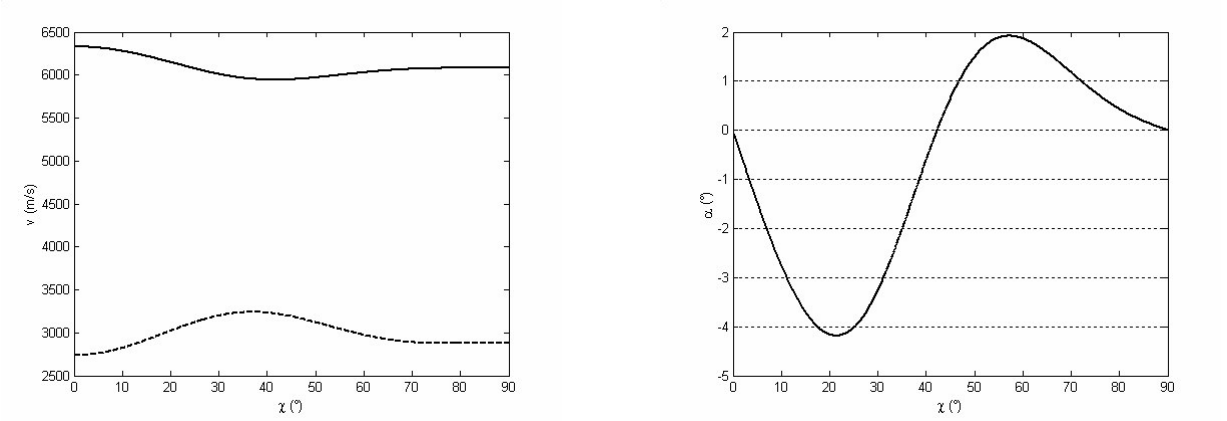

a) *b)*

Figure 2.3 : a) Acoustic velocities of quasi-longitudinal (solid line) and quasi-shear (dashed line) modes; b) polarization angle α with respect to the propagation direction; both as a function of the inclination angle χ.

Generally, by solving the eigenvalue equation (2.23), the velocities and polarization angles of the quasi longitudinal, quasi shear and pure shear modes can be found for any material orientation and any propagation direction. The results are usually plotted in so-called slowness-curves, representing the inverse of the acoustic velocities. The velocity for a polarization in x_2 direction, corresponding to a pure shear wave mode, which is independent of χ, can be calculated in a similar way. It was omitted here, as this mode cannot be excited in our standard FBAR configuration. The corresponding acoustic velocity is 2735 m/s, which in case of χ=0° also corresponds to the velocity of the quasi-shear mode.

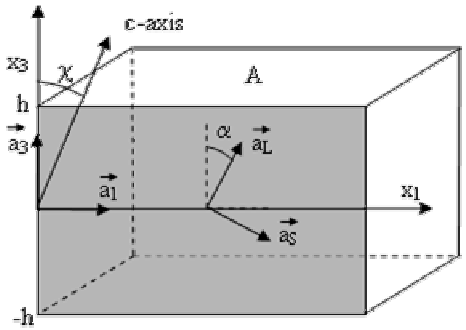

Figure 2.4 : Simple FBAR with c-axis inclined ZnO of thickness 2h and with infinitesimal thin electrodes.

2.3.2. Electrical impedance and coupling coefficient for a simple resonator

In the following, the expression of the impedance of a resonator consisting of a c-axis inclined ZnO layer with infinitively small electrodes will be derived. The plane wave solutions derived in the previous section will be used with appropriate boundary conditions. Electrodes on both faces of the transducer are considered perfectly conducting and infinitesimally thin. The thickness of the resonator is 2h, as shown in Figure 2.4. In solving for the impedance, two sets of boundary conditions are considered. First, *zero mechanical stress* is assumed at the electrodes because they are unconstrained. Second, a *sinusoidal input current* is applied

between both electrodes. The two parallel plates are large in the x_1 and x_2 directions, so only an E-field in the x_3-direction is considered.

We want to solve for the motion of the resonator in response to an input current I of radial frequency ω. In the following, it will be omitted that the real part of the expressions must be considered to obtain the real physical solution.

$$I = I_0 \exp(j\omega t) \tag{2.39}$$

The electrical displacement D_3 is related to the input current I by:

$$D_3 = \frac{I_0}{j\omega A}\exp(j\omega t) = D_{30}\exp(j\omega t) \tag{2.40}$$

Where A is the area of the FBAR. Both plane-wave solutions (2.32) and (2.33) of the deflection are required and must be expressed in the system (x_1,x_3). Hence, the total deflection $\vec{u}(x_3)$ can be expressed as:

$$\vec{u}(x_3) = \vec{u}_L(x_3) + \vec{u}_S(x_3) \tag{2.41}$$

Remembering the expressions for $\vec{a}_L$ and $\vec{a}_S$, it can be expressed as:

$$\vec{u}(x_3) = \vec{a}_3 \underbrace{\left(u_{L0}(x_3)\cos\alpha - u_{S0}(x_3)\sin\alpha\right)}_{u_3} + \vec{a}_1 \underbrace{\left(u_{L0}(x_3)\sin\alpha + u_{S0}(x_3)\cos\alpha\right)}_{u_1} \tag{2.42}$$

The solution for the electrical potential $\varphi(x_3)$ is obtained by integrating equation (2.28) twice:

$$\varphi(x_3) = \frac{e'_{35}}{\varepsilon'_{33}}u_1(x_3) + \frac{e'_{33}}{\varepsilon'_{33}}u_3(x_3) + ax_3 + b \tag{2.43}$$

Where a and b are constants. As we are only interested in a difference of potential between x_3=h and x_3=-h, b can be taken as 0. By using this expression in (2.15) for the electrical displacement D_3, one finds that:

$$a = -\frac{D_{30}}{\varepsilon'_{33}}\exp(j\omega t) \tag{2.44}$$

The stress components $T_{33}(x_3)$ and $T_{31}(x_3)$ can be obtained by integrating Newton's law (2.17) along direction x_3 using the appropriate terms of equation (2.42):

$$\begin{aligned} T_{33} &= \int \rho \frac{\partial^2 u_3}{\partial t^2} dx_3 \\ T_{31} &= \int \rho \frac{\partial^2 u_1}{\partial t^2} dx_3 \end{aligned} \tag{2.45}$$

Which when developed gives the following expressions (the constant terms are obtained by considering equation (2.11) and (2.43)):

$$\begin{aligned} T_{31} = {} & j\omega Z_L \exp(j\omega t)\sin\alpha\left[U_{L1}\exp(j\omega x_3/v_L) - U_{L2}\exp(-j\omega x_3/v_L)\right] \\ & + j\omega Z_S \exp(j\omega t)\cos\alpha\left[U_{S1}\exp(j\omega x_3/v_S) - U_{S2}\exp(-j\omega x_3/v_S)\right] - e'_{35}a \end{aligned} \tag{2.46}$$

$$\begin{aligned} T_{33} = {} & j\omega Z_L \exp(j\omega t)\cos\alpha\left[U_{L1}\exp(j\omega x_3/v_L) - U_{L2}\exp(-j\omega x_3/v_L)\right] \\ & + j\omega Z_S \exp(j\omega t)\sin\alpha\left[-U_{S1}\exp(j\omega x_3/v_S) + U_{S2}\exp(-j\omega x_3/v_S)\right] - e'_{33}a \end{aligned} \tag{2.47}$$

With Z_L and Z_S being defined in the following way:[11]

$$Z_L = \rho v_L \tag{2.48}$$
$$Z_S = \rho v_S \tag{2.49}$$

The boundary conditions for the stress are:[12]

$$T_{33}(h)=T_{33}(-h)=0 \tag{2.50}$$
$$T_{31}(h)=T_{31}(-h)=0 \tag{2.51}$$

By using these boundary conditions in expressions (2.46) and (2.47) and after a considerable amount of algebra, one finds the expressions for U_{L1}, U_{L2}, U_{S1} and U_{S2}:

$$U_{L1} = -U_{L2} = U_L = \frac{\left(e'_{33}\cos\alpha + e'_{35}\sin\alpha\right)a}{2j\omega Z_L \cos(\omega h / v_L)\exp(j\omega t)} \tag{2.52}$$

$$U_{S1} = -U_{S2} = U_S = \frac{\left(e'_{35}\cos\alpha - e'_{33}\sin\alpha\right)a}{2j\omega Z_S \cos(\omega h / v_S)\exp(j\omega t)} \tag{2.53}$$

As expected, since the air-to-electrode interface is an ideal reflector and the structure is symmetric, the amplitudes of the deflections are equal. These two expressions can now be introduced in expression (2.42) to find the complete expressions of the displacement components $u_3(x_3)$ and $u_1(x_3)$. These expressions can then be introduced in equation (2.43) of the electrical potential. The difference of the potential between the top and the bottom electrode (x_3=h and x_3=-h) can at last be found, again after a lot of algebra:

$$\varphi(h)-\varphi(-h) = 2ah\cdot\left[1-\frac{\left(e'_{33}\cos\alpha + e'_{35}\sin\alpha\right)^2}{\omega Z_L h\varepsilon'_{33}}\tan(\omega h / v_L) - \frac{\left(e'_{35}\cos\alpha - e'_{33}\sin\alpha\right)^2}{\omega Z_S h\varepsilon'_{33}}\tan(\omega h / v_S)\right] \tag{2.54}$$

Finally, the electrical impedance Z of the resonator is found by relating this potential difference to the applied input current I:

$$Z = \frac{\varphi(h)-\varphi(-h)}{I} = \frac{\varphi(h)-\varphi(-h)}{j\omega A a\varepsilon'_{33}} \tag{2.55}$$

Which when inserting expression (2.54) gives the following expression for Z:

$$Z = \frac{1}{j\omega C}\cdot\left[1 - K_L^2\frac{\tan(\omega h / v_L)}{\omega h / v_L} - K_S^2\frac{\tan(\omega h / v_S)}{\omega h / v_S}\right] \tag{2.56}$$

With C being the "static" capacitance of the dielectric (piezoelectric) layer:

$$C = \frac{A\varepsilon'_{33}}{2h} \tag{2.57}$$

And:

[11] Z_L and Z_S are also called the characteristic acoustic impedances for the quasi-longitudinal and the quasi-shear mode respectively. This will be seen in greater detail in paragraph 2.4.2.

[12] When other layers are attached to the piezoelectric layer, as in the case of a composite FBAR with multiple layers, other boundary conditions must be applied, involving the acoustic impedance and thickness of the layers. This case will be treated in paragraph 2.4.

$$K_L^2 = \frac{\left(e'_{33}\cos\alpha + e'_{35}\sin\alpha\right)^2}{\varepsilon'_{33}\rho v_L^2} \tag{2.58}$$

$$K_S^2 = \frac{\left(e'_{35}\cos\alpha - e'_{33}\sin\alpha\right)^2}{\varepsilon'_{33}\rho v_S^2} \tag{2.59}$$

K_L^2 and K_S^2 are the **electromechanical coupling coefficients** for the longitudinal and the shear wave mode respectively.[13] Figure 2.5 shows the coupling coefficients as a function of the c-axis inclination angle χ. The material constants used are those of Table 3.1. As can be seen, they vary greatly in function of χ. Both K and K^2 are represented, but one has to keep in mind that for the determination of the FBAR impedance, only K^2 is of relevance.[14] As expected, at 0°, only longitudinal mode will be excited, and at 90°, only shear wave mode. Modes with specific inclinations will be discussed in the next section.

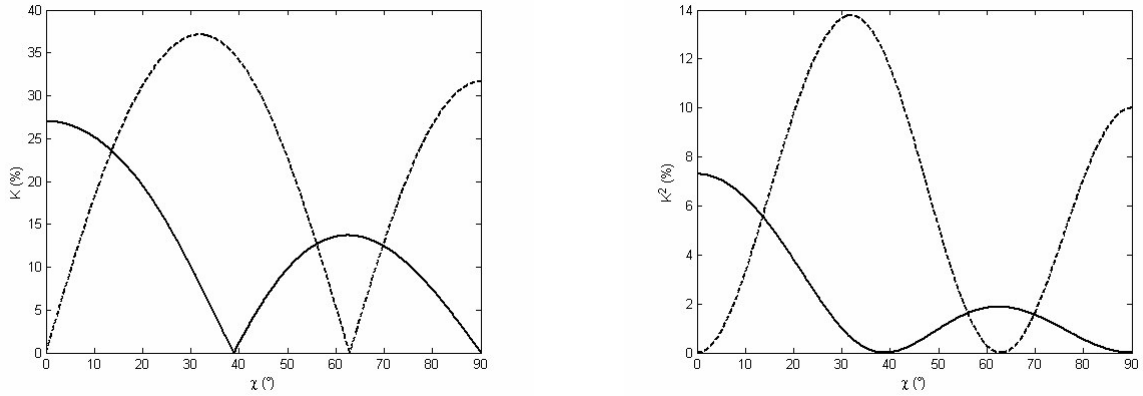

a) *b)*

Figure 2.5 : Electromechanical coupling coefficient K and coupling coefficient squared K^2 for longitudinal (solid) and shear wave mode (dashed) depending on c-axis inclination angle χ.

2.3.3. Electromechanical coupling and velocities for specific c-axis inclinations

The impedance expression found in the previous section can be greatly simplified when having pure modes, i.e. when the polarization angle α is zero. In that case, a longitudinal mode has a displacement collinear with the propagation and a shear wave mode a displacement perpendicular to the propagation. From expression (2.38) this is achieved when tan α is zero, i.e. when $c^*_{35} = 0$. When looking at the expression of c'_{35}, e'_{33} and e'_{35}, we find that pure modes are excited at inclination angles χ of 0° and 90°, and when:

$$c'_{35} = -\frac{e'_{33}e'_{35}}{\varepsilon'_{33}} \tag{2.60}$$

This happens for an angle of 42.25°. At this inclination, shear wave mode coupling greatly exceeds the

[13] They correspond to the expressions found by Foster in 1968 for a transducer, which is a good confirmation of the correctness of this derivation. See N. F. Foster, G. A. Coquin, G. A. Rozgonyi, F. A. Vannatta, IEEE Trans. Sonics Ultrason., **SU-15**, 28 (1968).
[14] In this work, both the coupling coefficient and the square of the coupling coefficient will be used. To make the distinction clear, the following convention widely used in literature is adopted: **the simple coupling is given in an absolute number, while the coupling squared is given in percentage**.

longitudinal coupling, but both modes are excited and are pure. Table 2.1 summarizes the characteristics obtained for these 3 angles.

The longitudinal coupling can also become zero at some angle other than 90°, and only quasi shear wave mode is excited. From equation (2.58) this is obtained when:

$$e'_{33}\cos\alpha + e'_{35}\sin\alpha = 0 \tag{2.61}$$

This corresponds to a c-axis inclination of 38.9°, resulting in a polarization angle of -0.09° and a quasi-shear mode coupling coefficient K_S^2 of 12.2%. Similarly, at 62.9°, only quasi-longitudinal mode is excited, with a polarization angle of 1.72°. Table 2.1 also summarizes the characteristics for these two cases.

Figure 2.6 a) shows the calculated amplitude and phase of the impedance for a pure longitudinal mode at 0° inclination. Figure 2.6 b) shows a simulation of the impedance for a pure shear mode at 90°. An area A of 200 µm × 200 µm and a thickness 2h of 1 µm were used.

TABLE 2.1
CALCULATED NUMERICAL VALUES OF A SIMPLE C-AXIS INCLINED FBAR FOR THE EXCITATION OF PURE MODES (α=0°) AND FOR THE EXCITATION OF SINGLE QUASI-MODES.

Property	χ=0° (pure longitudinal)	χ=90° (pure shear)	χ=62.9° (only quasi-longitudinal)	χ=38.9° (only quasi-shear)	χ=42.25° (pure longitudinal and pure shear)
K_L^2	7.3 %	0	1.87 %	0	0.12 %
K_S^2	0	10 %	0	12.2 %	10.4 %
v_L	6330 m/s	6080 m/s	6044 m/s	5946 m/s	5943 m/s
v_S	2735 m/s	2883 m/s	2940 m/s	3236 m/s	3217 m/s
α	0	0	1.72 °	-0.09 °	0

Generally both modes will be excited. At 13.6 ° for example, both quasi-longitudinal and quasi-shear are excited with the same coupling coefficients. In that case we have:

$$K_L^2 = K_S^2 = 5.57\ \% \tag{2.62}$$

Figure 2.7 shows the characteristic one obtains in this case. The wideband characteristic is displayed in part (a) and the narrowband view of the fundamental shear mode is given in part (b). On the wideband characteristic, the first fundamental shear and longitudinal resonances and the first shear harmonic can be seen.

The characteristics have a number of interesting attributes. The impedance is purely reactive, which is consistent with the fact that a loss mechanism has not yet been incorporated into the model. The wideband response can be approximately modelled by a capacitor with a value of C because K_L, K_S and the tangent term are small for most frequencies. Superimposed on this capacitance characteristic are multiple resonances spaced by twice the fundamental frequency for each mode. One sees that the fundamental shear and longitudinal resonances are spaced far from one another. More specifically, since the longitudinal acoustic

velocity is approximately twice the shear acoustic velocity, the fundamental longitudinal resonance is approximately double the fundamental shear resonance. There is a local impedance minimum and local impedance maximum in the narrowband response shown in Figure 2.7 b). These extrema offer the definition for the series and parallel resonance frequencies, respectively.

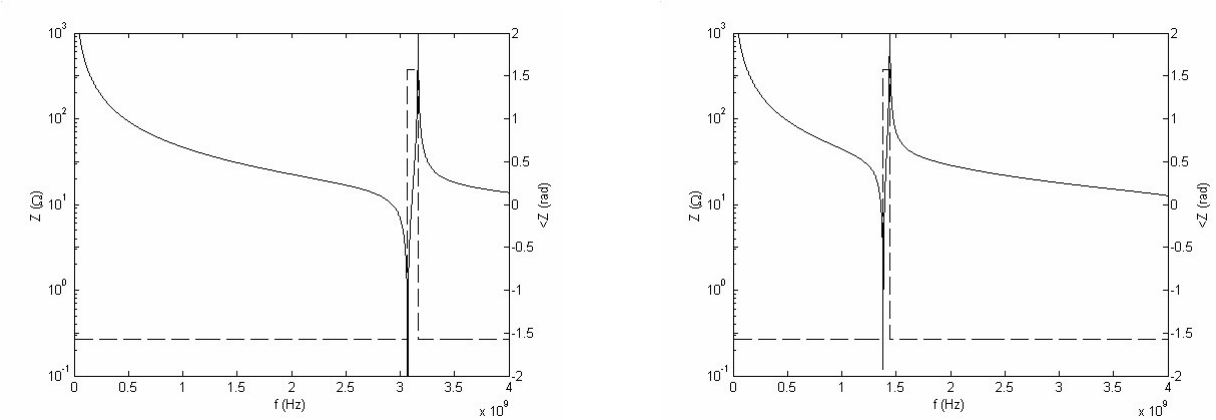

a) *b)*

Figure 2.6 : Impedance characteristic (solid: amplitude, dashed: phase) of a simple FBAR of c-axis inclined ZnO. a) Pure longitudinal mode (0°), b) pure shear mode (90°). The area is 200µm ×200µm and the thickness 1µm.

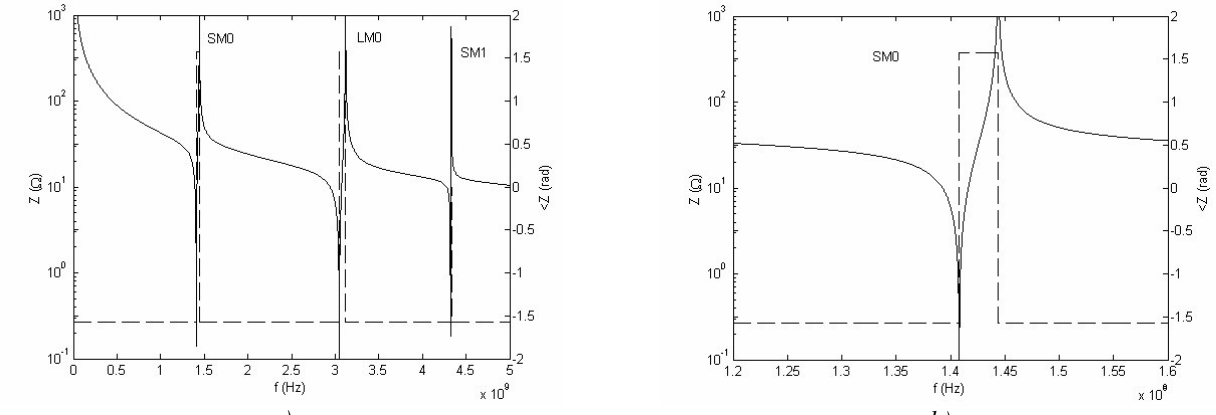

a) *b)*

Figure 2.7 : Impedance characteristic (solid: amplitude, dashed: phase) of a simple FBAR of 13.6° c-axis inclined ZnO. a) Wide-band, b) Narrow-band. The area is 200 µm × 200 µm and the thickness is 1 µm.

2.3.4. Definition of the resonance frequencies and influence of one mode on the other

The parallel resonance occurs when one of the tangent terms in Z explodes to infinity. This gives the following expression for the **parallel resonance frequency f_p** for the n^{th} shear or longitudinal mode:

$$f_{p(S,L)}^{(2n+1)} = (n+\frac{1}{2})\frac{v_{(S,L)}}{2h} \tag{2.63}$$

For an FBAR where only one single mode is excited the **series resonance f_s** occurs when the impedance of

the resonator becomes zero, which happens when the respective single tangent term becomes equal to 1. This gives the following relationship between f_s and f_p:

$$K^2_{(S,L)} = \frac{(2n+1)\frac{\pi}{2} f_{s(S,L)} / f_{p(S,L)}}{\tan\left((2n+1)\frac{\pi}{2} f_{s(S,L)} \Big/ f_{p(S,L)}\right)} \tag{2.64}$$

This equation shows that $K^2_{(S,L)}$ is related to the ratio of series and parallel resonances of a particular mode. Since $K^2_{(S,L)}$ is a small positive number, the tangent term is large, implying that f_s is slightly smaller than f_p. The spacing between f_s and f_p defines the maximum bandwidth of a filter which can be realized with a simple FBAR.[15] It can be shown that the points of series and parallel frequencies also correspond to the points where the phase of the impedance is zero or where the slope of the phase is minimal or maximal.

In the general case of the excitation of both quasi-longitudinal and quasi-shear modes, the impedance becomes zero when the sum of both tangent terms of equation (2.56) becomes equal to 1. This is the case at a frequency slightly lower than at the series resonance of the pure mode. Figure 2.8 a) shows the two tangent terms of equation (2.56) for a c-axis inclination of 13.6°, where both modes are excited with the same strength. At the shear resonances in particular, it can be recognized that the longitudinal contribution is not zero, which will shift the series resonance. Figure 2.8 b) shows a narrow-band view around the fundamental shear resonance, with the shear tangent term, the longitudinal tangent term, and the sum of both. As can be seen (lines), the point where the sum of both tangent terms becomes one, corresponding to the series resonance, is slightly shifted with respect to the point were the only the shear tangent terms becomes one, which corresponds to the series resonance in case of a FBAR where only one mode is excited.

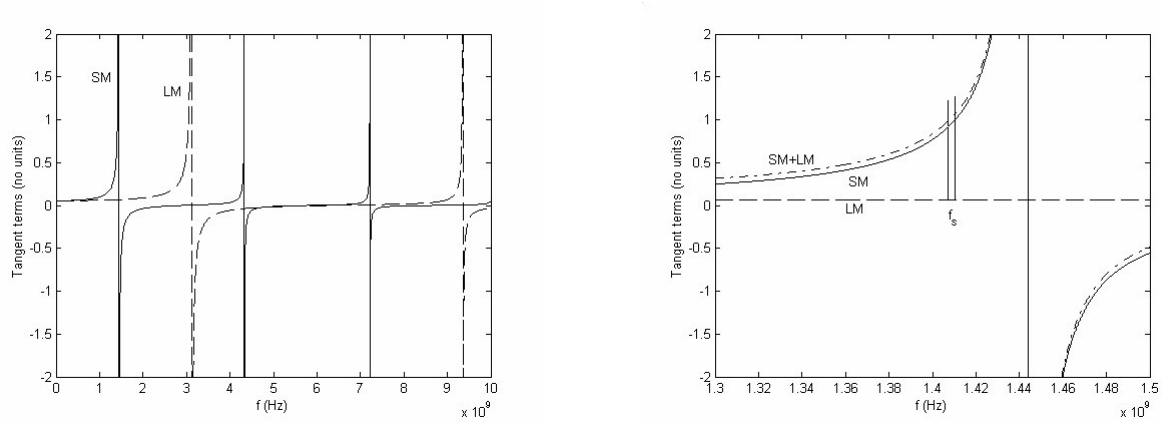

a) *b)*

Figure 2.8 : Quasi-shear (solid line) and quasi-longitudinal (dashed line) tangent terms for a simple FBAR of c-axis inclination 13.6° as a function of frequency; a) broad-band view and b) narrow-band view. The narrow band view also shows the sum of both tangent terms. The area of the simulated FBAR is 200 μm × 200 μm and the thickness is 1 μm.

One can still define the series resonance frequency f_s of a particular mode at the point were the impedance becomes zero. The relation to the parallel frequency f_p can in that case be expressed as:

[15] K. M. Lakin, G. R. Kline, K. T. McCarron, *IEEE Trans. Microwave Theo. Techn.*, **41**, 2139 (1993).

$$K^2_{app(S,L)} = \frac{\frac{\pi}{2} f_{s(S,L)} \Big/ f_{p(S,L)}}{\tan\left(\frac{\pi}{2} f_{s(S,L)} \Big/ f_{p(S,L)}\right)} \tag{2.65}$$

Where $K^2_{app(S,L)}$ is the **apparent coupling coefficient** for that particular mode. Figure 2.9 shows a simulation of the apparent coupling coefficient for the first shear mode as a function of the c-axis inclination and normalized to the shear coupling coefficient at that inclination. As can be seen, near 0° and 62.9°, the simulation becomes unstable, since at those angles the shear mode coupling coefficient goes to 0 and no resonance is seen. Also at inclinations of 38.9° and 90°, the apparent coupling equals the shear mode coupling coefficient, since only shear mode is excited and there can be no influence of the longitudinal mode. Generally, the difference between the shear mode coupling and the apparent coupling is less than 5%. This means that for shear coupling coefficient simulation and extraction methods, the longitudinal mode can be ignored. However, it is important to keep in mind that in general, the longitudinal part of the vibration at the shear wave resonance is not equal to zero. This means that longitudinal stress and displacement components will be excited. The FBAR will not perform solely shear mode vibrations, but also *pump* energy into a longitudinal mode. During operation in liquids, these longitudinal components will dissipate into the liquid and thus present an additional loss mechanism.

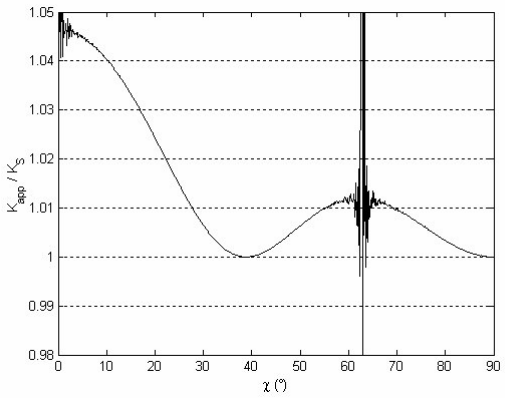

Figure 2.9 : Apparent coupling coefficient of the first shear mode as a function of c-axis inclination normalized to the shear coupling coefficient at the inclination.

2.4. Composite FBAR with multiple layers

2.4.1. Problem statement and pure mode simplification

The derivation of the impedance for a simple FBAR which was done in paragraph 2.3 provides the basis on which to derive expressions for more complicated FBAR structures. Complete models must take into account the other layers above and below the piezoelectric, like electrodes and acoustic mirrors. The composite resonator is shown in Figure 2.10. These layers can be viewed as segments of an acoustic transmission line terminated by an air-to-solid interface. Compared to the derivation in section 2.3.2, only the boundary conditions (equation (2.50)) on both sides of the piezoelectric layer have to be changed.

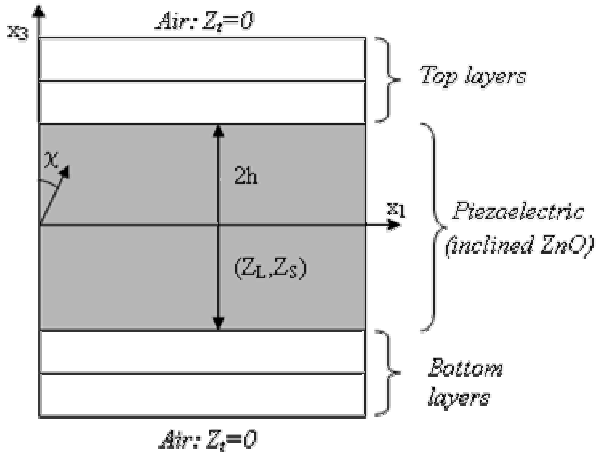

Figure 2.10 : Composite FBAR structure with multiple layers.

Generally, the modes propagating into layers attached to the piezoelectric will be complicated. There will always be propagation of both longitudinal and shear waves whose strength depends not only on the coupling coefficients for quasi-longitudinal and quasi-shear mode, but also on the polarization angle α. For example, the shear component at the interface to an adjacent layer will be composed of the x_1 component of both $\vec{u}_S$ and $\vec{u}_L$. In the case of ZnO however, α is small (<5°) as can be seen on Figure 2.3 b). We will therefore make the approximation that the **piezoelectric excites only pure modes,** which means that we will take α equal to zero. Expressed in formulas, this means that the deflection $\vec{u}(x_3)$ is:

$$\vec{u}(x_3) = \vec{a}_3 u_3(x_3) + \vec{a}_1 u_1(x_3) \tag{2.66}$$

With formulas (2.32) and (2.33) becoming:

$$u_3(x_3) = U_{L1}\exp\left(j\omega(t + x_3/v_L)\right) + U_{L2}\exp\left(j\omega(t - x_3/v_L)\right) \tag{2.67}$$

$$u_1(x_3) = U_{S1}\exp\left(j\omega(t + x_3/v_S)\right) + U_{S2}\exp\left(j\omega(t - x_3/v_S)\right) \tag{2.68}$$

Similarly, the stresses in the piezoelectric (equations (2.46) and (2.47)) become:

$$T_{31} = j\omega Z_S \exp(j\omega t)\left[U_{S1}\exp(j\omega x_3/v_S) - U_{S2}\exp(-j\omega x_3/v_S)\right] - e'_{35}\,a \tag{2.69}$$

$$T_{33} = j\omega Z_L \exp(j\omega t)\left[U_{L1}\exp(j\omega x_3/v_L) - U_{L2}\exp(-j\omega x_3/v_L)\right] - e'_{33}\,a \tag{2.70}$$

This does not mean that only one mode is excited and propagating. Generally, both modes are excited, even though at different strength depending on the respective electromechanical coupling coefficients.

The following example illustrates the approximation. The maximum α is 4.2° for a c-axis inclination of 21.4°. In this case, the maximum deflection in u_1 direction, corresponding to the shear component, would be:

$$\begin{aligned} U_1 &= U_L \sin\alpha + U_S \cos\alpha \\ &= 0.073 \cdot U_L + 0.997 \cdot U_S \end{aligned} \tag{2.71}$$

This means that the contribution from the quasi-longitudinal mode $u_L(x_3)$ is around 14 times smaller than the direct contribution from the quasi-shear mode $u_S(x_3)$. Moreover, at that inclination, quasi shear mode is excited with an electro-mechanical coupling of 10.6%, whereas the quasi longitudinal mode is only excited

with a coupling of 3.4%, meaning that the contribution of the longitudinal mode will be even less. The approximation that $u_1(x_3)$ equals $u_S(x_3)$ is thus not very important. A similar calculation can be made for the longitudinal mode, which justifies the approximation of considering only pure modes.

A second simplification that will be done is that we will assume that the modes actuated by the piezoelectric layer propagate into the other films as pure modes. The more complicated general case was treated by several authors, but is not necessary for the purpose of this work.[16] As a matter of fact, most materials used in thin film form in this work are either amorphous or polycrystalline, and can be considered isotropic in-plane, in which case the excited pure mode continues propagation as a pure mode.

2.4.2. Equivalent terminating acoustic impedance

In order to solve for the electrical impedance of a composite resonator, the concept of acoustic impedance is introduced. It is defined as:

$$Z_{ac}(x_3) = -\frac{T(x_3)}{v(x_3)} \tag{2.72}$$

With units of [$kg.s^{-1}.m^{-3}$]. $T(x_3)$ and $v(x_3)$ are the stress and velocity at a particular point within a solid and propagation is assumed to be in x_3 direction.

$$v(x_3) = \partial u(t)/\partial t \tag{2.73}$$

In general, T and v can be composed of waves of different modes and travelling in both the positive and negative directions. A characteristic acoustic impedance Z_{ac} can also be defined for a *given mode*:

$$Z_{ac} = -\frac{T_+}{v_+} \tag{2.74}$$

Where the plus sign indicates a positive travelling wave. The characteristic acoustic impedance is different from the acoustic impedance since it does not account for reflected waves. It is defined in an infinite media and therefore does not have a positional dependence. For example, a longitudinal mode travelling in the x_3-direction of a cubic crystal has a characteristic impedance of $\sqrt{\rho c_{33}}$. The characteristic acoustic impedances for c-axis inclined ZnO have been found in section 2.3.2 and are given in (2.48) and (2.49) for quasi-longitudinal and quasi-shear modes respectively. In general, they can be written in the form:

$$Z_{ac} = \rho v_{ac} \tag{2.75}$$

Where ρ is the density of the material and v_{ac} is the acoustic velocity of the mode which is considered. It can be found by solving the Christoffel equation for the material and the propagation in direction x_3. Z_{ac} is thus valid for a particular mode (shear or longitudinal) with acoustic velocity v_{ac}.

If the acoustic impedance is known at a certain point within a layer, it can be calculated at another point of the layer situated at a distance h_0 using the **transmission line impedance equation**:[17]

---

[16] K. M. Lakin, *45th Annu. Symp. Freq. Contr.*, 201 (1991); H. Nowotny, E. Benes, *J. Acoust. Soc. Am.*, **82**, 513 (1987).
[17] K. M. Lakin, G. R. Kline, K. T. McCarron, *IEEE Trans. Microwave Theo. Techn.*, **41**, 2139 (1993).

$$Z_{in} = Z_0 \left[\frac{Z_t \cos(\omega h_0 / v_{ac}) + jZ_0 \sin(\omega h_0 / v_{ac})}{Z_0 \cos(\omega h_0 / v_{ac}) + jZ_t \sin(\omega h_0 / v_{ac})} \right] \quad (2.76)$$

Where Z_0 is the characteristic impedance of the layer and Z_t is the mechanical impedance which is known. The impedance can also be calculated in the other layers of the acoustic stack, since the mechanical impedance is continuous across an interface due to the continuity of mechanical displacement and stress.

In the case of a composite FBAR, each acoustic stack on the top and the bottom of the piezoelectric layer is terminated with an air-to-solid interface. This interface has an acoustic impedance of zero because at that point we assume that T=0. With the help of equation (2.76) and the continuity of the impedance across an interface, we can find the mechanical impedances at the interfaces which contact the piezoelectric. In other words, we find the equivalent terminating impedances for the top and bottom acoustic stacks, for the shear and longitudinal modes respectively. An analogy between electrical and mechanical domains can be done to further illustrate the transmission line impedance equation. In that case, T is analogue to an electrical voltage, and v represents an electrical current. Equation (2.76) can then be represented as in Figure 2.11. A zero impedance Z_t, as in the case of air, can be represented with a short circuit.

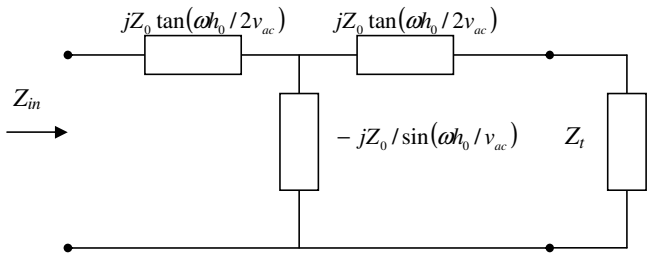

Figure 2.11 : Equivalent representation of the transmission line equation for a layer of thickness h_0 and a mode of acoustic velocity v_{ac}.

2.4.3. Impedance derivation of a composite FBAR / Mason Model

When the acoustic stacks on both sides of the piezoelectric film have been expressed as equivalent terminating impedances $Z_{T,L}$ and $Z_{B,L}$ for the longitudinal mode, and $Z_{T,S}$ and $Z_{B,S}$ for the shear mode, the impedance derivation of the complete FBAR can be done. It follows the derivation done in paragraph 2.3, but with other boundary conditions. We assume that the exciting electrodes lie on each side of the piezoelectric layer of thickness 2h and that there are no other layers in between.[18] The mechanical impedances of the electrodes have been included in $Z_{T,L}$, $Z_{B,L}$, $Z_{T,S}$ and $Z_{B,S}$ (see Figure 2.12). In this case, the first boundary condition does not change. We again want to solve for the motion of the resonator in response to an input current I of radial frequency ω:

$$I = I_0 \exp(j\omega t) \quad (2.77)$$

[18] For most of the FBARs in this thesis, an additional buffer layer is needed between the piezoelectric ZnO layer and the bottom electrode. This is electrically more complicated than for the simple FBAR, because the buffer-layer is dielectric and reduces the E-field seen by the piezoelectric layer, which reduces the effective coupling coefficient for the structure. This problem is treated in Chapter 4, where the real structures of the solidly mounted FBARs are presented in more detail.

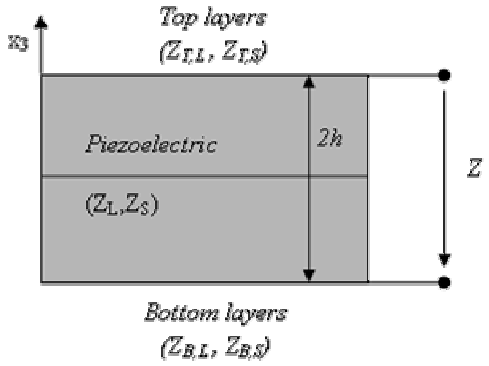

Figure 2.12 : Composite FBAR structure with top and bottom acoustic stacks represented by equivalent terminating impedances.

The boundary conditions on each side of the piezoelectric layer, at x_3=h and x_3=-h, are the continuity of mechanical displacement and stress. Using the mechanical impedances, this means:

$$-\frac{T_{33}(h)}{\frac{\partial u_3(h)}{\partial t}} = Z_{T,L} \qquad -\frac{T_{33}(-h)}{\frac{\partial u_3(-h)}{\partial t}} = Z_{B,L} \tag{2.78}$$

$$-\frac{T_{31}(h)}{\frac{\partial u_1(h)}{\partial t}} = Z_{T,S} \qquad -\frac{T_{31}(-h)}{\frac{\partial u_1(-h)}{\partial t}} = Z_{B,S} \tag{2.79}$$

As before, these 4 equations can then be used to find the expressions for U_{L1}, U_{L2}, U_{S1} and U_{S2}. They are now not identical, since the conditions on the upper side and the lower side of the piezoelectric are not necessarily the same. These expressions can be introduced in the displacement expressions and then in equation (2.43) of the electrical potential. Again, the difference of the potential between the top and the bottom electrode (x_3=h and x_3=-h) can be found with a lot of algebra. Afterwards, the electrical impedance Z of the resonator is found by relating this potential difference to the applied input current I, which gives the following expression for Z:

$$Z = \frac{1}{j\omega C}\cdot\left[1 - K_L^2\frac{\tan(k_L h)}{k_L}\cdot\frac{(Z_{T,L}+Z_{B,L})\cos^2(k_L h) + jZ_L\sin(2k_L h)}{(Z_{T,L}+Z_{B,L})\cos(2k_L h) + j(Z_{T,L}Z_{B,L}/Z_L + Z_L)\sin(2k_L h)} - K_S^2\frac{\tan(k_S h)}{k_S}\cdot\frac{(Z_{T,S}+Z_{B,S})\cos^2(k_S h) + jZ_L\sin(2k_S h)}{(Z_{T,S}+Z_{B,S})\cos(2k_S h) + j(Z_{T,S}Z_{B,S}/Z_L + Z_L)\sin(2k_S h)}\right] \tag{2.80}$$

With $k_L = \omega/v_L$ and $k_S = \omega/v_S$. C is the static capacitance of the piezoelectric layer, given by formula (2.57). K_L^2 and K_S^2 are the electromechanical coupling coefficients for longitudinal and shear mode respectively, which are expressed by formulas (2.58) and (2.59).

Equation (2.80) is similar to equation (2.56), the impedance of a simple c-axis inclined ZnO FBAR seen in section 2.3.2. There are additional factors representing the additional top and bottom acoustic stacks, for shear and longitudinal modes. If there are no additional stacks and we have solid-to-air interface on the top and bottom of the piezoelectric, $Z_{T,L}$, $Z_{B,L}$, $Z_{T,S}$ and $Z_{B,S}$ reduce to zero and equation (2.80) becomes (2.56).

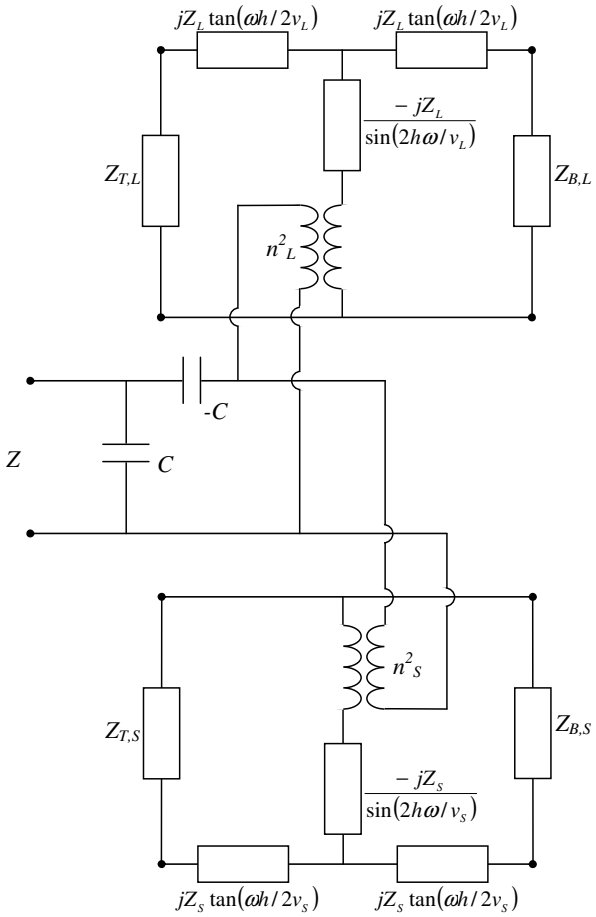

Figure 2.13 : Mason Model for a piezoelectric layer, with top and bottom impedances, representing the upper and lower acoustic stacks for shear and longitudinal modes.

Equation (2.80) can be written in the following form:

$$\frac{1}{Z}=\left[\frac{-1}{j\omega C}+\left\{\frac{1}{n_L^2}\left(\frac{-jZ_L}{\sin(2\omega h/v_L)}+\frac{1}{\frac{1}{jZ_L\tan(\omega h/v_L)+Z_{T,L}}+\frac{1}{jZ_L\tan(\omega h/v_L)+Z_{B,L}}}\right)^{-1}\right.\right.$$
$$\left.\left.+\frac{1}{n_S^2}\left(\frac{-jZ_S}{\sin(2\omega h/v_S)}+\frac{1}{\frac{1}{jZ_S\tan(\omega h/v_S)+Z_{T,S}}+\frac{1}{jZ_S\tan(\omega h/v_S)+Z_{B,S}}}\right)^{-1}\right\}^{-1}\right]^{-1}+j\omega C \tag{2.81}$$

$$n_L^2=\frac{2\omega h/v_L}{K_L^2\omega C Z_L} \qquad n_S^2=\frac{2\omega h/v_S}{K_S^2\omega C Z_S} \tag{2.82}$$

This derives the so-called **Mason Model**, represented in Figure 2.13.[19] The purpose of the transformer is to convert from mechanical units to electrical units, as is evident from the units of n^2 [Pa^2/A^2].

[19] The typical Mason Model is less complex, since it was computed for a single pure mode. As we have c-axis inclined ZnO, two modes can be excited, and we need two transformers and two acoustic lines.

The Mason Model has been used in this thesis to model the composite FBARs prior to their fabrication, in order to find the correct layer thicknesses for a given frequency. The composite FBARs used in this work are realized as solidly mounted FBARs, meaning that they are realized on an acoustic mirror. The thicknesses of the whole acoustic stack, especially the thicknesses of the layers of the acoustic mirror, have to be optimized for one specific mode, either shear or longitudinal mode. This is why only one branch of the Mason Model was implemented in MATLAB. Either the shear mode or the longitudinal mode can be chosen to be simulated.

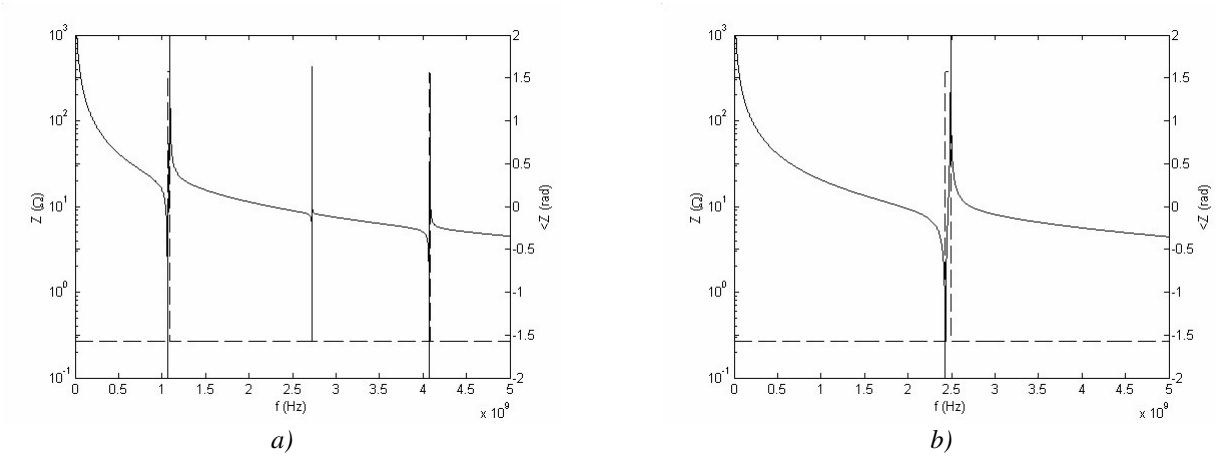

Figure 2.14 : Broad-band impedance characteristic (solid: amplitude, dashed: phase) of a composite ZnO FBAR of 13.6° c-axis inclination. a) shear-mode, b) longitudinal mode.

To illustrate this, a simple structure, consisting of a top Au electrode (of thickness 100 nm), a 13.6 ° inclined ZnO layer (of thickness 500 nm) and a bottom Pt electrode (of thickness 200 nm) has been simulated. The area was again taken as 200 µm × 200 µm. The broad band response for the shear mode branch is shown on Figure 2.14 a). It includes the fundamental mode and the next two higher modes. Figure 2.14 b) shows the simulation for longitudinal mode for the same stack. A narrow-band view of the fundamental shear mode is shown in Figure 2.15.

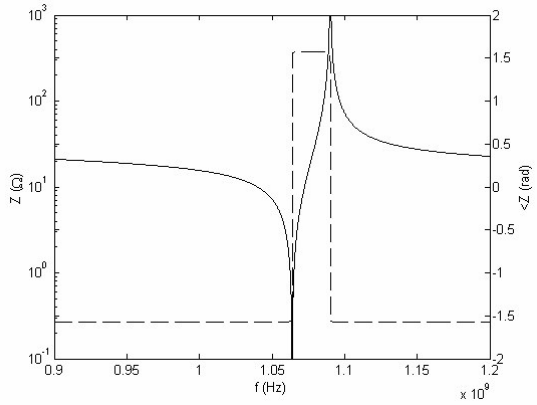

Figure 2.15 : Narrow-band impedance characteristic (solid: amplitude, dashed: phase) of the fundamental shear mode of a composite ZnO FBAR of 13.6° c-axis inclination.

Each mode of the composite FBAR has the same general shape as the mode of a simple FBAR derived in paragraph 2.3, as can be seen by comparing Figure 2.7 b) and Figure 2.15. Because of this similarity, an

effective simple FBAR impedance equation can be assumed for each composite FBAR mode. This is because the tangent terms in equation (2.80) of the FBAR impedance become relevant only in a small frequency band around the resonance. Moreover, the tangent term of a particular mode generally exceeds the tangent terms of other modes. The composite FBAR impedance equation can thus be approximated by:

$$Z = \frac{1}{j\omega C}\left[1 - K_{eff}{}^2 \frac{\tan\left(\omega h_{eff}/2v_{eff}\right)}{\omega h_{eff}/2v_{eff}}\right] \tag{2.83}$$

It is assumed to be valid over a small frequency range around the mode and the resonance of interest. $K_{eff}{}^2$ is called the **effective electromechanical coupling coefficient**. The effective parameters depend on the material constants and thicknesses of the films constituting the acoustic stack as well as the mode number and type (shear or longitudinal). For a simple c-axis inclined FBAR without any other layers attached, the effective coupling coefficient $K_{eff}{}^2$ equals the apparent coupling coefficient $K^2_{app(S,L)}$ found in section 2.3.4 for shear or longitudinal mode. In the case of an FBAR exciting only one pure or quasi-mode, $K_{eff}{}^2$ and $K^2_{app(S,L)}$ equal $K^2_{(S,L)}$ defined in equations (2.58) and (2.59).

2.4.4. Acoustic loss and quality factor Q

Acoustic losses in the bulk of the materials can be accounted for by adding a viscosity term in the constitutive stress relation (2.11):

$$T_\alpha = c^E_{\alpha\beta} S_\beta + \eta^E_{\alpha\beta} \frac{\partial S_\beta}{\partial t} - e_{i\alpha} E_i \tag{2.84}$$

$\eta^E_{\alpha\beta}$ has dimensions of [Pa.s]. If a sinusoidal steady state response is assumed, as in the previous paragraphs, the stress can be written as:

$$T_\alpha = c^E_{\alpha\beta} S_\beta + j\omega\eta^E_{\alpha\beta} S_\beta - e_{i\alpha} E_i \tag{2.85}$$

Or:

$$T_\alpha = \bar{c}^E_{\alpha\beta} S_\beta - e_{i\alpha} E_i \tag{2.86}$$

Where:

$$\bar{c}^E_{\alpha\beta} = c^E_{\alpha\beta} + j\omega\eta^E_{\alpha\beta} \tag{2.87}$$

$\bar{c}^E_{\alpha\beta}$ is an effective stiffness matrix which can be used as a substitute for $c^E_{\alpha\beta}$ when acoustic losses need to be considered. The resulting impedance equation for a composite FBAR has the same form than equation (2.80), but with all parameters calculated with the effective stiffness tensor. The Mason Model can thus be found again, with v_L and v_S becoming:

$$\bar{v}_L = \left[\frac{\bar{c}^*_{33} + \bar{c}^*_{55}}{2\rho} + \sqrt{\left(\frac{\bar{c}^*_{33} - \bar{c}^*_{55}}{2\rho}\right)^2 + \left(\frac{\bar{c}^*_{35}}{\rho}\right)^2}\right]^{1/2} \tag{2.88}$$

$$\bar{v}_S = \left[\frac{\bar{c}_{33}^* + \bar{c}_{55}^*}{2\rho} - \sqrt{\left(\frac{\bar{c}_{33}^* - \bar{c}_{55}^*}{2\rho} \right)^2 + \left(\frac{\bar{c}_{35}^*}{\rho} \right)^2} \right]^{1/2} \tag{2.89}$$

Which can also be written as:

$$\bar{v}_L = v_L \sqrt{1 + j\omega\eta_L / c_L} \tag{2.90}$$

$$\bar{v}_S = v_S \sqrt{1 + j\omega\eta_S / c_S} \tag{2.91}$$

η_L, η_S, c_L and c_S depend on the viscosity and stiffness tensors at a particular c-axis inclination. Of course, Z_L, Z_S, K_L^2 and K_S^2 are also changed since they include the acoustic velocities.

The impedance can again be simplified in a small frequency range around a particular mode of interest:

$$Z = \frac{1}{j\omega C} \left[1 - \bar{K}_{eff}^{\ 2} \frac{\tan\left(\omega h_{eff} / 2\bar{v}_{eff}\right)}{\omega h_{eff} / 2\bar{v}_{eff}} \right] \tag{2.92}$$

With

$$\bar{v}_{eff} = v_{eff} \sqrt{1 + j\omega\eta_{eff} / c_{eff}} \tag{2.93}$$

$$\bar{K}_{eff}^2 = K_{eff}^2 \frac{1}{1 + j\omega\eta_{eff} / c_{eff}} \tag{2.94}$$

The effective parameters depend on the mode, the acoustic stack and the chosen resonance. The viscosity term $\omega\eta_{eff} / c_{eff}$ is small compared to unity for most materials, meaning that the acoustic losses have only a slight influence on the acoustic velocities and coupling coefficients. In the other layers of a composite resonator, losses can be introduced via the acoustic impedance, also by replacing v_{ac} by $\bar{v}_{ac}$.

Viscosity losses in the bulk of the material are not the only loss mechanisms in a composite FBAR. Other loss mechanisms, which generally are much more important than the viscous losses, include losses at the interfaces between two layers because of a certain roughness (wave scattering),[20] imperfect reflections in the case of an acoustic mirror. Generally, all sorts of losses can be described in terms of the quality factor Q. It is one of the two figures of merit the FBAR community has established. For resonant devices the physical definition of Q is:

$$Q = \frac{\omega(\text{Stored Energy})}{\text{Dissipated Energy per Cycle}} \tag{2.95}$$

A well-known definition of the Q at series (s) or parallel (p) resonance of a particular mode is defined as:

$$Q_{s,p} = \frac{f_{s,p}}{2} \frac{d\angle Z}{df}\bigg|_{f_{s,p}} \tag{2.96}$$

Where the phase of the impedance $\angle Z$ has units of radians. **This definition originates from a simple RLC series network** and equation (2.95).

The viscous losses in a layer can also be expressed by a material quality factor Q_M:[21]

---

[20] J. Weber, M. Link, R. Primig, D. Pitzer, W. Wersing, M. Schreiter, *IEEE Trans.Ultrason.Ferroelec.Freq.Contr.,* submitted.
[21] J. Rosenbaum, *Bulk Acoustic Wave Theory and Devices*, Artech House, Norwood, MA (1988).

$$Q_{M,(S,L)} = \frac{v_{ac}^2 \rho}{\omega \eta_{(S,L)}} = \frac{c_{(S,L)}}{\omega \eta_{(S,L)}} \tag{2.97}$$

Of course, Q_M depends on the quality of the material as well as on the particular chosen mode and propagation direction. This permits to express the acoustic velocity in a layer by:

$$\overline{v}_{ac} = v_{ac}\sqrt{1 + j/Q_M} \tag{2.98}$$

This formula permits to easily use the Mason Model and transmission line equation when the Q of a layer is known. Typical values for Q_M at 1 GHz are 450 for Au, and in the order of 10^5 for single crystalline Si. The total Q-factor of the FBARs will be smaller than Q_M, because of the other loss mechanisms mentioned above. The total Q can be estimated from the individual Q-factors Q_1, Q_2, Q_3, … with the following formula:

$$\frac{1}{Q_{Total}} = \frac{1}{Q_1} + \frac{1}{Q_2} + \frac{1}{Q_3} + ... \tag{2.99}$$

2.4.5. Butterworth-Van Dyke Model

Equation (2.80) where loss mechanisms have been included provides an analytical expression for the electrical characteristics of a composite FBAR. The resonance frequencies and the effective coupling coefficient of each mode (shear or longitudinal, fundamental or higher) are included in that equation. For the design and analysis of FBARs however, a simple equivalent circuit is desired. Figure 2.16 shows such a model, called the **Butterworth-Van Dyke (BVD) Model**. It describes the electrical characteristics of the FBAR in a frequency range around one resonance. It is a model widely used by quartz filter designers because of its simplicity. The BVD parameters can be used to define the series and parallel resonances of a given mode. In addition, an expression for the quality factor Q can be found.

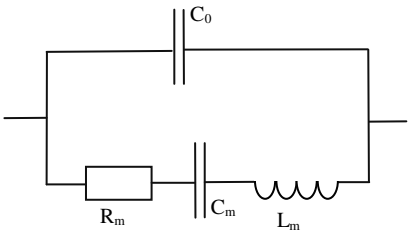

Figure 2.16 : Butterworth-Van Dyke model.

The BVD can be derived from equation (2.92), which is valid at a small frequency range around a particular mode. Since the BVD is a single resonance model, an approximation must be made. The tangent term in equation (2.92) can be expressed by an infinite sum of rational functions:[22]

$$\tan x = \sum_{n=0}^{\infty} \frac{2x}{\left[(2n+1)\frac{\pi}{2}\right]^2 - x^2} \tag{2.100}$$

[22] J. J. Lutsky, *A sealed cavity thin-film acoustic resonator process for RF bandpass filters*, Thesis, MIT (1997).

When x is an odd multiple of π/2, tan x explodes to infinity, which can also be seen in this expression. Around that nth point, tan x can be approximated by the n^{th} rational term of this sum. Since equation (2.92) is only valid at only one resonating mode and one is free to choose the fundamental, we take n=0. Using this approximation, the FBAR impedance becomes:

$$Z \approx \frac{1}{j\omega C}\left[1-\frac{2\bar{K}_{eff}^{\,2}}{\left(\frac{\pi}{2}\right)^2-\left(\frac{\omega h_{eff}}{\bar{v}_{eff}}\right)^2}\right] \tag{2.101}$$

Considering (2.93) and (2.94), equation (2.101) can be manipulated into:

$$Z \approx \frac{1}{j\omega C}\frac{\left(\frac{\pi}{2}\right)^2-2K_{eff}^{\,2}}{\left(\frac{\pi}{2}\right)^2}\left[\frac{1-\left(\frac{\omega h_{eff}}{v_{eff}}\right)^2\frac{1}{(\pi/2)^2-2K_{eff}^{\,2}}+j\left(\frac{\omega\eta_{eff}}{c_{eff}}\frac{K_{eff}^{\,2}}{(\pi/2)^2-2K_{eff}^{\,2}}\right)}{1-\left(\frac{\omega h_{eff}}{v_{eff}}\right)^2+j\left(\frac{\omega\eta_{eff}}{c_{eff}}\right)}\right] \tag{2.102}$$

The form of this equation is the same as that of the impedance of the BVD model represented in Figure 2.16, which can be written in the following form:

$$Z_{BVD}=\frac{1}{j\omega(C_m+C_0)}\frac{1-\omega^2L_mC_m+j(\omega R_mC_m)}{1-\omega^2L_m\frac{C_0C_m}{C_m+C_0}+j\left(\omega R_m\frac{C_0C_m}{C_m+C_0}\right)} \tag{2.103}$$

By comparing both expressions, one can find the following expressions for the components of the model:

$$C_0=C=\frac{A\varepsilon_{33}'}{2h} \tag{2.104}$$

$$C_m=\frac{2K_{eff}^{\,2}}{(\pi/2)^2-2K_{eff}^{\,2}}C \tag{2.105}$$

$$L_m=\frac{h_{eff}^2}{2K_{eff}^2v_{eff}^2}\frac{1}{C} \tag{2.106}$$

$$R_m=\frac{\eta_{eff}}{c_{eff}}\frac{(\pi/2)^2}{2K_{eff}^2}\frac{1}{C} \tag{2.107}$$

These BVD parameters are related to the geometry, the material constants and the chosen mode of the FBAR. Both capacitor values are proportional to the device area. The inductor and the resistor values are inversely proportional to area. When the acoustic loss approaches zero, the resistor value approaches zero. The ratio of C_m to C_0 relates to the effective electromechanical coupling coefficient. The inductor is the only parameter dependent on the acoustic velocity and has the largest dependence on thickness. The influence of the finite conductivity of the electrodes can be included in the model by adding a series resistance R_s. This is of no importance in this chapter, but will be used in Chapter 4 and Chapter 5. Figure 2.17 shows the comparison of the simulated data of a simple FBAR of pure shear mode to the BVD model impedance. The FBAR has a Q-factor of 100 at the resonance frequency. The fit is not perfect, which is indicated by the 2 arrows. This is because the BVD model is only an approximation of the first tangent mode. Nevertheless, it

is sufficiently precise for the purposes of this work. One should also note that since losses have been introduced, the amplitude of the impedance does not become infinite anymore at the parallel frequency. Also, it does not become zero at the series resonance. This means that the phase of the impedance does not necessarily reach $+\pi/2$ between the two resonance peaks.

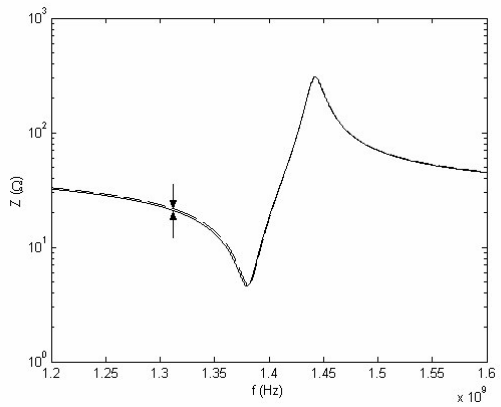

Figure 2.17 : Simulated impedance amplitude (solid line) of a simple FBAR of pure shear mode (90° c-axis inclination) compared to the BVD model impedance for the same FBAR (dashed line). The Q-factor has been taken as 100, the area of the simulated FBAR is 200µm ×200µm and the thickness is 1µm.

It is interesting to see how the BVD parameters can be written in the case of a simple pure mode FBAR, consisting of 90° c-axis inclined ZnO. In that case, K_S^2 becomes $e_{15}^2/(\varepsilon_{11}^S \rho v_S^2)$ and v_S is approximately $\sqrt{c_{55}^E/\rho}$, so K_S^2 is $e_{15}^2/(\varepsilon_{11}^S c_{55}^E)$ and equations (2.104) to (2.107) can be written as:

$$C = \frac{A\varepsilon_{11}^S}{2h} \tag{2.108}$$

$$C_m = \frac{4}{\pi^2}\frac{e_{15}^2}{c_{55}^E}\frac{A}{h} \tag{2.109}$$

$$L_m = \frac{\rho h^3}{Ae_{15}^2} \tag{2.110}$$

$$R_m = \frac{\pi^2}{4}\frac{\eta_{55}}{e_{15}^2}\frac{h}{A} \tag{2.111}$$

It can be seen that C_m is dependent on the geometry of the FBAR, and its piezoelectric and elastic constants. L_m is very dependent on the thickness of the FBAR and its density. It represents the mass of the FBAR and does not change with its elastic properties. R_m is the only parameter depending on the viscosity.

2.5. Characterization of FBARs and figures of merit

The most important parameters of a certain mode of a composite FBAR are the series and parallel resonance frequencies, the spacing between those two frequencies, the losses and the capacitance C. The capacitance is determined by the device area and the frequency is fixed by the application. The spacing between the frequencies and the losses are dependent on the material constants and thicknesses of all the films of the stack. They can be characterized by two figures of merit widely accepted in the FBAR community: the

effective coupling coefficient and **quality factor Q**. This paragraph will explain how to determine these.

2.5.1. Impedance measurement setup and representation

The first tasks in the characterization of an FBAR are the electrical measurements of its impedance. The most common electronic setup of a FBAR is as the frequency determining element in a feedback loop of an oscillator circuit.[23] The oscillator circuit keeps the sensor at one of its resonance frequencies. This work is concerned with the optimization of the physical structure of the FBAR and not its final electronics circuit. In that case, the most complete information about the FBAR can be obtained by the measurement of its electrical impedance as a function of the frequency.

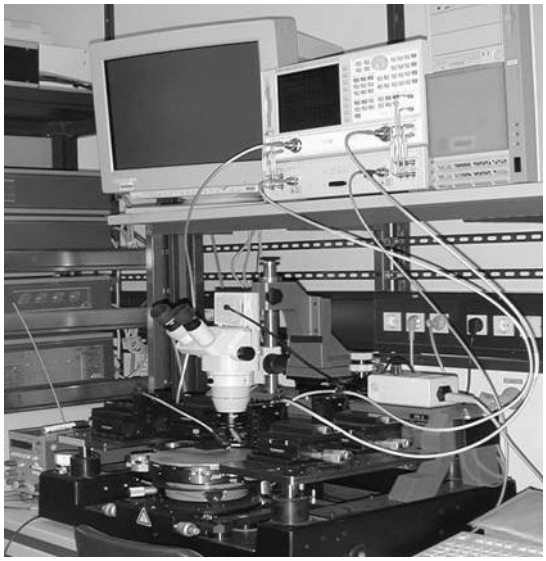

Figure 2.18 : Photograph of the measurement setup-up: network analyzer, microscope and RF prober test set.

For this impedance characterization a network analyser 8513A from *Hewlett Packard*, Böblingen, Germany is adapted to a RF prober test set PM8 from *SÜSS MicroTec AG*, Garching, Germany, which permits to contact the FBARs using probes from *GGB Industries Inc*, Naples (FL), USA (see Figure 2.18). The equipment is capable for measurements in a frequency range from 100 kHz to 26 GHz. A dedicated MATLAB program permits to save the measured points. Impedance characteristics are calculated from the scattering parameters (s-parameters), which are a measure of the reflected and transmitted power of the FBAR. The incoming wave is "scattered" by the circuit and its energy is divided between all the possible outgoing waves on all the other lines connected to the circuit. The parameter S_{11} describes the power reflection. It is also called reflection coefficient γ and is related to the electrical impedance Z of the resonator and the characteristic impedance Z_0 of the measurement setup, which in most cases is 50 Ω, as follows:

$$\gamma = \frac{Z - Z_0}{Z + Z_0} \tag{2.112}$$

$$Z = Z_0 \frac{1+\gamma}{1-\gamma} \tag{2.113}$$

[23] E. Benes, M. Gröschl, F. Seifert, A. Pohl, *Proc. IEEE Int. Freq. Contr. Symp.*, 5 (1997).

For S_{11} equal to -1, the signals are inverted and reflected (reflection at short circuit with terminating impedance Z = 0 Ω). For impedance matching (Z = 50 Ω) no reflections will occur and S_{11} equals zero. For an open end (Z = ∞) voltage amplitudes are reflected (S_{11} = 1).

The impedance characteristics can be represented in two ways shown in Figure 2.19: a) the classical view of the amplitude and phase of the impedance; or b) the representation of the reflection coefficient γ in a Smith-Chart. The Smith-Chart is a polar representation of γ. The point in the middle of the chart corresponds to a γ of 0, which is an impedance of Z_0. The far right corresponds to an open circuit, and the far left to a short circuit. The lower part of the Smith-Chart is capacitive, the upper part is inductive. Usually, additional lines of constant amplitude for certain values of impedances are also represented on a Smith-Chart.

The frequency response of the FBAR shown in Figure 2.19 has the same parameters than the one of Figure 2.7, but with a Q-factor of 100. In both charts, the fundamental shear and longitudinal modes, as well as the first shear harmonic, can be seen. The first two modes become inductive in resonance, since the phase becomes positive. For the first shear harmonic however, the phase stays negative, even in resonance. This can be seen in the Smith-Chart, by recognizing that the curve corresponding to this mode does not cross the upper part, which corresponds to positive phase values.

When the impedance characteristic has been recorded, there are two different ways to calculate the characteristics of the FBAR. One way is to look directly at the obtained impedance characteristics, and extract the parameters by looking at the minimum and maximum of the amplitude, or the slope of the phase. The other method is to fit the impedance characteristic (either amplitude or phase) to the BVD model presented in section 2.4.5. Both methods will be presented in the next two sections for the determination of the two main figures of merit of an FBAR.

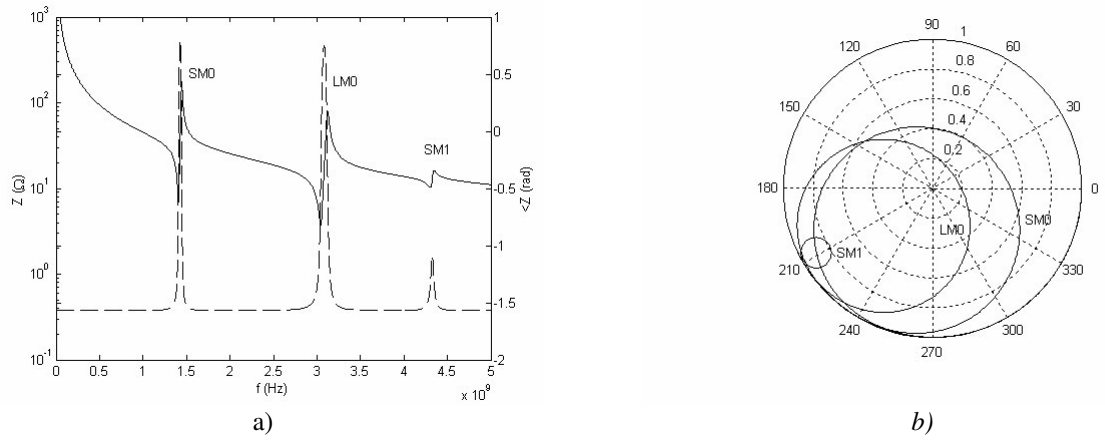

a) b)

Figure 2.19 : a) Wide-band impedance characteristic (solid: amplitude, dashed: phase) and b) Smith-Chart of a simple ZnO FBAR of 13.6° c-axis inclination, with a Q of 100. The area is 200 µm x 200 µm and the thickness is 1 µm.

2.5.2. Effective coupling coefficient determination

Similarly to what was done in section 2.3.4 for a simple FBAR, the parallel resonance f_p of a particular mode of a composite FBAR *without loss* characterized by equation (2.83) is defined when the amplitude of the

impedance becomes infinite. This gives the following expression for f_p:

$$f_p = \frac{v_{eff}}{2h_{eff}} \tag{2.114}$$

The series resonance f_s is defined when the amplitude of the lossless FBAR equals zero, which gives the following relationship between f_s and f_p:

$$K_{eff}^2 = \frac{\frac{\pi}{2}\frac{f_s}{f_p}}{\tan\left(\frac{\pi}{2}\frac{f_s}{f_p}\right)} \tag{2.115}$$

This is the suggested definition for the effective coupling coefficient of a resonator.[24] The effective coupling coefficient can be related to the relative separation between both resonances frequencies by approximating the tangent with the first term of equation (2.100). The approximation is valid for ZnO, where K_{eff}^2 is small.

$$K_{eff}^2 \approx \left(\frac{\pi}{2}\right)^2 \frac{f_p^2 - f_s^2}{f_p^2} \tag{2.116}$$

For FBARs without loss, the effective coupling coefficient of a particular mode is thus defined by the local extrema of the impedance amplitude, or the points of maximum slope of its phase. We will call these definitions the *conventional formulas* for finding the resonance frequencies. For composite FBARs *with loss*, characterized by equation (2.92), these points shift. The points of the extrema of the amplitude do not coincide with the same points for the lossless FBAR, and in addition, they also do not correspond to the points of maximum phase slope.[25] If these points are still used for the definition of the resonance frequencies, the resulting effective coupling coefficient will be dependent on loss. The separation between resonance frequencies calculated from the maximum of the impedance will be larger and the calculated coupling coefficient will appear larger. What is desired for the characterization of the FBAR are two figures of merit independent of each other. So to keep the definition of the effective coupling coefficient, the definition of the resonance frequencies for lossy FBARs must be changed. The BVD model can be used to define f_s, f_p and the respective quality factors Q_s and Q_p. Expression (2.103) can be rewritten in the following form:[26]

$$Z_{BVD} = \frac{1}{j\omega C_0} \frac{1 - \frac{f^2}{f_s^2} + j\frac{f}{f_s Q_s}}{1 - \frac{f^2}{f_p^2} + j\frac{f}{f_p Q_p}} \tag{2.117}$$

where

$$f_s = \frac{1}{2\pi}\sqrt{\frac{1}{C_m L_m}} \tag{2.118}$$

$$f_p = f_s\sqrt{1 + \frac{C_m + C_0}{C_0}} = \frac{1}{2\pi}\sqrt{\frac{C_m + C_0}{C_m C_0 L_m}} \tag{2.119}$$

[24] K. M. Lakin, *IEEE Trans. Ultrason., Ferroelec., Freq. Contr.* **52**, 707 (2005).
[25] R. S. Naik, J. J. Lutsky, R. Reif, C. G. Sodini, *IEEE Trans. Ultrason., Ferroelec., Freq. Contr.*, **45**, 257 (1998).
[26] J. D. Larson III, P. D. Bradley, S. Wartenberg, R. C. Ruby, *Proc. IEEE Ultrason. Symp.*, 863 (2000).

$$Q_s = \frac{2\pi f_s L_m}{R_m} \tag{2.120}$$

$$Q_p = \frac{2\pi f_p L_m}{R_m} \tag{2.121}$$

The resonance frequencies and Q-factors can thus be found with the help of the BVD parameters. An additional series resistance due to electrical losses can be included in the expression of Q_s by adding it to R_m. The resonance frequencies permit to find the effective coupling coefficient of the mode using equation (2.115). The advantage of this method is that the loss effects, represented by R_m in the BVD model, have no influence on the obtained resonance frequencies. The BVD model thus provides a characterization method for fabricated composite FBARs. Figure 2.20 a) shows the coupling coefficient K^2_{SLOPE} calculated using conventional formulas for f_s and f_p normalized to the value computed with the BVD model K^2_{eff}. As can be seen, both K^2_{eff} values differ significantly from each other (more than 10%) for $K^2_{eff} \cdot Q$ values lower than 5.

When the impedance characteristic has been measured, the BVD parameters can be found by fitting the characteristic to the BVD-model. For this work, a computer program was realized permitting to visualize the impedance and fit the BVD model. The calculations and user interface were implemented in MATLAB. The fitting was done using a Levenberg-Marquardt nonlinear regression algorithm.[27] Figure 2.21 shows a screen-shot of the graphical user interface of the fitting tool.

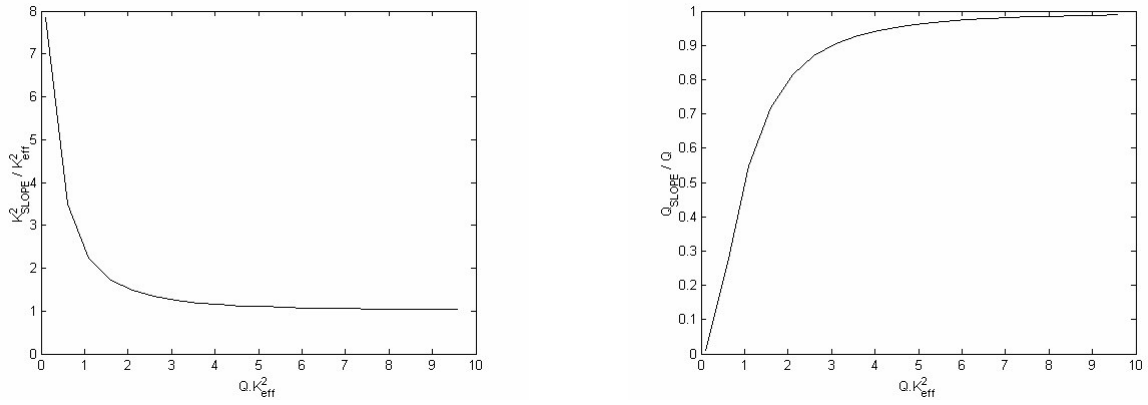

a) b)

Figure 2.20 : K^2_{SLOPE} (a) and Q_{SLOPE} (b) using conventional calculation formulas normalized to K^2_{eff} and Q found with the BVD parameters in dependence of K^2_{eff}.Q.

2.5.3. Q-factor determination

For the determination of the series and parallel quality factors, a similar analysis can be done. The formula to find Q is given in equation (2.96). This formula originates from a simple RLC network composed of a resistance, a capacitor and an inductance in series. The Q computed by this way will be called Q_{SLOPE}. For the simple RLC network, Q_{SLOPE} is identical to the Q computed by equation (2.120).

[27] J. R. Macdonald, Solartron, http://www.jrossmacdonald.com/levminfo.html.

In general however, this formula is not applicable to the BVD model, which has an additional capacitance in parallel compared with the simple RLC network. By applying this formula to the BVD impedance equation (2.117), for example at series resonance, we get:[28]

$$Q_{SLOPE(S)} = \frac{f_S}{2}\left.\frac{d\angle Z}{df}\right|_{f_S} = \frac{Q_s}{2}\left[2 - \frac{1+\frac{f_p^2}{f_s^2}}{1+Q_S^2\left(\frac{f_p^2}{f_s^2}-1\right)^2}\right] \approx Q_S\left[1-\frac{1}{1+Q_S^2K_{eff}^4}\right] \qquad (2.122)$$

We see that formula (2.96) is an approximation of Q_S only if the product $Q_S K_{eff}^2$ is large. When the product is less than 5, Q_{SLOPE} deviates substantially (10%) from Q_S. This can be observed on Figure 2.20 b).

A more accurate approach is thus to use the BVD parameters to obtain Q with equations (2.120) and (2.121). In conclusion, for low coupling resonators as the ones realized in this work, the BVD parameters provide a better way of finding K_{eff}^2 and Q. However, the extraction time is a little longer, since the BVD model must be fitted on the impedance characteristic.

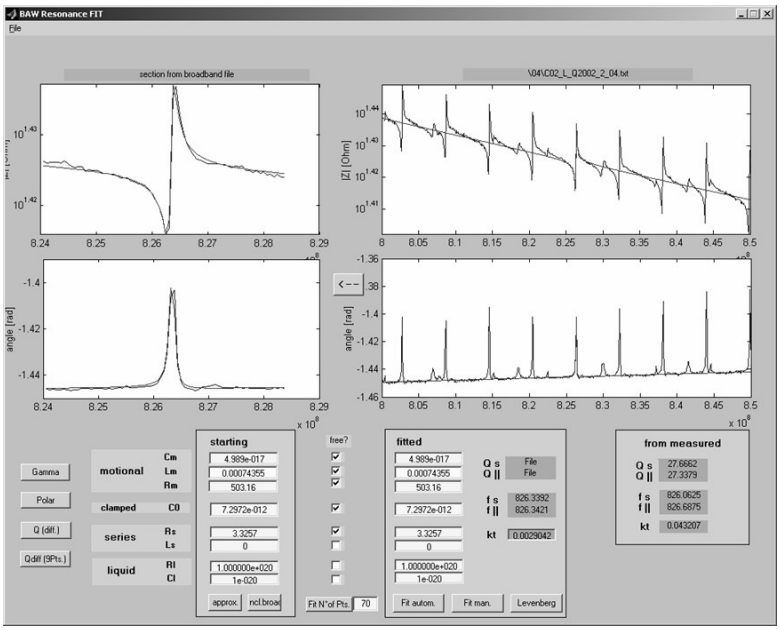

Figure 2.21 : Screen-shot of the graphical user interface of the fitting tool implemented in Matlab.

2.6. Piezoelectric thin film characterization using over-moded FBARs

An integral part of FBARs is the polycrystalline ZnO thin film, which ideally consists of a single crystallographic orientation and is free of defects. In the majority of cases, the x-ray diffraction intensity and rocking curve of the particular crystallographic orientation are used as a measure of the film quality. Other

[28] J. J. Lutsky, *A sealed cavity thin-film acoustic resonator process for RF bandpass filters*, Thesis, MIT (1997).

techniques include electron beam diffraction and atomic force microscopy.[29] However these purely material characterization techniques are not sufficient to make reliable conclusions on the piezoelectric activity of the film since no information about the polarity of the individual grains and possible influences of grain boundaries are available. These indirect measurements require experimental data to establish the connection between a film property and the piezoelectric property. On the other hand, measurements relying on the relationship between mechanical and electrical properties can be used to directly characterize the piezoelectric activity. The information can be extracted using a composite FBAR (solidly mounted or membrane-based) with the characterization techniques presented in paragraph 2.5, but the fabrication for such structures is complex and time-intensive. Moreover, very accurate and reliable values are needed for the thickness, density, and stiffness of all the layers involved. This paragraph shows how over-moded FBARs can be used for the piezoelectric characterization of thin films. They can be used as rapid and reliable tools to see if piezoelectric activity is taking place in the ZnO film, control what wave modes are excited, and determine the coupling coefficient of the film.

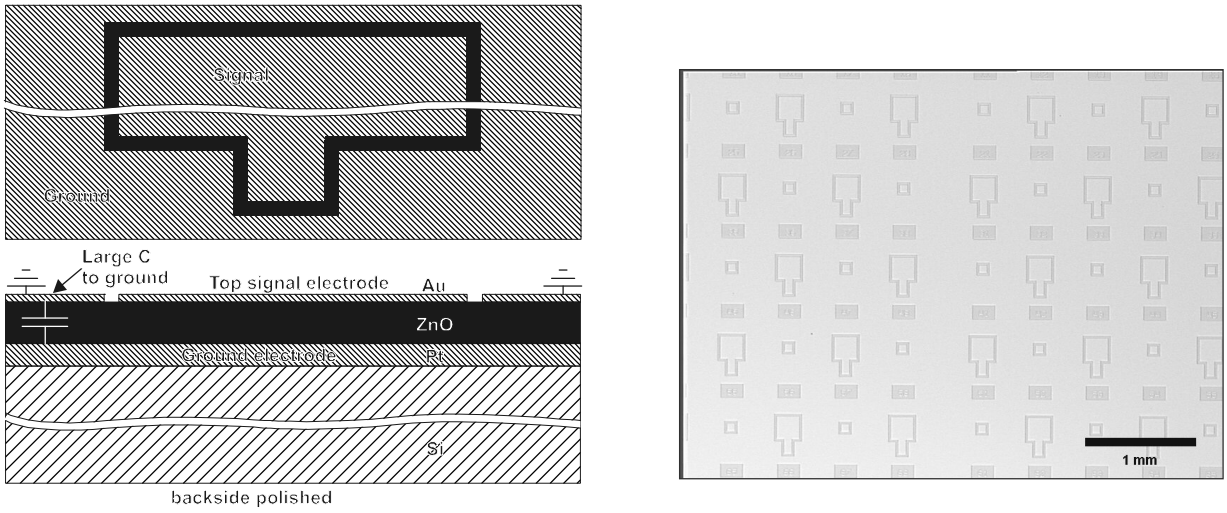

a) *b)*

Figure 2.22 : a) Schematic top view and cross-section of highly over-moded FBARs. b) Picture of a simple mask used to pattern the top electrode of over-moded FBARs.

2.6.1. Structure and fabrication

An over-moded FBAR is a one-mask device consisting of ZnO sandwiched between two electrodes on a double-polished Si substrate (see Figure 2.22 a)). The ZnO film is used as a transducer to excite waves travelling through the substrate and being reflected at its polished back-side. If the substrate is many wavelengths thick, the FBAR operates at a large mode number. In that case, the piezoelectric film occupies only a small fraction of the resonator volume and is weakly coupled to the standing wave.[30] This over-moded FBAR can be modelled using the composite FBAR impedance presented in paragraph 2.4. Such FBARs can exhibit a high-Q impedance response, as the loss mechanism is due mostly to intrinsic material properties of the monocrystalline substrate having high Q compared with the thin-film. Figure 2.22 b) shows the utilized

[29] F. S. Hickernell, *Proc. IEEE Ultrason. Symp.*, 235 (1996).
[30] K. M. Lakin, G. R. Kline, K. T. McCarron, *IEEE Trans. Microwave Theo. Techn.*, **41**, 2139 (1993).

mask containing FBARs of two different areas ($70 \times 70\ \mu m^2$ and $200 \times 200\ \mu m^2$). The high density of the structures permits to study changes of film properties within small areas, which is especially useful for films where the properties are very inhomogeneous, as for example in the case of PROCESS II, discussed in paragraph 3.5. The fabrication process for an over-moded FBAR is straightforward. The clean-room techniques used to deposit and structure the different layers will be explained in detail in Chapter 4. The deposition of ZnO films will be explained in Chapter 3. In short, 400 µm thick Si (110) substrates were used in most cases. A 100 nm thick Pt bottom electrode was first deposited by bias sputtering in a *Perkin Elmer* PE 2400. In some cases, a dielectric buffer-layer was then deposited on the Pt. Then the ZnO thin film was sputtered. Finally, the patterned Pt top electrode was fabricated. This was done by sputter-deposition of 100 nm Pt followed by a standard photo-lithography step with photo-resist deposition and development, sputter-etching of Pt and resist stripping.

2.6.2. Mode recognition using over modes

The measurement of over-modes proofs that a piezoelectric activity takes place in the films. The spacing between these over-modes shows which mode is predominantly excited, as it mainly depends on the acoustic properties of the substrate. From the acoustic speeds v_{ac} of the shear or longitudinal mode in the substrate and its thickness h, one can easily calculate the fundamental resonance frequency of each mode, which corresponds to the spacing Δf of the over-modes, by using the following formula:

$$\Delta f = \frac{v_{ac}}{2h} \tag{2.123}$$

Table 2.2 gives the over-modes spacing for the Si substrates used in this work. The exact separation can slightly vary depending on the top layers. This variation is not relevant for mode recognition. Figure 2.23 shows two narrow-band impedance characteristics of an over-moded FBAR on a 400 µm Si (110) substrate. Different spacing and thus different modes can be recognized. This method provides a convenient way to check which mode is excited. For (110) Si, additional care must be taken, since the over-modes corresponding to pure and quasi shear mode have different spacing. In practice it was seen that when the c-axis is inclined in direction of the main axes of the Si, only one of the two modes is excited.

TABLE 2.2
OVER-MODES SPACING (MHZ) AND ACOUSTIC VELOCITIES (IN BRACKETS) FOR THREE SUBSTRATES USED IN THIS WORK[31]

	Si (110) 400 µm	Si (100) 525 µm	Si (100) 675 µm
(Quasi-) Longitudinal mode	11.42 (9133 m/s)	8.032 (8433 m/s)	6.247 (8433 m/s)
(Pure) Shear mode	7.305 (5844 m/s)	5.566 (5845 m/s)	4.329 (5845 m/s)
(Quasi-) Shear mode	5.843 (4674 m/s)	-	-

[31] The acoustic velocities are from: http://www.geocities.com/SiliconValley/Bay/4104/silicon.html.

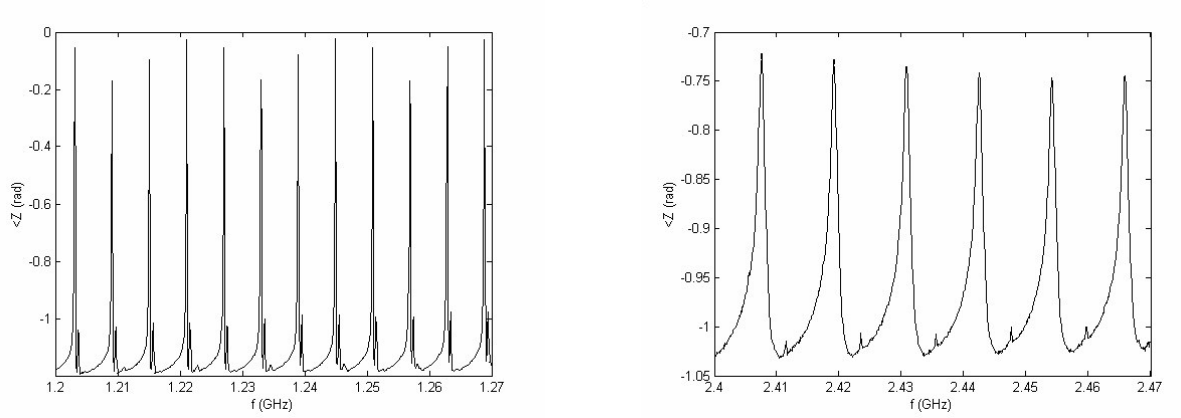

Figure 2.23 : Over-modes for an over-moded FBAR with inclined ZnO. The spacing between resonances is different at different frequencies, depending if shear (a) or longitudinal mode (b) is excited.

2.6.3. Coupling coefficient extraction method

This section describes a method used to extract the electromechanical coupling coefficient of the ZnO thin films with the help of over-moded FBARs. It is comparable to the methods presented by Hickernell[32], Naik *et al.*,[33] and Zhang *et al.*,[34] and was used extensively to characterize the thin inclined ZnO films deposited in this work. This method was successfully applied in a number of publications, for example by Naik *et al.* to characterize AlN film quality,[35] or by Yanagitani *et al.* to determine the electromechanical coupling coefficient of inclined ZnO films[36]. Theoretically it can also be used to extract the viscosity and the Q-factor of the thin film, but this aspect was not of interest in this work.

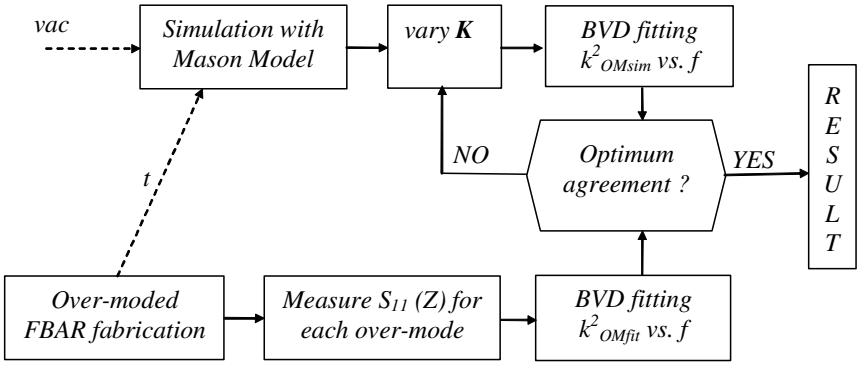

Figure 2.24 : Schematic explaining the principle of coupling coefficient extraction using over-moded FBARs.

The method, illustrated on Figure 2.24, requires measurement fittings and simulation steps. First, the over-moded FBARs are fabricated and measured. The over-modes are recorded in the region around the resonance

[32] F. S. Hickernell, *Proc. IEEE Ultrason. Symp.*, 235 (1996).
[33] R. S. Naik, J. J. Lutsky, R. Reif, C. G. Sodini, *IEEE Trans. Ultrason., Ferroelec., Freq. Contr.*, **45**, 257 (1998).
[34] Y. Zhang, Z. Wang, J. David N. Cheeke, *IEEE Trans. Ultrason., Ferroelec., Freq. Contr.*, **50**, 321 (2003).
[35] R. S. Naik, J. J. Lutsky, R. Reif, C. G. Sodini, A. Becker, L. Fetter, H. Huggins, R. Miller, J. Pastalan, G. Rittenhouse, Y.-H. Wong, *IEEE Trans. Ultrason., Ferroelec., Freq. Contr.*, **47**, 292 (2000).
[36] T. Yanagitani, N. Mishima, M. Matsukawa, Y. Watanabe, *Proc. IEEE Ultrason. Symp.*, 1824 (2005).

of the top layers (top and bottom electrode, ZnO film). Each over-mode is fitted to a BVD-model using a Levenberg-Marquardt nonlinear regression algorithm. The effective coupling coefficient k^2_{OMfit} of each over-mode is extracted with the help of equation (2.115). These k^2_{OMfit} values are plotted against their respective resonance frequencies. The second step involves simulations of the over-moded FBAR using the Mason Model explained in section 2.4.3. The thicknesses of the different layers used in the simulation have to correspond to the thicknesses of the fabricated and measured device. Analogously to the first step, the effective coupling coefficients k^2_{OMsim} of each simulated over-mode are taken and plotted against their resonance frequencies. Figure 2.25 shows the result of such a simulation. Finally, both curves are compared. The electromechanical coupling coefficient of the ZnO film in the simulation is varied until both curves of k^2_{OMfit} and k^2_{OMsim} match. If the thicknesses are not known precisely, they can be adjusted so that the peaks and shapes of both curves match. Theoretically, if the thicknesses and acoustic velocities would be known with very high precision, only one single over-mode measurement would be needed to find the coupling of the ZnO film.

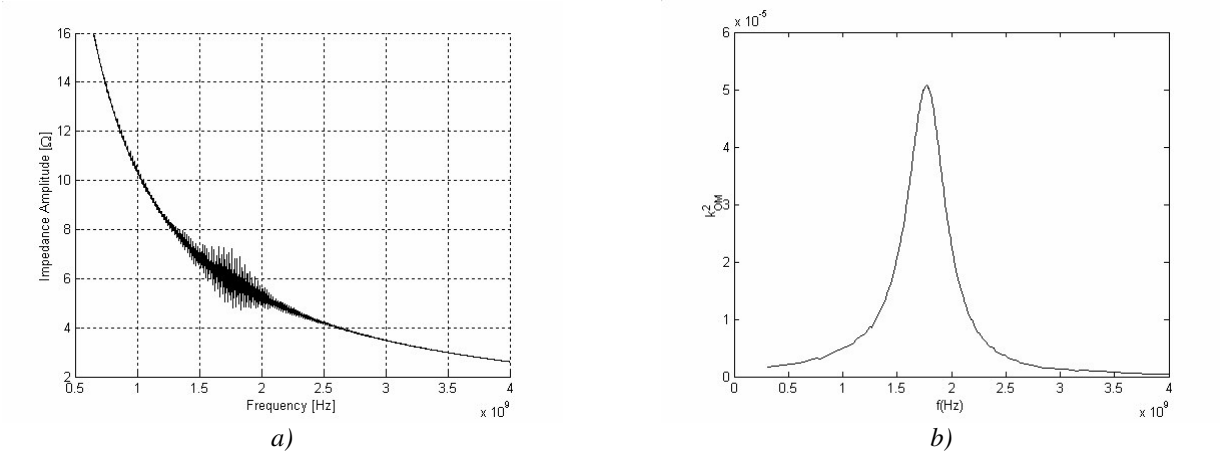

a) *b)*

Figure 2.25 : a) Simulated broad-band view of the impedance of an over-moded FBAR and b) computed effective coupling coefficients k^2_{OMsim} as a function of the frequency.

To illustrate the method explained in the previous lines, Figure 2.26 a) shows a narrow-band view of measured shear over-modes and the curve of the fitted BVD model for one resonance. Figure 2.26 b) shows the result of the over-modes simulation method. In this case, an apparent electromechanical coupling coefficient $K_{app,S}$ of 0.075 was derived. As was explained in section 2.3.4, this apparent coupling coefficient is very close to the electromechanical coupling coefficient K_S.

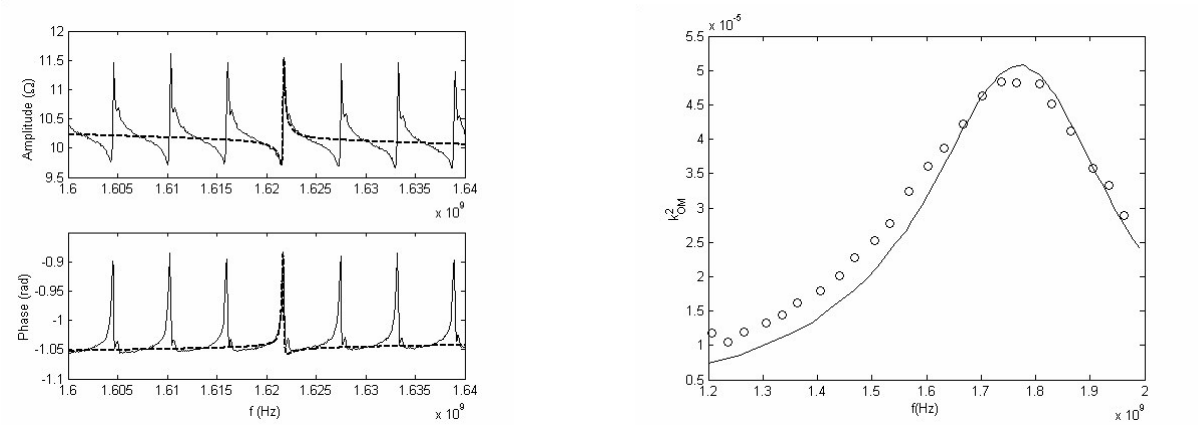

Figure 2.26 : a) Measured narrow-band impedance characteristic of a highly over-moded FBAR (solid line) with the fitted BVD characteristic of one over-mode (dotted line). b) Coupling coefficient of the over-modes against the frequency: measured over-modes (circles) and simulated over-modes (solid line).

2.6.4. Precision of the extraction method

There are different aspects that have to be considered when evaluating the accuracy of the coupling coefficient extraction method explained in the previous section.

Firstly, one has to make sure that each single over-mode resonance is not influenced by its neighbour resonances. Because the BVD model is only valid in a small frequency range around one resonance, there will be erroneous results when the bandwidth of a single resonance, as measured by the separation between the frequencies of minimum an maximum impedance, is large enough that neighbouring resonances affect one another. In other words, the resonances must be spaced sufficiently not to influence each other. To achieve this, the substrate should be thin and have high acoustic velocities. In addition, the over-modes should be clearly seen, so the wafer should have low loss and a polished backside for good reflection. This error source is further explained by Naik *et al.*[37]

Secondly, there is an inaccuracy arising through the fact that the acoustic velocities and, more importantly, the thicknesses of the layers involved are not necessarily known precisely. Owing to limitations in process reproducibility and inherent thickness inhomogeneities, the exact thicknesses of the individual layers at a certain point of the wafer differ in general from the nominal value. Moreover, the thickness measurement methods have some imprecision. It was analyzed how these imprecision in film thickness influences the accuracy of the determined coupling coefficient. Each imprecision in thickness induces an error on the final result for $K_{(S,L)}^2$. Figure 2.27 shows the relationship between the errors of the determined coupling coefficient K and the bottom electrode thickness imprecision for an electrode with nominal thickness of 100 nm. For a typical maximum thickness imprecision of ± 10 % the impact on K is below 2 %, which is precise enough for the FBARs examined in this work. Zhang *et al.* looked at the imprecision arising when the electrodes are approximated as very thin. They found that when the thickness of the electrodes is within 10 % of the ZnO

[37] R. S. Naik, J. J. Lutsky, R. Reif, C. G. Sodini, IEEE Trans. Ultrason., Ferroelec., Freq. Contr., **45**, 257 (1998).

film, the error on K is less than 5 % when the electrodes are omitted in the simulations.[38] The impact of thickness fluctuations of an Al_2O_3 buffer-layer on K was also investigated. The measurement of the Al_2O_3 film thickness was not easily feasible in this work and thus the error on film thickness could be as high as ± 20 %. But even for such an error, the error for K is less than 5 %. Zhang *et al.* also investigated the accuracy of the method by numerical simulation. He found that the values determined by this method are accurate to 3.5 %, which is quite acceptable for high frequency devices.

In summary, the over-modes fitting method provides reliable results for the electromechanical coupling coefficient K. Concerning the bottom electrode and the buffer-layer thickness, an imprecision of 10 % on these thicknesses gives a worst case error of the computed K of less than 5%. This is sufficient for a quick characterization and a comparison of sputtered ZnO films.

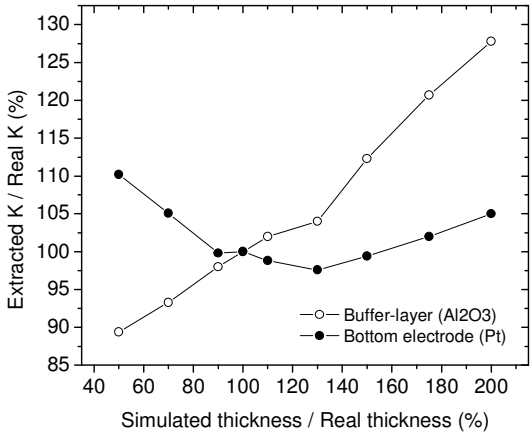

Figure 2.27 : Deviation of the extracted K from the real K as a function of the thickness error for a Pt bottom electrode and an Al_2O_3 buffer-layer.

2.7. Chapter conclusion

This chapter explained the functioning of film bulk acoustic wave devices (FBARs) based on c-axis inclined ZnO. After presenting the basic equations of elasticity, piezoelectricity and acoustic wave propagation, an expression for the electrical impedance of an ideal FBAR consisting of only the ZnO layer was derived. This permits to define basic resonator parameters such as the series and parallel frequencies, the coupling coefficient and the Q-factor. It was shown that both the longitudinal and shear wave modes are excited depending on the amount of c-axis inclination. At 0° and 62.9°, only longitudinal mode is excited. At 90° and 42.25°, only shear mode results. At all other inclinations, both modes are excited. At an inclination of 13.6°, both modes are excited with equal coupling coefficients.

Afterwards, composite FBARs with multiple layers similar to the devices realized in this work were examined. Models like the transmission line model, the Mason Model and the Butterworth-Van Dyke Model were introduced. It was shown that around each particular mode of interest, the impedance of a composite

[38] Y. Zhang, Z. Wang, J. David N. Cheeke, *IEEE Trans. Ultrason., Ferroelec., Freq. Contr.*, **50**, 321 (2003).

FBAR resembles the impedance of a simple one, and accordingly, similar parameters and models can be defined. The characterization of the FBARs using electrical measurement of the S-parameters was explained. It was shown that care must be taken in determining the coupling coefficient and quality factors of lossy FBARs. Regular formulas for the determination of the resonance frequencies at the points of maximum impedance slope and the corresponding formula for the Q-factor (2.122) can only be applied when the product $K_{eff}^2 \cdot Q$ is bigger than 5. The determination of these parameters with the help of the Butterworth-Van Dyke circuit is always correct, provided the fitting procedure gives good results and the impedance is only looked at in a short frequency range around the resonance peak of interest.

A method of characterizing thin piezoelectric films with the help of highly over-moded FBARs was introduced. It was shown that they permit to see if the film is piezoelectrically active and which mode is predominately excited at what frequency. They also permit to derive the electromechanical coupling coefficient of the film using a method combining measurement, fittings and simulations.

The models derived in this chapter are useful before and after device realization. More precisely, the Mason Model permits to calculate the correct layer thicknesses for a specified target resonance frequency, including the necessary acoustic mirror. After fabrication of the devices, it helps to determine which recorded resonance peaks correspond to which wave modes. The Butterworth-Van Dyke model permits to fit the obtained impedance characteristics and compute the device parameters, even for lossy devices. The combination of both models gives a powerful characterization method of over-moded FBARs. The formulas, models and methods described in this Chapter will therefore be used during the thin film process optimization described in Chapter 3, the simulation and realization of composite solidly mounted FBARs and their characterization in air described in Chapter 4, and the analysis of the performance of these devices as sensors in liquid environments, described in Chapter 5.

3. Deposition of c-axis inclined ZnO thin films

Dépôt de couches minces de ZnO à axe c incliné — *Résumé*: Ce chapitre débute par une présentation du dépôt par pulvérisation de couches minces de ZnO à axe c incliné. Ces couches sont nécessaires pour exciter les modes de cisaillement dans des FBARs. La croissance de couches minces de ZnO avec une orientation inclinée s'avère difficile, puisque **la forte tendance du ZnO à cristalliser dans la direction perpendiculaire doit être surmontée et qu'en même temps, l'axe c de tous les grains doit pointer dans la même direction spécifique**. Le dépôt de couches possédant une orientation appropriée pour l'excitation du cisaillement a été mentionné dans quelques articles avec des méthodes et sur des substrats très différents. Un aperçu en est donné, après un rappel des principes fondamentaux de la pulvérisation réactive magnétron, de la croissance de couches minces et des techniques de caractérisation. Les objectifs de cette partie de la thèse étaient a) d'obtenir du ZnO incliné aussi **rapidement que possible** afin de pouvoir réaliser des SMRs, b) d'utiliser l'équipement de pulvérisation et son **système de chargement planaire existant**, c) d'utiliser des **wafers 4"**, et d) de pouvoir déposer le ZnO sur des **couches amorphes ou polycristallines**. Les procédés développés satisfont à ces critères. Des inclinaisons allant jusqu'à 9° ont été obtenues avec le procédé I, sans aucune modification de l'équipement. Cependant, les propriétés des couches obtenues varient fortement en fonction de la distance au centre du wafer, et uniquement 19% de sa surface peut être utilisé. Pour le procédé II, un **cache rectangulaire** est positionné entre la cible et le substrat, permettant d'obtenir une incidence oblique des particules sans devoir incliner le wafer. Des **inclinaisons de 16° sont obtenues, avec des coefficients de couplage allant jusqu'à 0.105**. Néanmoins, les propriétés dépendent fortement de la distance au cache, et uniquement 30% de la surface peut être utilisé. Enfin, le procédé III utilise un système de caches plus complexe et permet de faire bouger latéralement le wafer pendant le dépôt. Des **couches homogènes** sont obtenues, avec une **inclinaison de 10° et des coefficients de couplage de 0.136**. A ma connaissance, il s'agit du premier procédé de dépôt permettant de déposer des couches inclinées homogènes sur de si grandes surfaces. Il est montré que l'incidence oblique des particules est responsable de la croissance du ZnO à axe c incliné.

3.1. Introduction

As was discussed in paragraph 1.4 of Chapter 1, ZnO is a well investigated piezoelectric material which has been proved to be suitable for FBARs with high coupling coefficients and quality factors.[1] Table 3.1 gives its main material characteristics. A schematic representation of its structure was shown in Figure 1.8. ZnO can be deposited using various physical and chemical vapour deposition techniques, including sputtering. In Chapter 2 the inclination of the ZnO c-axis with respect to the surface normal was showed to be a necessary

---

Parts of this chapter have been released in the following publications: M. Link, M. Schreiter, J. Weber, R. Gabl, D. Pitzer, R. Primig, W. Wersing, M.B. Assouar, O. Elmazria, *J. Vac. Sci. Technol. A* **24**, 218 (2006); M. Link, M. Schreiter, J. Weber, D. Pitzer, R. Primig, M.B. Assouar, O. Elmazria, *Proc. IEEE Ultrason. Symp.*, 202 (2005); E. Aubert, E. Wenger, M. Link, B. Assouar, C. Didierjean, C. Lecomte, *J. Appl. Cryst.*, accepted (2006). 4 related patents have been filed at the German Patent Office.

[1] C. Vale, J. Rosenbaum, S. Horwitz, S. Krishnaswamy, R. Moore, *Proc. IEEE Ultrason. Symp*.,332 (1990); K. M. Lakin, J. S. Wang, *Appl. Phys. Lett*. **38**, 125 (1981).

requirement towards shear wave mode excitation in FBARs. However, the growth of ZnO films with inclined orientation is difficult, as the strong trend of the ZnO to crystallize in the perpendicular direction must be surmounted and the polar c-axis of all different grains must point into the same particular direction. Consequently, one has to be able to control the preferred orientation of the polar c axis not only along one but along two specific directions.

In paragraph **3.2**, the principle of reactive magnetron sputtering will be explained. The basics of thin film growth will be given and the different characterization techniques will be exposed. Diverse methods to deposit inclined ZnO are mentioned in literature, including epitaxial growth on mono-crystalline substrates, incorporation of other materials into the film, adjustment of sputtering parameters, and oblique particle incidence. These methods will be summarized in paragraph **3.3** together with the process planning of this work. In paragraphs **3.4**, **3.5** and **3.6**, the main processes (PROCESS I, II and III) developed during this thesis will be detailed. The obtained inclinations and electrical characteristics of the thin films will be given and some growth mechanisms will be proposed. Each paragraph will also give some perspectives for future inclined ZnO thin film optimization.

TABLE 3.1
PHYSICAL PROPERTIES OF BULK ZNO SINGLE CRYSTAL[2,3]

Property (unit)	Value
Crystal group	6 mm (wurtzite)
Lattice constant (Å)	a = 3.24265; c = 5.1948
Sublimation point (°C)	1975 ± 25
Relative dielectric constants	ε_{11}^S=8.33; ε_{33}^S=8.84
Piezoelectric constants (C/m^2)	e_{15}=-0.59; e_{31}=-0.61; e_{33}=1.14
Stiffness constants (GPa)	c_{11}^E=210 ; c_{12}^E =121 ; c_{13}^E =105 ; c_{33}^E =211; c_{55}^E =42,5
Density	5665 kg/m^3

3.2. Sputtering, thin film growth and characterization

Sputtering is widely used for the deposition of metallic, dielectric and active thin films. It permits a deposition at low temperatures, often below 100°C, making it possible to use substrates with electronic CMOS circuitry. This paragraph explains the basics of low density plasmas, the principle of sputtering, the mechanisms of thin film growth and the different characterization techniques employed in this work. *The reader familiar with these topics can drop this paragraph and directly jump to paragraph 3.3.*

3.2.1. Low density plasma basics and sources

Sputtering is a physical process where atoms of a solid target are ejected due to the bombardment by energetic ions (e.g. Argon). These ions are generated in a plasma, which is a weakly ionized gas with an

[2] K. Wasa, S. Hayakawa, Handbook of Sputter Deposition Technology, Noyes Publication (1992).
[3] N. F. Foster, G. A. Coquin, G. A. Rozgonyi, F. A. Vannatta, IEEE Trans. Sonics Ultrason., **SU-15**, 28 (1968).

equal number of positive and negative charges. To maintain constant electron and ion densities, an **ionization process** must balance the recombination process, which requires an external energy source. There are many types of plasma energy sources such as discharges created by direct current (DC), capacitively coupled radio-frequency (RF) current, inductively coupled RF and microwaves. For thin film deposition, DC or RF plasma sources are usually used. In this case, an electrical field directly acts on the charged particles. By natural cosmic radiation there are always some ionized Ar^+ ions and electrons available, permitting to start the process. Through collisions with neutrals the supply of ions is maintained. The light electrons do not transfer efficiently kinetic energy to the much heavier atoms and molecules. Therefore, the electrons are not thermalized and possess a much higher energy that the ions. The typical electron temperature is in the range of 2-5 eV, whereas that of ions and neutrals is only a few times the room temperature (0.026 eV). The high electron energy is enough to excite high temperature electron-molecule reactions. Temperatures of more than 1000°C would be required to generate the same reactive species without plasma. The plasma used in micro-systems and micro-electronics processing is therefore called a **low-temperature plasma**. A typical sputtering setup is shown on Figure 3.1. The DC or RF voltages are applied between two electrodes, typically the target and the sputtering chamber walls. The substrate is generally kept at the same potential than the chamber walls. Similar to a regular gas, a **mean free path (MFP)** λ can be defined for the plasma:

$$\lambda = \frac{k \cdot T}{4\pi \cdot r^2 \cdot p} \tag{3.1}$$

where k is Boltzmann's constant ($1.38 \cdot 10^{-23} JK^{-1}$) and r is the effective radius of the gas atom.[4] For pure Argon, temperatures of 0°C to 300°C and pressures of 0.1 to 1 Pa, the MFP varies from 3 to 15 cm. The typical distances between target and substrate for sputtering processes are 1 to 10 cm. This distance and the MFP determine how many collisions the particles experience on their way from the target to the substrate. In this work, the distance is around 6 cm with pressures of around 0.5 Pa, meaning there will be very few collisions and the particles will mainly retain the direction they had when leaving the target.

Since the electrons have a higher energy then the ions, they are more mobile and diffuse quicker to the surface of any solid in contact with the plasma. This surface will build up a negative potential with respect to the plasma and an electric field will be created between the surface and the plasma, repelling additional electrons. The plasma acquires a positive potential with respect to the walls, the **plasma potential**. The region in which the electrical field builds up is depleted of electrons and is usually called the **sheath**. At the negatively biased target the sheath is more pronounced and is called the **dark space** (since no electronic excitation occurs there and no glow is observed). The width of the sheath can vary between fractions of a millimetre to several millimetres.[5] Since all surfaces are negative with respect to the plasma, they will attract ions resulting in an **ion bombardment**. At the substrate it can have an influence on thin film growth by enhancing surface diffusion. At the negatively biased target, the ion bombardment is much higher and responsible for sputtering. Since the acceleration of the ions occurs in the plasma sheath, which follows the contour of the body, the ion bombardment will generally be normal to the surface.

---

[4] N. St. J. Braithwaite, *Plasma Sources Sci. Technol.*, **9**, 517 (2000). For Argon gas with r_{Ar} the radius of an argon atom ($1.5 \cdot 10^{-10}$ m), the formula for the MFP is: $\lambda = T/(20489 \cdot p)$.

[5] G. F. Iriarte, PhD Thesis, Acta Universitatis Upsaliensis (2003).

DC sputtering can be applied if both electrodes are conducting, since the net current is a DC electron current. Only conductive materials like metals or semiconductors can be processed. High pressures and voltages are generally needed due to the low ionization efficiency (typically 10 Pa). If the material of the target is non-conductive, only **RF sputtering** can be used. In this case the power is coupled capacitively to the plasma. The applied frequency is typically 13.56 MHz and has been reserved for RF sputtering purposes. Usually one electrode (e.g. the chamber walls) has an area much bigger than the other (e.g. the target). It can be shown that the electrode with the smaller area will have a much bigger potential than the electrode of bigger size.[6] High-frequency electric fields cause more efficient ionization in a discharge than DC fields and the minimum operating pressure thus decreases (typically 0.5 Pa). However, the efficiency of the discharge is still not very high, since no sputtering of the target takes place during the positive cycle. An additional increase of the efficiency of the gas discharge is achieved with **DC-pulsed discharges**. In this case the polarity of the target is periodically switched from negative to positive for a short time interval. With this method one can also deposit insulating films. The positive pulse is used to discharge the surface and avoid arcing. This is particularly advantageous for sputtering of metallic targets in a reactive atmosphere. The ratio between the positive and the negative pulse time is called the **duty cycle** and is typically in the order of a few percent. This results in higher efficiencies for DC-pulsed discharges than for RF discharges.

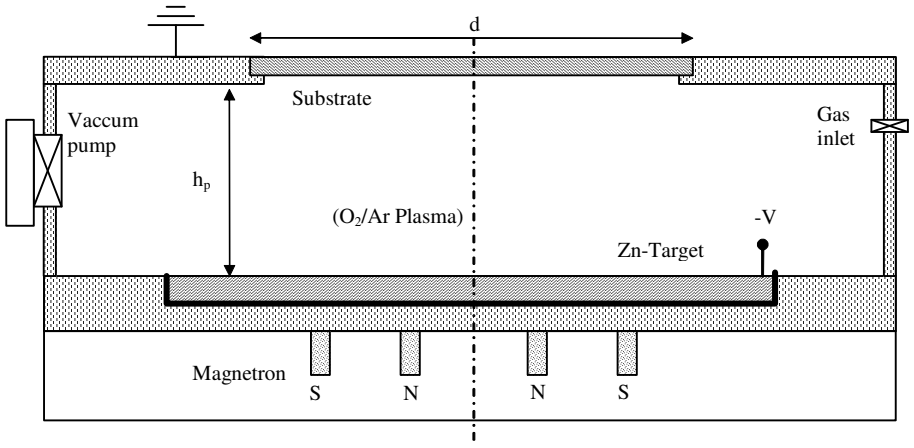

Figure 3.1 : Simple schematic of a magnetron sputtering system.

3.2.2. Principle of sputtering

The impact of energetic atoms or ions from the plasma on the target surface produces **sputtering** from the surface as a result of the momentum transfer between the incident particle and the target atoms.[7] The target material (e.g. Zn) is detached by the impingement of the ions and deposited on a substrate in the vicinity. There is no melting of the target material. The whole process is realized in a closed recipient, which is

[6] W. J. Goedheer, course on low temperature plasma physics and applications, Bad Honnef, Germany, 28.9.2004.
[7] The verb "sputter" originates from Latin "sputare" (to emit saliva with noise).

pumped down to a vacuum base pressure before the deposition begins. Figure 3.1 shows a schematic view of the recipient. A picture of the equipment used in this work is shown on Figure 3.4.

The use of a magnetic field to enhance the sputtering rate leads to the term **magnetron sputtering.** A permanent magnet placed below the sputtering target creates a strong magnetic field close to the target surface. This field forces the electrons to travel along spiral trajectories due to the Lorentz force. Typical magnetic field strengths attained in the sputtering equipment used in this work are 34 kA/m. By keeping the electrons close to the target surface, the ionization efficiency of the discharge and the sputtering rate increase. The discharge can be sustained at pressures lower than 0.1 Pa. Lower pressures give higher MFPs resulting in higher kinetic energies for the sputtered particles. The excess energy for the particles results in increased surface diffusion, and hence film densification and improved crystal growth.

During **reactive sputtering** a metallic target is sputtered in a reactive atmosphere. As the sputtered atoms are deposited onto the substrate, they react with the reactive gas molecules forming the desired compound. In this work, Zn was sputtered in an O_2 ambient. Zn reacts with the oxygen to form ZnO. Reactive sputtering has some important advantages as compared to sputtering from a compound target. Metal targets can easily be manufactured and are cheaper. They have a high thermal conductivity enabling efficient target cooling and hence the possibility to apply higher powers without the risk of melting the target. In addition, a particular metal can be used for the synthesis of different compounds. A disadvantage of reactive sputtering is its high complexity. In order to obtain desirable results, process understanding and optimization of all the parameters influencing film quality is required.

A lot of research has been done in the field of **particle and target surface interactions**. As an incident ion collides with the surface of the target and slows down, energy in excess of the lattice binding energy may be transferred to an atom of the target and remove it from its original site. This atom can then also transfer energy to other atoms in the lattice and a collision cascade develops. Some atoms involved in the collision cascade can be ejected out of the lattice, leading to the sputtering phenomenon. The incident ion can be absorbed in the crystal, or be reflected and escape from the lattice. The **sputtering yield** is the average number of atoms ejected from the lattice by one incident projectile. The sputtering yield, the probability of absorption or reflection, and the energy and angular distribution of emitted atoms depend on the incident species, the material composition of the target, the texture of the target, and the angle and energy of incidence. The **angular distribution** of sputtered atoms is of some importance in the second half of this chapter, where PROCESS I, PROCESS II and PROCESS III will be developed. For a non-textured polycrystalline metal target where the crystallites are randomly oriented, as with the Zn target used in this work, the angular distribution of sputtered particles has a **cosine form**.[8] In this case, the probability of emission is proportional to the cosine of the polar angle of the sputtered atom with respect to the surface normal. It has a uniform distribution in azimuthal angle direction.

[8] H. Tsuge, S. Esho, *J. Appl. Phys.* **52**, 4391 (1981); A. Wucher, W. Reuter, *J. Vac. Sci. Technol. A* **6**, 2316 (1988).

3.2.3. General growth theory of thin films

Thin films can be classified in three different categories, depending on the short and long range ordering of the atoms: **amorphous, singly crystalline and polycrystalline**. Polycrystalline films are mainly characterized by the size of the individual grains, their texture and the film density. They can be divided into three sub-categories: a) Non-textured polycrystalline films, where the grains have random crystallographic orientations; b) Textured films, where the grains all have a preferred orientation; c) Epitaxial polycrystalline films, where the grains have specific crystallographic relationships with substrate surface. The ZnO thin films considered in this work are **textured polycrystalline films**. The properties of thin films may be very different from those of the bulk material. They exhibit a wide variety of microstructures characterized by the grains size and crystallographic orientation, lattice defects, phase composition, and morphology. They are influenced by the processes occurring during film growth. These processes will be briefly reviewed in the following lines. Four process stages can be distinguished: **nucleation and island growth, coalescence of islands, channel formation and grain coarsening, and formation of a continuous film by film growth**.[9]

When the particles impinge on the substrate they are thermally **accommodated**. They can adsorb and stick permanently on the surface, diffuse and interact with other adsorbed atoms, or be reevaporated. In the case of diffusion on the surface, the particles are called **adatoms**. The condensation of the particles is initiated by the formation of small clusters through the combination of several adatoms. These clusters are called **nuclei**, and the cluster formation is called **nucleation**. When the nuclei have reached a critical stable size, they can start to grow in an attempt to decrease total free system energy. The size of a critical nucleus is independent of the surface diffusion ability of single adatoms. In contrast, the rate of formation of such critical nuclei is dependent on the **surface diffusion of the adatoms and the binding energy between adsorbed atoms and the substrate**. If the activation energy for surface diffusion of adatoms at the substrate is very large, the diffusion distance before reevaporation will be small, and nuclei can grow only from material received by direct impingement from the plasma. The stronger is the binding energy between adsorbed atoms and substrate, the smaller is the critical nucleus and the higher is the nucleation density. A micro-roughness of the substrate increases the nucleation rate since the surface mobility is decreased.

After nucleation, the nuclei start to grow, which is known as the **island stage**. If there was a large nucleation barrier with large critical nuclei, the film will consist of only a few but large islands. This island structure will persist up to relatively high average film thicknesses. If the nucleation barrier was small, the film will consist of many small islands since the critical nuclei size is small, but the nucleation density is large. In that case the film will become continuous at a relatively low average film thickness since the islands touch and grow together at an early stage. Eventually these islands form a continuous film. After this **coalescence stage**, the effect of nucleation can still be visible through the grains: high-nucleation barrier films will give a coarse-grained film, while low-nucleation barrier films will give a finer-grained film. Different nucleation barriers can therefore cause very different structures in thin films. In the **channel stage**, the islands become elongated and join to form a continuous structure where the grains are separated by long irregular and narrow

[9] I. Petrov, P. B. Barna, L. Hultman, J. E. Greene, *J. Vac. Sci. Technol. A* **21**, 117 (2003); P. B. Barna, M. Adamik, *Thin Solid Films* **317**, 27 (1998).

channels. During the formation of the **continuous film**, considerable changes in the orientation of islands can occur. Recrystallization can produce grains much larger than the average separation of initial islands.

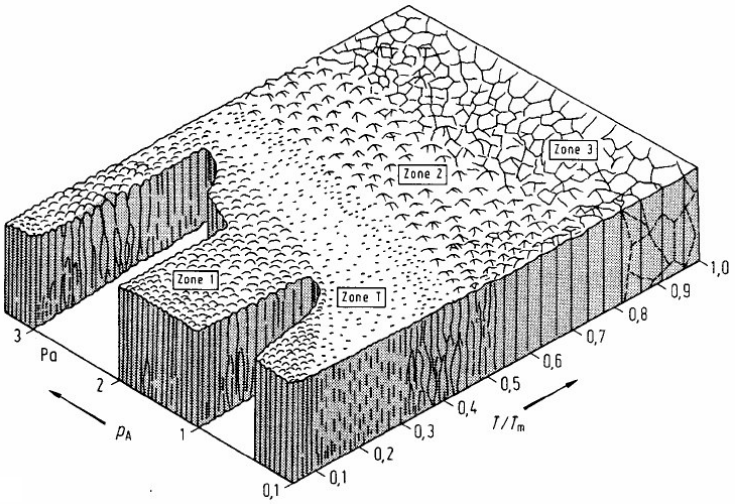

Figure 3.2 : Thornton's structure zone mode.[11]

The final structure of the film is very much dependent on surface and bulk diffusion, desorption and shadowing phenomena. These depend mainly on the deposition temperature T_s normalized to the melting temperature of the material T_m and the energy of the depositing atoms, which is dependent on the pressure. The different nucleation and growth processes are summarized in so-called **structure-zone models (SZM)**, which systematically categorize self-organized structure evolution as a function of process parameters. In 1969, Movchan and Demchishin observed the structure of evaporated films as a function of T_s/T_m which resulted in a SZM with three characteristic zones.[10] In 1977, Thornton extended their model to include the influence of the pressure.[11] An additional transition zone was included. His well-known diagram is given in Figure 3.2 and shows the different zones depending on the gas pressure and the normalized substrate temperature. The sputtering processes examined in this work are realized at pressures around 0.5 Pa and substrate temperatures of around 200°C. Since the melting point of ZnO is about 1975°C, **zones 1 or T** in the lower corner of the diagram are relevant. Zone T is typical for sputtering processes. In this region, **surface diffusion is small** and the film consists of fibrous grains or columns a few tens of nm in diameter, which can be separated by voids for Zone 1 or exhibit dense grain boundaries in Zone T. Surface and bulk diffusion increase with increasing temperature. Zone 2 and Zone 3 exhibit larger grains, with a diameter increasing with T_s/T_m. This model does not take into account the influence of ion bombardment, which moves all zones towards lower T_s/T_m, increasing nucleation rates and film density, and decreasing average grain size.[12]

At temperatures which are less than 0.2-0.3 of the melting point T_m, film synthesis takes place far from thermodynamic equilibrium. Microstructure during deposition typically evolves in a **competitive fashion**,

[10] B. A. Movchan, A. V. Demchishin, *Fiz. Met.* **28**, 83 (1969).
[11] J. A. Thornton, *Ann. Rev. Mater. Sci.* **7**, 239 (1977).
[12] I. Petrov, P. B. Barna, L. Hultman, J. E. Greene, *J. Vac. Sci. Technol. A* **21**, 117 (2003).

explained with the **evolutionary selection model** of Van der Drift in 1967.[13] The consequence of competitive growth is a change in crystallographic orientation and film texture as a function of film thickness. At the beginning of the growth the crystallographic orientation of the grains is mainly influenced by the substrate. Polycrystalline substrates can favour the development of islands with a particular orientation through local epitaxy. For amorphous substrates, the islands have a random orientation.[14] It is only after the island formation **during island coalescence and island growth that a preferred orientation develops**. The final orientation results from the **differences in growth rates** between different crystal faces of the grains on the surface of the film. Grains oriented with their fastest growing directions perpendicular to the incident flux are preserved while slower growing grains are cut off as they intersect the column walls of taller grains. Different mechanisms for this difference of growth rates have been proposed. It may be related to the thermodynamic preference of deposited atoms to condense on low- rather than high-energy surfaces in order to minimize the surface energy. The low-energy orientations typically coincide with the densest planes, which are (111) for fcc, (002) for hcp and (110) for bcc.[15] This is why the (002) orientation is typically found for ZnO films. An alternative explanation is that the preferential growth is affected by differences in re-sputtering rates by ion bombardment.[16] The films the less affected by ion bombardment are those with the densest packed orientations. So both explanations give the same result. Since the evolutionary selection starts at the coalescence of the islands, a preferred orientation will be seen at lower film thicknesses if the initial nucleation density is higher. This explains why thicker films generally exhibit better orientations.

While these last lines concern the formation of a preferred crystallographic orientation, other mechanisms permit to explain the formation of a certain **texture**, or **morphology of the film**. The phenomenon of **shadowing** plays a predominant role. An atom which is deposited close to the side of a grain is pulled towards the grain edge due to the attractive part of the interatomic potential. This gives the depositing atom a component of velocity in the direction towards the side of the grain, thereby giving it a net growth rate in the outward direction. This causes the taller grains to grow laterally at the expense of neighbour grains. As this lateral growth continues, the taller grains begin to physically “shadow” the lower grains. If the atom mobility is low, this can lead to the formation of an overhang, which pinches off the lower grain and creates a void. This situation is typical for Zone 1. If there is sufficient surface mobility of the atoms, this leads to a simple pinching off the lower grain without the creation of a void, which is characteristic for Zone T and results in denser films.

In conclusion, to get a preferred texture in thin films, one should increase the atom kinetic energy to favour the quicker growing grains, for example by reducing the pressure, and set the temperature at an intermediate level to control the surface diffusion of the atoms between the creation of voids in Zone 1 and the recrystallization in Zone 2 and 3. A higher sputtering rate can increase the initial nucleation density. For low-temperature and low-pressure sputtering processes these conditions are generally fulfilled.

[13] A. Van der Drift, *Philips Res. Rep.* **22**, 267 (1967).
[14] P. B. Barna, M. Adamik, *Thin Solid Films* **317**, 27 (1998).
[15] I. Petrov, P. B. Barna, L. Hultman, J. E. Greene, *J. Vac. Sci. Technol. A* **21**, 117 (2003).
[16] F. Ying, R. W. Smith, D. J. Srolovitz, Appl. Phys. Lett. 69, 3007 (1996).

3.2.4. Characterization techniques of thin films

This section will briefly explain the characterization techniques of thin films used in this work. The most important film properties needed for the realization of FBARs are their piezoelectric activity and their thickness. For a film to be piezoelectric it is necessary that it is of the proper crystal class and that it has a good crystallographic orientation. Measurements of the surface morphology, film composition, dielectric and optical properties, crystallographic orientation and internal microstructures can be related to the piezoelectric activity. These measurements are indirect and require a calibration to take place between the measured property and the quantitative direct measurements of the piezoelectric activity discussed in paragraphs 2.5 and 2.6 of Chapter 2. The indirect measurements provide information about necessary but often not sufficient conditions for piezoelectricity.[17] A direct method to characterize the piezoelectric activity of thin films via the determination of the electromechanical coupling constant using over-moded FBARs has already been described in paragraph 2.6.

X-Ray Diffraction (XRD) is an analytical method for determining the structural properties of materials, such as crystal structure and orientation, lattice parameters, grain size and stress. The crystallographic orientation of the ZnO thin films is an important parameter, since piezoelectric properties depend strongly on it. In this work, XRD was mainly used to a) see if the deposited ZnO film had the proper crystal structure and b) determine the c-axis inclination angle. The method uses x-rays, often from a Cu source, that are diffracted by the crystal lattice. The basic principle can be used in a variety of different measurement modes, depending on the variation of the x-ray incidence and substrate angles. Some modes are explained in the following. The angles employed in this description are given in Figure 3.3 a).

In a **θ–2θ scan** the incident angle ω and the reflected angle θ are equal. The x-ray source and the x-ray detector are coupled during the scan. From the obtained XRD diffractogram one extracts the lattice parameter, film texture and grain size. 2θ is the angle observed between source and detector, θ is the value between source and substrate. By comparing the obtained lattice parameters with known parameters from literature, this type of scan permits to determine which crystallographic orientations are present in the sample. The (002) θ peak for bulk ZnO lies at 34.43°.[18] To obtain a **rocking curve**, the source and detector are fixed at an angle fulfilling the Bragg-condition for a certain lattice plane. The sample is then rotated ("rocked") in θ-direction, bringing the plane in and out of the Bragg condition. The width of the measured peak, often measured in terms of the Full-Width at Half Maximum (FWHM), gives information about the orientation distribution of this plane. It is widely used to compare the crystalline quality of thin films. The **χ-scan** is similar to the rocking-curve scan, but the sample is tilted in a direction perpendicular to the incident x-ray. Similarly, one obtains the information of how much the measured plane is off the surface normal. This type of scan was extensively used in this work to determine the c-axis inclination angle and orientation of the ZnO film. A χ-scan was used instead of the rocking curve since in typical diffractometers the substrate can perform bigger movements in χ than in θ direction. The **φ-scan** is also similar to the rocking curve and the χ-scan. Again, the incident x-ray is locked at a certain angle θ fulfilling the Bragg-condition for a certain plane.

[17] F. S. Hickernell, *Proc. IEEE Ultrason. Symp.*, 235 (1996).
[18] J. G. E. Gardeniers, Z. M. Rittersma, G. J. Burger, *J. Appl. Phys.*, **83**, 7844 (1998).

The φ-scan is performed by rotating the sample around its normal. The in-plane orientation can then be determined. A complete **pole figure** for a certain crystallographic plane can be obtained by combining the χ-scan and φ-scan.

In this work, a three circle diffractometer with Cu Kα radiation and a two-dimensional detector from *Bruker AXS*, Karlsruhe, Germany, was mainly used.[19] A picture of the source, the sample holder and the detector are shown in Figure 3.3 b). θ-2θ and χ-scans, which are most important for this work, can be obtained with only one measurement by integration along the χ or θ directions respectively. Caution must be taken since in such an integrated θ-2θ scan, also planes with orientation at certain χ angles will appear. Figure 3.21 a) shows the image obtained by such a scan for 16° inclined ZnO. The corresponding θ-2θ scan and the χ-scan obtained are shown in Figure 3.21 b) and c) respectively. As can be seen, the (002) peak is also visible on the θ-2θ scan obtained by integration. For perfectly inclined ZnO, a (002) peak would not be seen on a regular θ-2θ scan. For most measurements of this work, the samples were simply fixed on the holder by adhesive tape. The resulting imprecision was estimated to be less than ±1°.[20]

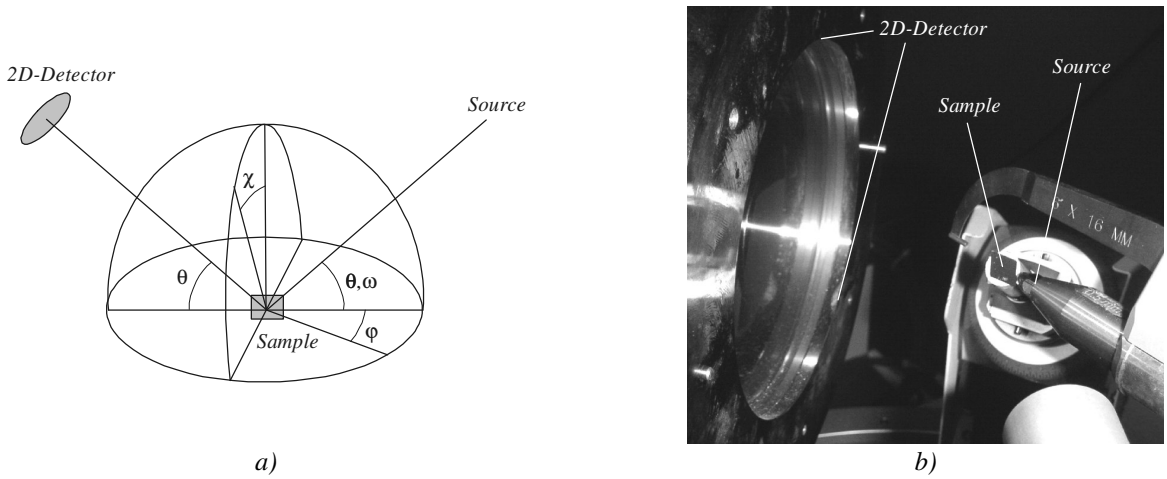

Figure 3.3 : A schematic illustration of the x-ray diffraction with θφχ geometry and a picture of the 2D-detector, sample-holder with sample and source of the XRD equipment used in this work.

Different techniques were used to measure the **thickness** of the deposited films. The **α-step** method represents the oldest tool for measurement of surface profiles. The film has to present a step on a flat substrate. A diamond needle is moved with a constant speed over the surface and the height of the step is measured with an electric system. The measurement range lies between around 5 nm and a few tens of µm with a precision down to a few Å. The advantage of this system is the big scanning length of several cm. The disadvantage is the mechanical stress on the surface due to the needle and the limitation to one-dimensional scans. In this work, an Alpha-Step 200 from *Tencor Instruments*, New York, USA, was used. A **white-light**

[19] Most measurements were done at the Institute of Applied Physics of the JKU in Linz (Austria). Some measurements were also done with other XRD equipments at Siemens CT MM7 in Munich, and the LCM^{3}B of the UHP in Nancy.
[20] Personal communication from B. Jobst, Siemens CT MM7.

interferometer was also used. It functions like a regular interferometer but with light of low coherence-length. The test sample is positioned in one arm of the interferometer. It can be used to measure surface profiles of samples with a precision of a few nm. In this work, a system from *SENTECH Instruments GmbH*, Berlin, Germany was used. The thickness of conducting films can be estimated by the measurement of its **conductivity** with a 4-point prober. The obtained sheet resistance can be linked to the film thickness if the specific conductivity of the material is known. This method was used to determine the thickness of Pt thin films. A 4-point prober M700 from *Magnetron Instruments*, Palo Alto (CA), USA was used. The precision of this method is limited by the fact that the conductivity of a material in thin film form does not necessarily correspond to the value of the bulk material. It was therefore validated with α-step measurements. Film **texture and morphology** can be assessed using a **Scanning Electron Microscope** (SEM). A SEM S1400 from *Hitachi* was used. The advantage of the SEM is its high resolution. As the wavelength of electrons is much smaller than that of light, the resolution is many orders of magnitudes better than that of a regular light microscope.

Surface **roughness** can be estimated using the **α-step** method. However a maximum resolution of only 10 nm is achievable. For this reason **Atomic Force Microscopy** (AFM) was also used. Unlike the SEM which provides a two-dimensional image of a sample, the AFM provides a true three-dimensional surface profile. Additionally, samples viewed by an AFM do not require any special treatment that would destroy the sample. The main disadvantage of the AFM is the image size. The SEM can show an area on the order of mm^2 while the AFM can show a maximum area of around $100 \times 100\ \mu m^2$. An AFM CPIII Autoprobe TM from *Veeco*, Santa Barbara (CA), USA was used.

3.3. Inclined ZnO deposition by sputtering: literature review

3.3.1. Difficulty of depositing c-axis inclined ZnO films

It is straightforward to prepare high resistive ZnO films with perpendicular (002) orientation for transducers working in the longitudinal mode by sputtering. First reports about reactive sputtering of ZnO from a Zn target in O_2 appeared in 1965.[21] Since then, numerous articles have shown the sputtering of high-quality (002) oriented films with rocking curve FWHMs of less than 0.3° and coupling coefficients nearing the theoretical maximum of 0.27.[22] The facility to grow ZnO with perpendicular orientation can be attributed to the strong trend of ZnO to crystallize in the (002) direction. As explained in section 3.2.3, this is well understood. The (002) plane is the plane with the lowest energy and grains with (002) orientation generally grow fastest and outgrow the other grains. Another effect may support the (002) orientation. For FBAR applications, the films are usually deposited on metal layers forming a bottom electrode. Metal layers often exhibit (111) orientations, which further favour the hexagonal (002) orientation.[23]

[21] H. W. Lehmann, R. Widmer, *J. Appl. Phys*. **44**, 3868 (1973).
[22] J. Kaitila, M. Ylilammi, J. Molarius, *Proc. IEEE Ultrason. Symp.*, 803 (2001); N. H. Kim, H. W. Kim, *Brit. Cer. Trans*. **103**, 15 (2004).
[23] K. Wasa, S. Hayakawa, T. Hada, *IEEE Trans. Sonics Ultrason.* **SU-21**, 298 (1974).

The growth of polycrystalline ZnO films with inclined c-axis orientation is more difficult. In fact, two conditions must be realized. First, the strong trend of the ZnO to crystallize in the perpendicular direction must be overcome. As will be seen in the next section, this can be done by various methods like choosing an appropriate substrate material or the incorporation of impurities into the growing film. This gives an **inclined texture** in direction χ to the film. But generally the orientations of the different grains are centro-symmetric with respect to the normal of the film, meaning that the mean in-plane component of the c-axis is zero. Therefore, a second condition to the film is that there is an **in-plane texture** ensuring that the average in-plane component is non-zero. In other words, the polar c-axis of all different grains must point into the same specific direction. Thus, one has to be able to control the preferred orientation of the c-axis of the ZnO films for shear wave mode generation not only along one but along two directions. As will be seen, both conditions can be simultaneously realized by oblique particle incidence. Foster and co-workers were among the first to deposit inclined ZnO by sputtering using oblique particle incidence and small hydrocarbon additions in 1969.[24] Since then, many groups have succeeded in depositing inclined ZnO by sputtering with various methods. Section 3.3.2 will give a review of the methods found in literature. Based on the findings of these articles, the planning of the inclined ZnO processes used in this work will be presented in section 3.3.3.

3.3.2. Literature review

As stated in the previous section, the difficulty of depositing c-axis inclined ZnO films with an orientation suitable for shear wave mode excitation lies within the fact that the c-axis must be oriented along two directions. Therefore, one has to distinguish in literature between methods favourising an inclination in χ direction and methods giving the c-axis an in-plane orientation in φ direction. Some articles explicitly mention the difference in these two requirements and present methods were both requirements are fulfilled, for example with inclination of the substrate. Other articles mention a method to incline the c-axis in the χ direction, but admit that they need another mechanism to achieve an in-plane orientation, for example an oblique incidence of the particles**. The following lines will give a brief overview of the different articles found in literature**. This review is limited to articles about ZnO deposition, but similar techniques can be found for the deposition of AlN.

3.3.2.1. Substrate choice and incorporation of other materials

There are a number of articles mentioning an inclination of the c-axis **by choosing the right substrate material.** A complete inclination of 90° with an orientation of (100) was achieved through epitaxial growth on monocrystalline substrates such as R-sapphire.[25] This method gives homogeneous films on extended regions. However, a well defined mono-crystalline surface is required. This makes it difficult to fabricate an acoustic layer or an electrode below the ZnO, as these layers are usually amorphous or polycrystalline. Kadota *et al.* report on a shear wave transducer where a highly Al-doped ZnO layer is used as a bottom electrode, which keeps a suitable orientation.[26] However, the resistivity of such a layer is high ($3 \cdot 10^{-4}$ Ω.cm)

[24] N. F. Foster, *J. Appl. Phys.* **40**, 3887 (1969).
[25] Y. J. Kim, Y. T. Kim, H. K. Yang, J. C. Park, J. I. Han, Y. E. Lee, H. J. Kim, *J. Vac. Sci. Technol. A* **15**, 1103 (1997).
[26] M. Kadota, T. Miura, Jpn. J. Appl. Phys. **41**, 3281 (2002).

compared to metals (typically a few 10^{-6} Ω.cm) and electrical losses are considerable. The authors do not mention the coupling coefficient achieved with their method. It is expected to be very small, since the method in itself cannot guarantee an in-plane texture. Some articles also mention polycrystalline films on which ZnO tends to grow with the c-axis lying in-plane. Lehmann and Widmer obtained parallel orientation by sputtering ZnO on an indium tin oxide (ITO) on quartz substrate.[27] The orienting effect of the ITO films was attributed partly to some chemical reaction at the ZnO/ITO interface and partly due to a surface microstructure. The material makes ZnO grow with an in-plane orientation, but does not favour an in-plane texture. By tilting their substrates and sputtering the ZnO and ITO at the same oblique incidence of 45°, they obtained films with an in-plane texture and measured a coupling coefficient of 0.21. They also obtained inclined ZnO on Zn thin films, which provide suitable crystallographic conditions. However, Zn oxidizes easily after deposition making this solution difficult for practical applications. Moreover, they found that the resistivity of the ZnO films sputtered on Zn was very low so that they were not suitable for transducers. Veselov and Dzhumaliev, and Yanagitani *et al.* showed that ZnO can also grow with an in-plane c-axis on Al polycrystalline films.[28] However, since Al oxidizes very quickly in an O_2 environment such as air, they probably sputtered on a thin Al_2O_3 buffer-layer.

Another group of articles mention the deposition of inclined ZnO by **adding other materials to the growing film**. In one of the earliest articles, Foster found that the addition of small hydrocarbons in the Ar/O_2 atmosphere promotes crystallites with the c-axis aligned preferentially in the film plane.[29] Foster also needed an additional oblique incidence of the particles by tilting of the substrate to achieve in-plane texture. He obtained coupling coefficients of 0.12 to 0.18. He observed that the orientation of the films got worse with decreasing film thickness. The films less than 1 µm thick had a more random arrangement of the c-axis in the film plane. Foster used Au substrates, but the addition of hydrocarbons at the beginning of the process created an organic polymer film on which the ZnO tended to grow in parallel orientation. Wasa *et al.* co-sputtered Zn with small amounts of Al in an oxidizing atmosphere on SiO_2 and Au substrates.[30] The films showed (110) orientation with a relatively broad in-plane texture. It was thought that co-sputtered Al formed fine crystallites of Al_2O_3 that reduced the surface mobility of the ZnO particles at the substrates during film growth. This may have inhibited the growth of the normal orientation and enhanced the growth of the parallel one. Films without addition of Al were (002) oriented. Wasa *et al.* found coupling coefficients of 0.05 to 0.08 for ZnO films with thicknesses of 1 to 5 µm. These films had Al contents from 3.5 to 13 %.

3.3.2.2. Parameter influence and substrate position

Since the simple choice of the substrate or the incorporation of impurities into the film it not sufficient to achieve an inclined ZnO film with in-plane texture, additional mechanisms are needed. Some articles achieve this by adjustment of different sputtering parameters without tilting the substrate. Veselov and Dzhumaliev showed that it is possible to obtain inclined films **by adjusting the shape of the plasma**.[31] They inferred that

[27] H. W. Lehmann, R. Widmer, *J. Appl. Phys*. **44**, 3868 (1973).
[28] A. G. Veselov, A. S. Dzhumaliev, *Techn. Phys.* **45**, 497 (2000) ; Yanagitani, N. Mishima, M. Matsukawa, Y. Watanabe, *Proc. IEEE Ultrason. Symp.*, 1824 (2005).
[29] N. F. Foster, *J. Appl. Phys.* **40**, 3887 (1969).
[30] K.Wasa, S. Hayakawa, T. Hada, *IEEE Trans. Sonics. Ultrason.* **SU-21**,298 (1974).
[31] A. G. Veselov, A. S. Dzhumaliev, *Techn. Phys.* **45**, 497 (2000).

an inhomogeneity of the plasma caused an inhomogeneity of the density of sputtered particles, which explained the formation of an inclined texture through migration of the adatoms. They did neither measure the inclination nor the coupling coefficient of their films. Krishnaswamy *et al.* deposited 10° to 15° inclined ZnO on glass (Corning 7059) substrates placed about 1" radially off the target centre.[32] The obtained ZnO columns oriented towards the target centre. The variation of the inclination as a function of radial position was shown to be similar to the thickness variation. Perpendicular orientation was retained for films at the centre of the target and for films on CrAu substrates. ZnO/ITO/quartz films showed mixed orientation and the c-axis in-plane component was not preferential. They operated at as **low gas pressure** as possible (0.8 Pa at a 25 mm substrate-target distance) and with a floating substrate. They do not report about the obtained coupling coefficient. Other authors also report about the influence of the **substrate position** and the gas pressure. Kupranidhi and Sayer found that below a pressure of 10 mTorr the film orientation depends on the position of the substrates with respect to the target.[33] Jen *et al.* used 16° inclined films obtained with the Kupranidhi method to excite shear waves, but did not mention the obtained coupling coefficient.[34] The dependence of the orientation on the position is attributed to a nonuniform distribution of sputtered material as an inherent feature of magnetron sputtering due to the confinement of the plasma to a specific area of the target by the magnetic field. Again, this inhomogeneity is only retained at low pressures.

Some authors also report about the influence of **film thickness** on the orientation of the film.[35] It has been observed that as the films become thicker, c-axis orientation changes from normal to the substrate to parallel to the substrate, i.e. it changes from (002) to (101) to (110). The atomic packing density also decreases in this order. With the same idea, **high sputtering pressure** results in films with (100) and (110) orientation whereas a (002) orientation is favoured at low pressure, since (100) and (110) orientations need less energy for their formations.[36] For high pressures, there are more collisions between target and substrate and in consequence, the atoms have less energy. For both mechanisms however, the problem is that the in-plane texture is not controllable and an additional mechanism is needed, e.g. the positional dependence with respect to the target. This additional mechanisms are generally obtained at low pressure with a high mean free path, favouring the (002) orientation by enhancing the energy of the incoming atoms. Inclined films with in-plane texture can thus not be obtained by solely increasing the pressure or increasing the film thickness.

Two articles mention the influence of an **electrical field** on the growing ZnO film. In a series of articles in 1982 and 1983, Wang and Lakin reported the sputtering of 25° inclined ZnO on Si substrates.[37] A peripheral anode structure with a potential of 40 V was used to collect the electron current and prevent arcing to the substrate. The electric field distribution created by this anode was thought to have an apparent orienting effect on the growing film. When the wafer was tilted by 15°, the oblique incidence added inclination to the c-axis thereby reaching 40°. However, it is questionable if the electric field really had an influence. A particular distribution of particle fluxes between cathode and anode could also have been responsible for the

[32] S. V. Krishnaswamy, B. R. McAvoy, W. J. Takei, *Proc. IEEE Ultrason. Symp.,* 476 (1982).
[33] S. B. Kupranidhi, M. Sayer, *J. Appl. Phys.* **56**, 3308 (1984).
[34] C.-K. Jen, K. Sreenivas, M. Sayer, *J. Acoust. Soc. Am.* **84**, 26 (1988).
[35] Y. E. Lee, J. B. Lee, Y. J. Kim, H. K. Yang, J. C. Park, H. J. Kim, *J. Vac. Sci. Technol. A* **14**, 1943 (1996).
[36] M. B. Assouar, PhD Thesis, LPMIA, UHP Nancy I, p. 154 (2001);
[37] J. S. Wang, K. M. Lakin, *Appl. Phys. Lett.* **42**, 352 (1983); J. S. Wang, K. M. Lakin, *Proc. IEEE Ultrason. Symp.*, 480 (1982).

inclination. Furthermore, Wang and Lakin deposited films with a thickness of 2.8 µm and gave no indication of the quality of their films with lower thicknesses. They found a coupling coefficient of 0.17. Cerven *et al.* also proposed an influence of an electrical field on their films.[38] They mentioned an interaction of the electrical fields existing in the proximity of the substrate surface with the in-situ arising electrical dipoles in the films. The electrical fields were attributed to external voltages as well as self-induced charge on the film surface. However, they have not proved this suggestion.

3.3.2.3. Substrate tilting and oblique particle incidence

The vast majority of the articles mentioning inclined ZnO growth use the tilting of the substrate to achieve **oblique particle incidence** and inclined film growth. The mechanisms of inclined ZnO due to oblique particle incidence are reasonably well understood and will be presented in section 3.4.5. For ZnO, Foster showed for the first time in 1969 that a certain directivity of the incoming particles is essential for the control of the in-plane texture of his 90° inclined films.[39] Since then, a couple of articles explain how inclined ZnO can be obtained by oblique particle incidence using the tilting of the wafer.

By tilting their wafer by 15°, Wang and Lakin added 15° of inclination to their 25° inclined films, thereby reaching an inclination of 40°.[40] Lehmann and Widmer obtained parallel orientation by rf bias sputtering ZnO on an indium tin oxide (ITO) / quartz substrate.[41] By tilting their substrates and sputtering the ZnO and ITO at the same oblique incidence of 45°, they obtained films where the (100) planes were parallel to the substrate plane within ±5° and c-axes were aligned parallel to the target within ±20°. With these films, Lehmann and Widmer achieved coupling coefficients of 0.21. Howell *et al.* deposited ZnO on Si (111), Al_2O_3 and SiO_2 substrates. They inclined their substrates by 40° but studied also the dependence on the distance from target centre.[42] ZnO films of samples positioned at outer radius (1.5") were oriented by 40°. Samples at 0.5" radius were oriented by 10-20°. For films sputtered on TiAu, the c-axis was normal over a range of tilts from 0° to 60° and reached 20° for wafer-tilts near 80°. They did not report about the obtained coupling coefficient. Lee et *al.* investigated the effects of oblique sputtering on micro structural modification of ZnO films.[43] By tilting their SiO_2 substrates from 0° to 90°, they obtained films with (002) orientation at low tilt angles and with (101) orientation at high tilt angles, i.e. inclinations of 62°. They did not excite shear waves with their films. Cerven *et al.* sputtered 1.5 µm ZnO films on TiN and SiO_2 covered Si wafers which have been tilted by 0° to 60° degrees. They obtained c-axis inclinations from 0.4° to 6.6° respectively, confirming the fact that the inclination increases with the tilt angle. However, they observed a tilt in opposite direction to the incoming particle flux. As mentioned above, they also mentioned an interaction of the c-axis with electrical fields. They did not report about the obtained coupling coefficient.[44] Recently, Yanagitani *et al.* obtained completely inclined (90°) in-plane textured films using oblique incidence at 30°.[45] They

[38] I. Cerven, T. Lacko, I. Novotny, V. Tvarozek, M. Harvanka, *J. Cryst. Growth* **131**, 546 (1993).
[39] N. F. Foster, *J. Appl. Phys.* **40**, 3887 (1969).
[40] J. S. Wang, K. M. Lakin, *Appl. Phys. Lett.* **42**, 352 (1983).
[41] H. W. Lehmann, R. Widmer, *J. Appl. Phys*. **44**, 3868 (1973).
[42] D. Howell, L. Goddard, B. T. Khuri-Yakub, *Proc. IEEE Ultrason. Symp.*, 381 (1987); M. D. Howell, S. Akamine, L. J. LaComb, B. Hadimioglu, T. R. Albrecht, B. T. Khuri-Yakub, L. C. Goddard, T. E. Carver, *Proc. IEEE Ultrason. Symp.*, 677 (1988).
[43] Y. E. Lee, S. G. Kim, Y. J. Kim, H. J. Kim, *J. Vac. Sci. Technol. A* **15**, 1194 (1997).
[44] I. Cerven, T. Lacko, I. Novotny, V. Tvarozek, M. Harvanka, *J. Cryst. Growth* **131**, 546 (1993).
[45] Yanagitani, N. Mishima, M. Matsukawa, Y. Watanabe, *Proc. IEEE Ultrason. Symp.*, 1824 (2005).

obtained a coupling coefficient of 0.24 using substrates covered by Al. Their substrate was set behind a glass window and moved forward and backward using a vacuum motorized stage during sputtering deposition to obtain ZnO films with uniform thickness.

TABLE 3.2
REVIEW OF C-AXIS INCLINED ZNO DEPOSITION IN LITERATURE

Method	Author* (year)	Substrate material (area)	Inclination (thickness)	Coupling coefficient K **	Remarks
Mono crystalline substrate	Kadota (2002)	R-Sapphire (~5 × 5 mm^2)	90° (2.9-6.8 µm)	n.a.	ZnO film with low resistivity (Al-doped) as bottom electrode.
	Kim (1997)	R-Sapphire (n.a.)	90° (n.a.)	n.a.	Change from (002) polycrystalline to (110) epitaxial by adjustment of power and pressure.
Incorporation of other materials	Wasa (1974)	SiO_2, Au (<10 × 10 mm^2)	90° (1-5 µm)	0.05-0.08	Al added; (110) orientation achieved, but broad
	Foster (1969)	Au (n.a.)	90° (0.25-2 µm)	0.06-0.18	Hydrocarbons added. Tilting necessary for in-plane texture.
Parameter influence	Veselov (2000)	Al (∅ 60 mm)	n.a. (n.a.)	n.a.	Negative Glow Region influenced by Magnetron.
	Krishnaswamy (1982)	ITO, SiO_2 (n.a.)	10-15° (0.3-0.9 µm)	n.a.	No inclination seen on CrAu. Low pressure needed.
	Jen (1988) Krupanidhi (1984)	SiO_2 (n.a.)	16° (6 µm)	n.a.	SM and LM excited simultaneously.
	Wang (1983) (1982)	Si (100) (∅ 2")	25° and 40° (2.8 µm)	0.17	Influence from an additional anode. Additional tilting of 15° brings 40° inclination.
Oblique substrate	Howell (1987) (1988)	Si (111), Al_2O_3, SiO_2 (~∅ 1")	10°-40° (n.a.)	n.a.	Inclination also studied in function of distance from target centre. No inclination on TiAu.
	Lehmann (1973)	ITO, Zn (<10 × 10 mm^2)	~90° (1-3 µm)	0.21	ITO makes ZnO grow with parallel orientation, tilting is needed for parallel alignment.
	Cerven (1993)	SiO_2, TiN (n.a.)	0.4°-6.6° (1.5 µm)	n.a.	Tilt of 0° to 60°. Inclination opposite to incoming flux. Possible electrical effect.
	Lee (1997)	SiO_2 (n.a.)	62° (3-4 µm)	n.a.	Tilt of 0° to 90°. Investigation of film morphology.
	Yanagitani (2005)	Al, Cu (10 × 25 mm^2)	90° (5.5-9.8 µm)	0.24	Homogeneous film thickness due to substrate moving.

** see footnotes on the previous pages to obtain complete reference.*
*** coupling coefficient for shear wave mode generation*

3.3.2.4. Overview

Table 3.2 gives an overview over the methods described in the previous sub-sections. Some authors obtain very high inclinations with good orientations and sometimes outstanding piezoelectric properties, with coupling coefficients K nearing the theoretical limit of 0.32.[46] However, all these results must be handled with caution. First, it is important to consider the **area** of the substrates used in these articles. In this work,

[46] See section 2.3.2 or N. F. Foster, G. A. Coquin, G. A. Rozgonyi, F. A. Vannatta, *IEEE Trans. Sonics Ultrason.* **SU-15**, 28 (1968).

the primary aim was to develop a deposition method for 4" to 6" wafers. Most of the methods presented above, especially those requiring a tilting of the substrate, are not realizable in standard sputtering equipment with 4" wafers. For example, Yanagitani *et al.* used a substrate size of only 10 mm × 25 mm. Another critical point to consider in the articles is that many authors do not give an indication of the **coupling coefficient** they obtain. Since the grains in the films can be of opposite polarity, the resulting coupling coefficient can be significantly lower than the theoretical value. Finally, it has been shown in literature that generally the orientation of the grains, i.e. the FWHM of the XRD peak, and by that also their piezoelectric activity (coupling) gets better with increasing **film thickness**. [47] Generally, the films mentioned in the articles are rather thick, in the order of a few µm, whereas the films projected in this work have thicknesses of less than 500 nm.

3.3.3. Process requirements and planning

The aim in this work was to **obtain c-axis inclined ZnO as fast as possible** in order to fabricate solidly mounted shear wave mode FBARs and test them in liquid environments. Another requirement was to **use the existing planar wafer charging system**, so that the sputter chamber would not have to be pumped down after each process, giving a process-time gain and allowing the use of standardized systems. Yet another necessity was to **use at least 4" wafers**, which in the best case should have an inclined c-axis on the whole surface, so that the yield per wafer is maximized.

The only methods relevant to our research were the ones where ZnO could be **deposited on polycrystalline or amorphous films**, since the planned solidly mounted FBARs needed acoustic mirrors and bottom electrodes below the ZnO. This excludes the sputtering on monocrystalline substrates. Methods which incorporate other materials into the growing film were also excluded, since this was technically more difficult in the available sputtering equipment and also since the influence of such impurities on the piezoelectric properties was not predictable. Moreover, as was seen in the previous section, these methods need additional adaptation of the sputtering parameters or inclination of the substrate to ensure an in-plane texture of the film.

From the literature review of the previous section, one concludes that the most rapid way to get inclined ZnO with in-plane preferred orientation is oblique particle incidence. On one hand it promotes the c-axis inclination in χ direction, and on the other hand it favours an in-plane orientation in φ direction. Both required effects are combined in a single process. Even methods using appropriate buffer-layers and the incorporation of other materials need this oblique incidence in order to orient the c-axis in-plane. During this work this oblique particle incidence by **tilting of the substrate** has first been tried. Inclinations up to 15° were obtained on Si substrates covered by amorphous oxide layers. However, the resulting film thickness was very inhomogeneous and moreover, the samples had only a maximum size of 20 mm × 20 mm, due to geometric limitations of the sputtering equipment. Additionally, the standard charging system could not be used. Since these results were not compatible with the requirements, the substrate tilting method was not furtherly pursued.

[47] F. Martin, P. Muralt, M.-A. Dubois, A. Pezous, *J. Vac. Sci. Technol. A*, **22**, 361 (2004).

Three different processes to deposit c-axis inclined ZnO films have been investigated in greater detail and will be exposed in paragraphs 3.4, 3.5 and 3.6 respectively. **PROCESS I** uses the regular sputtering setup with adapted sputtering parameters and without additional modification of the equipment. Although it finally gave good results, at the time of its development, a second process looked more promising and was investigated more intensively. **PROCESS II** uses additional blinds which are positioned between the substrate and the target. The obtained films were utilized for further development of complete solidly mounted FBARs and their application in liquid environments, as described in Chapter 4 and Chapter 5. Both PROCESS I and PROCESS II gave inhomogeneous films. **PROCESS III**, whose development began 6 months before the end of this thesis, builds on the results of PROCESS II to obtain homogeneous films on large surfaces with good piezoelectric properties. In the following paragraphs, only the 26 wafers useful for the comprehension and analysis of the processes are described. In total around one hundred 4" and 6" wafers were processed.

a) *b)*

Figure 3.4 : a) Photograph of the DC-pulsed reactive magnetron sputtering equipment from Von Ardenne Anlagentechnik CS730S utilized in this work. At the front, the handler chamber with the glass top, at the back, the sputter process chamber. b) Photograph of the inside of the sputtering chamber showing 4 targets.

3.4. PROCESS I: no chamber modification

3.4.1. Description of the sputtering equipment

All processes were realized in a conventional DC-pulsed magnetron sputtering equipment. The model used is a CS730S from *Von Ardenne Anlagentechnik*, Dresden, Germany. A picture of the equipment is shown in Figure 3.4. It allows the development and production of metallic and dielectric films in a single sequence under vacuum. Substrates **up to 6"** can be processed. The equipment has a handler chamber with a separate high-vacuum pumping system and four intermediate storing positions. Inside the process chamber, 4 different 8" targets can be installed. The substrates are positioned on a rotary table of 630 mm diameter with space for 4 wafers and rear-side heating. A high-vacuum pumping system assures the correct pressure. O_2 and Ar process gases are available. The whole equipment can be controlled by an operating system.

3.4.2. Basic starting process: deposition on Pt electrodes

The starting point for the development of the inclined layers was an already established process developed at CT MM2.[48] This process yields (002) c-axis oriented films with good quality. The parameters summarized in Table 3.3 were found to be optimal for ZnO deposition in terms of crystalline orientation, residual stress, resistivity and film thickness homogeneity. The main development steps are briefly summarized in the following lines.

The ZnO thin films were deposited reactively from an 8" 99.995 % pure Zn target in an Ar/O_2 ambient. During the development of this process in 2001, a series of films were sputtered on silicon wafers coated with (111) oriented Pt thin films forming the bottom electrode of future FBARs. Different process parameters that were expected to influence the film properties were varied like heater temperature, pressure and gas composition. Nearly stoechiometric films were found for the whole temperature range from 280°C to 530°C. Low process temperatures and low pressures increased the compressive stress in the film. A permittivity of about 10 was found. Measurements confirmed that the ZnO films had a sufficiently high resistivity for high frequency applications such as for FBARs at about 1 GHz.

TABLE 3.3
SPUTTERING PARAMETERS OF INITIAL PROCESS FOR ZNO FILMS WITH C-AXIS ORIENTATION

Parameter Description	Parameter value
Discharge power	500 W, pulsed DC
Temperature	280°C
Pressure	0.4 Pa (O_2+Ar)
Sputtering rate	~60 nm/min

The films grow with a **(002) orientation independent of the sputtering parameters**. The high crystalline orientation of the film (Rocking curve FWHM of ~2.5 °) was expected since the (002) orientation will preferentially be formed on any substrate.[49] This is well understood since the c-plane of the ZnO crystallites corresponds to the densest packed plane (see section 3.2.3). Another effect may also have an influence: ZnO can easily grow in (002) direction on Pt (111) because of the given hexagonal template of the Pt. The Pt-Pt distance in the (111) Pt plane, 2.77 Å, correspond grossly to the in-plane lattice constant (a-axis) in the (002) ZnO plane, 3.24 Å. The a-axis of ZnO is only 16.8% bigger than the lattice constant of Pt (111), which according to literature is low enough to allow for an epitaxial influence.[50]

The piezoelectric activity of the films was assessed by depositing ZnO films on substrates covered by an acoustic mirror to realize solidly mounted FBARs, whose fabrication and characterization will be given in Chapter 4. The over-modes characterization method described in paragraph 2.6 was not available at that

[48] The development of this process is described in: N. Hdadach, Internship report, Siemens/Ensil (2001).
[49] H. W. Lehmann, R. Widmer, *J. Appl. Phys.* **44**, 3868 (1973).
[50] S. V. Krishnaswamy, B. R. McAvoy, W. J. Takei, *Proc. IEEE Ultrason. Symp.*,476 (1982).

time. Since the films did not show a c-axis inclination, only longitudinal modes could be excited. By fitting the impedance characteristic on a BVD model, longitudinal coupling coefficients K_L of about 0.23 were found, which corresponds to 85 % of the maximum achievable value.

3.4.3. Experimental: deposition on amorphous buffer-layers

In this work, it was first tried to obtain inclined ZnO by applying some changes to the existing process. It is known from literature that by adapting the sputtering parameters correctly, inclined ZnO can result at certain points with respect to the target.[51] Krishnaswamy *et al.* obtained no inclination at the centre of their target, but an inclination of 10° to 15° at a distance of 35 mm. However, they used a substrate of less than 2" diameter.[52] In 2004, Bjurström *et al.* obtained AlN thin films with inclinations varying from 0° at the centre of a 4" wafer to 16° near the border at a distance of 35 mm from the centre.[53] Very recently, they presented a ameliorated method were they obtained inclinations of up to 32 ° at the border with a small exclusion zone in the middle of the wafer, where no inclinations were recorded.[54] As will be explained later, the reason for inclined film growth can be attributed to an **asymmetric deposition flux**.

6" Si (100) wafers were used, since it was expected that the effect of asymmetric sputtering would be biggest at a higher distance of the centre of the target. The wafers were first covered with a 100 nm thick Pt thin film, which would later function as a bottom electrode to the FBARs. To decouple the crystallographic influence of the Pt thin film on the growing ZnO film, amorphous buffer-layers were then deposited onto the bottom electrode. A similar solution was chosen by Bjurström *et al.* who report about a two-stage process in which a low-texture film is deposited prior to the inclined AlN, or by Krishnaswamy *et al.* who deposit a thin ITO film on a CrAu bottom electrode. In this analysis, **quasi-amorphous SiO_2 and Al_2O_3 buffer-layers** with thicknesses varying from 100 nm to 300 nm were used. The SiO_2 layers were deposited by CVD with a Multiplex Cluster System from *STS*, Newport, UK. The Al_2O_3 layers were sputtered using a *Perkin Elmer* PE 2400, Palo Alto (CA), USA. Since the roughness of the substrate is important for film growth, an AFM characterization of the bottom-electrode and the buffer-layers was done. Figure 3.5 shows the recorded AFM pictures.[55] The Pt bottom electrode thin film had a rms-roughness of less than 5 Å. Both the SiO_2 and the Al_2O_3 films had a roughness of about 6.5 Å, which is very low but typical for amorphous films. They exhibit a different morphology, the SiO_2 film having bigger grains.

The 400 nm ZnO thin films were deposited reactively with the equipment described in section 3.4.1. The distance between target and substrate was around 60 mm. The sputtering chamber was pumped down to $1 \cdot 10^{-6}$ Pa prior to introduction of Ar and O_2 gas. The Zn target was presputtered during 15 min. Table 3.4 summarizes the stack and sputtering properties of the most relevant samples of PROCESS I.

---

[51] A. G. Veselov, A. S. Dzhumaliev, *Techn. Phys.* **45**, 497 (2000); S. V. Krishnaswamy, B. R. McAvoy, W. J. Takei, *Proc. IEEE Ultrason. Symp.*,476 (1982); M. D. Howell, S. Akamine, L. J. LaComb, B. Hadimioglu, T. R. Albrecht, B. T. Khuri-Yakub, L. C. Goddard, T. E. Carver, *Proc. IEEE Ultrason. Symp.*, 677 (1988).
[52] S. V. Krishnaswamy, B. R. McAvoy, W. J. Takei, *Proc. IEEE Ultrason. Symp.*, 476 (1982).
[53] J. Bjurström, D. Rosén, I. Katardjiev, V. M. Yanchev, I. Petrov, *IEEE Trans. Ultrason., Ferroelec., Freq. Contr.* **51**, 1347 (2004).
[54] J. Bjurström, G. Wingqvist, I. Katardjiev, *Proc. IEEE Ultrason. Symp.*, 321 (2005).
[55] The pictures were treated with a freeware program from Nanotec Electrónica : WSxM© ; http://www.nanotec.es

TABLE 3.4
RELEVANT ZNO FILMS WITH DIFFERENT PROCESS PARAMETERS FOR PROCESS I DEVELOPMENT

Sample number	Buffer-layer material	Pressure	Temperature	Power	Maximum Inclination
PIa	300 nm SiO_2	0.4 Pa	280°C	100W	7.3°
PIb	100 nm SiO_2	0.4 Pa	280°C	100W	11.9°
PIc	300 nm SiO_2	0.4 Pa	150°C	100W	8.8°
PId	300 nm SiO_2	7 Pa	150°C	500W	0.7°
Pie	300 nm Al_2O_3	0.4 Pa	280°C	100W	25.2°
PIf	100 nm Al_2O_3	0.4 Pa	100°C	100W	11.5°
PIg	100 nm Al_2O_3	0.4 Pa	150°C	100W	3.6°

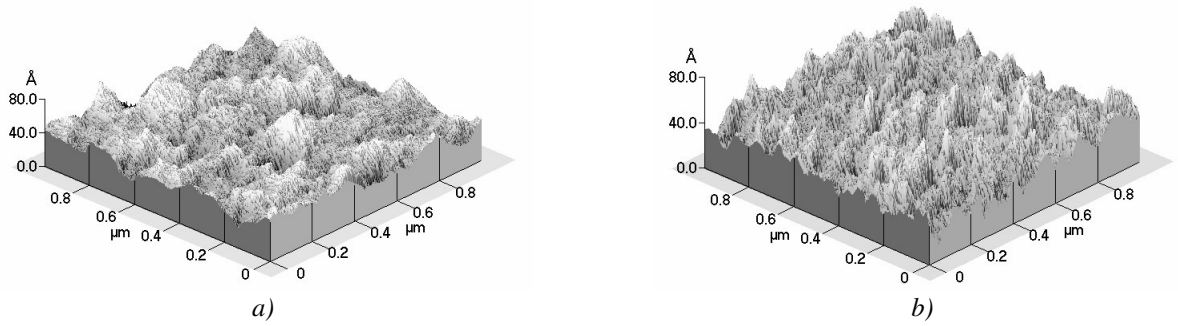

Figure 3.5 : AFM pictures for different buffer-layers: a) CVD deposited SiO_2 with roughness of 7.12 Å and b) sputtered Al_2O_3, with roughness of 6.42 Å; both are deposited on Pt with an rms-roughness of less than 5 Å.

3.4.4. Results and discussion

3.4.4.1. Films sputtered on SiO_2 buffer-layers

The films sputtered on **SiO_2 buffer-layers** were first analyzed by XRD. θ-2 θ scans have confirmed that the films grow preferentially with a (002) orientation. χ-scans have permitted to obtain the c-axis inclination angle. Figure 3.6 shows the obtained c-axis inclination and FWHM values for samples PIa, PIb, PIc and PId. Both are plotted with respect to the distance towards the centre of the substrate. The maximum obtained inclination is reported in Table 3.4. Figure 3.7 a) shows a typical recorded 2D detector image. Both the c-axis inclination and the FWHM were obtained by fitting a Gaussian response on the XRD curve. In the majority of cases, the fit is accurate enough. An example of a fit is given in Figure 3.7 b). The proportion N(χ) of grains with an orientation χ is then given by:

$$N(\chi) = \frac{1}{\sigma\sqrt{2\pi}} \exp\left[-\frac{(\chi-\mu)^2}{2\sigma^2}\right] \qquad (3.2)$$

assuming a Gaussian distribution with an average μ and standard deviation of σ. The standard deviation and the FWHM of the peak are related:

$$2\sigma = \frac{\mathrm{FWHM}}{\sqrt{2\ln 2}} \approx 0.849 \cdot \mathrm{FWHM} \tag{3.3}$$

For samples PIa, PIb and PIc the inclination **increases gradually with increasing distance** from the wafer centre, confirming observations in literature. The **c-axis inclines in the direction of the wafer centre**. PIa and PIb were both sputtered with similar sputtering conditions than those of the basic process to obtain c-axis oriented films. The only difference was that the power was lowered to 100 W and the pulse width increased to reduce arcing problems. The sputtering rate was reduced to around 7.1 nm/min.

As can be seen on Figure 3.6, inclinations of up to 11.9° were measured in the border region of the 6" wafers for PIb sputtered on 100 nm SiO_2. It has slightly higher inclinations than PIa with a buffer-layer thickness of 300 nm, where the maximum inclination is only 7.3°. PIb also has higher FWHM values, indicating a higher spread of the inclinations in the different grains. Since the sputtering conditions were the same, the substrate surface, i.e. the SiO_2 buffer-layer surface must have been slightly different (roughness).

For sample PIc sputtered at a lower temperature of 150°C, the inclination is slightly higher than for PIa. Since the other sputtering conditions and the buffer-layer were the same, one can assume that **a lower temperature increases the inclination**. The higher inclinations are accompanied by a higher FWHM. Sample PId was sputtered at a higher pressure of 7 Pa. At this pressure, the MFP becomes very small and the particles experience many collisions on the way from the target to the substrate. As can be seen, there is no inclination of the c-axis. Additionally, the FWHM is very high, which can be explained by the fact that the particles arrive from all directions on the substrate and do not diffuse very much due to the low temperature.

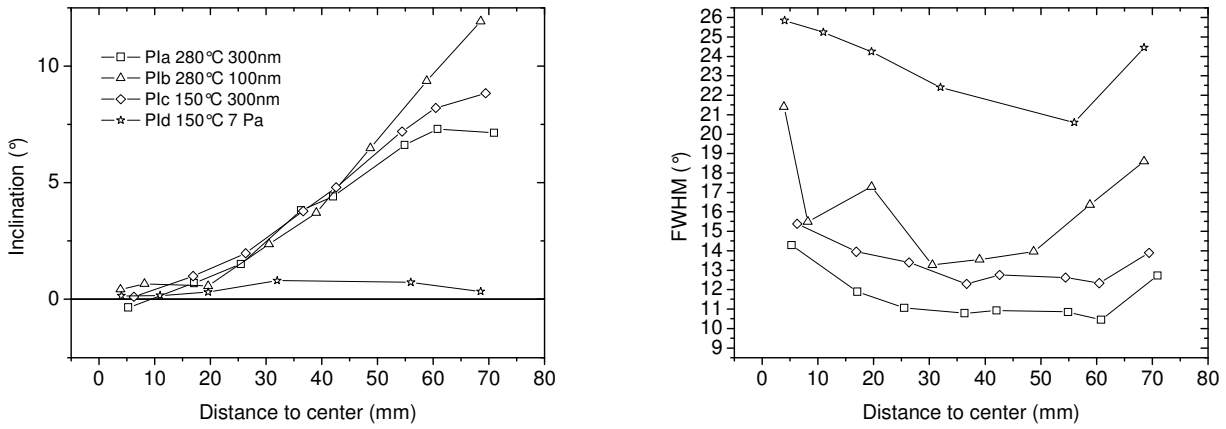

a) *b)*

Figure 3.6 : C-axis inclination (a) and FWHM (b) as a function of the distance towards the centre of the wafer for PROCESS I with different parameters on SiO_2 buffer-layers.

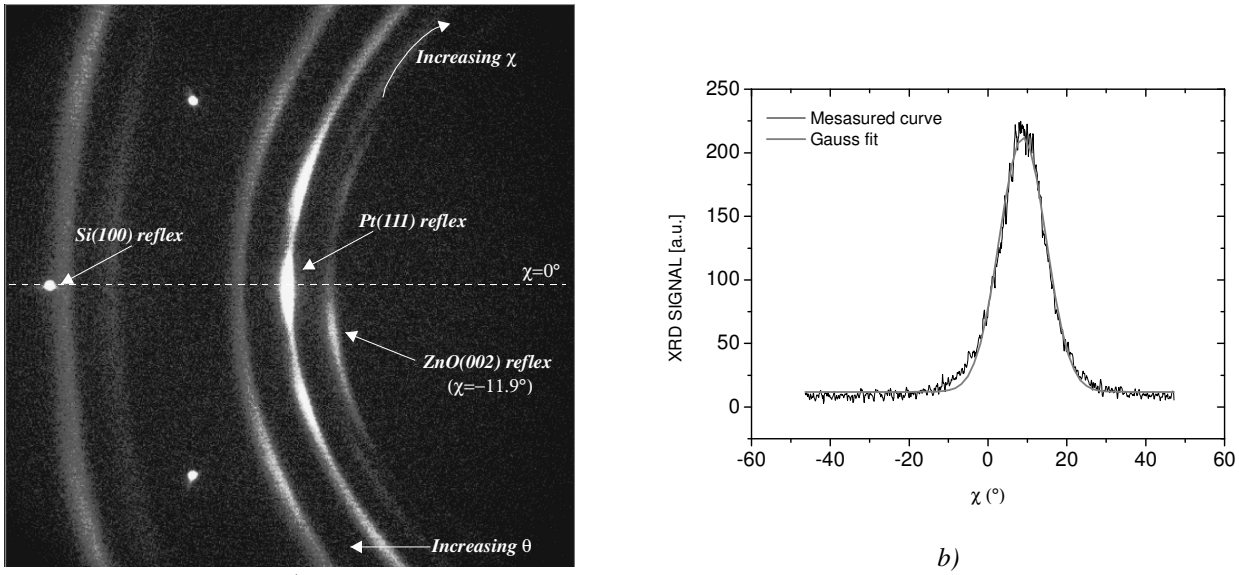

Figure 3.7 : a) Typical XRD 2D detector image with the dashed line representing χ=0° and b) χ-scan with Gaussian fit curve for the point with the highest inclination of -11.9° of sample PIb at around 70 mm from the wafer centre.

3.4.4.2. Films sputtered on Al_2O_3 buffer-layers

The wafers where ZnO was sputtered **on Al_2O_3 buffer-layers** were analyzed in a similar way. Figure 3.8 shows the inclination and FWHM with respect to the distance to the wafer centre for samples PIe, PIf and PIg. The inclination increases again with increasing distance to the centre of the wafer up to a maximum inclination at the border. PIe, which was sputtered at the same conditions than PIa and PIb, boasts the highest inclinations, reaching about 25° at a distance of 70 mm from the wafer centre. This is much higher than the inclinations reached with sample PIa, indicating that the Al_2O_3 buffer-layer is better suited. The FWHM values are also much higher.

Samples PIf and PIg were both sputtered on 100 nm Al_2O_3, at different lower temperatures. Interestingly, the inclinations recorded for both of these wafers are smaller than for sample PIe, which would indicate that a thicker Al_2O_3 buffer-layer favours higher inclinations. However, the high inclinations of PIe could not be repeated in following experiments. This could be explained by the unreliable functioning of the PE 2400. As a matter of fact, although the nominal sputtering conditions were the same, the buffer-layer of PIe was sputtered at around 1.75 nm/min, while the buffer-layers of sample PIf and PIg for example, were sputtered at around 2 nm/min. A higher sputtering rate could imply a higher heating of the substrates. Generally, a higher temperature goes along with a smoother surface. It was not possible to measure the roughness of the Al_2O_3 after ZnO deposition and afterwards, the sputtering rate stayed at around 2 nm/min.

From Figure 3.8 it can be recognized that sample PIf, sputtered at 100°C, has higher inclinations than sample PIg, sputtered at 150°C. The Al_2O_3 buffer-layers used for both wafers were sputtered one after another with the same nominal sputtering conditions and the same sputtering rate. It can be assumed that they have a similar surface. Thus, the difference in inclinations must stem from the fact that PIf was sputtered at a lower temperature, confirming what was seen with the SiO_2 buffer-layers. However, the inclinations recorded for

PIg are extremely small, and an additional influence by the buffer-layer cannot be excluded. The FWHM values increase with increasing inclination values.

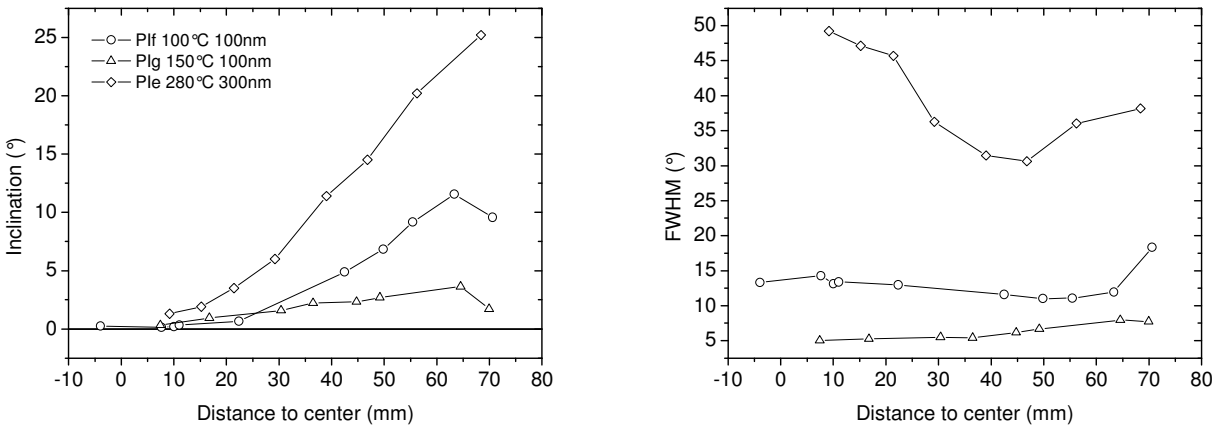

a) *b)*

Figure 3.8 : C-axis inclination (a) and FWHM (b) as a function of the distance towards the centre of the wafer for Process I with different parameters on Al_2O_3 buffer-layers.

3.4.4.3. Piezoelectric characterization

To characterize the **piezoelectric activity** of the films, a 100 nm top Pt electrode was added on the stack and structured with a simple photolithographic process. In that way, highly over-moded FBARs were realized. The bottom electrode served as electrical ground plane, and the top electrode was patterned in a ground-signal-ground configuration. The active device area was 200 µm × 200 µm. Unfortunately the wafers were not double polished so that an extraction of the electromechanical coupling coefficient such as described in section 2.6.3, was not possible. However the recognition of the excited wave mode was possible by calculating the spacing of the over-modes. Figure 3.9 a) shows the recorded phase broadband characteristics of samples PIg and PId, for two points at the centre and at the border of the wafer. **Although the resonance characteristics show up in both the magnitude and phase of the impedance, only the phase is shown in subsequent plots for convenience**. Both samples did not exhibit significant c-axis inclinations, so that it is expected that only longitudinal mode is excited. For PIg, there are some resonances occurring at a frequency of 3 GHz, and for PId, they occur at around 1.4 GHz and around 3.2 GHz. Simulations using the Mason Model show that these resonances correspond to the fundamental longitudinal mode for sample PIg, and the fundamental and first over-mode for sample PId. The wave mode is confirmed by a narrow-band look at these resonances. For example, Figure 3.9 b) shows the over-modes for sample PId at 1.4 GHz. The measured spacing between resonances is about 5.88 MHz, corresponding to an acoustic velocity of 7941 m/s in the substrate. This is close to the theoretical value of 8433 m/s of the longitudinal mode acoustic velocity in (100) Si (see Table 2.2).

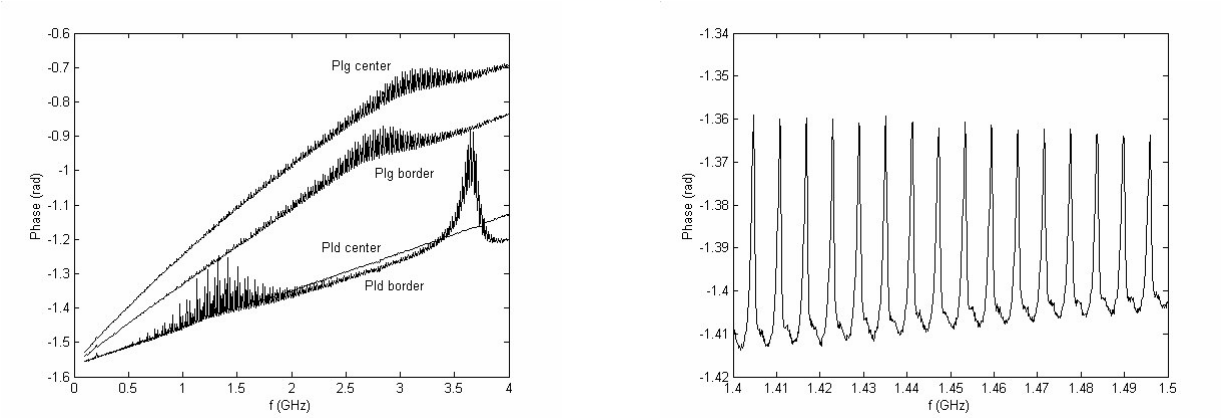

a) *b)*

Figure 3.9 : a) Broad-band characteristic of the impedance phase for sample PId and PIg for two points lying at the centre and at the border of the wafers and b) Narrow-band characteristic for PId.

Samples PIf and PIa with 300 nm SiO_2 buffer-layers exhibit maximum inclinations of approximately 10°. Figure 3.10 a) shows the recorded broadband characteristics for two points at the centre and at the border of the wafer. Longitudinal mode (LM) and shear mode (SM) peaks are seen. As expected, the shear mode peaks appear only at the border of the wafer where the c-axis is inclined. For sample PIa, the first shear over-mode resonance can be seen. The resonance modes have also been confirmed with narrow-band measurements. For example, Figure 3.10 b) shows a narrow-band view from sample PIf where a spacing of 4.17 MHz can be recognized. This corresponds to an acoustic velocity of 5625 m/s in the substrate, which is close to the theoretical shear mode velocity of 5845 m/s in (100) Si.

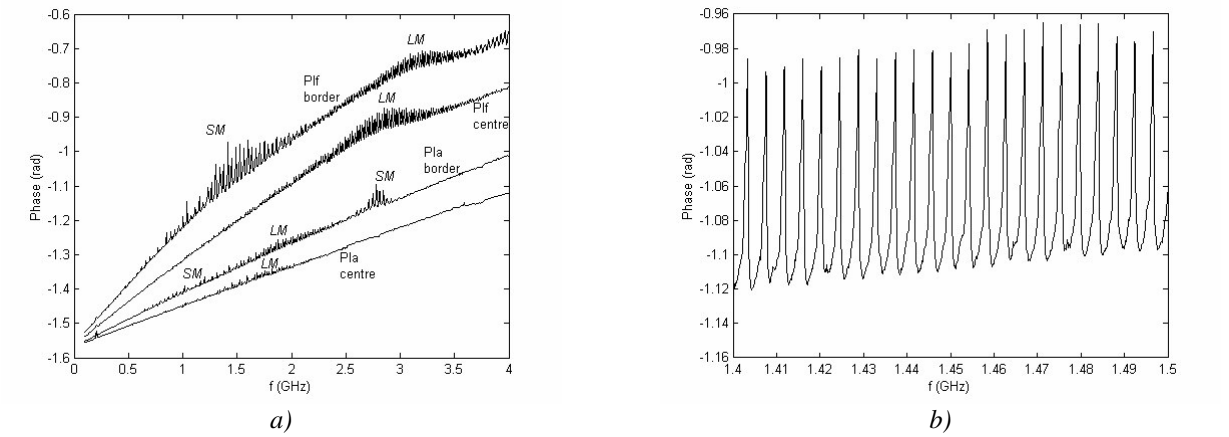

a) *b)*

Figure 3.10 : a) Broad-band characteristic of the impedance phase for sample PIa and PIf for two points lying at the centre and at the border of the wafers and b) Narrow-band characteristic for PIf.

Interestingly, the remaining three samples PIb, PIc and PIe show only very weak resonances or no resonance at all, neither shear nor longitudinal. This could be due to an average zero polarity of the films, meaning that there is an equal number of grains with the O-plane on the surface than with the Zn plane on the surface. No

net polarity results in zero effective electromechanical coupling.[56] For sample PIe, with the highest inclinations, another effect could be responsible. As can be seen on Figure 3.8 b), the FWHM can reach values as high as 50°. This can considerably lower the effective coupling coefficient, reaching such low values that no waves are excited (see section 3.5.5). Moreover, the buffer-layer also decreases the effective coupling coefficient, since it acts like an additional capacitance in between the exciting electrodes (see Chapter 4). These three samples clearly show that a c-axis orientation and inclination alone does not guarantee a piezoelectric activity in the film.

3.4.5. Explanation: oblique particle incidence and inclined film growth

3.4.5.1. Oblique particle incidence, simulations

The inclined growth can be attributed to an **asymmetric particle flux** in the border regions of the wafer. The results are comparable to those found by Krishnaswamy *et al.* in 1982. They deposited 10° to 15° inclined ZnO on glass substrates placed about 25 mm radially off the target centre.[57] As with our samples, the c-axis inclined towards the target centre. Similarly, perpendicular orientation was retained for films at the centre of the target. They explained the inclination of their films by referring to substrate **self-bias potential** and **bombardment effects** for magnetron sputtered ZnO films. In 2000, Veselov and Dzhumaliev also indirectly observed a c-axis inclination by exciting shear-waves at the border of 3" amorphous quartz substrates.[58] They explained this inclination by the control of charged particle fluxes which, depending on the negative glow region of their plasma, were incident normally or at an angle to the substrate. In their opinion, the "irregular-in-density" flux of particles bombarding the substrate produced a **temperature gradient** along its radius. This gradient caused the adatoms to migrate from an area with an elevated density of incident particles to an area where the density was reduced, which would explain the inclined-texture regions. They also mention the fact that the net particle flux in the centre of the wafer would be incident to the substrate at right angle producing non-inclined films. They referred to a recombination zone, where particles recombine on the way to the substrate. Outside this recombination zone, only ordinary perpendicular oriented texture is formed. To our opinion, the height of this recombination zone corresponds to the MFP. After that distance, the particles will have experienced a collision with other atoms thereby cancelling the irregular flux. This explains the missing inclination for sample PId sputtered at 7 Pa with a small MFP.

A recent explanation for the inclined film growth was given by Bjurström *et al*.[59] With AlN sputtering they found an inclination increasing from the centre of the 4" wafer towards the border. They obtained maximum c-axis inclinations of around 30°. They explained that the net flux direction varies across the radius of the substrates, attributing this to the fact that in magnetron systems, the sputtered flux is predominantly emanated from a circular race-track. For the centre region of the wafer, the net flux is perpendicular, since it is at equal distance from the erosion race-track. The farther the receiving point is from the centre, the higher the **asymmetry of the deposition flux** becomes. If the sputtered particles experience very few collisions in

[56] J. G. E. Gardeniers, Z. M. Rittersma, G. J. Burger, *J. Appl. Phys.*, **83**, 7844 (1998).
[57] S. V. Krishnaswamy, B. R. McAvoy, W. J. Takei, *Proc. IEEE Ultrason. Symp.*, 476 (1982).
[58] A. G. Veselov, A. S. Dzhumaliev, *Techn. Phys.* **45**, 497 (2000).
[59] J. Bjurström, G. Wingqvist, I. Katardjiev, *Proc. IEEE Ultrason. Symp.*, 321 (2005).

the plasma, this initial asymmetry is retained at the substrate, resulting in an **oblique incidence angle and c-axis inclined film growth**. This explanation reflects best the situation for our equipment. As shown schematically on Figure 3.11, the net particle flux is inclined at the border of the target, resulting in inclined film growth. At a pressure of 0.4 Pa and a temperature of 200°C, the MFP is around 6 cm, which is equal to the target-substrate distance. The initial asymmetry is thus retained at the substrate.

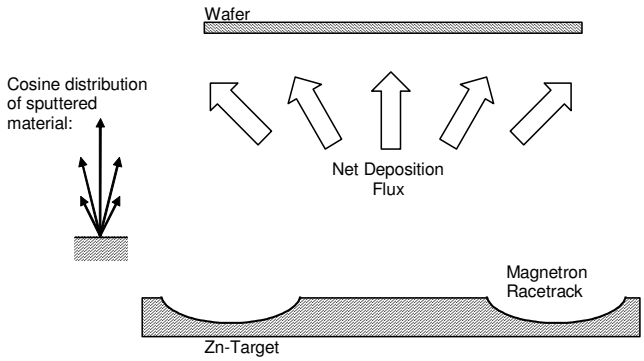

Figure 3.11 : Schematic of the substrate and target showing the direction of the net deposition flux of sputtered particles for low pressure processes. The inclination of the flux on the border of the substrate is due to the magnetron racetrack and the cosine distribution of sputtered material.

Simulations have been performed using MATLAB to verify this last explanation geometrically. The target and the substrate have been divided in a grid of equally distant points. As discussed in 3.2.2, the particles leave the target with a **cosine distribution,** which has been assumed for every point of the target. The particle trajectories have then simply been extended towards the substrate. The mean incidence angle has been calculated for each point of the substrate by looking at how many particles arrive from what direction. The target erosion race-track due to the magnetron has been taken into account by increasing the number of particles in that zone. Starting from the centre no sputtering occurs up to a radial distance of 50 mm. Afterwards the sputtering increases up to a distance of around 75 mm then decreases again to the target border, which defines the characteristic erosion track. The increase and decrease have been approximated linearly in the simulations. The sputtering profile is shown in Figure 3.12 a). A simulation neglecting the magnetron was also run, i.e. with the same amount of particles emanating from all points of the target.

The simulations confirm that an oblique incidence can be obtained. It increases with increasing distance to the centre of the substrate as shown on Figure 3.12 b). The c-axis points towards the centre of the wafer. At a distance of 50 mm from the centre corresponding to the border of a 4" wafer, a mean incidence of about 30° has been simulated. This result has been cross-checked by researchers at Uppsala University.[60] For a 6" wafer, incidence angles of 43° would be possible at the border. The inclination obtained without magnetron, with the same number of particles coming from all points of the target, gives a similar inclination.

Figure 3.13 shows the results of the simulations along a radial axis of the substrate and the measured inclinations from samples PIb with SiO_2 buffer-layer and PIe with Al_2O_3 buffer-layer. The simulated incidence angles obtained with or without the magnetron follow the same trend as the measured values and

[60] Personal communication from Johan Bjurström, Uppsala University, February 2006.

give a qualitative confirmation of the hypothesis of oblique particle incidence. Both the measured c-axis inclination and the simulated incidence point towards the substrate centre. The difference between simulated and measured curves has several reasons: (a) the simulations are simple and do not necessarily reflect the exact sputtering conditions, e.g. the distribution of the sputtered particles and shape of the erosion track; (b) the simulations give the oblique incidence angle of the particles whereas the measurements give the inclination of the film, which are not necessarily equal;[61] and (c) the influence of the substrate and sputtering parameters has not been considered. Nevertheless these simulations give strong support to the inclined particle incidence assumption. For sample PId sputtered at high pressure, the particles lose the preferential incidence because of the low MFP and multiple collisions on the way between target and substrate.

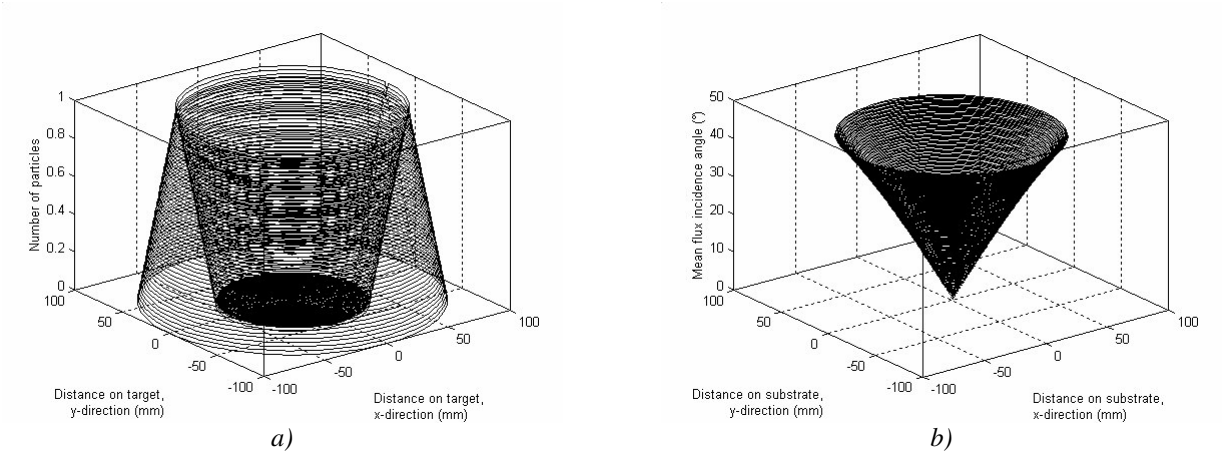

a) *b)*

Figure 3.12 : a) Simulated sputtering profile and b) simulated oblique incidence for points on a 4" wafer.

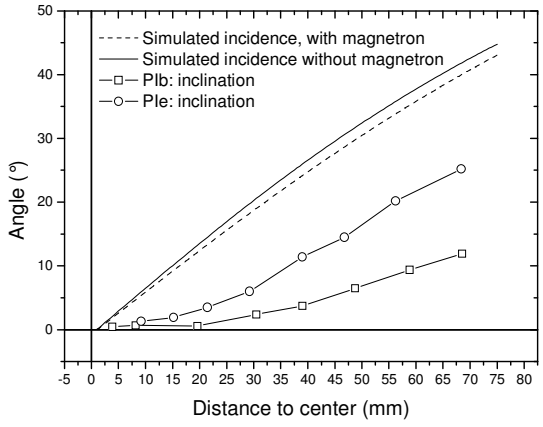

Figure 3.13 : Simulations and measurements of PROCESS I. The lines show the simulations for sputtering with (dashed) and without (solid) magnetron. The points show the measured points for samples PIb (squares) and PIe (circles).

3.4.5.2. Inclined film growth

The simulations and comparison with the literature have shown that the observed inclined c-axis growth results from an oblique incidence of the particles on the growing film. The **relationship between oblique**

[61] Y. E. Lee, S. G. Kim, Y. J. Kim, H. J. Kim, *J. Vac. Sci. Technol. A* **15**, 1194 (1997).

incidence and inclined growth has been observed by many authors and has been under investigation since its discovery in 1959. [62] It is generally accepted that inclined film growth is the result of the low mobility of the adatoms resulting in a competitive growth regime and shadowing. The basic mechanisms of texture formation during competitive film growth with the important roles of different grain growth rates and shadowing have been discussed in section 3.2.3. These models can be adapted to inclined film growth. One has to distinguish between the obtained **crystallographic orientation**, which is of primarily interest in this work, and the **morphology** which concerns the shape, size and inclination of the grains.

The preferred inclined **crystallographic orientation** results from the same mechanisms as explained in section 3.2.3. During sputtering at low temperatures, film growth typically proceeds in a competitive growth. Grains with a fast growth rate are preserved while slower growing grains are cut off. For ZnO, the (002) direction has the fastest growth rate. It is the densest packed plane, the one with the lowest surface energy, and the one with the least back-sputtering. When the particles arrive in an oblique angle, the grains that have the fast crystallographic growth directions aligned with this fast geometric growth direction outgrow the grains that do not exhibit this alignment.[63] This explanation is schematically shown on Figure 3.14.

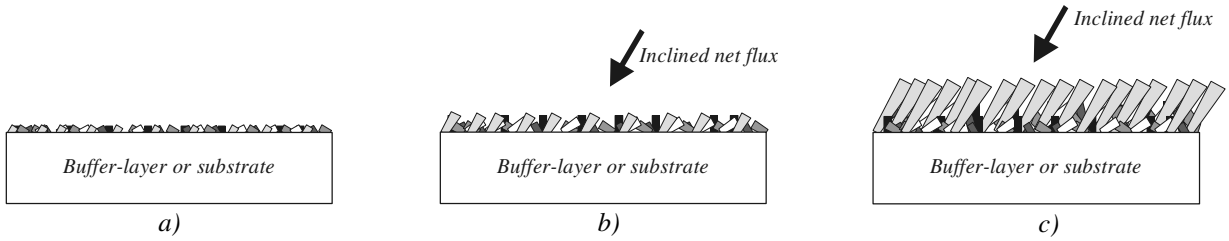

Figure 3.14 : Explanation for inclined film growth due to oblique particle incidence. a) in the nucleation phase, islands have many different orientations. b) and c) during the growth phase, grains oriented in the direction of the inclined net flux grow faster and outgrow the others.

One requirement is that in the **nucleation** phase, there are some islands present exhibiting a preferred orientation in direction of the sputtering flux. For this to happen, the **substrate** must either allow the nucleation of tilted islands, or create conditions for the subsequent growth of tilted islands and grains. In our case, the amorphous SiO_2 and Al_2O_3 buffer-layers allow all possible orientations. [64] There will be islands with their (002) orientation in direction of the flux, which will grow fastest. In contrast, on polycrystalline (111) oriented Pt, the islands will have a (002) preferred orientation collinear with the substrate normal already in the nucleation phase, which explains that no inclined growth was observed. Another method of having a high number of inclined oriented islands would be to have a certain surface micro-roughness. The nucleation density at the first stage of the growth process would thus be higher, so that the proportion of grains with an orientation in direction of the incidence would be higher. The higher micro-roughness of the Al_2O_3 buffer-layer (see Figure 3.5) could explain why the recorded inclinations were bigger than for the SiO_2.

[62] L. Abelmann, C. Lodder, *Thin Solid Films* **305**, 1 (1997).
[63] O. P. Karpenko, J. C. Bilello, S. M. Yalisove, *J. Appl. Phys.* **82**, 1397 (1997).
[64] P. B. Barna, M. Adamik, *Thin Solid Films* **317**, 27 (1998).

The **morphology** of the thin films was not analyzed extensively in this work. Some pictures of inclined grains, or columns, are shown in the paragraph about PROCESS II in Figure 3.23. Nevertheless, we will briefly explain how inclined grains can result. As expected, since the grains preferably grow in the direction of the oblique sputter flux, they will be inclined. Several models have been published on the relation between the columnar inclination angle β and the angle of vapour incidence α. Early measurements indicate that α and β are approximately related by $\tan(\beta)=1/2\tan(\alpha)$, which is often referred to as the **tangent rule**.[65] Due to its simplicity, this empirical relationship is still used nowadays, even though large deviations have been observed. The rule does not have any physical meaning; it is only a description which seems to fit a number of measurements. The inclination of the columns and their in-plane texture can be explained by **shadowing**, which was explained in section 3.2.3 in the case of normal incidence. Oblique incidence leads to a variation of in-plane growth rates, where the fast growth direction is normal to the plane defined by the substrate normal and the incident flux direction. This geometric growth anisotropy leads to the formation of elliptically shaped elongated grains in the plane of growth.[66]

3.4.6. Perspectives

PROCESS I permits to obtain c-axis inclined ZnO without a modification of the sputtering equipment, and without a tilting of the substrate. On an area corresponding to a 4" wafer, inclined ZnO with maximum inclinations of around 9° can reliably be deposited. PROCESS I has several **advantages**. Inclinations can be obtained relatively easily, without modification of the sputtering equipment. The process needs no inclination of the substrate to obtain an oblique incidence of the particles. It is a simple planar sputtering process and the usual standard charging systems of the sputtering equipment can be used. Moreover, the sputtering rate of 7.1 nm/min is quite high with homogeneity over the wafer better than ± 5%. However, PROCESS I also has some **disadvantages**. The obtained inclinations are very inhomogeneous. From the inherent working principle of this process, it is not possible to obtain inclinations on the whole wafer surface. The centre of the wafer will always have a net zero inclination, since the net flux will be symmetric there. The maximum usable surface for shear wave resonators is estimated to about 19 %, if a minimum inclination of 5° is taken as reference. Moreover, simulations have shown that the maximum incidence obtainable at the border of a 4" wafer is limited to 30°, which, using the tangent law, corresponds to a maximum c-axis inclination of 16°.

The advantages of this process would certainly justify further investigations and optimizations. As was shown by Bjurstöm *et al.* for AlN, reliable deposition of piezoelectric films with inclinations up to 30° could possibly be obtained if the sputtering parameters and the substrate material are adapted correctly.[67] In this work a second process (PROCESS II) was developed, which looked more promising, and PROCESS I was not further developed.

[65] L. Abelmann, C. Lodder, *Thin Solid Films* **305**, 1 (1997).
[66] O. P. Karpenko, J. C. Bilello, S. M. Yalisove, *J. Appl. Phys.* **82**, 1397 (1997).
[67] J. Bjurström, G. Wingqvist, I. Katardjiev, *Proc. IEEE Ultrason. Symp.*, 321 (2005).

3.5. PROCESS II: additional blinds

3.5.1. Initial idea and results

3.5.1.1. Modification of the sputtering chamber

In this paragraph, a second technique to deposit c-axis inclined ZnO is explored. Instead of relying on the geometric environment of the sputtering equipment, it was tried to influence the film growth locally. It was based on the idea that an electrical field influences the c-axis during film growth. Wang and Lakin concluded that the electric field distribution created by an additional anode near the substrate had an apparent orienting effect on the growing film.[68] Cerven *et al.* mentioned an interaction of electrical fields in the proximity of the surface with in situ arising electrical dipoles in the ZnO film.[69] Based on this idea, two electrodes made of stainless steel (length 100 mm, height h_B of 15 mm, thickness 2 mm) were initially positioned next to the substrate (see Figure 3.15). One electrode was kept grounded, i.e. at the same potential than the substrate and the chamber walls. The other electrode was attached to an external voltage source. This can be seen on the picture in Figure 3.16. The cable with the white ceramic coating is the electrical connection to the voltage source outside the recipient.

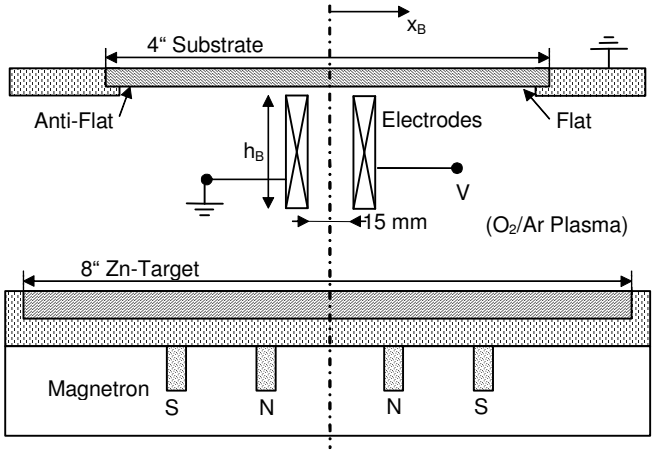

Figure 3.15 : Schematic diagram of the modified reactive magnetron sputtering system with additional electrodes positioned between target and substrate. Their height h_B is 15 mm. x_B is the distance to the middle of both electrodes.

525 µm thick 4” Si (100) wafers were used. They were first covered with a 100 nm thick Pt bottom electrode. Amorphous SiO_2 buffer-layers were deposited onto the bottom electrode. They were realized by CVD, as with the experiments for PROCESS I described in paragraph 3.4. The 400 nm ZnO thin films were deposited reactively with the equipment described in section 3.4.1. The distance between target and substrate was around 60 mm. The sputtering chamber was pumped down to $1 \cdot 10^{-6}$ Pa prior to introduction of Ar and O_2 gas. The ZnO processes were all done at 280°C, a power of 100 W and a pressure of 0.4 Pa. The 8” Zn target was pre-sputtered during 15 min. Table 3.5 summarizes the buffer-layers and applied voltages of the blind for the most relevant samples of these initial experiments for PROCESS II. Generally, the used buffer-layers were thicker than the ones used for PROCESS I. This was because these experiments were partly done

[68] J. S. Wang, K. M. Lakin, *Appl. Phys. Lett.* **42**, 352 (1983).
[69] I. Cerven, T. Lacko, I. Novotny, V. Tvarozek, M. Harvanka, *J. Cryst. Growth* **131**, 546 (1993).

prior to PROCESS I and at that time, the bad influence of a thick buffer-layer on the effective coupling coefficient had not yet been realized.

Figure 3.16 : Picture of the modified reactive magnetron sputtering system with additional electrodes positioned between target and substrate.

TABLE 3.5
RELEVANT ZNO FILMS WITH DIFFERENT PROCESS PARAMETERS FOR INITIAL EXPERIMENTS OF PROCESS II

Sample number	Buffer-layer material	Electrode voltage	Maximum Inclination
PIIa	1000 nm SiO_2	+50 V	8°
PIIb	500 nm SiO_2	+50 V	8°
PIIc	1000 nm SiO_2	0 V	8°
PIId	none (on Pt)	+50 V	0°
PIIe	50 nm SiO_2	+50 V	0°

All samples realized at 0.4 Pa and 280°C, with a DC pulsed power of 100 W.

3.5.1.2. Results and discussion

The results of these initial experiments were surprising. Inclined ZnO could effectively be found near the electrodes. θ-2 θ XRD scans confirmed that the films grow preferentially with a (002) orientation and χ-scans permitted to obtain the c-axis inclination angle. However, the inclination was not found between both electrodes where it was expected, but on the outside of each electrode, in direction of the flat and anti-flat. Figure 3.17 shows the χ-scan results for sample PIIa. The inset shows the inclination situation schematically. The highest inclination of around 8° was obtained at a distance of ±10 mm towards the anti-flat and flat, starting from the middle-line between both electrodes, i.e. only 3 mm outside the electrodes. At a distance of ±6 mm, which is just before the electrodes on the inside, a slight inclination of 5° was seen. On the middle line, the c-axis was not inclined. The c-axis inclined away from the electrodes, i.e. it inclined in direction of the anti-flat and flat for points lying outside the electrodes. Considering an electric field which would exist

between both electrodes, the contrary would have been expected. The influence of an applied electrical field is thus questionable.

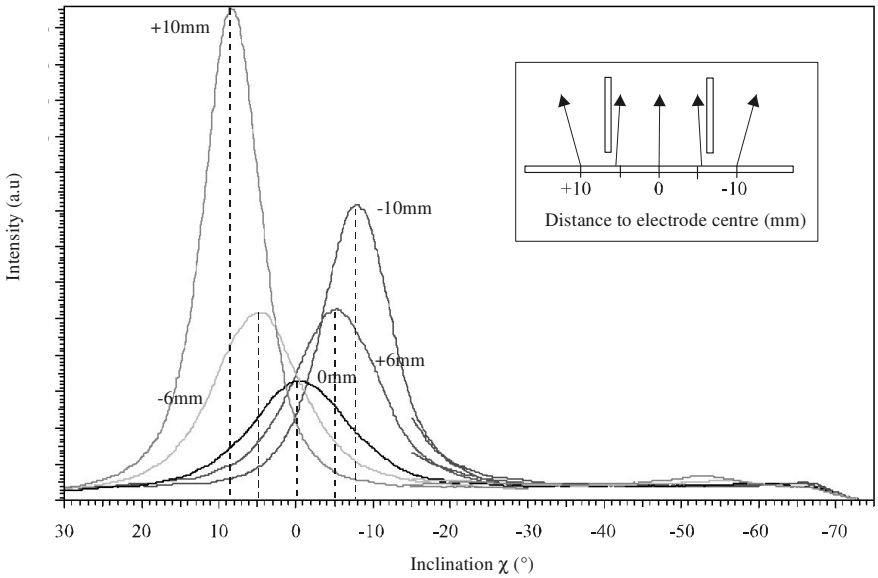

Figure 3.17 : XRD χ-scan at different distances from the electrodes centre (shown near the curves) of sample PIIa. Sample PIIc has a very similar look. The inset shows a schematic view of the inclination situation.

Sample PIIc was sputtered with the same conditions and the same buffer-layer than PIIa, except that no voltage was applied. The inclinations recorded for this wafer closely resemble those of sample PIIa (see also Figure 3.17). This further strengthens the supposition that the applied voltage does not have an influence on the inclination. In retrospective, the idea to generate an electrical field with additional electrodes within a plasma seems inconsiderate. Later during this thesis it became clear that with sheaths forming along every wall in contact with the plasma, all electrical fields exist only within these sheaths only fractions of mm wide. At distances such as those planned with this setup the voltage from the electrodes will not have an influence. Of course, such a sheath also exists at the surface of the substrate, and there it could have an influence on the growing film.[70] But it seems improbable that this field would incline with respect to the surface, since an inclination could only stem from charge inhomogeneities, which would quickly be equalized by the plasma. Nevertheless, c-axis inclinations were recorded and this method was further investigated.

A closer analysis of the inclination was realized with sample PIIb outside one electrode. Again, the same inclinations than on samples PIIa and PIIc were found, showing that a reduction of the SiO_2 buffer-layer from 1000nm to 500nm did not have an influence on the obtained inclination. The χ-scan results are shown on Figure 3.18. The inclination increased from the electrode up to a maximum of 8°, which lies approximately at 4 mm from the electrode. With further distance, it decreased. At the border, no inclination was recorded. The inclined c-axes pointed away from the electrode. Sample PIId and PIIe did not show any inclination. For PIId, this is understandable, since the (111) Pt forces a (002) orientation of the ZnO.[71] For

[70] I. Cerven, T. Lacko, I. Novotny, V. Tvarozek, M. Harvanka, *J. Cryst. Growth* **131**, 546 (1993).
[71] S. V. Krishnaswamy, B. R. McAvoy, W. J. Takei, *Proc. IEEE Ultrason. Symp.*, 476 (1982).

PIIe, it shows that for thinner SiO_2 buffer-layers, no inclination can be obtained. This is contrary to the trend shown with the 6" experiments in PROCESS I, where a reduction of the SiO_2 BL thickness from 300 nm to 100 nm slightly increased the obtainable inclinations.

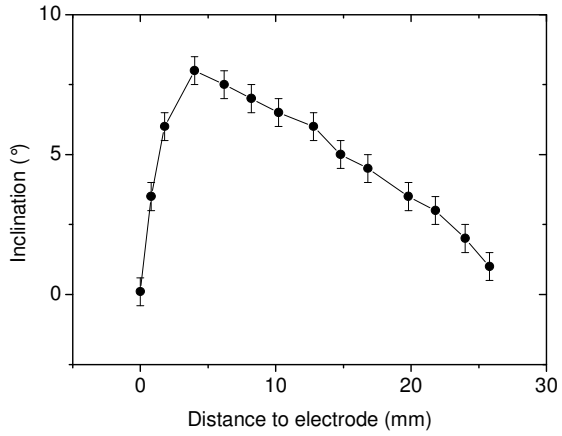

Figure 3.18 : C-axis inclination (from maximum of χ-scan XRD curve) as a function of the distance towards the electrode for sample PIIb.

3.5.1.3. Piezoelectric characterization

To characterize the **piezoelectric activity** of the films, a 100 nm top Pt electrode was added on the stack and structured to obtain highly over-moded FBARs. As with the PROCESS I experiments, the wafers used in this analysis were not double polished and an over-mode analysis such as described in section 2.6.3 was not possible. However the recognition of the excited wave mode was possible. The FBARs were measured at all points where XRD points were recorded. Samples PIId and PIIe did not exhibit a c-axis inclination and accordingly, no shear modes could be recorded. The electrical characteristics only showed longitudinal wave modes and closely resembled the impedance of sample PIg and PId given in Figure 3.9 with different resonance frequencies since the thicknesses of the different layers were different.

Samples PIIa, PIIb and PIIc with identical XRD characteristics gave also very similar electrical impedance results. Figure 3.19 a) shows the recorded broadband characteristics for sample PIIb for the point with the highest inclination at around 4 mm of the electrode and a point at the border of the wafer. The recorded peaks can be attributed to a shear (SM) or longitudinal (LM) mode using simulations with the Mason Model. The shear mode peaks only appear for the resonance curves taken near the electrodes, as is expected from the XRD measurements. The resonance modes have also been confirmed with narrow-band measurements. Figure 3.19 b) shows a narrow-band view of the shear mode resonance with over-modes corresponding to an acoustic velocity in the stack of 5526.3 m/s, close to the theoretical velocity of 5845 m/s in (100) Si. Figure 3.19 c) shows the narrow-band view of the longitudinal mode resonance with spacing of 7.69 MHz, corresponding to an acoustic velocity of 8076.9 m/s, close to the theoretical longitudinal mode velocity of 8433 m/s in (100) Si. As expected, no shear-mode was excited in the region between both electrodes.

Since a piezoelectric activity was recorded in the regions exhibiting c-axis inclination, the sputtering parameters and buffer-layer seemed to be acceptable concerning the polarity and size of the grains. They were used as starting parameters for the continuation of PROCESS II development.

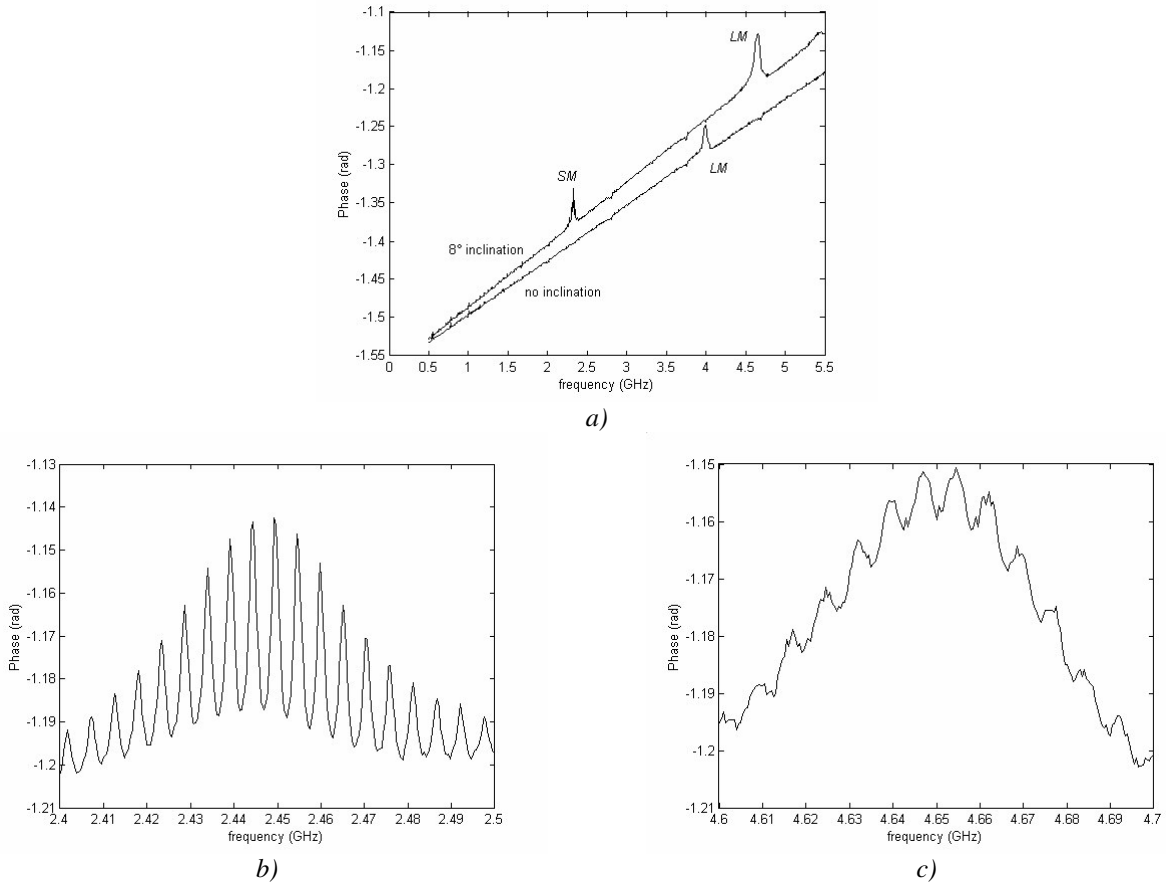

Figure 3.19 : a) Broad-band characteristic of the impedance phase for sample PIIb at a point of maximum inclination at around 4 mm from the electrode and at the border of the wafer, where no inclination has been recorded; and narrow-band characteristic for the shear mode (b) and longitudinal mode (c).

3.5.1.4. Preliminary conclusion and further planning

As the previous experiments have shown, c-axis inclined ZnO films with inclination of up to 8° have been observed on SiO_2 buffer-layers. However, these inclinations were not found between both electrodes, where they were expected, but outside the electrodes. They decreased with increasing distance from the electrode and the c-axis looked away from the electrode. Moreover, the inclination does not seem to be influenced by the applied electrical voltage. The reasons for the inclination of the c-axis could not clearly be determined. They could be of mechanical or of electrical nature: changed incidence angle of the particles, substrate microstructure, changed plasma conditions, thickness variations of the film or electrical field influence due to inhomogeneous incidence of charge particles on the film. However, it seems clear that inclinations should also be possible with a single electrode without any applied voltage. In the remaining research concerning PROCESS II, a **single electrode** was therefore used, and the denomination was changed to **blind**.

3.5.2. Experimental: process modification

400 nm ZnO thin films were deposited with the equipment described in section 3.4.1 as with the first part of PROCESS II development. Total chamber pressure ranged from 0.2 to 0.4 Pa. The heater temperature was varied from 150 °C to 280 °C, resulting in a temperature around 70°C to 200°C for the substrate. The pulsed DC power applied to the cathode was 100 W. Compared with the first part of the PROCESS II development, only one single blind was positioned between the substrate and the target (see Figure 3.20). The blind was made of stainless steel and had a height h_B varying of 15 or 35 mm. It was placed at the centre of the substrate. Compared to the photograph shown in Figure 3.16, only the left one of the two electrodes was kept. To support the results found in the first part, there was again the possibility to apply an electrical potential of -100 V to +100 V with respect to the grounded substrate and study its influence. For some experiments the magnetron was removed to realize a homogeneous sputtering rate across the target.

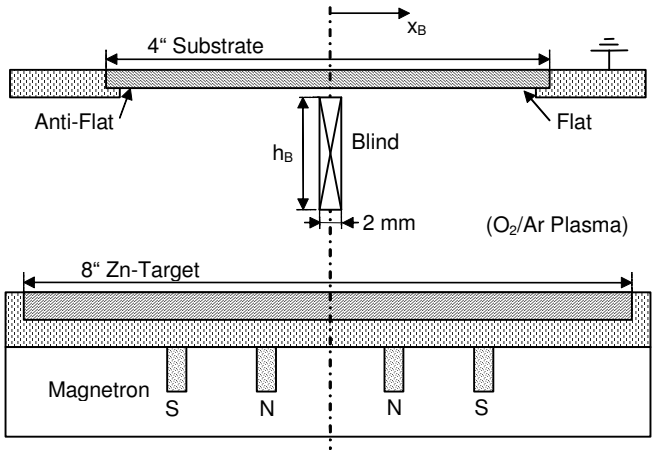

Figure 3.20 : Modified reactive magnetron sputtering system with an additional blind positioned between target and substrate. The blind height h_B varies between 15 and 35 mm. x_B is the distance to the blind.

The ZnO films were deposited on 400 µm thick double-polished 4” Si (110) wafers covered with a 100 nm thick Pt thin film. Unlike the substrates used for PROCESS I and the first experiments of PROCESS II the over-modes fitting method described in 2.6.3 could be used with these substrates in order to determine the coupling coefficient of the ZnO films. This will be shown in section 3.5.5. Different buffer-layers were deposited onto the bottom electrode; mostly CVD deposited SiO_2 and sputtered Al_2O_3, as with the experiments of PROCESS I. Table 3.6 summarizes the stack and sputtering properties of the most relevant samples.

3.5.3. Results and discussion

Similarly to what was observed with the preliminary experiments using the two electrodes, inclined ZnO films were obtained in the vicinity of the blind. As expected, films with c-axis inclination could be found on either side of the blind. Sample PIIf was sputtered at the same conditions than sample PIIb on a SiO_2 buffer-layer of 500 nm thickness. The inclination was measured by XRD at a distance of 10 mm on either side of

the blind. An inclination of 7° was obtained, which corresponds approximately to what was seen with sample PIIb at the same distance from the electrode (see Figure 3.18). Again, the c-axis looked away from the blind. It was assumed that the same trend would have to be expected, confirming that the **same inclination could be obtained with a single blind instead of two electrodes**. A series of experiments was started afterwards to investigate this in more detail.

TABLE 3.6
RELEVANT ZNO FILMS WITH DIFFERENT PROCESS PARAMETERS FOR PROCESS II DEVELOPMENT

Sample number	Buffer-layer material	Pressure, Temperature, Power	Blind height; Other	Maximum inclination
PIIf	500 nm SiO_2	0.4 Pa; 280°C; 100 W	15 mm	8°
PIIg	500 nm SiO_2	0.4 Pa; 280°C; 100 W	15 mm; voltage -100V	8°
PIIh	500 nm SiO_2	0.4 Pa; 280°C; 100 W	15 mm; voltage +100V	8°
PIIi	100 nm SiO_2	0.4 Pa; 280°C; 100 W	15 mm	8°
PIIj	100 nm Al_2O_3	0.4 Pa; 150°C; 100 W	15 mm	16°
PIIk	100 nm Al_2O_3,	0.4 Pa; 280°C; 100 W	15 mm	10.9°
PIIl	100 nm Al_2O_3,	0.4 Pa; 280°C; 400 W	15 mm	15°
PIIm	100 nm Al_2O_3,	0.2 Pa; 280°C; 100 W	15 mm	3.5°
PIIn	100 nm Al_2O_3,	0.4 Pa; 280°C; 100 W	35 mm	11°

The highest inclinations were recorded with sample PIIj, which was sputtered on 100 nm Al_2O_3 at 150°C. Figure 3.21 a) shows a typical XRD 2D detector image recorded at the point of maximum inclination at a distance x_B of ~5 mm of the blind. The (002) reflex is located at an angle of 16°. It is moved above the centre line, whereas in Figure 3.7 for sample PIb it was moved below the centre line. The position gives information in which direction the c-axis inclines. Figure 3.21 b) shows the corresponding θ-2θ scan. Besides the different peaks relative to platinum layer and silicon substrate, a (002) ZnO preferential orientation can be observed. Small peaks of (101) and (103) orientations are also present. Figure 3.21 c) gives a χ-scan of the film clearly showing the 16° inclination. The grey line represents a fitted Gaussian response as explained in sub-section 3.4.4.1. These results confirm that the synthesized ZnO films have a wurtzite hexagonal structure with a c-axis inclined 16° to the surface normal. The χ-peak has a relatively broad FWHM of 15.3°. A φ-scan was also recorded and is shown in Figure 3.21 d). Here a high FWHM of 47° was recorded. These FWHM values indicate a broad angular spread of the inclination angle in the different grains. The influence of this spread on the coupling coefficient will be analyzed in section 3.5.5.

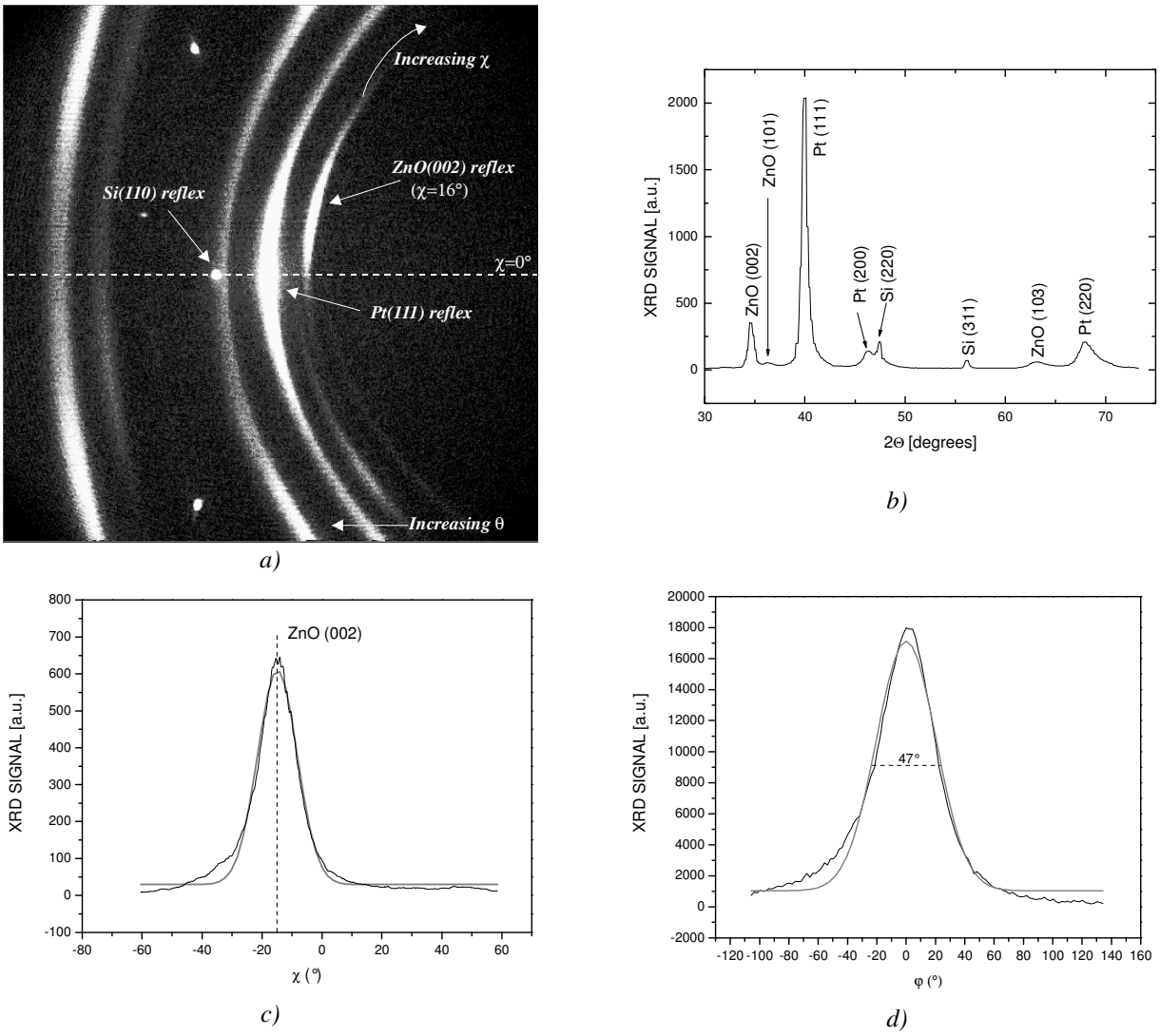

Figure 3.21 : a) Typical XRD 2D detector image for sample PIIj with the highest inclinations, with b) the corresponding θ-2θ scan, c) the χ-scan of the (002) orientation revealing an inclination of ~16° with a FWHM of 15.3° and c) the φ-scan revealing a FWHM of 47°. On the θ-2θ scan the Pt peaks appear because of the 100 nm Pt layer below the ZnO. The Si peaks correspond to the Si (110) substrate.

3.5.3.1. Dependence of characteristics to the distance to the blind x_B

Similar to what was seen with PROCESS I, the inclinations were very much dependent on the sputtering parameters and the buffer-layers. Samples without buffer-layers where ZnO was sputtered directly on Pt did not exhibit c-axis inclinations. Samples on SiO_2 or Al_2O_3 buffer-layers followed the same trend depending on the distance to the blind. Figure 3.22 shows the inclination as a function of distance to the blind for sample PIIj with the highest recorded inclination. Starting from the blind, the inclination first increases up to a maximum angle at approximately 5 mm from the blind, then diminishes gradually towards the border of the wafer. The sputtering rate and thus the thickness of the films are very inhomogeneous. The rate varies from approximately 3 nm/min near the blind to 14 nm/min at the flat and anti-flat (see Figure 3.22). Without the blind, the same process gave a deposition rate homogeneity better than ± 5 %, as was shown with PROCESS I. The thickness increases slightly below the blind. The ZnO with maximum inclination can be found in the

region of lowest thickness. The c-axis is pointing away from the blind. The χ scan FWHM of the film follows the same trend as the inclination, varying from 6.6° for the non-inclined ZnO to 15.3° for the maximal inclined ZnO.

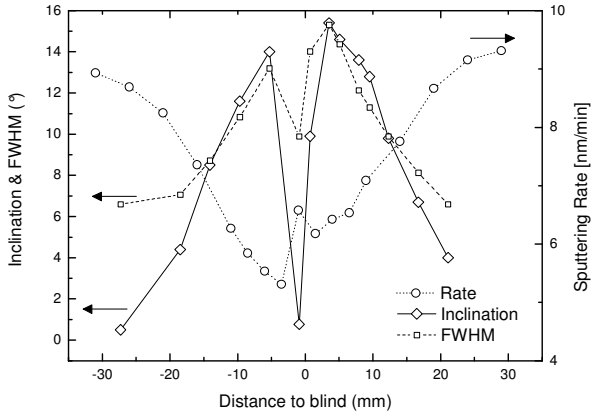

Figure 3.22 : C-axis inclination, χ scan FWHM and sputtering rate for sample PIIj as a function of distance x_B to the 15 mm high blind. This film was sputtered at 150°C on an Al_2O_3 buffer-layer.

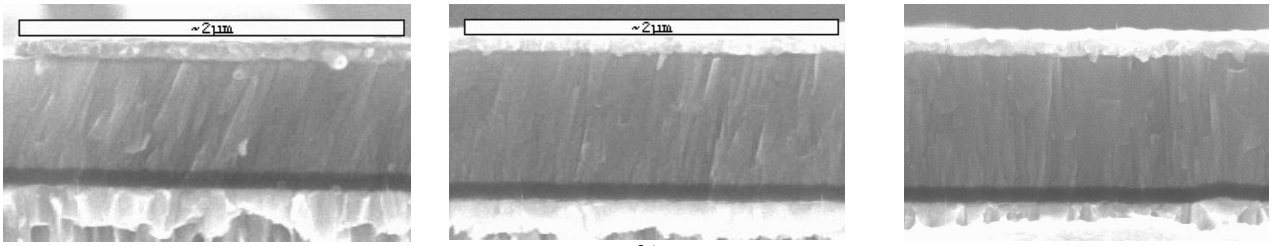

a) *b)* *c)*

Figure 3.23 : SEM pictures of a typical c-axis inclined ZnO film (sample PIIj). a) 23° inclined columns at a distance of 5 mm from the blind, b) 11° inclination at 17mm and c) 0° at the border of the wafer. A 100 nm thick top Pt electrode and a 100 nm Al_2O_3 buffer-layer below the ZnO can be seen.

Figure 3.23 shows SEM pictures of cross-sections of sample PIIj. They were taken at three different distances from the blind. As can be recognized, the film has a columnar structure, which is an indication of a growth regime in Zone 1 or Zone T (see section 3.2.3 about film growth). The inclination of the columns can be recognized. Similar to the c-axis inclination, it decreases with increasing distance from the blind. At 5 mm from the blind, which corresponds to the point of highest c-axis inclination, the column inclination is approximately 23°, which is slightly more than the crystallographic inclination. At 17 mm from the blind, the column inclination is only 11°, and at the wafer border, no columnar tilt can be observed. As was explained in section 3.4.5, the columnar tilt is not necessarily equal to the c-axis tilt. This has been observed in various articles in literature.[72]

[72] Y. E. Lee, S. G. Kim, Y. J. Kim, H. J. Kim, *J. Vac. Sci. Technol. A* **15**, 1194 (1997); L. Abelmann, C. Lodder, *Thin Solid Films* **305**, 1 (1997).

3.5.3.2. Parameter and applied voltage influence

The c-axis inclination variation as a function of the distance to the blind depends on the applied sputtering parameters and the substrate material. The reasons for the obtained inclination are difficult to evaluate. Many parameters can influence the film deposition in reactive magnetron sputtering. With identical sputtering conditions and without the additional blind, ZnO grows preferably in (002) direction on Pt, SiO_2 and Al_2O_3 in the centre region of the wafer, as was seen with PROCESS I. The blind changes the sputtering conditions drastically and allows inclined ZnO growth. In this work, a limited parameter analysis was done. Due to the high inhomogeneities of the films, the characterization was difficult, be it by XRD or over-modes fitting. Some dependencies were found and are given in the following.

The **voltage** applied to the blind did not have an influence on the obtained inclination. Voltages varying from -100 V to 100 V did not change the inclination of the ZnO on SiO_2 buffer-layers. They all exhibited a maximum inclination of 8°. The recorded XRD χ-scan inclination and FWHM of samples PIIg and PIIh match those of sample PIIf. However, the glow region of the plasma was slightly changed. There was a higher deposition rate for wafers sputtered with a blind with higher voltage due to a higher plasma density, which is why for all other wafers, a voltage of +50V was still applied. As with the initial experiments of PROCESS II presented in section 3.5.1 these results do not confirm reported results on influencing the inclination of ZnO with an additional electric field.[73] As the c-axis points away from the blind and not towards it, the influence of an applied electrical field is questionable. Nevertheless, intrinsic electrical fields exist on the surface of the wafer and could have an effect on the orientation. As the wafer is constantly bombarded with electrons from the plasma, a boundary sheath is building up resulting in high electric fields over the growing layer. With homogeneous sputtering, these fields are perpendicular to the substrate, especially when there is a metal surface. With inhomogeneous sputtering, as in our case, inhomogeneous charging of the dielectric buffer-layers and the growing film could result in an inclined field on the surface of the wafer and influence the film inclination.[74]

As seen with PROCESS I, a lower sputtering temperature should favour a higher inclination. This was also observed with PROCESS II. PIIk was sputtered with the same parameters and the same buffer-layer than sample PIIj, except that the temperature was 280°. As is shown on Figure 3.24, sample PIIj has a higher inclination of 16°. The FWHM of both samples is nearly the same. Sputtering with a higher power of 400W yielded slightly higher inclinations, which is shown on Figure 3.24 for sample PIIl. The inclinations correspond approximately to the inclinations recorded for sample PIIj sputtered at 150°C. However, the FWHM of this sample is much higher, reaching values as high as 38°. Lowering the **pressure** from 0.4 Pa to 0.2 Pa doubles the mean free path. As can be seen, this reduced the inclinations and the FWHM significantly. It should be noted that while the maximum inclination changed with the applied parameters, the span of the regions in which inclined films were observed stayed constant.

[73] J. S. Wang, K. M. Lakin, *Appl. Phys. Lett.* **42**, 352 (1983).
[74] I. Cerven, T. Lacko, I. Novotny, V. Tvarozek, M. Harvanka, *J. Cryst. Growth* **131**, 546 (1993).

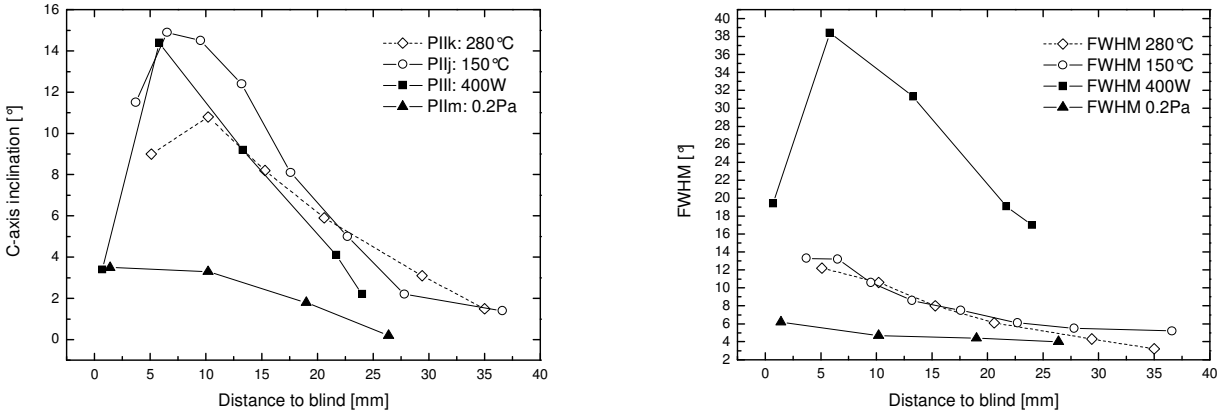

a) *b*

Figure 3.24 : a) C-axis inclination and b) χ scan FWHM as a function of distance to the blind for samples PIIk, PIIj, PIIl and PIIm.

3.5.3.3. Blind geometry and magnetron influence

When using a higher blind, the maximum inclination did not change, but the span of the inclined regions was extended, as shown on Figure 3.25 a) with samples PIIk and PIIn. The FWHM of both curves varies accordingly as seen on Figure 3.25 b). Both effects can be explained by oblique particle incidence under conditions of low adatom mobility as explained later. To see the influence of the magnetron, it was removed in one experiment, using the same sputtering parameters and buffer-layer than for sample PIIf. Inclined ZnO films were still obtained, but the inclinations were lower. The maximum of the inclination also moved closer to the blind and the span of the inclined region was diminished.

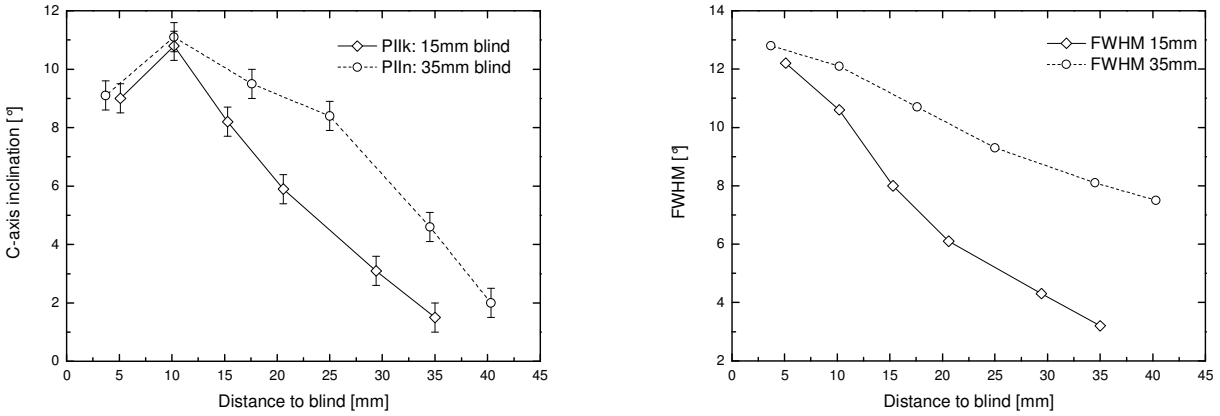

a) *b)*

Figure 3.25 : a) C-axis inclination and b) FWHM of ZnO films as a function of distance to the blind for samples PIIn and PIIk sputtered with a blind of 35 mm and 15 mm respectively.

3.5.3.4. Buffer-layer influence

The substrate material has a decisive influence on the inclination. For crystalline or polycrystalline films, epitaxial relationships can favour or inhibit growth in a certain direction. Directly on a Pt layer, without buffer-layer, no inclination was observed and the obtained film was highly (002) oriented. However, on SiO_2, a maximum inclination angle of 8° was measured, and for Al_2O_3, a maximum inclination of 16° was recorded. Both the SiO_2 and the Al_2O_3 are amorphous layers, so epitaxial effects can be ruled out. Fine crystallites of Al_2O_3 could be responsible for this difference by reducing the surface mobility of the ZnO particles at the substrate during film growth.[75] Additionally the higher micro-roughness of the Al_2O_3 buffer-layer (see Figure 3.5) could have resulted in a higher nucleation density at the beginning of the growth process having a positive influence on the inclination.

Other buffer-layers that were tested in this work include amorphous Si, TiO_2 and ZrO_2 with thicknesses varying between 100 nm and 300 nm. This selection was based on thin film materials available in the CT MM2 clean room facilities. The amorphous Si was deposited by CVD and the ZrO_2 and TiO_2 were sputtered in the same equipment than the ZnO films. For Si and TiO_2, the recorded inclinations were in the same range than for SiO_2, with maximum inclinations of 8°. For ZrO_2, inclinations of 13° were seen, which could be explained through local epitaxy. More experiments would have been necessary to further examine the influence of different buffer-layers.

At the end, we aimed to achieve buffer-layers with thicknesses below or equal to 100 nm. This is because the buffer layers may have a direct influence on the effective coupling coefficient of complete FBARs due to the voltage drop across the additional series capacity (capacitive impact) and due to a change of the acoustic stack of the FBAR (acoustic impact). This has been confirmed by simulations based on the Mason-Model for FBARs with buffer-layers of SiO_2, Al_2O_3, TiO_2 and ZrO_2, and will be shown in Chapter 4 in section 4.3.2. The Al_2O_3 buffer-layers provided the highest inclinations and were also favourable from an electrical point of view.

3.5.4. Explanation: oblique particle incidence and inclined film growth

The most likely explanation for the obtained inclination is oblique particle incidence, similarly to what was seen with PROCESS I. As discussed in 3.2.2, the angle distribution of the sputtered particles typically has a **cosine form**. Most particles leave the target in normal direction, but a considerable amount of particles also leaves at oblique directions. At the pressure range used, most particles have a low probability of collisions between target and substrate, since the MFP is equal to the target-substrate distance (~60 mm). Thus they keep their initial preferred direction and hit the substrate with different angles. The blind positioned near the substrate surface blocks particles with certain incidence directions. For points near the blind, this results in an oblique mean incidence angle as shown schematically on Figure 3.26 a). It is known that inclined ZnO can grow with oblique particle incidence under conditions of low adatom mobility and competitive film

[75] K. Wasa, S. Hayakawa, T. Hada, , IEEE Trans. Sonics Ultrason. **SU-21**, 298 (1974)

growth.[76] Generally, the inclinations of the c-axis and of the columns are in the same direction than the flux of incoming particles.[77] Both effects have been shown for our films by XRD and SEM results. For points situated next to the blind, the effect is strongest resulting in the highest mean incidence, as confirmed by XRD measurements. As most particles are blocked, the thickness is also lowest for these points.

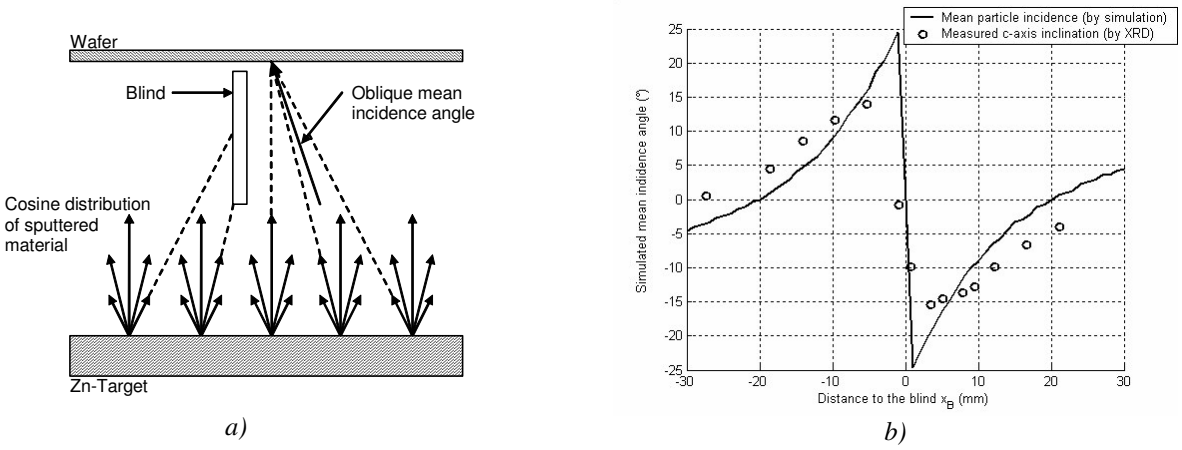

Figure 3.26 : a) Simple geometric explanation for the inclined ZnO films growth: oblique mean particle incidence results due to a blocking effect by the blind; b) Result of geometric simulations for a 15 mm blind compared to ZnO thin film inclinations obtained from XRD measurements for sample PIIk.

Simple two-dimensional **simulations** similar to those shown in section 3.4.5 for PROCESS 1 were performed using MATLAB software to verify this hypothesis geometrically. The plane of simulation was the one shown in Figure 3.20. A cosine distribution was assumed for points of the target lying on a diametrical line (length of 8") perpendicular to the blind. The particle trajectories were then simply extended towards the substrate, which was also simulated as a diametrical line perpendicular to the blind. The target erosion track due to the magnetron was taken into account by increasing the number of particles in that zone. The mean incidence angle was calculated for each point of the substrate by looking at how many particles arrive from what direction. By blocking the incidence angles corresponding to the blind, an inclined mean incidence angle results on the substrate depending on the distance x_B to the blind. For a 15 mm blind a maximum mean incidence angle of 25° has been obtained. As shown on Figure 3.26 b), the results of these simple simulations correspond quite well to the inclinations measured by XRD and give a qualitative confirmation of our hypothesis of oblique particle incidence. The sign of the inclination gives information in which direction the c-axis inclines. With increasing distance, the inclination becomes zero and then changes sign. At the border of the wafer, the blind does not have an influence and inclination results due to the mechanisms shown with PROCESS 1. By increasing the height of the blind to 35 mm, the maximum incidence angle does not change, but the span of the inclined ZnO changes, as was also observed with XRD measurements of sample PIIn.

[76] Y. E. Lee, S. G. Kim, Y. J. Kim, H. J. Kim, *J. Vac. Sci. Technol. A* **15**, 1194 (1997) and D. Howell, L. Goddard, B. T. Khuri-Yakub, *Proc. IEEE Ultrason. Symp.*, 381 (1987).
[77] L. Abelmann, C. Lodder, *Thin Solid Films* **305**, 1 (1997).

The actual film growth is thought to proceed in the same way than described in section 3.4.5 with PROCESS I. We are in a **competitive growth regime** and the grains which are oriented with their fastest growing direction in direction of the oblique incident flux will grow faster and outgrow other grains (see Figure 3.14). The initial nucleation phase is crucial to achieve a good orientation at the end of the growth. The number of islands oriented in direction of the oblique incidence should be as high as possible. This may explain why the inclination was increased in the case of a sputtering power of 400 W for sample PIIl. A higher power means a higher sputtering rate and a higher nucleation density, meaning that the number of islands with the correct orientation will be higher. During film growth, a higher sputtering power also gives newly arrived species less time to move to a stable site, which could explain the high FWHM value.[78] A higher nucleation density may also explain the higher inclinations observed on Al_2O_3 compared to SiO_2. As seen in section 3.4.3 and shown in Figure 3.5, although both layers have similar roughness, the Al_2O_3 layer seems to have a higher micro-roughness. This reduces the surface mobility and the nucleation density will be higher, and thus the number of islands with the correct orientation will be higher.[79]

The competitive growth regime also explains why a lower temperature gives a higher inclination for sample PIIj. The nucleation density at the beginning can then be higher. A lower temperature means a lower surface diffusion, meaning that the adatoms cannot easily jump from one crystal to another, which further favours the crystals in direction of the growth. A lower pressure means that the mean free path is increased, so that the particles have a higher energy when impinging on the substrate since they retain their initial energy. The surface diffusion is thus enhanced. This could explain why the obtained inclinations of PIIm were lower. Since the atoms would be able to move to other grains, the grains in the oblique sputter direction would not necessarily be favoured anymore. Another explanation might be that the buffer-layer used in this experiment was different, possibly less rough, thus providing less nucleation sites, similar to what was seen for PROCESS I in section 3.4.5.

The dependencies of the film properties to the sputtering conditions and buffer-layers must be completed by other characterizations to obtain further information about the orientation and texture formation mechanisms. This would allow for an optimization of the process. Since the films are very inhomogeneous such an analysis would have been very comprehensive and was not realized in this work. As will be seen in paragraph 3.6, PROCESS III provided homogeneous films on large surfaces, and in consequence, a broader parameter analysis was planned using that process.

3.5.5. Piezoelectric characterization

3.5.5.1. Obtained coupling coefficients

The over-modes fitting method described in section 2.6.3 can be used in order to determine the coupling coefficient of the ZnO films. This is possible since the polished back-side of the wafer effectively reflects the waves and the wafers are thin enough (400µm) to ensure that he over-modes are sufficiently spaced. Again, a 100 nm top Pt electrode was added on the stack and structured with a simple photolithographic process to

[78] Y. J. Kim, Y. T. Kim, H. K. Yang, J. C. Park, J. I. Han, Y. E. Lee, H. J. Kim, *J. Vac. Sci. Technol. A* **15**, 1103 (1997).
[79] G. F. Iriarte, PhD Thesis, Acta Universitatis Upsaliensis (2003).

realize highly over-moded FBARs. Shear modes were recorded in the vicinity of the blind in the region of c-axis inclination. At the border, only longitudinal modes were seen.

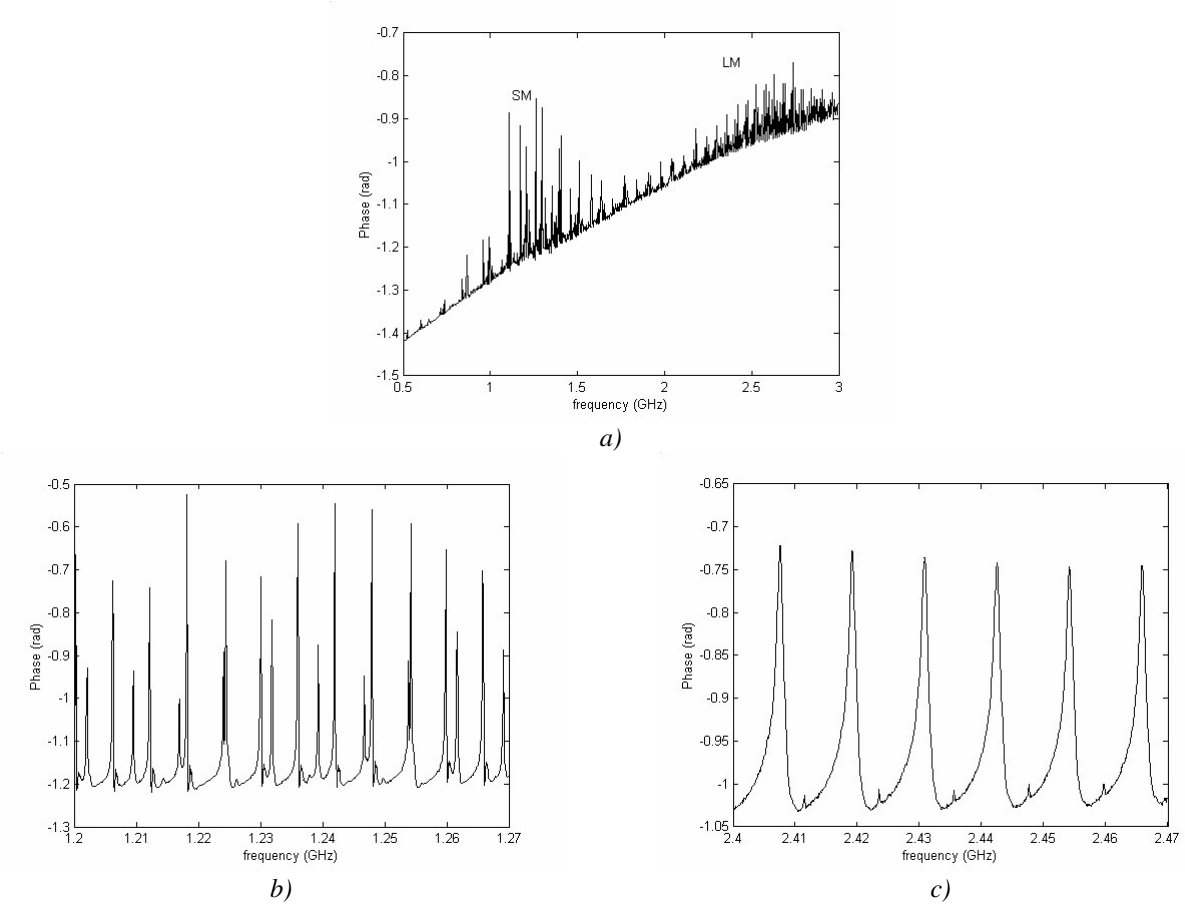

Figure 3.27 : a) Broad-band characteristic of the impedance phase for sample PIIj at the point of maximum inclination of 16° and narrow-band characteristic for the shear mode (b) and longitudinal mode (c).

Figure 3.27 a) shows the recorded broadband characteristics for sample PIIj for the point with the highest inclination at around 4 mm of the electrode. The recorded peaks can be attributed to a shear (SM) or longitudinal (LM) mode resonance using simulations with the Mason Model. The modes have been confirmed with narrow-band measurements. Figure 3.27 b) shows a narrow-band view of the shear mode resonance. Comparing with Figure 3.10 b) of PROCESS I and Figure 3.19 b) of the initial experiments of PROCESS II, the phase reaches much higher values at the resonance frequencies, which is a consequence of the higher inclination and the expected higher coupling coefficient. The figure shows over-modes with different spacing. The ones with a spacing of 5.93 MHz correspond to an acoustic velocity in the stack of 4746 m/s, which is close to the theoretical quasi-shear velocity of 4674 m/s in (110) Si. The other overmodes, which have a lower phase and lie in between the quasi-shear over-modes are spaced by 7.61 MHz. This corresponds to an acoustic velocity of 6088 m/s, which is close to the theoretical pure shear velocity of 5844 m/s in (110) Si. Figure 3.27 c) shows the narrow-band view of the longitudinal mode resonance at around 2.4 GHz.

The shear mode electromechanical coupling constant K of the ZnO film was determined for all samples on Al_2O_3. As expected, the obtained coupling coefficients vary in function of the distance to the blind in the same way than the c-axis inclination. The maximum coupling coefficients were recorded at the point of maximum c-axis inclination, which is consistent with the theory for inclinations below 30°. The coupling depending on the distance to the blind is given in Figure 3.28 for sample PIIj. The average maximum coupling K was 0.106 which is nearly half of the maximum theoretical value of 0.26 that can be obtained at this inclination. Some resonators even exhibit a coupling of 0.13. Table 3.7 gives the highest coupling coefficients for each sample along with their recorded inclination and the theoretical coupling coefficient at that inclination. All values are lower than expected. The biggest difference is seen for sample PIIl sputtered at 400 W. Although it has a high inclination of 15°, the coupling is only 0.021, which is only 8.2% of the theoretical value. The lower values can be explained by the broad distribution of the inclination angle of the c-axis in the different grains of the thin film, which will be shown in the next sub-section. In addition it might also be attributed to a partially opposite polarity of the grains. Both problems can be improved by optimizing the process parameters and potentially choosing other buffer-layers.

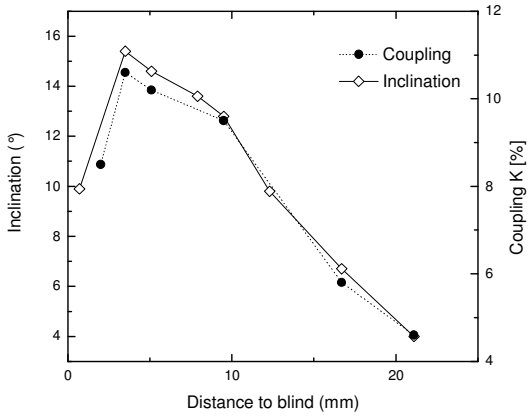

Figure 3.28 : Coupling coefficient and inclination of the c-axis against distance to the blind for sample PIIj.

TABLE 3.7
OBTAINED AND CALCULATED COUPLING COEFFICIENTS FOR ZNO FILMS DEPOSITED WITH PROCESS II

Sample number	Maximum inclination (FWHM)	Average maximum measured K_S	Expected K_S for perfectly inclined ZnO	Expected K_S with FWHM influence
PIIj	16° (13.3°)	0.106	0.268	0.259
PIIk	11° (10.6°)	0.07	0.197	0.193
PIIl	15° (38°)	0.021	0.255	0.191
PIIm	3.5° (6.2°)	0.043	0.067	0.066
PIIn	11° (10.6°)	0.071	0.197	0.193

3.5.5.2. Relation between piezoelectric response and film orientation

The obtained coupling coefficients are much lower than the theoretical maximum values at the corresponding mean c-axis inclination. The theoretical value is calculated with the assumption that the ZnO is mono-crystalline and perfectly oriented, i.e. all c-axes look in exactly the same direction. In the real case, we have a polycrystalline thin film, with grains, grain boundaries, defects and most importantly, different orientations in the different grains. One can analyze the influence of different directions of the grains without considering their polarity, i.e. without considering if the O-plane or the Zn-plane of the ZnO is oriented towards the surface. As seen in the previous sections, the films feature a high disorientation, i.e. the c-axes of the grains have different χ and φ directions. This can be recognized by their FWHM values in these directions. In this work, the FWHM was mainly analyzed in χ direction. The large FWHM value and disorientation is partly due to the fact that the particles arrive from many different incidence directions. It can also be related to substrate inhomogeneity or roughness.

In the following it was tried to obtain an estimation for the reduction of the coupling coefficient due to an FWHM value in χ direction. It was assumed that there is only a spread of the inclination in the different grains in the χ direction and that this spread can be described in a Gaussian distribution given by formula (3.2).[80] In the majority of cases, the fit is accurate enough as was seen in section 3.4.4. In Chapter 2, it was seen that the components of the elastic, piezoelectric and permittivity tensors of the ZnO depend on the c-axis inclination. The formulas for this dependence are given in equations (2.25). As there are different proportions $N(\theta)$ of grains with certain inclinations in the film, one has to calculate the average value for each of the components. If $<p>$ denotes this average and $p(\theta)$ denotes the dependence of this property towards θ, the following relation results:

$$< p >= \int_{-\pi/2}^{\pi/2} p(\theta) N(\theta) \, d\theta \tag{3.4}$$

Which assuming the Gaussian distribution of equation (3.2) can be written as:

$$< p >= \frac{1}{\sigma\sqrt{2\pi}} \int_{-\pi/2}^{\pi/2} p(\theta) \exp\left[-\frac{(\theta-\mu)^2}{2\sigma^2} \right] d\theta \tag{3.5}$$

The average components can then be used in the respective formulas to find K_S and K_L. Calculations were again performed with MATLAB. The results are plotted in Figure 3.29. Figure 3.30 shows the results for the special case of 16° and 13.6° inclined ZnO. To take into account the fact that no grains with inclination angles higher than 90° are present, the distribution formula was divided by the total area of the distribution. One sees that the effect of the spread of the inclination can indeed not be neglected for high FWHM values. However for lower FWHM values as for the samples of this work, the reduction is not significant. The theoretically expected reduction of the coupling for the piezoelectrically analyzed samples is also given in Table 3.7. As can be seen the high reduction of the coupling coefficients can not solely be explained by the

[80] Gardeniers did a similar analysis of his (002) oriented films: J. G. E. Gardeniers, Z. M. Rittersma, G. J. Burger, *J. Appl. Phys.* **83**, 7844 (1998).

broad disorientation of the films. So it is concluded that the polarity of the films is not unidirectional. In future, the polarity could be influenced by choosing appropriated buffer-layers.[81]

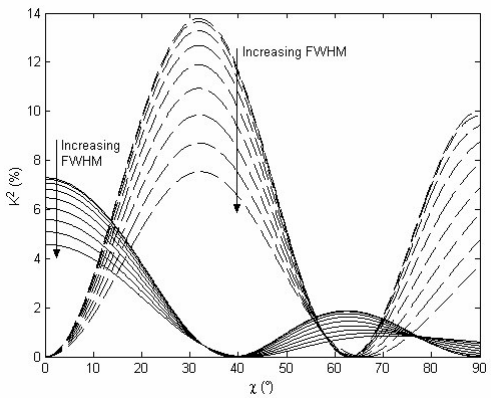

Figure 3.29 :Reduction of the coupling constant of shear (dashed) and longitudinal (solid) modes due to spread of the inclination in χ direction for different FWHMs: ideal case (0°), 5°, 10°, 15°, 20°, 25°, 30°, 35°,and 40°.

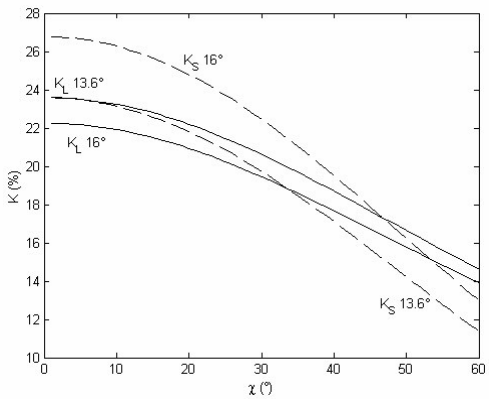

Figure 3.30 : Reduction of the coupling constant of shear (dashed) and longitudinal (solid) modes as a function of the FWHM in χ direction for an average inclination of 16° and 13.6°.

3.5.6. Perspectives

A new method permitting the growth of c-axis inclined ZnO thin films was presented. A blind was positioned between the substrate and the target and c-axis inclined ZnO films with inclinations varying from 0° up to 16° were found. The parameters of the best films are summarized in Table 3.8. The generation of shear mode bulk acoustic waves with an average electromechanical coupling constant K of up to 0.106 was obtained. PROCESS II has several **advantages**. It needs no tilting of the substrate and regular planar charging systems can be used. With the blind, inclinations can be obtained very locally and in principle one could chose the exact location of the inclinations. Since the growth of inclined ZnO on polycrystalline or amorphous substrates and layers is possible, the obtained films can be used for the realization of complete solidly mounted FBARs, which will be shown in Chapter 4. However, PROCESS II also suffers from several **disadvantages**. The method produces very inhomogeneous films, both in thickness, inclination and obtained coupling coefficients. The maximum oblique incidence angle that can be obtained is around 25°, as was shown with simulations. This means that the maximum obtainable inclination is also around 25°. Inclinations were only obtained near the blind, and not at the border. The bottom line is that only 30% of the surface of a 4" wafer can effectively be used for the excitation of shear mode. For research applications this is well enough. For industrial applications this yield is not acceptable.

A limited parameter analysis was done with PROCESS II. Due to the high inhomogeneities of the films, the characterization was difficult, be it by XRD or over-modes fitting. Nevertheless some dependencies were found. The analysis of PROCESS II has shown that in order to obtain inclined film growth due to an oblique incidence, one needs to create suitable conditions at the substrate during the nucleation and island growth phase. One way to do it would be to directly nucleate grains with tilted orientations. Another way is to create

[81] H. Kato, K. Miyamoto, M. Sano, T. Yao, *Appl. Phys. Lett.* **84**, 4562 (2004).

conditions that allow the subsequent growth of tilted grains. This could be obtained by roughening of the substrate (e.g. by dry or wet etching, or mechanical polishing), by using materials resulting in off-axis growth of ZnO (e.g. ITO or Al) or by having a material lacking a hexagonal symmetry or displaying a large lattice mismatch with the c-plane of ZnO, as was done in this work by using amorphous buffer-layers.

The results from PROCESS II have been utilized in the development of PROCESS III presented in the next paragraph. It is based on the idea that with adapted and geometrically more complex blinds, it should be possible to obtain controlled inclinations on the whole surface of the wafer.

TABLE 3.8
FINAL OBTAINED SPUTTERING PARAMETERS FOR PROCESS II

Parameter Description	Parameter value
Blind	15 mm
Discharge power	100 W, pulsed DC
Temperature	150°C
Pressure	0.4 Pa (O_2+Ar)
Sputtering rate	6.6 nm/min

3.6. PROCESS III: complex blind system

3.6.1. Overview and basic setup

The main problem of PROCESS I and PROCESS II, and also of most processes presented in literature, is the high inhomogeneity of the film properties. In most cases, the inclinations vary in very wide ranges over the surface of the used substrates. Both developed processes had inclinations varying from zero inclination up to a certain maximum. Similarly, the film thicknesses are inhomogeneous. In literature, the only method which provides homogenous inclinations and deposition rates over large substrate surfaces is epitaxial growth on mono-crystalline substrates like sapphire,[82] which is not suitable in this work since a bottom electrode and an acoustic mirror would be difficult to obtain.

The process described in this paragraph is an optimization of PROCESS II. It was tried to obtain a higher utilizable surface, in view of an industrial application of the process. Two important changes were made. First, a more complex blind setup was realized (see Figure 3.31). **Several blinds** were used on the whole surface of the wafer. Furthermore, the blinds were positioned at a **certain angle**, which could be adjusted between 0° and 90°. Secondly, the substrate was being **moved forward and backward** during the sputtering, similar to what was done by Yanagitani *et al.*[83] This is expected to bring the required homogeneity of inclination and thickness. At the end of this thesis, the development of PROCESS III was still

[82] M. Kadota, T. Miura, Jpn. J. Appl. Phys. **41**, 3281 (2002); Y. J. Kim, Y. T. Kim, H. K. Yang, J. C. Park, J. I. Han, Y. E. Lee, H. J. Kim, *J. Vac. Sci. Technol. A* **15**, 1103 (1997).
[83] Yanagitani, N. Mishima, M. Matsukawa, Y. Watanabe, *Proc. IEEE Ultrason. Symp.*, 1824 (2005).

underway and a comprehensive parameter analysis was planned. In the next lines, only first preliminary results are presented.

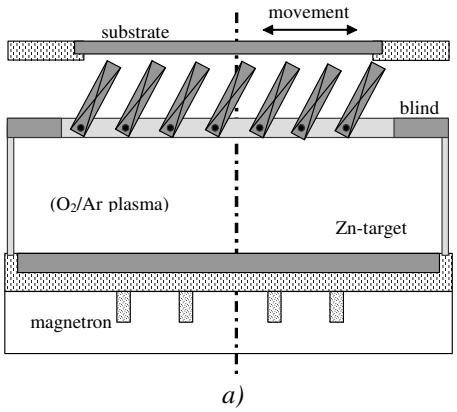

a)

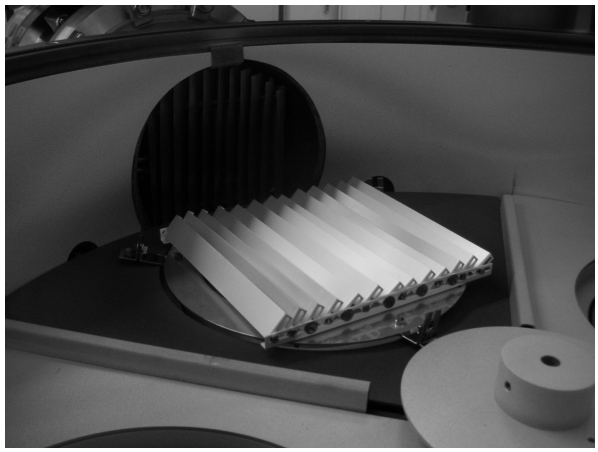

b)

Figure 3.31 : a) Schematic and b) photograph of PROCESS III and the complex blind.

3.6.2. Experimental

400 nm ZnO thin films were deposited reactively with the equipment described in section 3.4.1. These initial experiments were started with the best set of parameters obtained with PROCESS II given in Table 3.8. Sample PIIIa thus has the same parameters than sample PIIj. A complex blind setup was mounted between the target and the substrate. It was composed of 12 blinds made of stainless steel. They were placed at the centre of the target as shown on Figure 3.31 and an angle of 45° was used. The blind was grounded in order to eliminate charging and arcing effects. The ZnO films were deposited on 400 µm thick double-polished 4" Si (110) wafers covered with a 100 nm thick Pt thin film, which would later function as a bottom electrode to the FBARs. Amorphous Al_2O_3 buffer-layers were deposited onto the bottom electrode. Table 3.9 summarizes the sputtering properties for five samples. For the first two, the substrate was not moved during sputtering.

TABLE 3.9
RELEVANT ZNO FILMS WITH DIFFERENT PROCESS PARAMETERS FOR PROCESS III DEVELOPMENT

Sample number	Pressure, Temperature; Power	Forward and backward moving	Measured K_S
PIIIa	0.4 Pa; 150°C; 100 W	No	-
PIIIb	0.4 Pa; 150°C; 200 W	No	-
PIIIc	0.4 Pa; 150°C; 200 W	Yes	0.089
PIIId	0.4 Pa; 100°C; 200 W	Yes	0.097
PIIIe	0.4 Pa; 150°C; 500 W	Yes	0.136

All the wafers were sputtered on 100nm Al_2O_3 buffer-layers

3.6.3. Results and discussion

3.6.3.1. Piezoelectric excitation

As expected, samples PIIIa and PIIIb showed an inhomogeneous film thickness. A homogeneous thickness would have meant that the particles would have experienced collisions on their way from the blind to the substrate, cancelling the oblique incidence. The samples were first characterized piezoelectrically using highly over-moded FBARs. Figure 3.32 a) shows the recorded broadband characteristics for samples PIIIa and PIIIb at the centre of the wafer. The recorded peaks can be attributed to a shear (SM) or longitudinal (LM) mode resonance using simulations with the Mason Model. Comparing with Figure 3.10 of PROCESS I and Figure 3.19 of PROCESS II, we can see that the phase reaches much higher values at the resonance frequencies, which indicates high coupling coefficients. Figure 3.32 b) shows a narrow-band view of the shear mode resonance of PIIIb with over-modes spacing of 5.78 MHz. Similar measurements were done everywhere on the wafer. It was found that shear mode could be **excited on the whole wafer** surface in the regions with sufficient film thickness. PIIIb was sputtered at double power to get a double sputtering rate. Its recorded over-modes had larger phase amplitudes as shown on Figure 3.32 a), which is an indication of a higher coupling coefficient and of slightly bigger inclinations, confirming what was found with PROCESS II.

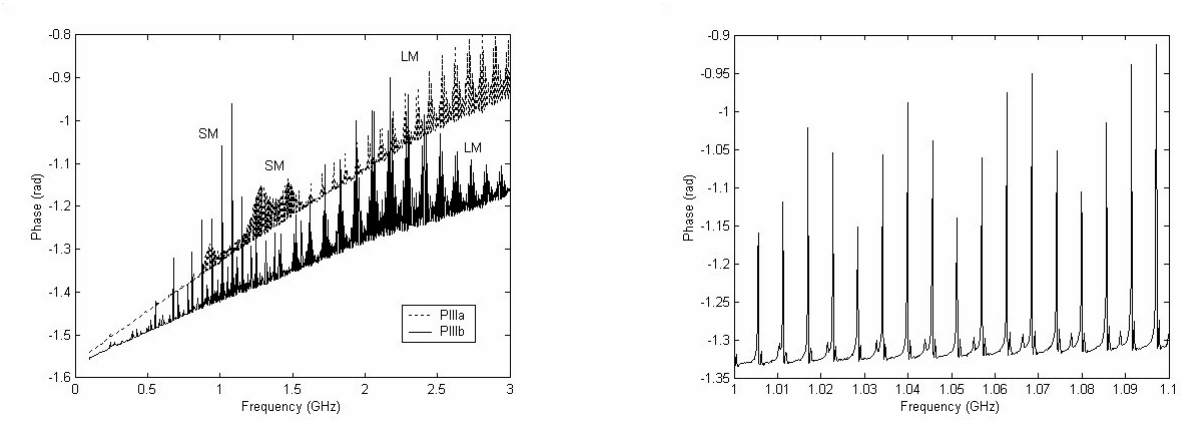

Figure 3.32 : a) Broadband impedance characteristics for samples PIIIa and PIIIb and b) narrowband for PIIIb.

For samples PIIIc, PIIId and PIIIe, the wafer was moved forward and backward during sputtering. This resulted in very homogeneous film thicknesses over the whole wafer. Interferometer measurements showed an homogeneity better than ±5%, which is comparable to PROCESS I. As expected the sputtering rate of sample PIIIc was lower than for sample PIIIb due to the movement of the wafer. This is why the power was further increased to 500W for sample PIIIe. Some arcing problems occurred here due to the high charging of the blinds. Figure 3.33 a) shows the recorded narrowband characteristic for sample PIIIe at three different points on the wafer. The points were recorded perpendicularly to the movement direction of the substrate at the borders and the centre. We can see that the phase amplitudes are similar for the three points, indicating a good homogeneity over the wafer surface. The phases of points on samples PIIIc and PIIId reach similar values, although sample PIIe has slightly higher values, which could indicate a higher coupling coefficient.

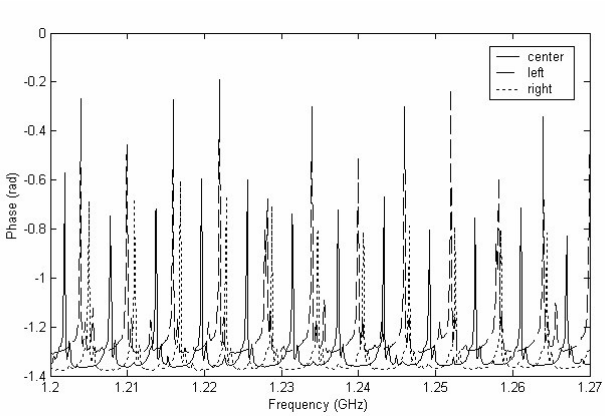

Figure 3.33 : Narrowband characteristics of sample PIIIe for three different points on the wafer.

3.6.3.2. Obtained coupling coefficients and XRD scans

The coupling coefficient of samples PIIIc, PIIId and PIIIe were extracted using the over-modes fitting method described in section 2.6.3. They were recorded at 5 different spots on the wafer to have an indication about the obtained homogeneity. For all three samples, the coupling **did not vary significantly** over the wafer surface. The obtained coefficients are reported in Table 3.9. The highest coupling coefficient of **0.136** was obtained for sample PIIIe sputtered at 500W. This confirms that an increase of the sputtering power increases the inclination. Sample PIIId sputtered at 100°C has a slightly higher coupling coefficient of 0.097 than sample Pc sputtered at 150°C, which confirms that the coupling and the inclination can be increased by lowering the temperature.

XRD χ scans were recorded on sample PIIIe at different points of the wafer perpendicularly to the movement direction. The scans look very similar which confirms the electrical measurements suggesting that the films are homogeneous on the whole wafer surface. The c-axis inclinations reach around **10°,** with a FWHM of approximately 20°, indicating a broad distribution of the c-axis inclination in the different grains, which can be related to the broad distribution of incidence angles. The measurements confirm the good homogeneity of the film on the whole surface.

3.6.4. Perspectives

The first results of PROCESS III are very promising. Very homogeneous films, both in thickness and inclination, have been obtained. To our knowledge, no process has been presented in literature realizing homogeneous inclined ZnO films suitable for shear wave mode excitation on whole 4", and possibly 6", wafers, with coupling coefficients of more than 0.13. Moreover, large improvements are still possible by adapting the sputtering parameters. The **advantages** of the process are the homogeneity on substrates with large size, the fact that the substrates do not need tilting during sputtering and that planar charging systems can still be used, and that inclined ZnO with high coupling coefficients can be sputtered on amorphous substrates. A **disadvantage** of this process is that ZnO is also being deposited on the blind, which must be

cleaned regularly. The sputtering rate of 4.1 nm/min is quite low, but could be improved by increasing the applied sputtering power.

Since the process yields homogeneous films an optimization of the processes is much easier to realize than with PROCESS I and PROCESS II. At the end of this thesis there were comprehensive experiments going on with the aim of optimizing the properties. Parameters varied included the temperature, the power, the pressure, the partial pressure, the inclination angle of the blinds and the pulse width. It was also planned to use different buffer-layers, some of which could favour more actively an inclination of the c-axis.

3.7. Chapter conclusion

In this chapter, the main processes developed to deposit c-axis inclined ZnO films suitable for shear wave mode excitation have been presented. First, the technique of sputtering, and more precisely reactive DC-pulsed magnetron sputtering, and the basics of thin film growth were introduced. The different thin film characterization techniques were shown. An overview of the different methods found in literature to deposit c-axis inclined ZnO was given. Afterwards the development of PROCESS I, PROCESS II and PROCESS III was explained. The requirements to the processes in this work were a) to **obtain c-axis inclined ZnO as fast as possible** in order to fabricate solidly mounted shear wave mode FBARs, b) to **use the existing planar wafer charging system**, c) to **use at least 4" wafers**, and d) to deposit the ZnO **on polycrystalline or amorphous films**. The three processes all resulted in the successful deposition of c-axis inclined ZnO films on amorphous substrates and used the existing planar charging systems with 4" wafers. Each one of them has its advantages and disadvantages. The main characteristics are summarized in Table 3.10.

PROCESS I did not use a modification of the sputtering equipment. Inclinations varied from zero inclination at the centre of the wafer up to a recorded maximum of 9° at the border. This process is inherently inhomogeneous and only 19% of the wafer surface can be used. However, due to its simplicity it would be worth being investigated in more detail. **PROCESS II** used a single blind positioned between the target and the substrates. The inclinations were found to depend strongly on the distance to this blind. The maximum recorded inclination was 16° and the inclination decreased with increasing distance to the blind. Here again, the process provides very inhomogeneous films. With this process however, it is possible to decide where to have the inclinations on the wafer. Around 30% of the surface could be used and coupling coefficients up to 0.105 were extracted. **PROCESS III** also used blinds positioned between the target and the substrate. The blinds permitted to cover the whole wafer surface and by moving the wafer during sputtering, homogenous films with inclinations of 10° were obtained on the whole wafer surface. Coupling coefficients of up to 0.136 were determined. To my knowledge, it is the first process permitting to sputter inclined ZnO films homogeneously on such large surfaces. With this, it can be thought of an industrial fabrication of inclined ZnO, since wafers up to 6" could even be processed.

For all three processes, the inclined film growth is a consequence of **oblique incidence** of the particles, which was shown with simple simulations. This relationship has been observed by numerous articles in literature, which obtained oblique particle incidence by tilting of the substrates. Although no comprehensive

study of the influence of the sputtering parameters on thin inclined film growth was done during this work, some mechanisms have been proposed and observed. For the three processes, it is expected that the ZnO films can be improved by adapting the sputtering parameters.

TABLE 3.10
MAIN CHARACTERISTICS OF PROCESSES I, II AND III FOR 4" WAFERS

Parameter	PROCESS I	PROCESS II	PROCESS III
Usable Wafer surface (on 4")	19 %	~ 30 %	~ 100 %
Thickness homogeneity	± 5 %	± 11 %	± 5 %
Electromechanical shear coupling coefficient	n.a.	0.105	0.136
C-axis inclination	0° to 9°	0° to 16°	10°
Maximum oblique incidence	30°	~25°	>60°
Sputter Rate	7.1 nm/min	6.6 nm/min	4.1 nm/min
Advantages	-no modification of the sputter recipient - high sputter rates	- choice of region of inclination by positioning of the blind	- c-axis inclination on whole surface - high shear mode coupling on whole surface - homogeneous film thickness
Disadvantages	- only border of wafer can be utilized for shear mode - inhomogeneous film properties	- very inhomogeneous film properties: rate, inclination, coupling	- lower sputter rate - blind cleaning necessary

4. SMR realization and characterization in air

Réalisation et caractérisation de SMRs à l'air — *Résumé*: Les couches minces de ZnO à axe c incliné, dont le développement a été décrit au chapitre 3, ont été utilisées pour réaliser des **résonateurs sur miroir acoustique (SMR)** vibrant en mode de cisaillement. Afin d'obtenir des capteurs biochimiques performants, la sensibilité et la résolution massique du SMR doivent être aussi bonnes que possibles. Ceci suppose une certaine épaisseur optimale des différentes couches du système et des facteurs de qualité suffisamment élevés. Pour ces raisons **une analyse de l'influence du miroir acoustique, de la couche intermédiaire nécessaire pour l'obtention du ZnO incliné, et des électrodes** a été faite. Les techniques de fabrication employées, ainsi que les différents designs et masques qui ont été utilisés, ont été brièvement expliqués. L'amélioration progressive des SMRs au cours de ce travail est présentée. Celle-ci a été réalisée en changeant les procédés de dépôt du ZnO ainsi que la structure du miroir acoustique. En utilisant le procédé II, des **SMRs vibrant à 749 MHz avec un coefficient de couplage maximal de 0.129 et des facteurs de qualité de 230** ont été obtenus sur un miroir acoustique de Pt et ZnO. Ces valeurs correspondent à une sensibilité relative théorique de -1000 cm^2/g et une résolution de moins de 10 ng/cm^2, ce qui est mieux que les valeurs typiques des QCMs. Comme l'inclinaison du ZnO varie fortement par rapport à la distance au cache, il en est de même avec les propriétés des SMRs ce qui rend utilisable qu'environ 30% de la surface du wafer. Avec le procédé III, qui donne des propriétés homogènes du ZnO sur toute la surface du wafer, des **fréquences de résonance de 731 MHz ±1.8%** ont été mesurées avec des **coefficients de couplage de 0.144 ±5.1 %** et des **facteurs de qualité de 244 ±8.5%.** Des capteurs SMRs avec de très bonnes performances peuvent ainsi être obtenus sur la surface entière du wafer, permettant d'envisager une fabrication à grande échelle de capteurs biochimiques intégrés.

4.1. Introduction

The c-axis inclined ZnO thin films described in Chapter 3 are used to realize FBARs. These require material interfaces that effectively confine waves to a finite volume. The method chosen in this work is to fabricate the resonator onto an acoustic mirror attached to a substrate to form **solidly mounted FBARs** (**SMR**). This prevents leakage of the acoustic wave into the substrate, since it will behave like an air interface. In comparison to thin membranes fabricated by bulk or surface micro-machining, this concept has the advantage of a planar technology, in particular simple fabrication and mechanical robustness. The latter is important since the SMRs have to undergo coating steps as well as packaging for their application as bio-chemical sensors. The absence of a special substrate preparation is also favourable for direct realization onto wafers with integrated circuitry. In 1965, Newell first described a method of transforming the impedance of a

Parts of this chapter have been released in the following publications: M. Link, M. Schreiter, J. Weber, R. Primig, D. Pitzer, R. Gabl, *IEEE Trans. Ultrason., Ferroelec., Freq. Contr.* **53**, 492 (2006); M. Link, J. Weber, M. Schreiter, W. Wersing, O. Elmazria, P. Alnot, *Sens. Act. B*, accepted, published online May 2006; M. Link, M. Schreiter, J. Weber, D. Pitzer, R. Primig et R. Gabl, *Proc. JNRDM*, Paris, 114 (2005); M. Link, M. Schmidt, J. Weber, R. Primig, D. Pitzer, R. Gabl, M. Schreiter, *Proc. Eurosensors XIX*, Barcelona, TB10 (2005); J. Weber, M. Link, R. Primig, D. Pitzer, W. Wersing, M. Schreiter, *IEEE Trans. Ultrason., Ferroelec., Freq. Contr.*, accepted.

substrate, e.g. a Si wafer, into a low effective impedance, resembling an air interface.[1] The technique uses quarter wavelength sections of materials with large impedance ratios and operates in the same way than an optical Bragg reflector, therefore termed **acoustic mirror**. A schematic view of the cross-section of such a structure is shown in Figure 4.1. The acoustic mirror is grown directly on a substrate, followed by a bottom electrode, a buffer-layer for inclined ZnO growth, a piezoelectric ZnO film, and a top electrode. The top of the resonator is thus similar to the highly over-moded FBARs described in paragraph 2.6 and used in Chapter 3.

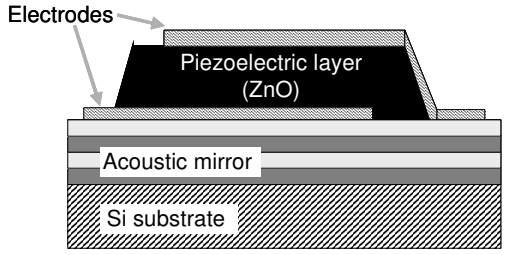

Figure 4.1 : Schematic view of a solidly mounted film bulk acoustic resonator (SMR).

The influence of the stack design, the coupling coefficient and the Q-factor on the sensitivity and mass resolution of SMR based sensors will be analyzed in paragraph **4.2**.The theory and simulation of SMRs will be treated in paragraph **4.3**. The fabrication technologies utilized in this work will be explained in paragraph **4.4**, along with different SMR designs. The objective was to have high resonator yields per wafer and a high homogeneity of the resonator properties. Both strongly depend on the chosen ZnO process. As was seen in Chapter 3, PROCESS II yields very inhomogeneous films but was used extensively to improve the ZnO deposition and the properties of the realized SMRs. The gradual progress will be detailed in paragraph **4.5** by analyzing their impedance in air. Finally, paragraph **4.6** will show some SMRs realized with PROCESS III, which yield good homogeneous properties.

4.2. Mass sensing characteristics of SMRs

The most important characteristics of a bio-chemical sensor are its selectivity, sensitivity and mass resolution.[2] The selectivity of a FBAR-based sensor is determined by the bio-chemical coating on the resonator surface and was not of interest in this work. The sensitivity of the device is closely related to its resonance frequency while the mass resolution also depends on the quality factor. In the following it will be seen how the properties of the SMR influence its sensing performance.

[1] W. E. Newell, *Proc. IEEE* **53**, 575 (1965).
[2] G. L.Coté, R. M. Lec, *IEEE Sensors J.* **3**, 251 (2003).

4.2.1. Sensitivity

The mass sensitivity is determined by the resonance frequency shift of the SMR with mass changes at its surface. For a simple FBAR consisting of only a piezoelectric film and infinitesimally thin electrodes on both sides, the absolute mass sensitivity can be described by the Sauerbrey relationship:[3]

$$S_a = \frac{\Delta f}{\Delta \mu} = -\frac{2}{\rho \cdot v_{ac}} f_0^2 \qquad (4.1)$$

v_{ac}, f_0 and ρ are the acoustic velocity, the resonance frequency and the density of the piezoelectric film. The absolute sensitivity of the device increases with the square of the resonance frequency. For a ZnO FBAR vibrating in shear mode at 800 MHz, which is the frequency projected in this work, the absolute sensitivity would be -807 Hz·cm^2/ng, giving a relative sensitivity of -1010 cm^2/g.

The sensitivity of SMRs can not be expressed in such a simple formula. The resonance frequency of a SMR is mainly determined by its top stack, consisting of the top and bottom electrodes, the piezoelectric layer, and sometimes, as in our case, different adhesion and buffer-layers. Simulations of this top stack have been done using the Mason Model to assess the influence on the sensitivity. The thickness of the electrodes was changed while the thickness of the ZnO was adapted to keep a resonance frequency of **800 MHz**. To simulate a mass attachment on the top electrode, its thickness was slightly varied.[4] Figure 4.2 shows how the relative sensitivity changes for a stack with the bottom and top electrodes having the same thicknesses. The thickness of the electrodes has an enormous influence on the sensitivity. As expected, it moves towards the Sauerbrey value of -1010 cm^2/g when the thickness of the electrodes approaches zero. With increasing thickness, the sensitivity for a device with Pt (Au) electrodes drops and approaches a value of around -430 cm^2/g (-600 cm^2/g) when nearing the limit value of 528 nm (372 nm) which is the quarter wavelength in Pt (Au).[5] Consequently to have the highest sensitivity, the thickness of the electrodes should be as thin as possible. However, with decreasing thickness the electrical resistance increases. The higher electrical losses would decrease the Q-factor of the device and degrade the signal. Therefore the thickness had to be limited to 100 nm, restricting the sensitivity to -813 cm^2/g for Pt and -697 cm^2/g for Au electrodes.

To avoid this sensitivity reduction while assuring good electrical conditions, another design of the top stack was necessary. As shown on Figure 4.3, the sensitivity can be increased when the bottom electrode thickness is adapted while keeping the thickness of the top electrode constant at 100 nm. For a Pt bottom electrode of a quarter wavelength, i.e. 528 nm, the sensitivity reaches a maximum of -1092 cm^2/g for both Pt and Au top electrodes, which is slightly higher than for a simple FBAR with no electrodes. These results were confirmed in experiments with longitudinal mode resonators.[6] In this case the bottom electrode efficiently acts as a **first mirror layer** and helps to confine most energy in the upper two films. The device is most sensitive when mass changes occur at points of high energy (or high deflection amplitude). This explains why the optimum

[3] G. Sauerbrey, *Zeitschrift für Physik* **155**, 206 (1959).
[4] To make sure that the simulated sensitivity was a pure mass sensitivity and had no acoustic component, the thickness variation had to be kept very small. The proper amount was ensured by considering several variations and looking only at the span in which the sensitivity stayed constant.
[5] The limit is reached when both electrodes are a quarter wave-length thick, i.e. a half wavelength in total, leaving no room for ZnO.
[6] R. Gabl, M. Schreiter, E. Green, H.-D. Feucht, H. Zeininger, J. Runck, W. Reichl, R. Primig, D. Pitzer, G. Eckstein, W. Wersing, *Proc. IEEE Sensors*, Toronto, 1184 (2003).

of a simple FBAR is reached when the electrodes are infinitesimally thin: the top and bottom interfaces of the piezoelectric then correspond to the points of maximum deflection. It is also known from SAW devices that the closer the energy is to the surface, the more sensitive the device becomes. For thin electrodes, the deflection will not change much with changing phase fractions in the electrode. This is the reason why no difference is seen between Au and Pt in Figure 4.3. In this work, it was decided to use a **quarter wavelength thick Pt bottom electrode** and a **100nm thick top electrode** in order to maximize the mass sensitivity of the device while keeping a low electrical electrode resistance.

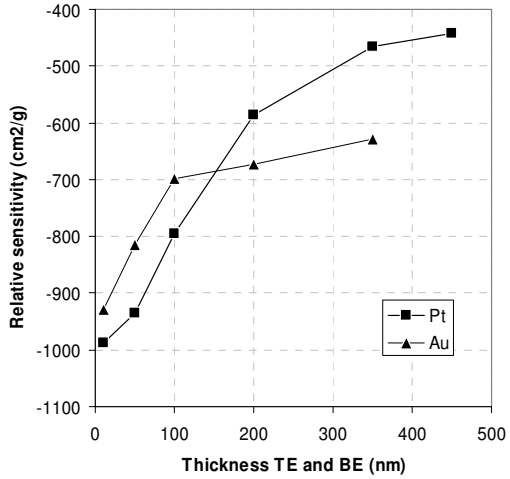

Figure 4.2 : Sensitivity change as a function of bottom and top electrode thicknesses for an FBAR vibrating at 800 Mhz.

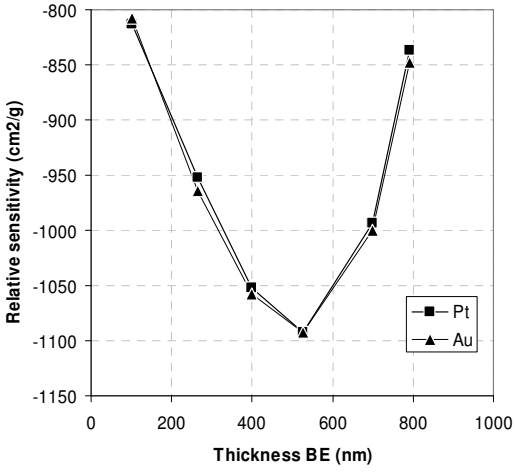

Figure 4.3 : Sensitivity change as a function of bottom electrode thicknesses. Top electrode thickness of Pt or Au is kept at 100 nm.

4.2.2. Mass resolution

The mass resolution is determined by the smallest frequency variation that can be detected by the electronic circuitry in which the resonator is inserted as a frequency determining element. The minimum frequency shift Δf and the mass resolution are related through the sensitivity of the device. In a simple oscillator circuit comprised of an amplifier and the SMR, the phase shift of the SMR impedance must add to the phase shift of the amplifier to yield a total phase shift in the system of $n \cdot 2\pi$ (n=0,1,2,3,…).[7] When the phase shift of the oscillator is fixed, the SMR vibrates at a frequency corresponding to such a phase that the total phase reaches $n \cdot 2\pi$. Often the required phase is 0°, which for a near-perfect FBAR corresponds to either the series or parallel resonance frequencies. When the frequencies shift, for example due to a mass adsorption on the FBAR surface, the corresponding phase-shift is detected. The larger the slope of the phase at the working point, the larger will be the phase shift due to a certain resonance frequency shift, i.e. the smaller will be the minimum detectable resonance frequency shift corresponding to the minimum detectable phase shift. This minimum detectable phase shift is dependent on the particular read-out circuitry. In this work, the measurements were performed with a **network analyzer**. The phase resolution is in this case related to the

[7] Lecture on Quartz oscillators, Prof. Reindl, IMTEK.

resistance and reactance of the impedance. If they match the internal impedance of the network analyzer (50 Ω), the phase resolution is optimal. Most resonators that have been measured have areas of $200 \times 200\ \mu m^2$ which for most of the stacks corresponds to an impedance amplitude between 30 and 50 Ω. In that case, the relative precision of the phase measurement is around 0.5%.[8] The phase resolution of the network analyzer is thus very dependent on the phase at which the measurement is done. With integrated electronic circuitry, this resolution is expected to be lowered.

In case of lossy resonators with a finite Q-factor, the phase shift $\Delta\varphi$ and the resonance frequency shift Δf at a certain frequency f_0 are related through formula (2.96) defining the Q-factor at that particular frequency:

$$Q = \frac{f_0}{2}\left.\frac{d\angle Z}{df}\right|_{f_0} \Rightarrow \Delta f = \frac{f_0}{2}\frac{\Delta\varphi}{Q} \tag{4.2}$$

The minimum detectable mass density μ_r can then be found by using the absolute sensitivity S_a:

$$\mu_r = \frac{f_0}{2}\frac{\Delta\varphi}{S_a \cdot Q} \tag{4.3}$$

Accordingly the mass resolution depends on the Q-factor at the phase or frequency of operation, chosen by the design of the read-out circuitry. This formula also shows that for a given $\Delta\varphi$ the mass resolution is relatively independent of the chosen resonance frequency, since typically the Q-factor is inversely proportional to the frequency. In section 2.5.3, we defined this Q-factor as Q_{SLOPE}, since it is determined by the slope of the phase. By considering formula (4.3), it becomes clear that both the sensitivity and the Q-factor of the SMR should be as high as possible. As was seen in paragraph 0, Q_{SLOPE} not only depends on the Q-factor of the SMR, which can be found by using the BVD model, but also on the effective coupling coefficient K_{eff}^2. For this reason, the objective of this work was to **realize SMRs both with high Q-factors and high coupling coefficients**, while at the same time ensuring a high sensitivity. Since $\mathbf{Q_{SLOPE}}$ varies depending at which frequency it is measured, we decided to define it **at the points of maximum and minimum phase slope**. For resonators with high Q-factors and high coupling coefficients, these points correspond to the series and parallel resonance frequencies.

4.3. Theoretical considerations and simulations

In section 4.3.1 the basic functioning of the acoustic mirrors used in this work is explained and their properties are simulated. In section 4.3.2, the different mechanisms influencing the effective coupling coefficient of an SMR are discussed. Simulations of complete SMRs are shown in section 4.3.3.

4.3.1. Acoustic mirrors

Analogous to an optical Bragg reflector, an acoustic mirror consists of a number of quarter wavelength layers of alternating high and low acoustic impedance. The mirror is the more efficient the larger the difference in

[8] Network Analyzer handbook.

acoustic impedances is. Depending on the impedance of the upper layer of the stack, a clamped or free interface can be obtained. Another important effect is the partial lateral stiffening of the piezoelectric layer, which minimizes spurious resonances normally observed in free plates.[9] This is particularly important in applications where the SMRs are used as filters.[10] In the following, the principle will be described in more detail and some material combinations will be analyzed in terms of reflectivity and obtained Q-factor. These values are theoretical values. In practice the Q-factors will be lower since there will be more losses than only those due to the imperfect reflectivity of the mirror (e.g. wave scattering, material losses, …).

4.3.1.1. Principle of an acoustic mirror

At the interface between two thin solid films of different acoustic impedances, an acoustic wave is partly transmitted and partly reflected. The reflection is characterized by the reflection coefficient R:

$$R = \frac{u_{reflected}}{u_{impinging}} \tag{4.4}$$

u is the displacement amplitude of the respective waves. R is dependent on the acoustic impedance mismatch ratio $z=Z_2/Z_1$ and can be calculated with:[11]

$$R = \frac{z-1}{z+1} = \frac{Z_2 - Z_1}{Z_2 + Z_1} \tag{4.5}$$

Z_1 and Z_2 are the acoustic impedances of the film carrying the incoming wave and the transmitted wave respectively. They are calculated using formula (2.75): $Z_{ac} = \rho v_{ac}$. R is always comprised between -1 and 1. When R is negative the phase-shift of the reflected wave is $+\pi$ and represents a free interface as for example an interface with air. When R is positive the reflected wave will experience no phase-shift and one has a clamped interface. At each interface of an acoustic mirror, the acoustic waves are reflected and transmitted, and |R| should be as high as possible. As the waves experience different phase-shifts at the interfaces, the layers of the mirror must have thicknesses of a quarter wavelength ($\lambda/4$) to assure that the waves interfere constructively. A phase shift of π at the interface means that the reflected wave is in phase with the incoming wave. A phase shift of zero means the reflected wave has the opposite phase than the incoming and will be subtracted.

When the quarter-wavelength condition is not perfectly fulfilled, the acoustic mirror will be less efficient. For frequencies other than the frequency for which the mirror was designed, the total mirror reflection will be lower. The total number of layers needed for a certain reflection depends on the ratio of acoustic impedance of the high and low impedance layers. The equivalent impedance of the acoustic mirror and the resulting reflection coefficient can easily be calculated by successive use of the transmission line impedance equation (2.76) presented in section 2.4.2. The impedance at the lower end of the acoustic mirror is most often the impedance of the Si substrate. A quality factor Q_{mirror} attributed to an imperfect mirror can be

[9] W. E. Newell, *Proc. IEEE* **53**, 575 (1965).
[10] K. M. Lakin, K. T. McCarron, R. E. Rose, *Proc. IEEE Ultrason. Symp*., 905 (1995).
[11] R. Lanz, PhD Thesis N°2991, EPFL, Lausanne (2004).

calculated in the following way. The energy of an incoming acoustic wave travelling in a medium of acoustic impedance Z_0 is:[12]

$$E = \frac{1}{2} Z_0 \omega^2 u_0^2 \tag{4.6}$$

ω is the angular frequency of the wave and u_0 is its maximum amplitude. The amplitude u_1 of the transmitted wave is related to the amplitude of the incoming wave by:

$$u_1 = \left(1 - |R|\right) \cdot u_0 \tag{4.7}$$

By considering the energy of the transmitted wave as lost, the mirror quality factor Q_{mirror} can be calculated with the help of formula (2.95), which yields:

$$Q_{mirror} = 2\pi \frac{1}{\left(1 - |R|\right)^2} \approx \frac{\pi}{1 - |R|} \tag{4.8}$$

This Q-factor is only associated with losses due to the imperfect reflectivity of the mirror. Other losses in the device are not taken into account. However, unlike Q_{mirror}, which improves when the number of acoustic mirror layers increases, the Q-factors due to these other losses generally diminish, since the roughness of the layers and the complete thickness of the mirror increase. It is known from literature that typical Q-factors of FBARs are between 300 and 1000.[13] For membrane FBARs, where nearly perfect reflections exist on both sides of the FBAR, one can assume that the Q-factor is mainly determined by material losses and scattering losses due to the roughness of the layers. In case of an SMR, the additional losses due to the imperfect reflectivity of the mirror should be kept negligible with respect to the material and scattering losses. Formula (4.8) is used to ensure that the overall Q of the solidly mounted FBAR will not be limited by the imperfect reflectivity of the mirror. If Q_{mirror} is set **to at least 2000**, which is well above the usual Q-factors obtained with solidly mounted FBARs, its absolute **reflection coefficient should be above 0.9984** according to equation (4.8). For comparison, if no acoustic mirror is used and the FBAR is put directly onto the Si substrate, the reflection coefficient would be -0.6062 representing a Q-factor of only 40.[14]

4.3.1.2. Materials and mechanical impedances of available materials

In this sub-section, some materials available at CT MM2 will be analyzed in terms of their usefulness for the realization of acoustic mirrors. It is known that one of the best combinations for realizing an acoustic mirror is SiO_2/W.[15] While this material combination was available at CTMM2 at the end of this thesis, other materials had to be used at the beginning of it. The most important property is their acoustic impedance. Their quarter wavelength thickness is also important, since it determines the whole thickness of the acoustic mirror. A larger thickness means a longer processing time and can also induce stress-problems. **In the best case, the chosen acoustic mirror pair should have a high acoustic impedance mismatch ratio z and a**

[12] J. Rosenbaum, *Bulk Acoustic Wave Theory and Devices*, Artech House, Norwood, MA (1988).
[13] K. M. Lakin, G. R. Kline, K. T. McCarron, *IEEE Trans. Microwave Theo. Techn.*, **41**, 2139 (1993).
[14] This supposes that the wave is completely lost when having entered the substrate. As seen in Chapter 2, this is generally not the case for polished crystalline substrates like Si and provides the starting point for over-moded FBARs.
[15] S.-H. Lee, K. H. Yoon, J.-K. Lee, *J. Appl. Phys.* **92**, 4062 (2002).

low thickness. Typically, metals have high acoustic impedances and oxides have low acoustic impedances. Table 4.1 gives the values of density, acoustic velocities and acoustic impedances for various materials for shear and longitudinal mode propagation available at CTMM2. For comparison Al and AlN are also shown. Figure 4.4 plots these materials as a function of their acoustic shear wave impedance and their acoustic velocity. The figure also shows the quarter-wavelength in the materials for a frequency of 800 MHz.

TABLE 4.1
MATERIAL PROPERTIES OF MATERIALS RELEVANT FOR MIRROR DEVELOPMENT

Material	Vac longitudinal [m/s]	Vac shear [m/s]	Density [kg/m3]	Zac long [10^7kg.s^{-1}.m^{-2}]	Zac shear [10^7kg.s^{-1}.m^{-2}]	Relative Permittivity
W	5320	2840	19270	10.3	5.47	-
Pt	4080	1690	21500	8.77	3.63	-
Au	3280	1190	19300	6.33	2.30	-
Ti	6260	2920	4505	2.82	1.32	-
Al	6360	3130	2698	1.72	0.84	
ZnO	6370	2830	5606	3.57	1.59	10.2
AlN	11400	6330	3260	3.60	2.06	10.5
ZrO_2	6965	3509	5680	3.96	1.99	12
SiO_2	5968	3764	2200	1.31	0.828	4
TiO_2	7360	4600	4260	3.14	1.96	80
Al_2O_3	11130	5790	3965	4.41	2.30	7.5
Si_3N_4	8230	6676	3100	2.55	2.07	7.5

References: D'Ans-Lax, Taschenbuch für Chemiker und Physiker, Springer-Verlag, 3. Auflage, 1967; [www.matweb.com]

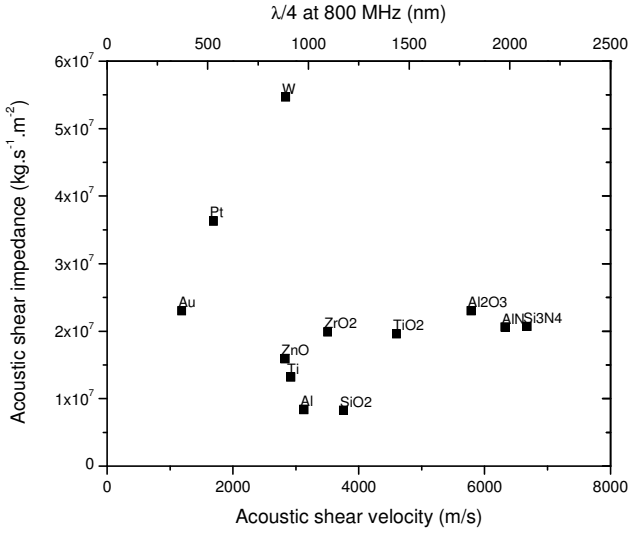

Figure 4.4 : Acoustic shear impedances and velocities for various materials available at CT MM2.

It is seen that the highest difference of acoustic impedances is given for **W-SiO_2**. Moreover, with a combined thickness of 2064 nm at a centre frequency of 800 MHz, its thickness is acceptable. Pt has the second highest

acoustic impedance and its combination with ZnO or SiO_2 is also a good choice. ZnO has the advantage of having one of the lowest thicknesses of the low-impedance materials and was easily available due to its use as piezoelectric layer. **The combinations Pt-SiO_2, Pt-ZnO and W-SiO_2 will be studied from a theoretical point of view**. Other important aspects in the development of the mirrors are layer adhesion, stress and roughness. The Pt-ZnO mirror was used for most SMRs realized in this work.

4.3.1.3. Simulations results and discussion

The mirror simulations focus on acoustic mirrors with centre frequencies of 800 MHz. The substrates used in this work are Si (100) wafers and have been oxidized at the surface yielding an additional 500 nm thick layer of SiO_2. At the centre frequency of the acoustic mirror, the quarter-wavelength condition is perfectly fulfilled, meaning that the phase shift in each layer will be $\pi/2$. In that case, the transmission line impedance equation (2.76) for each layer simplifies to:

$$Z_{in} = \frac{Z_0^2}{Z_t} \tag{4.9}$$

Starting at the lowest layer up to the uppermost layer of the mirror, this equation permits to find the **centre reflection coefficients depending on the number of acoustic mirror layers**. The results of this calculation are given in Figure 4.5. The reflection and the associated Q_{mirror} increase much faster for W-SiO_2 and Pt-SiO_2 mirrors with impedance ratios of 6.6:1 and 4.4:1 respectively, than for a Pt-ZnO mirror with a ratio of 2.3:1. According to the theoretical calculations of subsection 4.3.1.1, a reflection coefficient of 0.9984 is required in order not to limit the Q-factor of the SMR by the imperfect mirror reflectivity. This condition permits to find how many mirror pairs are needed for each combination of materials. For the W-SiO_2 and Pt-SiO_2 mirrors, 2 pairs are sufficient to reach this minimum reflection. For the Pt-ZnO mirror, 4 pairs are needed.

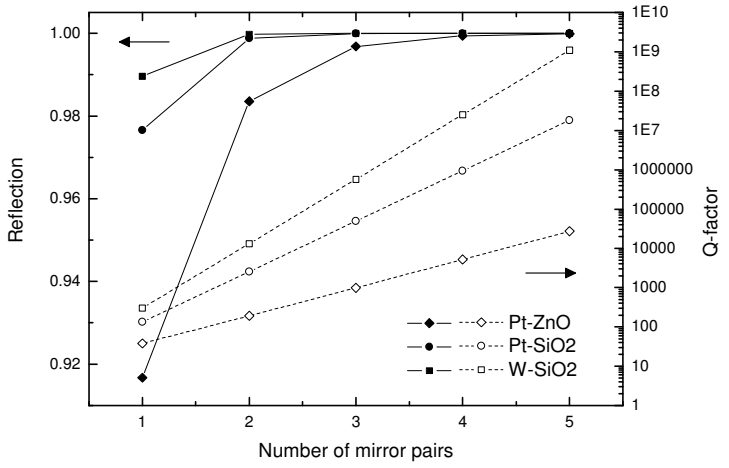

Figure 4.5 : Centre reflection coefficient (solid line) and corresponding Q-factor (dashed line) as a function of the number of mirror pairs for three different mirrors: Pt-ZnO, Pt-SiO_2 and W-SiO_2.

To find the complete frequency dependence of the reflection coefficient, the transmission line equation must be used for the whole frequency spectrum. For this, a MATLAB program was implemented. Starting with the impedance of Si, the transmission line equation was successively applied up to the uppermost mirror layer giving an effective acoustic impedance of the total acoustic mirror. The calculation of the reflection coefficient was done with respect to a Pt bottom electrode using equation (4.5). Figure 4.6 a) shows the results for the **Pt-ZnO mirrors** with 528 nm Pt and 884 nm ZnO. The comparison between n-fold mirrors is done, with n equal to 1, 2, 3 or 4. The centre reflection corresponds to the value given in Figure 4.5. For a 4-fold Pt-ZnO mirror, the reflection is 0.9994, corresponding to a Q_{mirror} of **5200**. For a 3-fold mirror, the minimum reflection is only 0.9968, which corresponds to a Q_{mirror} of 980. For a real SMR, Q_{mirror} will be even less, since often the resonance frequency of the upper stack does not perfectly correspond to the centre frequency. The mirror can also have imperfect layer thicknesses lowering the minimum reflection or shifting it to another frequency. The 2- and 1-fold mirrors do not yield reflections high enough to be exploited in this work. Figure 4.6 b) shows the equivalent impedance of the mirror. At the centre frequency, the acoustic impedance of Si, $8.91 \cdot 10^6$ kg·m^{-2}s^{-1}, is effectively transformed into an impedance nearing 0, which corresponds to an air-interface. For a 4-fold Pt-ZnO mirror, it has a value of around $0.02 \cdot 10^6$ kg·m^{-2}s^{-1}.

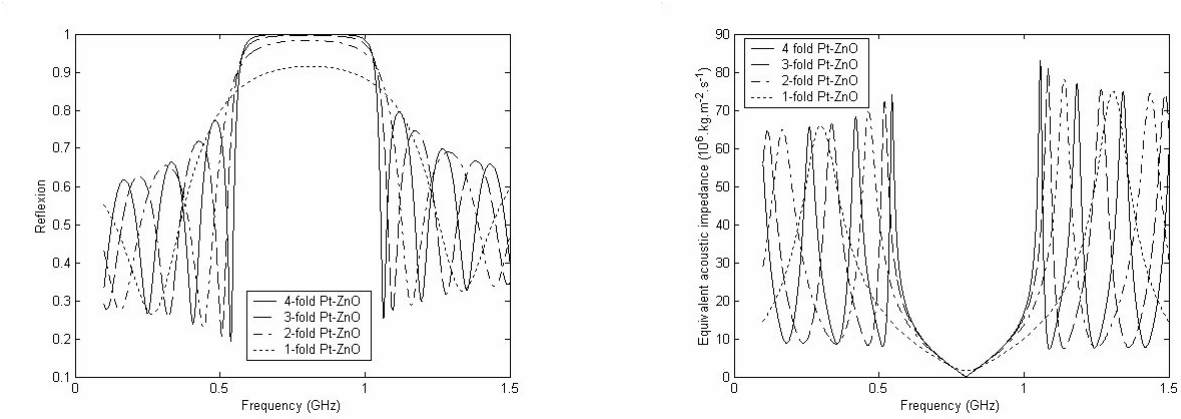

a) *b)*

Figure 4.6 : Reflection coefficient (a) and effective impedance (b) for Pt-ZnO acoustic mirrors with 1, 2, 3 or 4 pairs.

The **Pt-SiO_2 mirrors** were not realized in this work, since the SiO_2 layers were not easily available. However, at a later stage of this work, the top ZnO layer of the 4-fold Pt-ZnO mirror was replaced by a 1176 nm thick SiO_2 layer, which slightly improved the reflection as shown on Figure 4.7. The minimum reflection of the combined **Pt-ZnO-SiO_2 mirror** is 0.9998, giving a theoretical Q-factor of **15700**, which is higher than the Q-factor of the simple 4-fold Pt-ZnO mirror of 5200. While both Q-factors lie well-above the Q-factor limitations of the other loss mechanisms, it was found that the overall Q could nevertheless increase due to this layer change. One explanation for this could be a better surface roughness of the SiO_2 compared to the ZnO, yielding less scattering losses. A second explanation will be discussed in sub-section 4.3.2.3.

Figure 4.8 shows the simulation results for the **W-SiO_2 mirrors** with 888 nm W and 1176 nm SiO_2. As expected, low reflection coefficients can be obtained with a low number of mirror pairs. For a two-fold mirror, we get a reflection coefficient at the centre frequency of 0.99976, corresponding to a Q-factor of

13100, which is better than the simple 4-fold Pt-ZnO mirror, but less good than the combined Pt-ZnO-SiO2 mirror. A 3-fold mirror increases the theoretical reflection to a nearly perfect value of 0.99999, corresponding to a Q-factor of more than 500000. Compared with the 4-fold Pt-ZnO mirror with top SiO_2 layer, which is represented on Figure 4.8 as a dashed line, one can also see that the bandwidth of the mirror is significantly increased. This will be treated in more detail in the next sub-section.

Due to technological reasons various buffer-layers and adhesion layers with thicknesses of less than 25 nm were needed between the mirror layers. It was shown that these buffer-layers do not have a significant influence on the resulting reflection coefficient. In conclusion the following combinations provide sufficient reflection and were realized in this work: **4-fold Pt-ZnO, combined 4-fold Pt-ZnO with top SiO_2 layer, and 2- or 3-fold W-SiO_2**. A 3-fold Pt-ZnO mirror was used at the beginning of this work, since it was used previously for longitudinal mode SMRs.

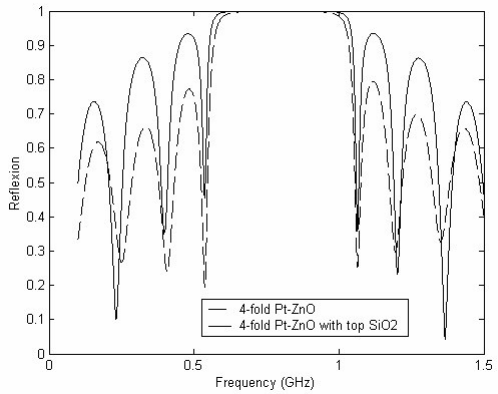

Figure 4.7 : Reflection coefficient for a 4-fold Pt-ZnO mirror with top SiO_2 layer.

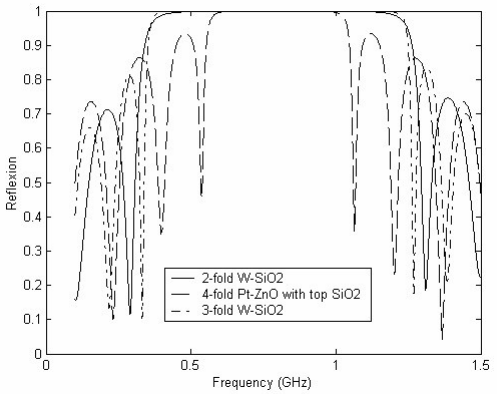

Figure 4.8 : Reflection coefficient for W-SiO2 mirrors.

4.3.1.4. Robustness of the mirror against layer thickness variations / errors

In all thin film processes there can be thickness errors, which relate directly to a change of resonance frequency for the top stack, and a change of centre frequency for the mirror. As was seen in Chapter 3, the ZnO layers can have a thickness inhomogeneity of up to ±11%. Since the thickness of the ZnO and the resonance frequency are related, this inhomogeneity translates into a frequency variation of ±4 % for a typical stack.[16] A change of the resonance frequency can be handled by the **bandwidth of the mirrors**. The bandwidth of the mirror increases with the acoustic impedance ratio.[17] We define the bandwidth of the mirror as the frequency span for which the reflection stays above **0.9984** corresponding to a Q-factor of 2000. The bandwidth of a 4-fold Pt-ZnO mirror is approximately 240 MHz. With a top SiO_2 layer, it increases to 350 MHz. The bandwidth of a 2-fold W-SiO_2 mirror has a much higher value of about 590 MHz. Since the impedance ratio is higher, most of the wave will already be reflected in the upper layers of the mirror, and it can work for a broad range of frequencies even when the constructive condition is not perfectly fulfilled. The bandwidths are sufficiently high to handle typical frequency variations.

[16] Simulation: 0.1Pt,0.4ZnO,0.1Al_2O_3,0.5Pt →894.2MHz, ZnO+11% →858.9MHz, ZnO-11% →932.5MHz, total → +/- 4%
[17] K. M. Lakin, *Proc. IEEE Ultrason. Symp*., 895 (1999).

An **error in mirror layers thicknesses** has an influence on the minimum reflection at the centre frequency, since the quarter-wavelength condition will not be fulfilled. The influence of a thickness variation on the resulting reflection coefficient and Q-factor was calculated for a Pt-ZnO 4-fold mirror. Figure 4.9 shows the result for a deviation of only the Pt, only the ZnO, or both layers simultaneously. For a thickness deviation of ± 10 % of either the Pt or the ZnO, which is more than what was typically observed in this work, the quality factor decreases by 13%. When both the Pt and ZnO layers vary by the same amount in the same direction the maximum deviation for a variation of ± 10 % is 35 %. The Q-factor drops to 3400, which is still above the chosen limit of 2000. When the Pt and the ZnO vary in opposite direction, the Q-factor variation of each of the layers is partly compensated and is therefore less than 10 %. In conclusion, typical process thickness errors do not influence greatly the reflection and the Q-factor, which is also confirmed in literature.[18]

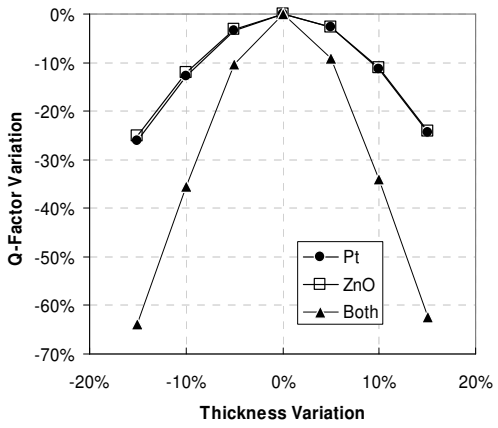

Figure 4.9 : Effect on a Pt-ZnO acoustic mirror Q-factor by thickness variation of the layers.

4.3.2. Effective coupling coefficient

The effective coupling coefficient K_{eff}^2 of the SMR is important in filter applications since it directly determines the bandwidth, as becomes clear by looking at equation (2.116), repeated here:

$$K_{eff}^2 \approx \left(\frac{\pi}{2}\right)^2 \frac{f_p^2 - f_s^2}{f_p^2} \tag{4.10}$$

In this work, the SMRs are used for sensing applications and the effective coupling coefficient as such is not important. However, as was seen in section 2.5.3, it influences Q_{SLOPE}, which determines the mass resolution of the sensing device given in equation (4.3). Accordingly, K_{eff}^2 should be as high as possible. The effective coupling coefficient depends for a big part on the electromechanical coupling coefficient of the piezoelectric ZnO layer. The high coupling coefficient of the ZnO was one reason why this material was chosen in this work. As was seen in Chapter 3, it can be significantly decreased depending on the crystallographic and morphological properties of the thin film. For SMRs, which are multi-layers systems, the effective coupling coefficient is not only related to the ZnO quality. In this section, we will see that the design of the acoustic

[18] S.-H. Lee, J.-H. Kim, G.D. Mansfeld, K. H. Yoon, J.-K. Lee, *Proc. IEEE Int. Freq. Contr. Symp.*, 45 (2002).

stack can also change the effective coupling coefficient. In sub-section 4.3.2.1, the effect of the electrode thicknesses on the effective coupling will be investigated. Sub-section 4.3.2.2 will show how additional dielectric layers between the electrodes lower the coupling coefficient. Finally, sub-section 4.3.2.3 will show that the effective coupling coefficient also depends on the utilized acoustic mirror.

4.3.2.1. Change of the coupling due to the electrodes

The coupling of the resonator decreases with increasing electrode thickness, as an increasing part of the mechanical energy is stored inside the metal. However, Lakin *et al.* showed that the effective coupling coefficient can be slightly increased above the ZnO value for certain electrode thicknesses.[19] This is due to a matching between the standing wave pattern of the electromechanical and electrostatic modes. For infinitesimally thin electrodes, these modes do not match, since their boundary conditions are different, leading to a lower coupling (the top interface is stress-free but exhibits a non-zero electric potential). Lakin *et al.* found that for equally thick top and bottom electrodes, the **maximum coupling is obtained at an electrode to piezoelectric ratio of 0.1**. With ZnO thicknesses of approximately 500 nm as in this work, this would mean an electrode thickness of only 50 nm, which is a problem due to the low electrical resistance. Simulations with the Mason Model have been done to assess how the effective coupling coefficient changes with changing electrode thicknesses. Figure 4.10 shows the result for varying electrode to piezoelectric thickness ratios. In the simulations, the thickness of the ZnO has been adapted in order to keep the resonance frequency at 800 MHz. As in the paper by Lakin *et al.*, a maximum at around 0.1 was found. With increasing electrode thickness, the coefficient decreases and at a certain ratio it drops below the value of the electromechanical coupling coefficient of the piezoelectric. For Pt the increase of the coupling coefficient works up to higher ratios than for Au electrodes, the reason being that Pt has a higher acoustic impedance, so that energy is better trapped inside the piezoelectric layer.[20]

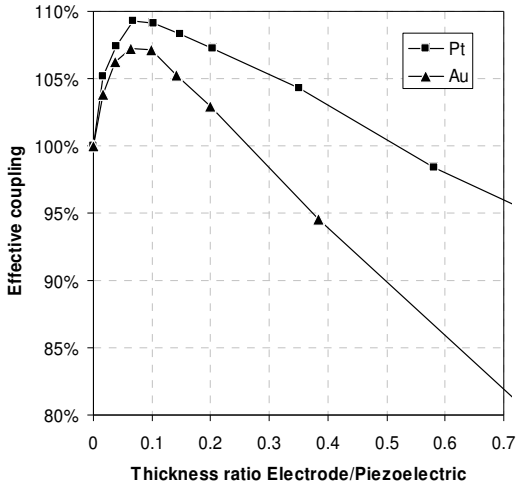

Figure 4.10 : Influence of top and bottom electrode thickness on effective coupling coefficient.

[19] K. M. Lakin, J. Belsick, J. F. McDonald, K. T. McCarron, *Proc. IEEE Ultrason. Symp.*, 827 (2001).
[20] A. Reinhardt, V. Laude, Th. Pastureaud, S. Ballandras, *Proc. IEEE Ultrason. Symp.*, 497 (2002).

The reduction of the coupling coefficient for the resonators of this work, which have a top electrode of 100 nm and a bottom electrode of 528 nm Pt to maximize the sensitivity as seen in section 4.2.1, can also be calculated. With a Pt top electrode, the **coupling coefficient drops to 90 % of the initial ZnO value**. For the Au top electrode, it drops slightly more, to 89 %. These simulations show that a trade-off must be made between sensitivity and coupling coefficient reduction. Although sensitivity is clearly more important in this work, one has to remember that if the coupling becomes too low, Q_{SLOPE} also becomes lower, having a negative effect on the mass resolution (see section 4.2.2).

4.3.2.2. Effective coupling reduction due to buffer-layers

An additional dielectric buffer-layer, in most cases amorphous Al_2O_3, is needed between the piezoelectric ZnO layer and the bottom electrode to ensure the ZnO inclination. Depending on the design of the acoustic stack, several thin adhesion layers must also be placed between both electrodes. All these layers will be called **buffer-layers** in the following. The situation is electrically more complicated than for the simple composite FBAR whose impedance was derived in section 2.3.2. In fact, those additional layers reduce the electric field seen by the piezoelectric layer, which reduces the effective coupling coefficient. It is insufficient to change the effective clamped capacitance to account for the electrical change; one must also consider the fact that an additional layer is inserted in the acoustic stack. The impedance and the Mason Model developed in section 2.4.3 have to be adapted. The derivation of the final impedance is similar to the derivation done in section 2.4.3, but the drop of the electric field over the additional buffer-layers must be taken into account. By attributing a capacitance C_n to each additional layer between both electrodes, the total capacitance C_{BL} due to the added buffer-layers between the electrodes can be calculated:

$$C_{BL} = \left(\frac{1}{C_1} + \frac{1}{C_2} + ... + \frac{1}{C_n} \right)^{-1} \tag{4.11}$$

The acoustic impedances of the buffer-layers above and below the piezoelectric layer are included in the equivalent terminating impedances of the top and bottom stacks, Z_T and Z_B respectively. For example, the acoustic impedance of the buffer-layer (SiO_2 or Al_2O_3) below the piezoelectric will be included in $Z_{B,L}$ or $Z_{B,S}$ depending on which mode is simulated. After a derivation comparable to the one done in section 2.4.3, one finds the electrical impedance of the resonator:[21]

$$Z = \frac{1}{j\omega C\xi} \cdot \left[1 - \xi K_L^2 \frac{\tan(k_L)}{k_L} \cdot \frac{(Z_{T,L} + Z_{B,L})\cos^2(k_L) + jZ_L \sin(2k_L)}{(Z_{T,L} + Z_{B,L})\cos(2k_L) + j(Z_{T,L}Z_{B,L}/Z_L + Z_L)\sin(2k_L)} - \xi K_S^2 \frac{\tan(k_S)}{k_S} \cdot \frac{(Z_{T,S} + Z_{B,S})\cos^2(k_S) + jZ_L \sin(2k_S)}{(Z_{T,S} + Z_{B,S})\cos(2k_S) + j(Z_{T,S}Z_{B,S}/Z_L + Z_L)\sin(2k_S)} \right] \tag{4.12}$$

This expression is similar to the one of equation (2.80), but $Z_{T,L}$, $Z_{B,L}$, $Z_{T,S}$ and $Z_{B,S}$ now also include the additional buffer-layers. The electrical field reduction is expressed by a correction factor ξ, which depends on the capacitances of the piezoelectric C (defined in (2.57)) and the additional C_{BL}:

[21] A similar expression has also been found in case of a single buffer-layer: J. J. Lutsky, PhD Thesis, MIT (1997).

$$\xi = \frac{C_{BL}}{C_{BL} + C} \tag{4.13}$$

From formula (4.12) it is evident that the clamped capacitance and both electromechanical coupling coefficients are reduced by ξ. Since formula (4.12) resembles formula (2.80), the remaining developments of paragraph 2.4 are still valid, especially the possibility to describe one particular resonance frequency with a simple model (the Butterworth-Van Dyke) using an effective electromechanical coupling coefficient K_{eff}^2 and effective parameters, giving a simplified form for the impedance valid around one resonance:

$$Z = \frac{1}{j\omega C}\left[1 - K_{eff}{}^2 \frac{\tan\left(\omega h_{eff}/v_{eff}\right)}{\omega h_{eff}/v_{eff}}\right] \tag{4.14}$$

The change of the effective coupling coefficient will be influenced both by the electrical field reduction and the change of the acoustic path. Similarly to what was done in section 2.4.3, expression (4.12) can be transformed to yield the Mason Model of Figure 2.13, but with the corrected clamped capacitance and coupling coefficients. The transformer ratios given in formulas (2.82) must both be divided by ξ^2 to account for the corrected values.

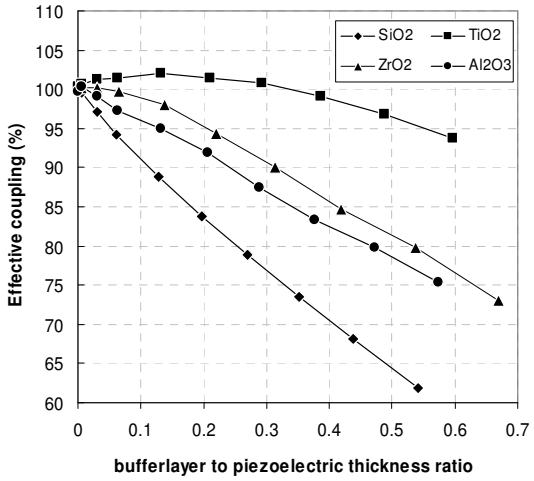

Figure 4.11 : Influence of a dielectric buffer-layer on the effective coupling coefficient K_{eff}.

The corrected Mason Model was implemented in MATLAB and simulations have been done to assess the change of effective coupling constant due to the additional buffer-layer. To exclude the influence of the electrodes, infinitesimally thin Pt top and bottom electrodes were taken (0.01nm). The buffer-layer thickness and material were varied. The ZnO thickness was adjusted such as to keep the resonance frequency constant at 800 MHz. Figure 4.11 shows the results for buffer-layers of SiO_2, ZrO_2, TiO_2 and Al_2O_3. As expected, the effective coupling coefficient is reduced with increasing buffer layer thickness. The reduction of the coupling coefficient depends on a large extend on the permittivity of the buffer-layer. The SiO_2 buffer-layer has the lowest permittivity and reduces the coupling by the biggest amount. The TiO_2 buffer-layer has the largest permittivity and the reduction is only very small. Moreover, the effect of the larger acoustic velocity of the TiO_2 is clearly visible, bringing a slight increase of the coupling for low thicknesses, with the same

mechanism as for the electrodes treated in the previous sub-section. In the best case, the **buffer-layer should thus be as thin as possible, and have high permittivity and acoustic velocity**. For a SiO_2 buffer-layer of 500 nm, which was used at the beginning of this work in PROCESS I and II development, K^2_{eff} diminishes by 80 %. For 100 nm Al_2O_3, which was mainly used in this work since it provided the highest ZnO inclinations, K^2_{eff} diminishes by less than 10 %. Since the inclinations obtained on Al_2O_3 exceeded those obtained on TiO_2 by more than 10 %, the choice of using Al_2O_3 was justified.

4.3.2.3. Change of coupling due to energy in mirror

A third effect can change the effective coupling coefficient K^2_{eff}. For SMR configurations, the acoustic mirror below the top stack does not only have an influence on the Q-factor, but also on the effective coupling. In fact, a fraction of the acoustic energy is stored in the nearest reflector layer.[22] Simulations using the Mason Model were run for the three mirrors described in section 4.3.1 with a top stack vibrating at 800 MHz and consisting of a 100 nm Pt top electrode, a 539 nm ZnO layer and a 528 nm Pt bottom electrode. As was seen in sub-section 4.3.2.1, this electrode configuration reduces the ZnO coupling coefficient by 10 %. With the simple 4-fold Pt-ZnO mirror, the coupling is further reduced by **15 %**, bringing the total coupling reduction of the ZnO to 23 %. For the combined Pt-ZnO-SiO_2 mirror, the additional reduction due to the mirror is only **9 %**. The situation is better in case of the 2-fold W-SiO_2 mirrors. Here, the additional reduction due to the mirror is only **3 %**. Since the reflection of the mirror is better, less energy will be stored in it. In case of a 3-fold W-SiO_2 mirror, the reduction due to the mirror is the nearly the same as for a 2-fold mirror.

4.3.3. Complete SMR simulations

Although the different mechanisms that exist for the coupling coefficient reduction have been treated separately in the previous sections, they have to be simulated all together for a particular SMR stack to obtain the **total effective coupling coefficient**. Complete simulations also provide valuable information about the fundamental shear and longitudinal frequencies of the stack, permitting the **design of the SMR prior to its realization**. Additional frequencies due to resonances in conjunction with the acoustic mirror can also be simulated, which helps **analyzing the observed impedance characteristics**. In fact, with composite SMRs, the resonance frequencies can be very different from those obtained with simple FBARs.

Figure 4.12 shows the simulations of a typical SMR with a 100 nm Au top electrode, a quarter-wavelength 528 nm Pt bottom electrode, a 520 nm ZnO layer and a 100 nm Al_2O_3 buffer-layer on a 2-fold W-SiO_2 mirror. The overall Q-factor has been set to 500 and the ZnO electromechanical coupling coefficient to 0.1. Since two Mason Models were implemented, one for the shear mode, one for the longitudinal mode, the impedance is shown as two superposed lines. As expected, the broadband characteristic is the same for both modes. It is specified on the figure which resonance belongs to which mode (SM for shear mode and LM for longitudinal mode). As can be seen, the various shear modes resonance peaks are not separated by the same frequency span, as would be expected for a simple FBAR. This is due to the multi-layer acoustic stack, which can produce resonances other than the simple fundamental and harmonics of the ZnO layer. The shear

[22] K.M.Lakin, *IEEE Trans. Ultrason., Ferroelec., Freq. Contr.* **52**, 707 (2005).

mode resonance peaks observed between 1.2 GHz and 1.5 GHz correspond to the local minima of the reflectivity of the acoustic mirror, as can be observed by comparing Figure 4.12 a) with Figure 4.8. The first shear mode frequency at 800 MHz is the one for which the acoustic mirror was designed and corresponds to the fundamental resonance frequency of the top stack. A narrow-band view is shown on Figure 4.12 b). The effective coupling coefficient that was extracted is at 73 % of the electromechanical coupling of the ZnO layer, i.e. it has been reduced by 27 %. When taking the different coupling reductions of the previous paragraphs separately, we arrive at a reduction of only 17%,[23] which shows that the complete stack has to be simulated to get a correct coupling reduction. The simulation of the same stack on a combined 4-fold Pt-ZnO mirror with top SiO_2 layer gives approximately the same result for the impedance than for the W-SiO_2 mirror. Complete simulations of the entire acoustic stack can give an indication of the effective coupling coefficient. The real coupling coefficient will of course depend on other factors, like the imprecision of the layer thicknesses and variations of their intrinsic properties, such as the acoustic velocity or permittivity.

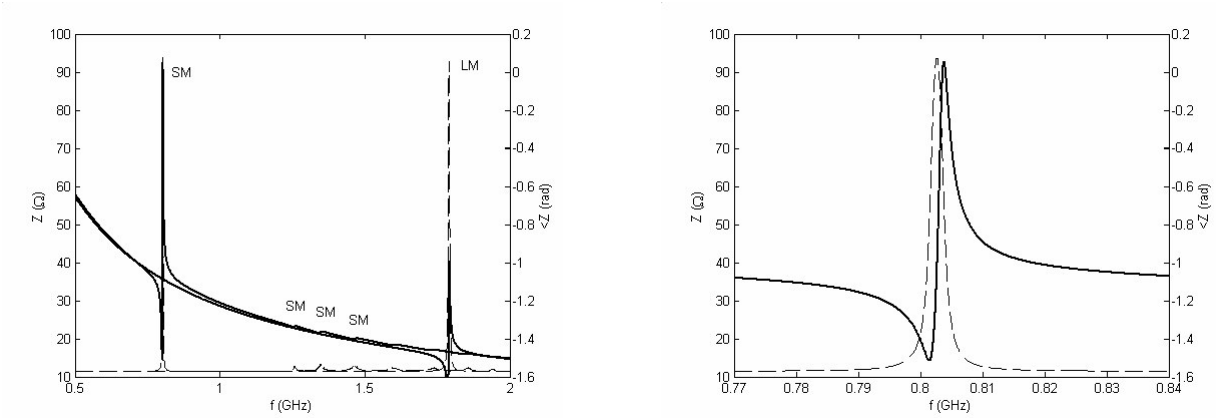

Figure 4.12 : Simulated impedance characteristic (a: broadband and b: narrow-band) of a typical solidly mounted FBAR on a 3-fold W-SiO_2 mirror with a total Q-factor of 500. The buffer-layer is 100 nm Al_2O_3.

4.4. Design and realization of SMRs

4.4.1. Fabrication technology

The different fabrication technologies employed in the realization of SMRs are well-known techniques of micro-technology and -electronics. Most procedures and processes were already available and well-established at CTMM2 and partner groups at the beginning of this work. Therefore they will not be explained in detail in this dissertation. For the sake of completeness, a brief description will be given, along with the experimental equipment that was used. For a complete explanation of the techniques we refer to the excellent work on micro-fabrication by Marc Madou.[24] Generally, the realization of the SMRs includes a series of processing steps, involving **deposition**, **etching** and **photolithographic** techniques.

[23] electrodes : 0.89, buffer-layer : 0.96, mirror : 0.97 → total reduction : 0.83
[24] M. J. Madou, *Fundamentals of Microfabrication*, CRC Press, Bacaraton, FL (2002).

Deposition techniques allow adding thin films to the wafer. The main technique used in this work was sputtering, which was extensively explained in Chapter 3. Besides the deposition of the inclined ZnO films, the sputtering technique was also used to deposit Pt, Al_2O_3, TiO_2, ZrO_2 and SiO_2 layers. The TiO_2, ZrO_2 and some SiO_2 layers were sputtered reactively in an Ar/O_2 ambient using the CS730S from *Von Ardenne Anlagentechnik*, Dresden, Germany, which has been presented in section 3.4.1. Pt and Al_2O_3 films were sputtered in pure Ar with a *Perkin Elmer* PE 2400, Palo Alto (CA), USA. Au layers that were needed for bio-chemical measurements and which were used as top electrodes, were deposited by thermal evaporation. The SiO_2 layers used for the fabrication of the acoustic mirrors and for some buffer-layers were deposited by CVD with a Multiplex Cluster System from *STS*, Newport, UK.

Photolithographic steps are needed to define the regions of the thin films that have to be removed. They involve the structuring of a photo-resist. After the photo-resist had been spun on the wafer using a Lithocluster EVG150 from *EV Group*, Schärding, Austria, it was illuminated by UV light shone through a mask containing the pattern to be transferred onto the wafer, with a MA150, from *Süss Microtech*, Munich, Germany. The mask is made of glass with a Cr layer defining the structures. The illumination can either polymerize the resist, in which case one speaks of a negative resist, or disrupt the polymer chains, in which case we have a positive resist. After this, the resist is developed, so that only either the illuminated or the shadowed polymerized regions remain. The next step is then an etching step, where the layer below the resist is structured, or a lift-off step, where some new material is deposited onto the resist. After this step, the remaining resist is stripped, leaving the structured thin film on the wafer.

Etching techniques allow structuring the previously deposited thin films. Usually, these steps are preceded by a photolithographic step used to pattern a photo-resist defining which regions are to be structured and which do not. Two different etching groups exist: dry etching and wet etching with chemical solutions. Dry etching mostly involves a plasma which can be reactive or not. Similar to sputtering, ions from the plasma permit to remove the atoms from the thin film. Most films including the Pt electrodes were dry etched in the Perkin Elmer PE 2400. Some layers like Pt and ZnO were etched in an ion beam etching (IBE) system, Milatron, from *CSC Commonwealth Scientific Corp*., Alexandria (VA), USA. Au films were mostly structured using the lift-off technique.

4.4.2. Stack design and mask layout

Two different stack designs were used in this work. They differ in the way the top stack is structured. Both designs use the same sort of acoustic mirrors below the top stack. The masks involved in the fabrication of the resonators of both stack designs were already available at the beginning of this work.

DESIGN 1, depicted on Figure 4.13 a) in the special case of 3-fold Pt-ZnO mirror, is very simple and only needs a single photolithographic step involving one single mask. It is similar to the design of the over-moded resonators described in section 2.6.1 and used in Chapter 3, except that an acoustic mirror is mounted below the top resonating layers. The active area of the device is determined by the area of the top signal electrode. Since the fabrication process is simple and rapid, it was used in most of the devices presented in this chapter to optimize the SMRs. The disadvantage of DESIGN 1 is that the bottom electrode is not contacted directly,

but capacitively coupled to a ground electrode on the top-layer. When the ground electrode on the top has a large surface, the capacitance is large and the impedance to the bottom electrode looks like a short-circuit. However, when single resonators are separated, this condition is not necessarily fulfilled anymore. Another disadvantage is that if working in a liquid environment, the signal and ground electrode are connected via an additional path through the liquid, which may add stray capacitances and resistances to the equivalent electrical circuit. Concerning the resonator shapes of the first design, two different **masks** have been used in the course of this work. They are shown in Figure 4.13 b) and c) The first mask (**classic**) has structures with long electrical lines, allowing using a flow-cell on the resonator surface for measurements in liquid environment while keeping the measurement needles dry. The second mask (**HD**) exhibits a **high density** of simple structures. It was used to do a mapping of the resonator properties over the surface of the wafer, which is particularly interesting for the very inhomogeneous PROCESS II.

DESIGN 2, depicted on Figure 4.14 a), solves both disadvantages of DESIGN 1. It is more complex and involves a series of several photolithographic steps. The main difference with the first design is that both the ZnO and the bottom electrode are structured. The advantage is that the ground and signal lines leading to the top and bottom electrodes are clearly separated and the ground electrode can be contacted directly. Some resonators are organized into arrays where the ground electrode is the same for all resonators and which are planned to be used for bio-chemical measurements (see Figure 4.14 b)). Additionally, more complex resonator shapes have been included on the masks. The second design was mostly used for experiments in liquid environments.

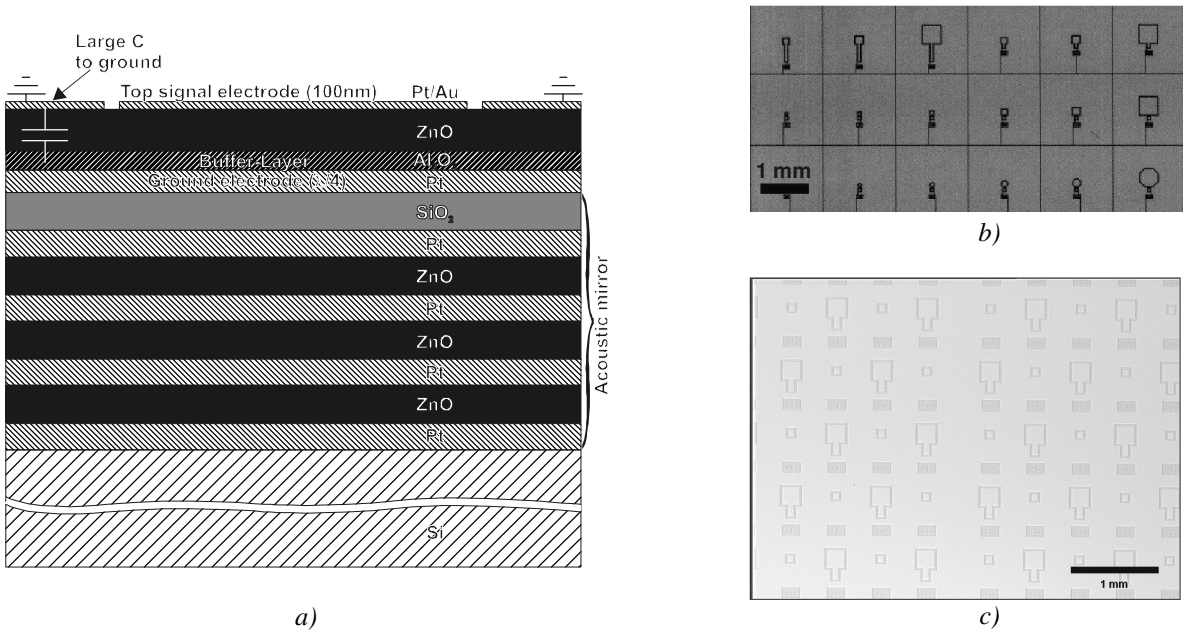

Figure 4.13 : a) Schematic cross-section of DESIGN 1 acoustic stack with a 4-fold Pt-ZnO mirror with top SiO_2 layer; b) classic mask picture and c) high density mask microscope view.

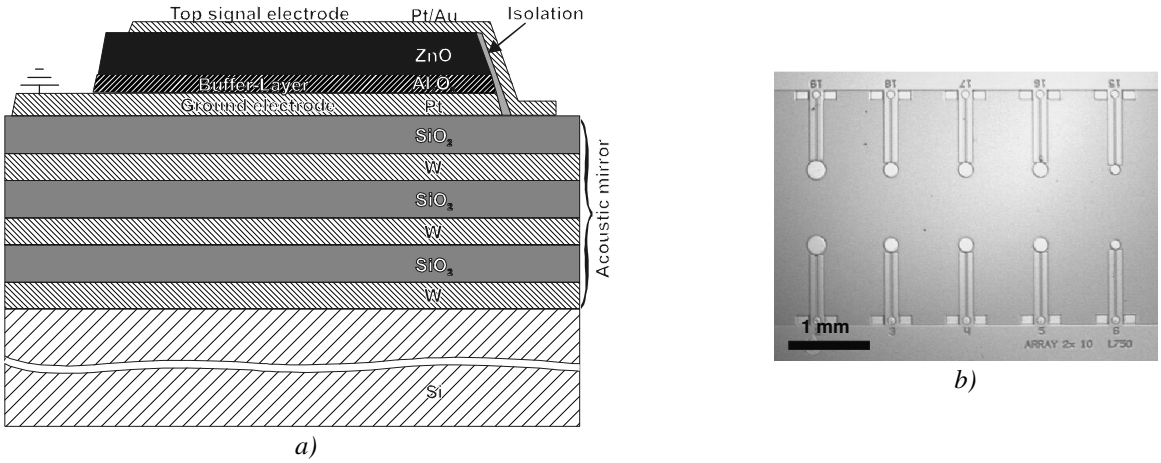

Figure 4.14 : a) Schematic cross-section of DESIGN 2 acoustic stack and b) microscope picture of a typical array.

TABLE 4.2
RELEVANT SOLIDLY MOUNTED FBAR SAMPLES

Sample number	Buffer-layer material (thickness)	ZnO Process ID	Acoustic mirror below BE	TE material	DESIGN
SIIa	SiO_2 (500 nm)	PIIb	ZnO/Pt/ZnO/Pt /ZnO/Pt	Au	1 (classic)
SIIb	Al_2O_3 (300 nm)	PIIk	ZnO/Pt/ZnO/Pt /ZnO/Pt	Au	1 (HD)
SIIc	Al_2O_3 (100 nm)	PIIk	ZnO/Pt/ZnO/Pt /ZnO/Pt	Pt	1 (HD)
SIId	Al_2O_3 (100 nm)	PIIk	ZnO/Pt/ZnO/Pt /ZnO/Pt/ZnO/Pt	Au	1 (HD)
SIIe	Al_2O_3 (100 nm)	PIIk	SiO_2/Pt/ZnO/Pt /ZnO/Pt/ZnO/Pt	Au	1 (classic)
SIIf	Al_2O_3 (100 nm)	PIIj	SiO_2/Pt/ZnO/Pt /ZnO/Pt/ZnO/Pt	Au	1 (classic)
SIIg	Al_2O_3 (100 nm)	PIIj	SiO_2/W/SiO_2/W /SiO_2/W	Au	2
SIIIa	Al_2O_3 (100 nm)	PIIIe	SiO_2/Pt/ZnO/Pt /ZnO/Pt/ ZnO/Pt	Au	1 (classic)
SIIIb	Al_2O_3 (100 nm)	PIIIe	SiO_2/W /SiO_2/W	Au	1 (classic)

The Tables with the ZnO process parameters can be found on pages 97, 108 and 113.

4.4.3. Overview and stack design of realized SMRs

Many SMRs have been realized during the course of this thesis. They differ by the **employed ZnO process**, the required **buffer-layer**, and the **acoustic mirror stack**. Wafers with the same stack design have been realized several times to check the reliability of the process and the obtained resonator properties. Table 4.2 shows the different samples that will be discussed in the following paragraphs with the employed mirror,

buffer-layer, top electrode (TE) material, ZnO process and stack design. All samples were planned at centre frequencies of 800 MHz. The exact ZnO thicknesses are given in the following sections. The samples have a quarter-wavelength Pt bottom electrode (i.e. 528 nm thickness). The top electrode is either Au or Pt (100 nm thickness) and wafers are either structured with DESIGN 1 (classic or HD mask layout) or DESIGN 2. The c-axis inclined ZnO films were deposited reactively from a Zn target with the modified dc pulsed magnetron sputtering equipment described in section 3.4.1. The Process ID refers to the different ZnO processes presented in Chapter 3. No complete SMRs with PROCESS I have been fabricated. This is because PROCESS II yielded better results, and because for PROCESS I significant inclinations could only be recorded on 6" wafers. In this whole analysis, 525 µm thick (100) Si 4" wafers were employed.

Figure 4.15 shows a SEM picture of a cross-section of sample SIIc. The succession of Pt and ZnO layers in the 3-fold acoustic mirror stack realized on the Si wafer can be recognized. On the top, one can recognize the 100 nm top electrode, the inclined ZnO, the buffer-layer and the 500 nm thick bottom electrode, which also acts as the uppermost mirror layer. Comparing the top ZnO layer with a ZnO layer of the acoustic stack, the 16° inclination of the columns can be recognized.

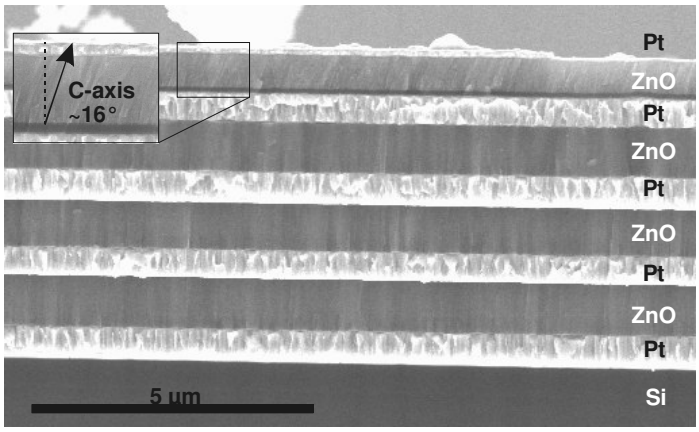

Figure 4.15 : SEM picture of a cross-section of sample SIIc.

4.5. Characterization of SMRs based on PROCESS II

The electro-acoustic characterization of the SMRs has been done with the equipment and methods presented in Chapter 2 in section 2.5.1. The obtained characteristics have been fitted to a BVD model to extract the coupling coefficient and the Q-factors, as described in section 2.5.2. In most cases, a line resistance R_s of a few Ω had to be placed in series with the BVD circuit to account for electrical losses from the contact lines. Since it was relatively small, Q_s and Q_p have similar values. In this paragraph, the SMRs realized with PROCESS II will be treated. **Section 4.5.1 shows the obtained impedance characteristics for a typical resonator of each of the samples of Table 3.4** and analyzes how their properties evolved during the course of this work. Section 4.5.2 examines how the characteristics vary over the surface of the wafer. Section 4.5.3 shows how the effective coupling coefficient relates to the values obtained by the slope of the impedance phase and what sensing characteristics are to be expected from these values.

4.5.1. Evolution of impedance characteristics

As has been seen in Chapter 3, the inclination and the thickness of the ZnO layer are very inhomogenous for PROCESS II. The wafers exhibit a point with maximum coupling coefficient corresponding to the point of maximum inclination. The sputtering time was adjusted to obtain the correct ZnO thickness in the region of highest inclination. In the following, the impedance characteristics of a resonator **situated in the region of maximum inclination** are looked at for the different samples of Table 3.4. To make it easier to compare their impedance characteristics, only resonators with a size of $200 \times 200\ \mu m^2$ are shown and analyzed.

4.5.1.1. SiO_2 buffer-layer

The first SMRs realized in this work were deposited on 3-fold Pt-ZnO mirrors. This has historical reasons since the first longitudinal mode SMRs realized at CTMM2 had these mirrors. The Q-factor associated with the imperfect reflectivity of this mirror is around 980. Process PIIb was used to deposit the 200 nm ZnO layer. A 500 nm SiO_2 buffer-layer was utilized. Figure 4.16 a) shows the recorded broadband impedance characteristic of a resonator from sample SIIa. The wide-band characteristics correspond to the expected decrease due to the capacitance. On top of it, two resonance peaks at 770 MHz and 1.48 GHz can be recognized. By comparing with Mason Model simulations it was shown that the first peak corresponds to the shear mode and the second to the longitudinal mode. Since the acoustic speed of the shear mode is approximately half of the longitudinal mode in most of the employed materials, the longitudinal mode can also be sustained with these mirrors. The phase of the SMR has a slight linear frequency dependency. A series resistance due to the electrodes and contact probes is responsible for this trend.

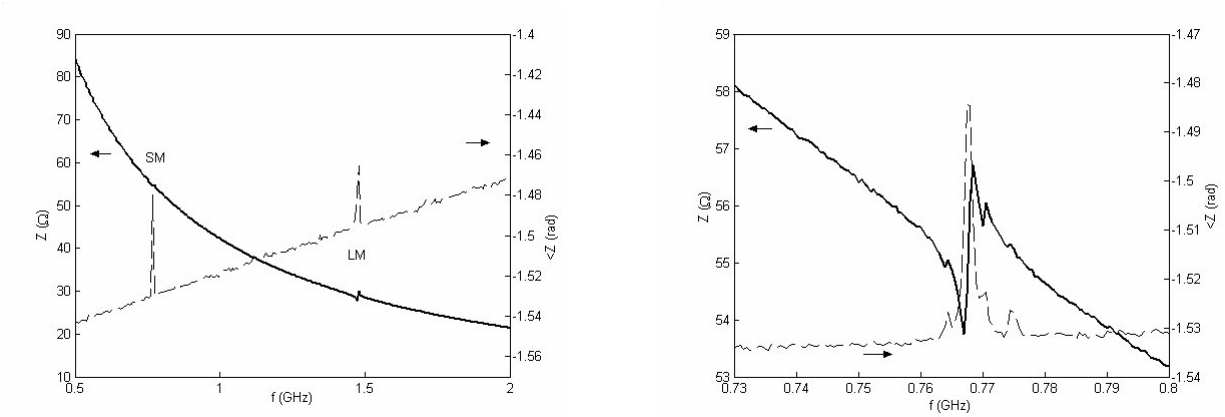

Figure 4.16 : Broadband (a) and narrowband (b) impedance characteristics of sample SIIa.

Figure 4.16 b) shows a narrow-band view of the shear-mode peak. The resonance is small with a phase peak amplitude of 0.04 rad. Some small ripples are superposed on the main peak. These could be spurious modes different from the 1D modes simulated with the Mason Model, but it is more probable that these are resonances of the Si substrate. The acoustic mirror is not perfect and some energy could be leaking through it, producing over-modes. The fitting of the main resonance peak was difficult, but after numerous tries and comparison with other resonators of the wafer, an effective coupling coefficient of 0.012 was extracted. This

low value is due to the low inclination of the ZnO, the thick SiO_2 buffer-layer and the imperfect reflectivity of the mirror. No reliable values could be extracted for Q_{BVD} and Q_{SLOPE}.

4.5.1.2. Al_2O_3 buffer-layer

For samples SIIb and SIIc, 3-fold Pt-ZnO mirrors were used again. An Al_2O_3 buffer-layer was employed yielding higher effective coupling coefficients. Process PIIk with a single blind was used. For this process, an electromechanical coupling coefficient of 0.07 had been extracted by the over-modes fitting method (see section 3.5.5). Two samples were realized: sample SIIb with a buffer-layer of 300 nm and sample SIIc with 100 nm. To reach a frequency of 800 MHz, 550 nm of ZnO were deposited for sample SIIb and 440 nm for sample SIIc. The broadband characteristics of both wafers exhibit the resonance frequency peaks expected from the simulations with the Mason Model. Figure 4.17 a) shows the characteristic of a resonator from sample SIIc. Compared with sample SIIa, the wideband amplitude of the impedance is lower, which is expected since the clamped capacitance is larger. Both the shear and longitudinal resonance peaks at 740 MHz and 1.65 GHz have a higher amplitude than SIIa, which is a sign that the coupling coefficient and Q_{SLOPE} have been increased. Some smaller peaks seen between the shear and longitudinal fundamentals have partly also been observed in the simulations with the Mason Model. They can be attributed to the presence of the acoustic mirror since they are not found in simulations of the top stack alone. The narrow-band characteristics of the fundamental shear mode (shown in Figure 4.17 b) for sample SIIc) are similar to those of sample SIIa, although it could be observed that the phase amplitude reached values of more than 0.2 rad. On top of the impedance characteristics, small overlaid resonances could again be seen. Since their spacing is 5.35 MHz, which is close to the pure shear-mode over-mode spacing in a 525 µm Si (100) substrate, it must be concluded that these are shear over-modes from the substrate, due to an insufficient reflection of the acoustic mirror. A coupling coefficient of 0.03 was extracted for sample SIIb and of 0.045 for sample SIIc. For both resonators, the device Q-factors Q_{BVD} lie around 180.

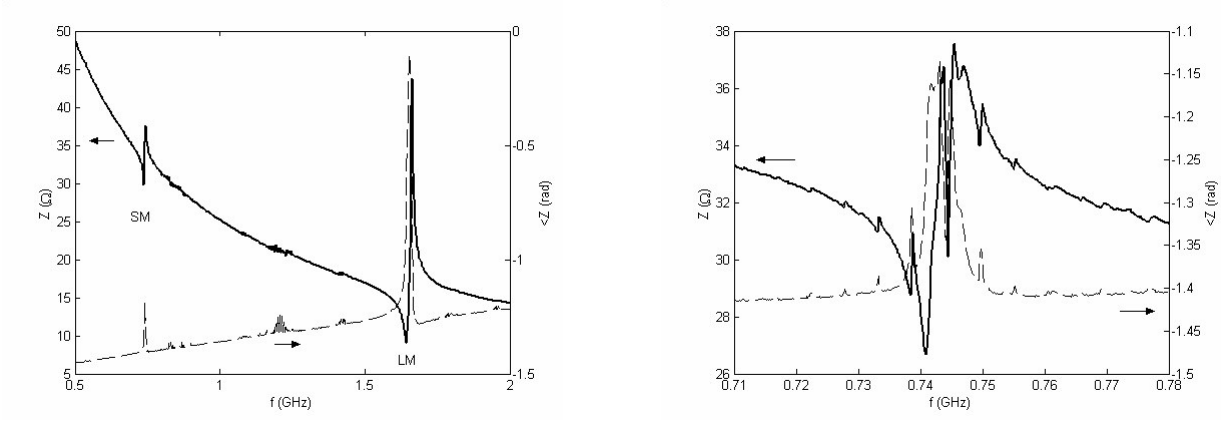

Figure 4.17 : Broadband (a) and narrowband (b) impedance characteristics of sample SIIc.

4.5.1.3. Increase of acoustic mirror pairs

For sample SIId, the number of mirror layer pairs was increased to 4 while keeping the same ZnO process PIIk and a 100 nm Al_2O_3 buffer-layer. Compared with sample SIIc, the top electrode was Au and

consequently the ZnO thickness had to be slightly increased to 480 nm to get a resonance frequency of around 800 MHz. Figure 4.18 a) shows a broadband view of a resonator from sample SIId. The fundamental shear mode is seen at 770 MHz and the fundamental longitudinal mode at 1.71 GHz. As can be seen, the fundamental shear mode is now much stronger. Between the fundamental shear and longitudinal peaks, a couple of other resonances, nicely visible in the impedance phase plot, can be observed. These peaks are also observed in the simulations of the SMR. By comparison with the curve of the reflection coefficient of the 4-fold Pt-ZnO mirror shown in Figure 4.6, it appears that those small resonances appear at the frequencies of the relative minima of the reflection coefficient. Pinkett *et al.* observed a similar effect with a 1.9 GHz longitudinal mode SMR.[25] Figure 4.18 b) shows a narrow-band view of the fundamental shear mode resonance. The reflections seen with the previous samples are gone. Only two small ripples have been seen. The phase amplitude at resonance is now 1.3 rad, i.e. the resonator becomes nearly inductive between series and parallel resonance. The BVD fitting of this sample yielded a coupling coefficient of 0.054 and a Q_{BVD} of nearly 459. The extracted Q_{SLOPE} was about 220. The better Q-factors are due to the increase of mirror pairs.

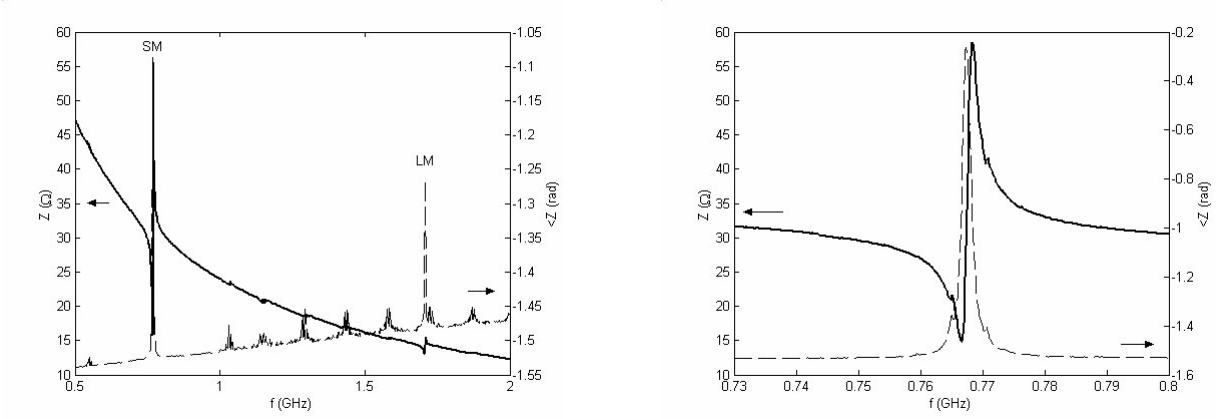

Figure 4.18 : Broadband (a) and narrowband (b) impedance characteristics of sample SIId.

For sample SIIe, the acoustic mirror was slightly adapted by using SiO_2 for uppermost layer of the mirror. The top stack of sample SIIe was the same than for sample SIId. Figure 4.19 a) shows a broadband view of the impedance characteristics. Compared with the previous sample, the shear mode at 780 MHz and the longitudinal mode at 1.75 MHz are stronger, and the shear over-modes seen at frequencies between 1 and 1.7 GHz are smaller. Both fundamental resonance peaks reach zero-phase crossing meaning that the resonator becomes inductive between series and parallel frequencies. Figure 4.19 b) shows a narrow-band view of the fundamental shear mode resonance. Only a single small ripple can be seen. The BVD fitting gave a coupling coefficient of 0.076 and a Q_{BVD} of 380. The measured Q_{SLOPE} was about 200. The Q-factors are slightly smaller than for sample SIId which is surprising since the reflectivity of the mirror increased, which was also expressed in the increased coupling coefficient.

[25] S. Pinkett, W. Hunt, B. Barber, P. Gammel, *Proc. IEEE Int. Freq. Contr. Symp.*, 15 (2002).

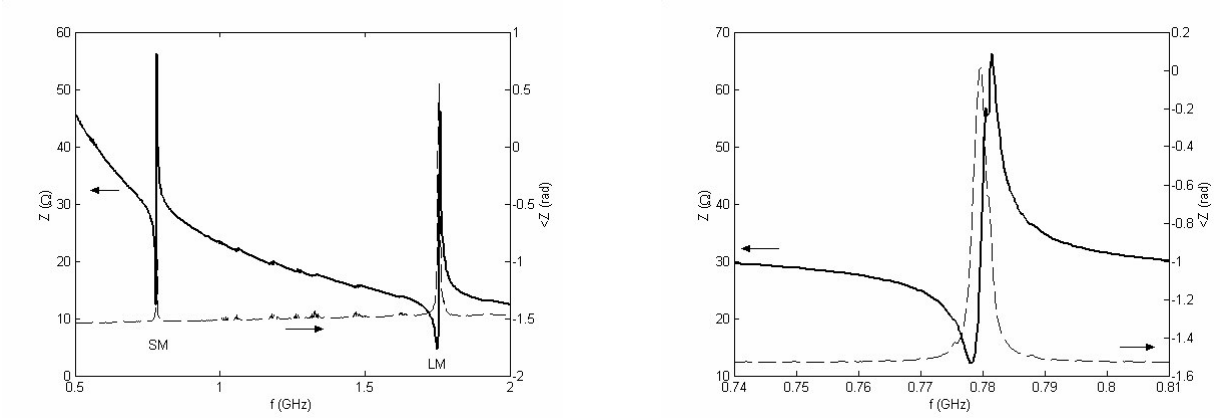

a) *b)*

Figure 4.19 : Broadband (a) and narrowband (b) impedance characteristics of sample SIIe.

4.5.1.4. Increase of electromechanical coupling coefficient

The next step in optimizing the shear mode SMRs was to choose the best ZnO process that was available, process PIIj, where the ZnO is sputtered at a lower temperature, giving electromechanical coupling coefficients of 0.106. For sample SIIf, the combined 4-fold Pt-ZnO mirror with a top SiO_2 layer was used again. Since the top stack was similar to samples SIId and SIIe, the ZnO thickness for sample SIIf was also 480 nm. Figure 4.20 a) shows the obtained broadband characteristic. Both fundamental resonances at 850 MHz and 1.87 GHz now clearly show a zero-phase crossing. A closer comparison between the simulated and measured curves has shown that both curves fit very well, indicating that the acoustic velocities used to perform the simulations are correct and that the materials exhibit the expected properties. Figure 4.20 b) shows a narrow-band view of the fundamental shear mode. Neither over-modes nor spurious modes can be recognized. The BVD fitting of this resonance gave a coupling coefficient of 0.129 and a parallel Q-factor of 380. Q_{SLOPE} was evaluated at 235. **Most of the experiments in liquids** were done with these SMR samples (Chapter 5).

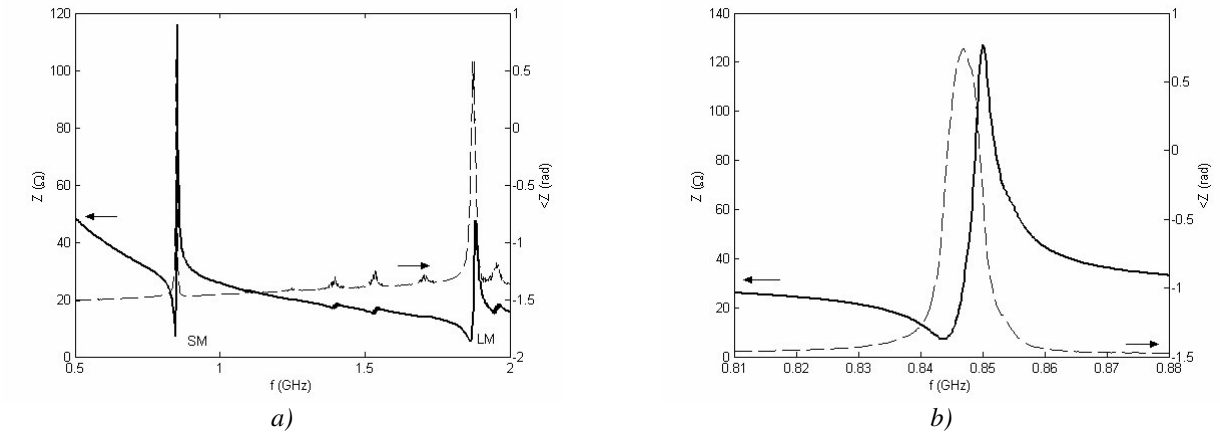

a) *b)*

Figure 4.20 : Broadband (a) and narrowband (b) impedance characteristics of sample SIIf.

4.5.1.5. W-SiO_2 mirrors

Near the end of the thesis, some SMRs on 3-fold W-SiO_2 mirrors were also realized. The top stack was the same than for sample SIIf, with a Au top electrode and process PIIj for the ZnO. As it was planned to use these wafers for bio-chemical experiments they were realized with DESIGN 2. Since several buffer- and adhesion-layers are incorporated, a thickness of 430 nm ZnO is needed to reach the 800 MHz. Figure 4.21 a) shows the broadband characteristic of a resonator from sample SIIg. The narrow-band view of Figure 4.21 b) can be compared with Figure 4.12 b) to see how well the measured and simulated impedance curves match. Both fundamental resonance peaks at 770 MHz and 1.7 GHz reach zero-phase crossing. Figure 4.21 b) shows the narrow-band characteristic of the fundamental shear mode. Neither over-modes nor spurious modes can be recognized, indicating a good reflection of the acoustic mirror. The BVD fitting provided a coupling coefficient of only 0.086, which is less than for sample SIIf. This difference is most probably due to the fact that the resonator was not measured at the location of the highest frequency since the mask layout did not allow for this. Q-factors similar to those of sample SIIf were extracted.

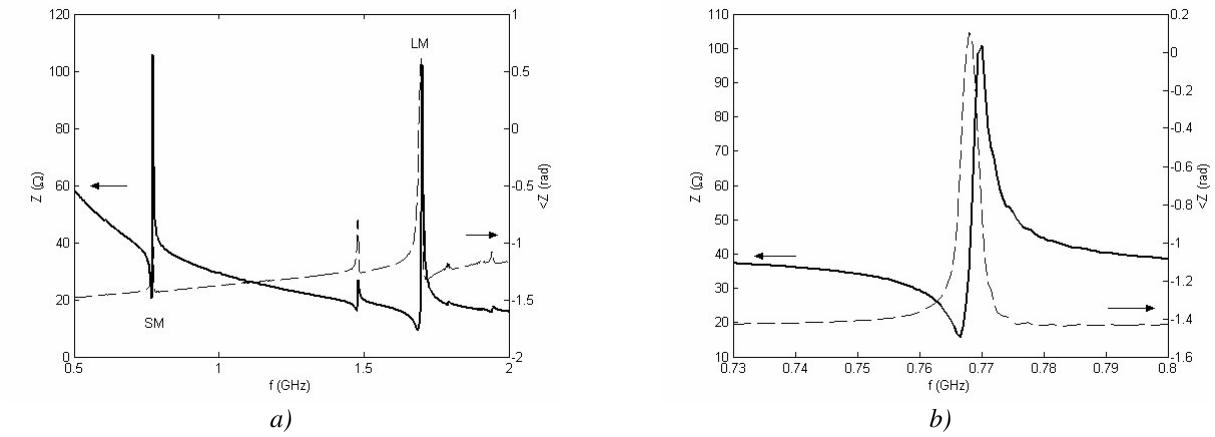

Figure 4.21 : Broadband (a) and narrowband (b) impedance characteristics of sample SIIg.

4.5.1.6. Overview

To conclude this overview of the evolution of the SMR properties during the course of this work, Figure 4.22 a) shows a Smith-chart view of the different recorded narrowband impedance characteristics of the fundamental shear mode. As can be seen, the curve associated with the resonance progressively grows in size. For sample SIIe, it slightly touches the middle line, confirming that the resonator becomes inductive for a small frequency span. For sample SIIf, the middle line is clearly crossed. Figure 4.22 b) shows how the effective coupling coefficient obtained by the BVD fitting increased gradually. Figure 4.22 c) shows the obtained Q_{BVD} and Q_{SLOPE} values. The Q-factors do not necessarily increase with better mirror reflectivity. This is because the resulting Q-factor is influenced by multiple loss mechanisms other than the properties of the acoustic mirror, such as the acoustic wave attenuation in the metal and piezoelectric films, the acoustic wave scattering loss due to the surface roughness, and the electrode electrical losses. No extensive Q-factor analysis was done in this work. It can be observed that the difference between both Q-factor narrows as the

effective coupling coefficient increases. This has been analyzed theoretically in section 2.5.3 of Chapter 2 and will be examined more closely in section 4.5.3.

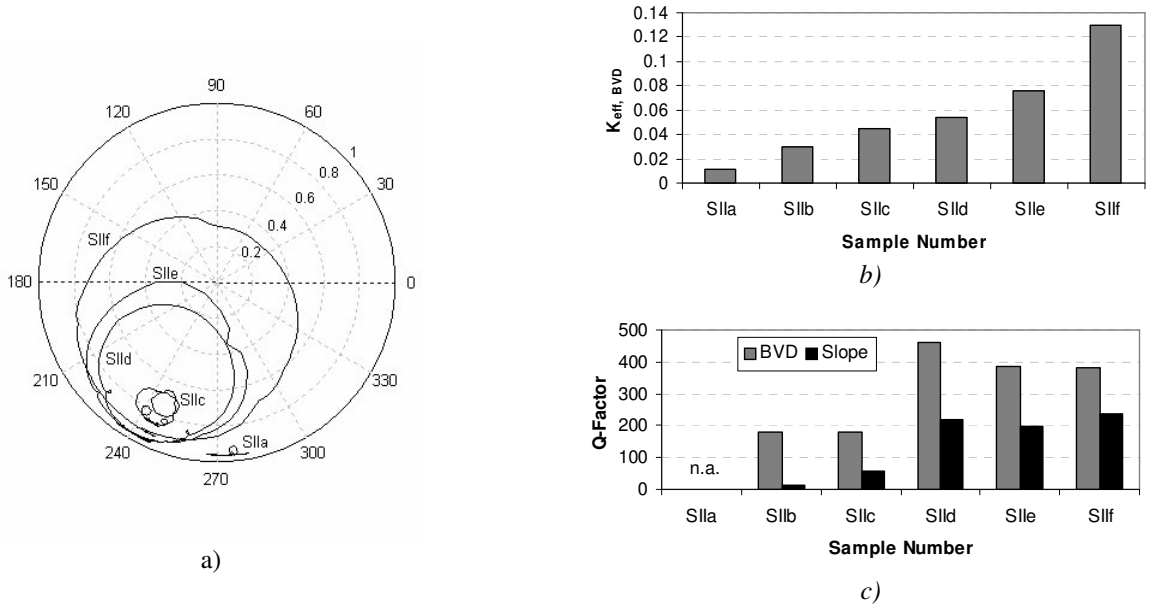

Figure 4.22 : a) Smith-chart representation of the impedances of samples SIIa to SIIf; b) evolution of the effective coupling coefficient and c) evolution of the Q-factors.

4.5.2. Characteristics depending on distance to the blind

For all SMRs realized with PROCESS II, the obtained characteristics vary with the distance towards the blind. As was shown in the previous section, depending on the process parameters, the employed buffer-layers and the acoustic mirror, different effective coupling coefficients and different quality factors resulted. However, the general behaviour of the coupling coefficient and the frequencies with respect to the distance to the blind was the same for all wafers. In this short section, we will analyze how the properties change over the surface of the wafer, and particularly, with respect to the distance to the blind.

Sample SIId was chosen for such a mapping of the properties, since it was designed with the high density DESIGN 1 mask and exhibited relatively high coupling coefficients. Figure 4.23 a) shows a 3D representation of the effective coupling coefficient found through fitting with the BVD model. As expected, the characteristics are very inhomogeneous. The location of the blind along the line y=0 can be recognized as a trench in the middle of the graph. From this trench, the coupling increases to a maximum of around 0.05 on both sides of the blind; this is where the impedance characteristic shown in Figure 4.18 was recorded. Afterwards, the coupling decreases towards the edge of the wafer. Figure 4.23 b) shows the average values and standard deviation along the projection of the points on the x-axis, i.e. perpendicular to the blind. On the same graph, the measured c-axis inclination is also shown. Both curves have the same shape proving that the shear mode effective coupling is indeed directly related to the c-axis inclination.

When considering the rule established in Chapter 3 that inclinations of at least 5° are necessary for the SMRs, a region of approximately 30 % of the wafer surface can be utilized. In this region, the mean coupling coefficient is 0.037 with a standard deviation of ±20 %. The mean resonance frequency is 749 MHz with a standard deviation of ±4%. This deviation is less than for the coupling coefficient, which is because the thickness variation is not as big (see Figure 3.22 in Chapter 3). The extracted Q_{BVD} values vary around 374 with a deviation of ±33 %. This high variation is probably due to imperfect fits which can be very difficult to obtain for small resonances. In principle, it is expected that the Q-factors do not vary significantly over the wafer surface, since the stack design is the same everywhere. For the remaining samples processed with PROCESS II, SIIe, SIIf and SIIg, it is expected that the spreading of the values is comparable since the geometry of the blind is the same and the different layer thicknesses due not vary extensively.

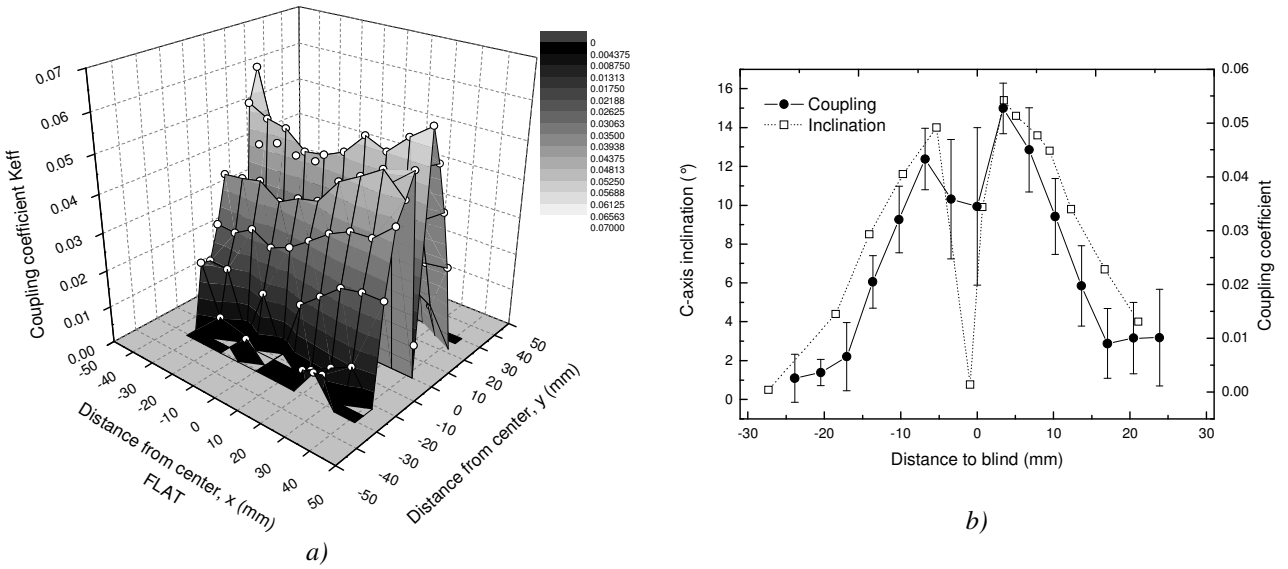

Figure 4.23 : a) 3D representation of the effective coupling coefficient distribution of sample SIId over the 4" wafer surface; b) average values and standard deviations of this distribution along the projection on the x-axis perpendicular to the blind compared with the recorded c-axis inclinations.

4.5.3. Effective coupling, Q_{SLOPE} and calculated sensing characteristics

On Figure 4.22 b) and c) it was seen how K^2_{eff}, Q_{BVD} and Q_{SLOPE} changed during the course of this work. In sections 2.5.2 and 2.5.3 of Chapter 2, the theoretical relationship between the resonator values extracted from the impedance characteristics and the values obtained by fitting the BVD has been established. The difference between K^2_{SLOPE} and K^2_{eff} and the difference between Q_{SLOPE} and Q was shown in Figure 2.20. Both vary as a function of the $K^2_{eff} \cdot Q$ product. This relationship could be confirmed by measurements of the impedance characteristics of resonators from samples SIIa to SIIf. The results are shown in Figure 4.24. As expected, the difference between the values extracted directly from the impedance phase slope and the values from the BVD, diminishes gradually with increasing $K^2_{eff} \cdot Q$ products. As mentioned above, the progression is mainly due to increasing effective coupling coefficients.

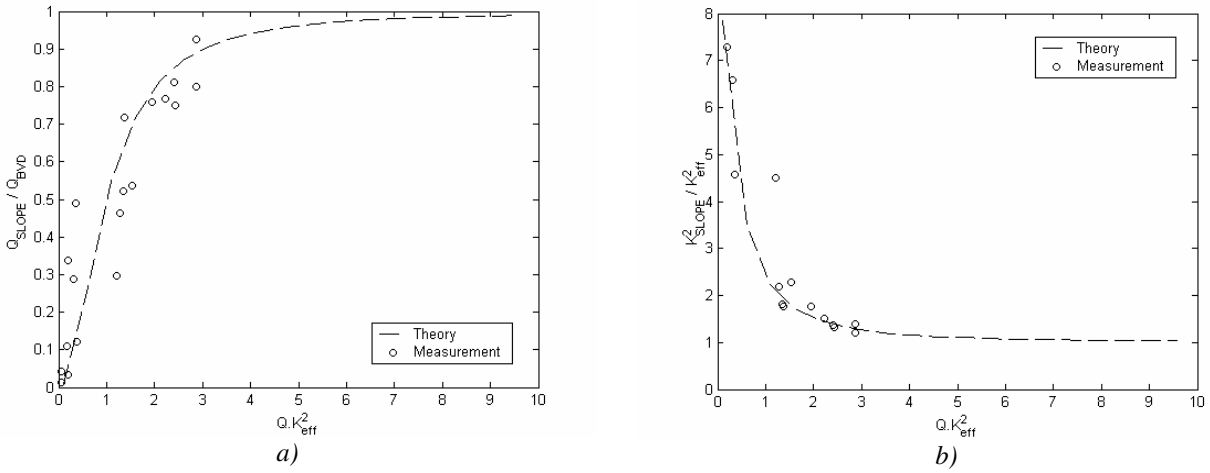

Figure 4.24 : Measured Q_{SLOPE} (a) and K^2_{SLOPE} (b) normalized to K^2_{eff} and Q extracted from fitted BVD characteristics (dots), and compared to the theoretical expectation (dashed line).

The obtained effective coupling coefficients depend on the properties of the ZnO layer and on a number of design considerations, as was examined in section 4.3.2. The coefficients that were obtained by fitting of the measured impedance characteristics are reported in Table 4.3 and compared with the expected coupling coefficients from simulations with the Mason Model. The simulated layers have the measured thicknesses. For sample SIIa, no simulation was run since no electromechanical coupling coefficient had been extracted during the ZnO process development. The measured coupling does not exactly correspond to the expected ones. But in general the difference is not very big. It can be explained by several things:

a) the thicknesses of the layers might be different for the particular resonator which was fitted;

b) the expected couplings are calculated by taking the electromechanical coupling coefficient that was found in the over-mode analysis for the particular ZnO process. Since the roughness of the mirror and the buffer-layer could be different from the roughness of the buffer-layer used in Chapter 3, the properties of deposited ZnO could slightly vary too. This could be the main reason for the difference observed for sample SIIf;

c) a third reason for the discrepancy could be the difficulty of correctly fitting the resonance, which is particularly true for low couplings, as in the case of sample SIIb.

It is expected that all samples realized with PROCESS II have a relative mass sensitivity of around -1010 cm^2/g (absolute sensitivity of around -800 $Hz \cdot cm^2/ng$), since they exhibit a top acoustic stack corresponding to a maximum sensitivity, i.e. with a quarter-wavelength electrode, and since they vibrate at approximately 800 MHz (see section 4.2.1). However, the real sensitivity can be different due to the variations of the layer thicknesses. Some real sensitivity values have been determined with bio-chemical measurements in Chapter 5. Measurements with longitudinal mode resonators with a similar stack design showed a good correspondence between simulated and measured sensitivities.[26]

The obtainable mass resolution depends on the sensitivity and the Q-factor extracted by the slope of the impedance phase. For sample SIIf which was mostly used for bio-chemical experiments, Q_{SLOPE} is around

[26] J. Weber, M. Link, R. Primig, D. Pitzer, W. Wersing, M. Schreiter, *IEEE Trans.Ultrason.Ferroelec.Freq.Contr.,* accepted.

230 at a phase of approximately -0.3 rad. For a measurement at that phase, the phase resolution of the network analyzer is 0.0015 rad (see section 4.2.2). Formula (0.3) permits to calculate an expected mass resolution of 3 ng/cm^2, which is comparable to typical values for QCMs. The measured mass resolutions have been assessed with bio-chemical experiments and will be presented in Chapter 5.

TABLE 4.3
COUPLING COEFFICIENT COMPARISON FOR SMRS USING PROCESS II

Sample number	Expected reduction	ZnO coupling from process	Expected coupling	Measured coupling
SIIb	-31%	0.07 (PIIk)	0.048	0.030
SIIc	-34%	0.07 (PIIk)	0.046	0.045
SIId	-33%	0.07 (PIIk)	0.047	0.054
SIIe	-29%	0.07 (PIIk)	0.050	0.076
SIIf	-27%	0.106 (PIIj)	0.077	0.129
SIIg	-31%	0.106 (PIIj)	0.073	0.086

Details of the design of the samples are given on page 150.

4.6. Characterization of SMRs based on PROCESS III

In the following, the first two shear mode SMRs realized with PROCESS III will be presented (samples SIIIa and SIIIb). The exact ZnO parameters are those of sample PIIIe presented in paragraph 3.6 and the stack design is given in Table 4.2. For sample SIIIa, a 4-fold Pt-ZnO acoustic mirror with a top SiO_2 layer is used, similar to the one used for samples SIIe and SIIf. For sample SIIIb, a 2-fold W-SiO_2 mirror is used. No comparable sample with PROCESS II exists. The electro-acoustic characterization of the SMRs has been done with the equipment and methods presented in Chapter 2 in section 2.5.1. Section 4.6.1 will show the obtained impedance characteristics for a typical resonator of each of the samples. Only resonators with a size of $200 \times 200\ \mu m^2$ are shown and analyzed. Section 4.6.2 will give the homogeneity characteristics for both wafers. It will also be examined how the effective coupling coefficient relates to the values obtained by the slope of the impedance phase and what sensing characteristics are to be expected from these values. The coupling coefficient found for process PIIIe was 0.136 (see section 3.6.3). The ZnO thickness was found to be homogenous over the whole wafer with a variation of less than $\pm 5\ \%$ and is expected to give good frequency homogeneity for the SMRs. The coupling coefficient is also expected to be very homogeneous.

4.6.1. Typical impedance characteristics

For sample SIIIa, the same top stack was planned identically to sample SIIf. However a thickness of 650 nm instead of 528 nm was obtained for the bottom electrode during the processing, that is why the thickness of the ZnO was reduced to 340 nm to obtain a resonance frequency of 800 MHz. A combined 4-fold Pt-ZnO mirror with a top SiO_2 layer was used. Figure 4.25 a) shows the recorded broadband characteristic of sample SIIIa for a resonator measured in the centre of the wafer. Both fundamental resonance peaks at 740 MHz and 1.68 GHz reach zero-phase crossing. The small peaks observed between these fundamentals are shear mode peaks, and are situated at the points of relative minimum reflectivity of the acoustic mirror (see Figure 4.7).

Figure 4.25 b) shows a narrow-band view of the fundamental shear mode. Neither over-modes nor spurious modes can be recognized. By fitting on the BVD, a coupling coefficient of 0.088 and a Q-factor of 330 have been extracted. Q_{SLOPE} was evaluated at 244. The Q-factors are not much different from those of sample SIIf, which is expected since the stack design is similar. The coupling coefficient is much lower than the electromechanical coupling coefficient of the ZnO, which was found to be 0.136. This can be explained by the influence of the buffer-layer, the electrodes and the mirror, which together are expected to reduce the coupling of the ZnO by 47%. The high reduction is mainly due to the thicker electrode. The expected coupling coefficient would then be 0.072, which compares well with the measured coupling.

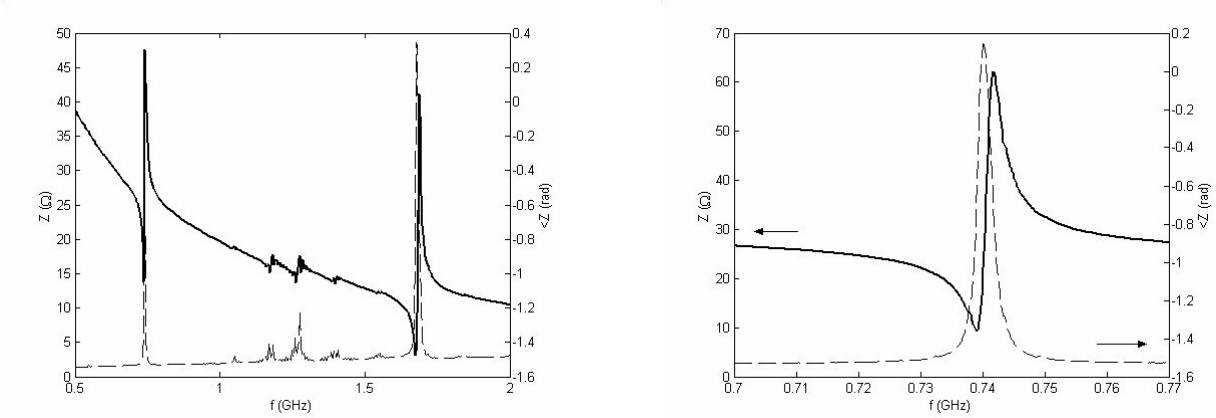

Figure 4.25 : Broadband (a) and narrowband (b) impedance characteristics of sample SIIIa.

Sample SIIIb has the same top stack than sample SIIf, with a ZnO thickness of 480 nm. A 2-fold W-SiO_2 mirror was used. Figure 4.26 a) shows the obtained broadband impedance characteristic for a resonator measured in the centre of the wafer. The two fundamental resonance peaks are found at 740 MHz and 1.61 GHz. Smaller peaks at 1.34 GHz and 1.7 GHz are also shear modes. Figure 4.26 b) shows the narrow-band characteristic of the fundamental shear mode. Some small over-laid resonances can be observed. They are spaced by 5.67 MHz, which shows that these are shear-mode over-modes from the 525 µm Si substrate (see Table 2.2). This is due to an insufficient reflection of the acoustic mirror, since only two W-SiO_2 pairs were used. For sample SIIIg with a 3-fold W-SiO_2 mirror, no such over-modes were seen (see Figure 4.21 b)). The effective coupling extracted with the BVD fitting method is **0.149, which is the highest coupling measured in this work**. For this acoustic stack and with an electromechanical coupling coefficient for the ZnO of 0.136, the expected reduction of -28% would give an expected effective coupling coefficient of 0.098. The higher measured coupling is probably due to better properties of the deposited ZnO, possibly originating from its increased thickness. The higher coupling might also explain why over-modes could be excited. Since more energy is pumped into the system, the waves that leak through the mirror are strong enough not to be attenuated in the Si substrate, and return to the top stack after a round-trip to the bottom of the substrate. The Q-factor of 220 is lower than for sample SIIIa, which could be anticipated since the reflectivity of the mirror is worse. The extracted Q_{SLOPE} has a value of 218, meaning that both Q-factors are now nearly equal. This can be understood by considering that the $K_{eff}^2 \cdot Q$ product is 4.5, at which point the

difference should become very small (see section 2.5.3). It is expected that the over-modes can be removed by increasing the number of mirror layers to 3.

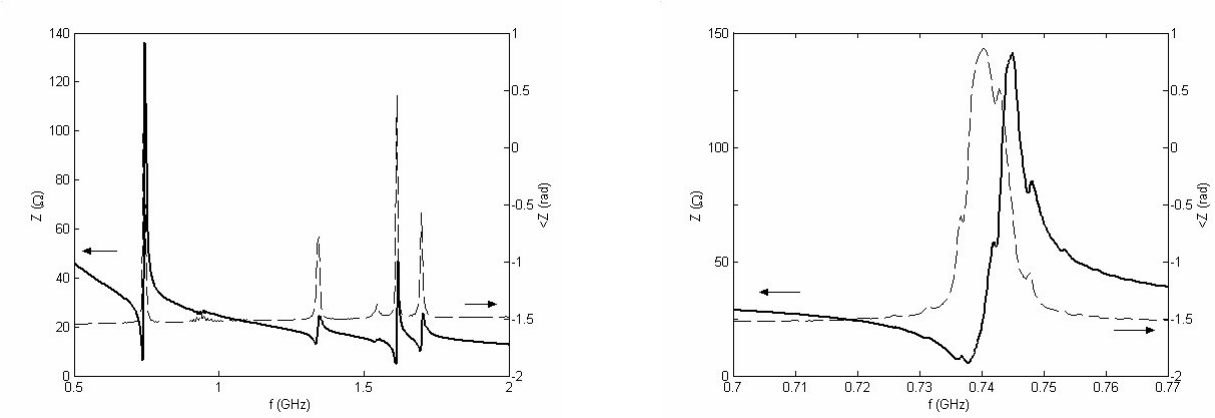

Figure 4.26 : Broadband (a) and narrowband (b) impedance characteristics of sample SIIIb.

4.6.2. Homogeneity and calculated sensing characteristics

As has been seen in Chapter 2, the big advantage of PROCESS III for the ZnO deposition is its good homogeneity in thickness and coupling coefficient. Since all layers other than the ZnO are equally homogeneous, it is expected that the SMRs based on PROCESS III are homogeneous concerning resonance frequency, coupling coefficient and quality factors. In view of an industrial application of these devices, these are important points since they translate directly into homogeneity of the sensitivity and the mass resolution. To assess the homogeneity of samples SIIIa and SIIIb, the impedance characteristics were recorded at 10 points all over the wafer surface. Figure 4.27 shows 3D representations of the effective coupling coefficient and the resonance frequency for sample SIIIb. The white points correspond to the measured resonators, the values in between are extrapolated for better visualization. By **comparing this figure with the 3D representation of PROCESS II in Figure 4.23 a), the homogeneity gain becomes obvious**. As can be seen on Figure 4.27 b), the frequency goes slightly up on the sides of the wafer, which is due to a thickness reduction in this region. For sample SIIIb, the average coupling coefficient is 0.144 (K^2=2%) with a standard deviation of only 0.007, i.e. a variation of only ±5.1 %. The average of the resonance frequency is 731 MHz with a standard deviation of 13 MHz, i.e. ±1.8 %. The Q-factor average is 244 with a variation of ± 8.5%. The homogeneity is also very good for sample SIIIa. The average coupling coefficient is 0.080 (K^2=0.64%) with a variation of ±6 %. The average of the resonance frequency is 760 MHz with a variation of ±2 %. The Q-factor average is 375 with a variation of ± 10.5%.

Since both samples vibrate at frequencies around 800 MHz, the expected relative mass sensitivity is around -1010 cm^2/g (see section 4.2.1). Since the frequency is very homogeneous over the wafer surface, the sensitivity will also be homogeneous. Q_{SLOPE} for sample SIIIb is 258 ± 11% at a phase of -0.3, which with the expected sensitivity gives a theoretical mass resolution with the network analyzer of 2.9 ng/cm^2 (see

section 4.2.2). This is slightly better than what was found for sample SIIf and comparable to typical values for QCMs. Q_{SLOPE} for sample SIIIa is similar, giving the same expected mass resolution.

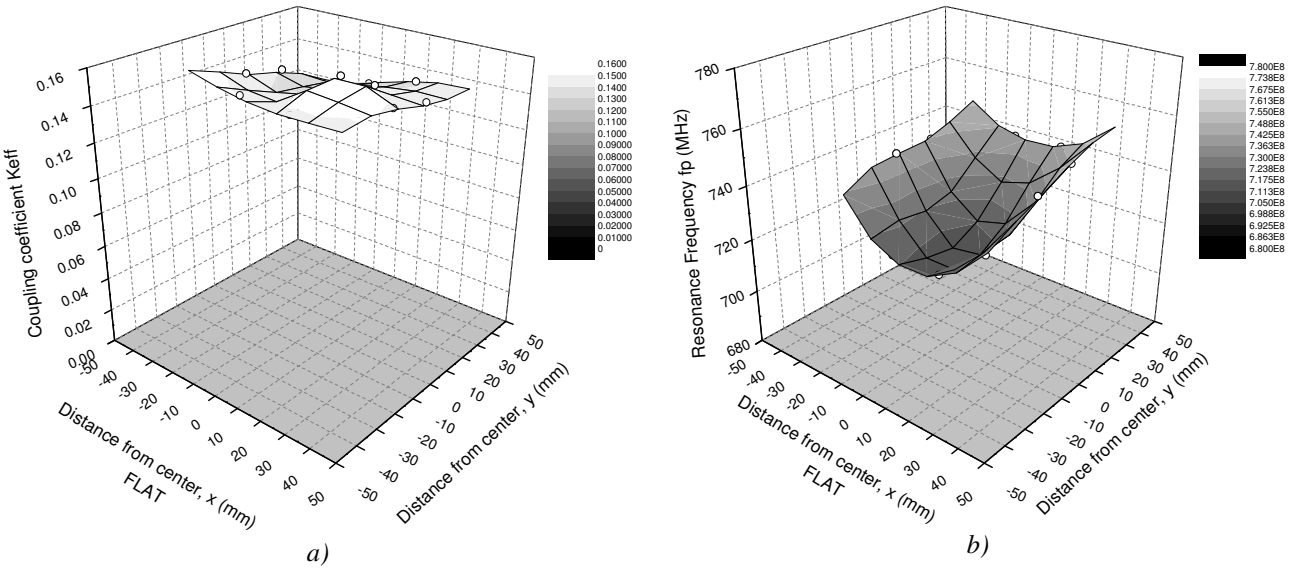

Figure 4.27 : a) 3D representations of the distributions of the effective coupling coefficient (a) and the resonance frequency (b) of sample SIIIb depending on the location on the 4" wafer surface.

4.7. Chapter conclusion

In this chapter we presented the simulation, realization and characterization of shear mode SMRs vibrating at around 800 MHz and based on the inclined ZnO thin films presented in Chapter 3. The influence of the acoustic mirror, the intermediate buffer-layer required for the ZnO inclination and the electrodes has been analyzed. Using simulations with the Mason Model, it was found that the sensitivity of the SMR to mass changes at its surface can be maximized for a 100 nm Au or Pt top electrode, and a quarter-wavelength Pt bottom electrode (528 nm). In fact in this frequency range a sensitivity corresponding to the Sauerbrey relative sensitivity of around -1000 cm^2/g was found. For electrical reasons, these electrodes thicknesses are better adapted. However, this slightly reduces the effective coupling coefficient of the device. Different acoustic mirror combinations and their respective reflections have been simulated. The different designs and fabrication techniques employed for the realization of the SMRs were presented. During the course of this work, the effective coupling coefficient of the SMR was continuously improved, jumping from 0.012 for sample SIIa to 0.149 for sample SIIIb. The final obtained characteristics of the SMRs realized with PROCESS II and PROCESS III are summarized in Table 4.4. Very homogenous properties have been obtained with PROCESS III based SMRs. The theoretical relationship between the effective coupling coefficient K^2_{eff} and the Q-factor extracted from the impedance phase slope, Q_{SLOPE}, could be confirmed. Q_{SLOPE} also increased from around 3.5 at the beginning of the work to around 235 at the end. This improvement of the SMR properties has positive consequences for the obtainable mass resolution. Some theoretical expected values are given in Table 4.4, which are comparable to values obtained with QCMs. Since the measured

impedance characteristics correspond very well to the simulated characteristics, it is expected that the sensitivity of the realized devices will also correspond. The expected relative mass sensitivity of all the samples is around -1000 cm^2/g, which is much better than typical values for QCMs. The real resolution and sensitivity of the realized SMRs has been assessed with bio-chemical measurements, which will be described in Chapter 5.

TABLE 4.4
MAIN CHARACTERISTICS FOR SMRS WITH PROCESS II AND III

Parameter	SMR BASED ON PROCESS II		SMR BASED ON PROCESS III
	SIID average value and variation	SIIF best value	SIIIB average value and variation
Short description	280°C ZnO Pt-ZnO mirror	150°C ZnO Pt-ZnO-SiO_2 mirror	150°C ZnO W-SiO_2 mirror
Usable 4" wafer surface	~30 %	~30 %	~100 %
Resonance frequency	749 MHz ± 4 %	838 MHz	731 MHz ± 1.8 %.
Effective coupling coefficient K	0.037 ± 20 %	0.129	0.144 ± 5.1 %
Effective coupling coefficient K^2	0.14 %	1.7 %	2.1 %
Quality factor Q	374 ± 33 %	380	244 ± 8.5 %
Quality factor Q_{SLOPE}	220	235	258 ± 11 %
Calculated relative sensitivity	-1092 cm^2/g	-1092 cm^2/g	-1092 cm^2/g
Assumed phase resolution	0.0015 rad	0.0015 rad	0.0015 rad
Calculated mass resolution	3.1 ng/cm^2	3 ng/cm^2	2.9 ng/cm^2
3D view of the coupling coefficient distribution over the wafer surface	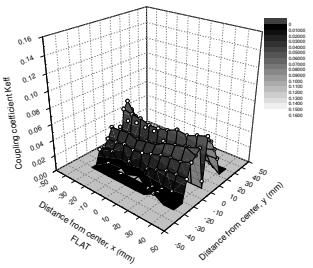		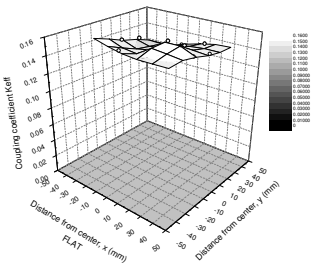

5. SMR characterization in liquids and sensing applications

Caractérisation de SMRs en milieux liquides et applications comme capteurs — *Résumé*: Dans ce chapitre sont analysées les **caractéristiques en milieux liquides des SMRs**, dont la réalisation et la caractérisation à l'air ont été décrites au chapitre 4. Les SMRs ont été testés à la fois dans de **l'eau pure, dans des solutions de glycérol avec différentes viscosités, et dans des solutions biochimiques**. L'effet de ces différents liquides sur les facteurs de qualité et la fréquence de résonance a été analysé. Ces expériences ont permis de montrer que les SMRs peuvent effectivement être utilisés comme capteurs biochimiques ou comme viscosimètres. Dans l'eau pure, des **facteurs de qualité allant jusqu'à 200** ont été obtenus, en gardant un facteur de couplage K de 0.14 à des fréquences de résonance aux alentours de 800 MHz. En analysant les caractéristiques à des viscosités plus élevées, il a été montré que les SMRs peuvent être utilisés jusqu'a 5 cP comme **viscosimètres avec une sensibilité de -10 MHz·cm^2·s$^{0.5}$·g^{-1}, soit 50 à 100 fois de plus que pour des QCMs** typiques. Des **mesures biochimiques** immunologiques (réaction Avidin-Antiavidin) ont permis de montrer une **sensibilité de 738 Hz·cm^2·ng^{-1}, soit environ 1000 fois supérieure à la sensibilité typique d'un QCM à 10 MHz** et correspondant aux attentes théoriques. De plus, une résolution massique de 3.5 ng/cm^2 a été obtenue, ce qui est 3 fois mieux que pour les QCMs. Les résultats de ce chapitre indiquent que des SMRs à hautes fréquences peuvent être utilisés en milieu liquide et constituent des systèmes attractifs pour des capteurs bon marché, jetables et intégrés pour le marché du diagnostic médical, avec de très hautes sensibilités et d'excellentes résolutions massiques.

5.1. Introduction

This chapter presents the application of shear mode solidly mounted resonators (SMR) as viscosity and bio-chemical sensors in liquid environments. Measurands that can be detected with a bio-chemical sensor are manifold and come from different sources. For example, cancer markers of different types, such as proteins or DNA strands, are found in body-tissues or -fluids, like urine, serum, saliva or blood. As explained in Chapter 1, the sensors should be able to directly sense measurands in their aqueous environment, which can have very different viscosities. At low viscosities and low frequencies, the behaviour of shear resonators is known through various measurements and theoretical developments with AT-cut quartz. At higher frequencies or higher viscosities, the liquid exhibits a certain elasticity and is said to be visco-elastic. In that case the usual formulas are not valid anymore. In this chapter it will therefore be analyzed how SMR properties change when immersed in liquids and what sensing characteristics can be obtained. For that purpose, the SMRs, whose realization and characterization was presented in Chapter 4, were characterized in

---

Parts of this chapter have been released in the following publications: M. Link, M. Schreiter, J. Weber, R. Primig, D. Pitzer, R. Gabl, *IEEE Trans. Ultrason., Ferroelec., Freq. Contr.* **53**, 492 (2006); M. Link, J. Weber, M. Schreiter, W. Wersing, O. Elmazria, P. Alnot, *Sens. Act. B*, accepted, published online May 2006; M. Link, M. Schreiter, J. Weber, D. Pitzer, R. Primig et R. Gabl, *Proc. JNRDM*, Paris, 114 (2005); M. Link, M. Schmidt, J. Weber, R. Primig, D. Pitzer, R. Gabl, M. Schreiter, *Proc. Eurosensors XIX*, Barcelona, TB10 (2005); J. Weber, W. M. Albers, J. Tuppurainen, M. Link, R. Gabl, W. Wersing, M. Schreiter, *Sens. Act. A* **128**, 84 (2006). 2 related patents have been filed at the German Patent Office.

solutions of different glycerol concentrations and different viscosities, and in bio-chemical solutions. As is known from QCM devices, the damping effects in liquids have a negative impact on the Q-factor, which worsens the SMR mass resolution.[1] Furthermore, the resonance frequency of the device is expected to decrease with increasing viscosity.[2]

Paragraph **5.2** describes the experimental setup which has been used. Paragraph **5.3** will analyze how the characteristics of the SMR change, more precisely the resonance frequency and the quality factors. It will also be seen how the BVD parameters are changing. The obtained properties of the SMR allow to estimate what gravimetric sensing properties are to be expected. In paragraph **5.4**, the sensing applications of the SMRs will be analyzed. The sensitivity of the SMR to viscosity changes will be treated in section 5.4.1. The SMRs could be used as high frequency viscosity sensors. Some results of bio-chemical measurements done in conjunction with European project partners using the SMRs developed in this thesis will be described in section 5.4.2. They proof the applicability of SMRs as highly sensitive gravimetric sensors in liquids.

5.2. Experimental setup

5.2.1. Measurement procedure and flow-cells

Various SMR samples described in Chapter 4 were used for the liquid measurements. In most cases, the resonator area was $200\,\mu m \times 200\,\mu m$. The parameters and stack designs of the different samples are summarized in Table 4.2 on page 150. The resonator active area was exposed to pure water, glycerol solutions, and bio-chemical liquids. The characteristics of the glycerol solutions are presented in section 5.2.2. The bio-chemical solutions will be presented in section 5.4.2.

The impedance of the SMR was measured by network analyzer S-parameter measurements. In general it was measured in a narrow band (about 100 MHz) around its resonant frequency with a 800 point resolution. For bio-chemical time-dependent measurements, the narrow-band was only 30 MHz with a 200 point resolution and was recorded at intervals of 14 s. The impedance data were loaded to a dedicated MATLAB program in a computer through a GPIB interface for SMR characteristics determination and monitoring. Paragraph 2.5.1 gives more details. To ensure stable measurement conditions, a constant temperature was assured by placing the wafer on a temperature chuck system (AirCool SP72 system from *ERS electronic GmbH*, Germering, Germany). This is important since the viscosity of glycerol solutions is very much temperature-dependent. In some experiments, the temperature was controlled by a Pt resistance integrated next to the resonators on the wafer. Care was also taken to prevent the measuring probes of touching the solution in order to ensure reliable measurements. Only the resonator active surface defined by the top electrode area was covered by liquid. Unlike the resonators presented in Chapter 4, the electrical signal line length of the resonators measured in this chapter was longer, in general 500 µm to 750 µm to permit the positioning of a liquid droplet or a flow-cell without touching the probes.

---

[1] R. Borngräber, J. Schröder, R. Lucklum, P. Hauptmann, *IEEE Trans. Ultrason., Ferroelec., Freq. Contr.* **49**, 1254 (2002).
[2] K. K. Kanazawa, J. G. Gordon, *Analytica Chimica Acta* **175**, 99 (1985).

Different methods have been used to apply the liquids to the resonators. The simplest was to deposit a small **droplet using a syringe**. This is shown on Figure 5.1 for resonators of DESIGN 1 and DESIGN 2. The volume of the droplet has been estimated to approximately 1µl, largely covering the resonator surface. This method has the advantage of being rapid and provides first results to evaluate the SMR performance. However, it is not absolutely reliable, since the volume of the droplet is not constant and the signal path can be covered by different extends, slightly influencing the resulting signal.

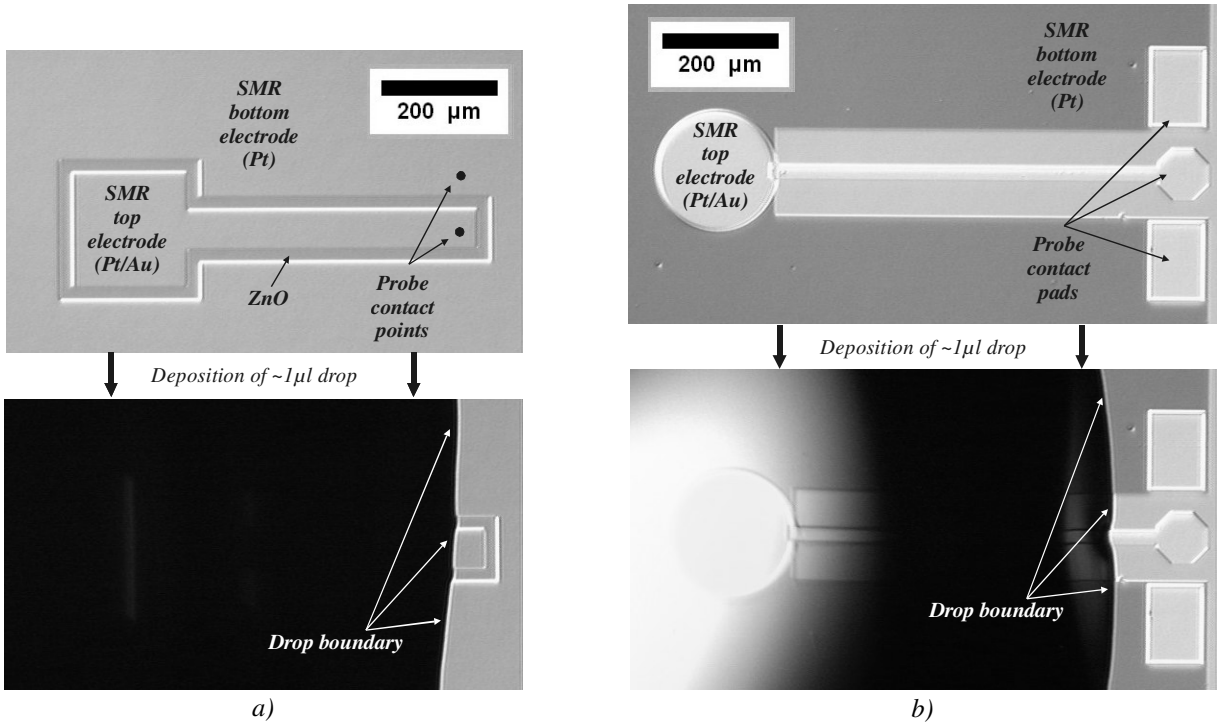

Figure 5.1 : Microscope view of two SMRs of DESIGN 1 (a) and DESIGN 2 (b) before and after the deposition of a droplet of pure water on the surface.

Reliable and constant measurements conditions have been obtained using **flow-cells**. They were fabricated in acrylic glass and positioned on top of the resonator active surface, leaving the contact pads free for contacting with the measuring probes. A viton strip between the flow-cell and the wafer ensured sealing and good control of the fluid inside the cell. An **open** flow cell, shown on Figure 5.2 a), was used for the measurements with different glycerol solutions. Here, the liquids were filled into the cell using a syringe. The volume in the open flow-cell could be adjusted between 50 µl and 180 µl. For glycerol experiments, the concentration could be increased stepwise by adding defined volumes of glycerol. For other measurements however, this setup was not convenient, since the flow-cell had to be removed for emptying it and cleaning of the wafer, prior to the use of another solution. A **closed** flow cell, shown on Figure 5.2 b), was therefore used for the bio-chemical experiments. The flow-cell chamber has an inflow and outflow that are connected to external pumps and fluidic systems. The volume of the liquid in the closed flow cell was 30 µl. For both flow-cells, the Pt temperature control resistance was inside the cells in contact with the liquid allowing correct temperature-monitoring.

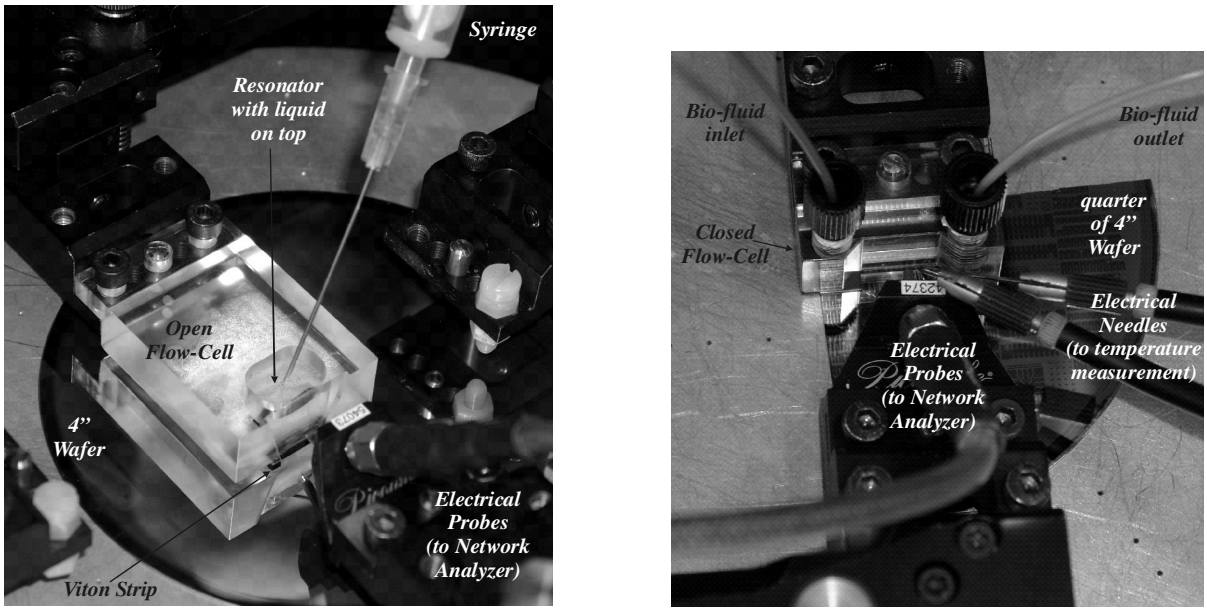

a) *b)*

Figure 5.2 : Photographs showing the open (a) and closed (b) flow-cells used for the applications of liquids on the resonator surface.

5.2.2. Glycerol solutions of various viscosities

To assess the influence of liquids on the resonator properties, glycerol solutions have been used. Depending on the glycerol concentration, the viscosity of the liquid is changed. Glycerol, $C_3H_8O_3$, is a molecule belonging to the alcohol family. At ambient temperature and pressure, it is a colourless and odourless liquid. It shows a very high viscous behaviour and is soluble in water. It is used in various industries to smoothen products.[3] One of the main advantages of glycerol solutions is the achievable viscosity range. Indeed, it shows a near exponential behaviour in function of the glycerol mass concentration from 0.89 cP (centiPoise = mPa.s) for pure water up to 934 cp for pure glycerol (at 25°C), i.e. more than 1000 times larger.[4] At the same time its density changes only about 26 % over the same concentration range, varying from 1 to 1.26 g/cm^3. Over the past 3 decades, it has therefore been used on various occasions to determine the properties of acoustic devices and sensors in liquids of different viscosities with QCM and SAW devices.[5] Recently, it has also been used in case of a shear mode AlN FBAR, in similar measurements as those presented in this work.[6]

Glycerol concentrations with various mass concentrations have been prepared. The viscosity of these solutions was assumed from tabulated values of the *CRC Handbook of Chemistry and Physics*,[7] which has also been done in various articles.[8] Figure 5.3 a) shows the variation of the viscosity with varying glycerol

[3] http://en.wikipedia.org/wiki/Glycerol
[4] D. R. Lide, *Handbook of Chemistry and Physics*, 76th Edition, CRC Press, Boca Raton, FL (1995).
[5] K. K. Kanazawa, J. G. Gordon, *Analytica Chimica Acta* **175**, 99 (1985); B. Jakoby, M. Vellekoop, *Sens. Act. A* **68**, 275 (1998).
[6] G. Wingqvist, J. Bjurström, I. Katardjiev, *Proc. IEEE Ultrason. Symp*., 50 (2005).
[7] D. R. Lide, *Handbook of Chemistry and Physics*, 76th Edition, CRC Press, Boca Raton, FL (1995).
[8] S. J. Martin, V. E. Granstaff, G. C. Frye, *Anal. Chem.* **63**, 2272 (1991); F. Teston, G. Feuillard, L. Tessier, L.P. Tran Hu Hue, M. Lethiecq, *J. Appl. Phys.* **87**, 689 (2000).

mass concentration. Figure 5.3 b) shows the variation of the density. The glycerol viscosity is also very dependant of the temperature. It drops from a value of 934 cP at 25°C to 14.8 cP at 100°C. In this work, the temperature was either kept at 20°C or 25°C. Both curves are shown on Figure 5.3. A cleaning procedure to remove the glycerol from the wafer was developed.[9] Before rinsing the wafer with water, the glycerol was diluted with isopropanol. No traces were found after drying the wafer in nitrogen.

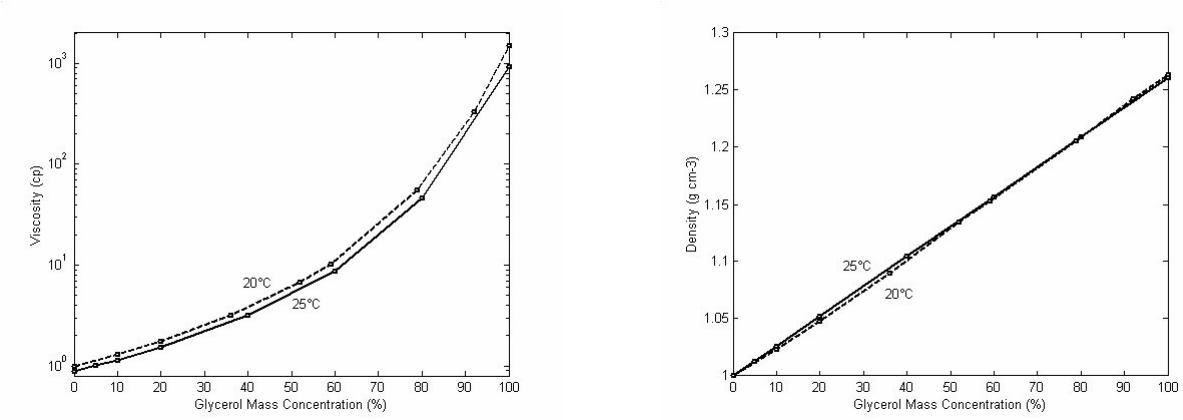

a) *b)*

Figure 5.3 : Dependence of viscosity (a) and density (b) of water-glycerol solutions on the mass concentration.[7]

5.3. Operation of SMRs in liquid environment

The bio-chemical measurands to be detected with a bio-chemical sensor are found in bodyfluids like urine, serum, saliva, blood and various body tissues.[10] Urine and serum have viscosities close to the viscosity of water, and often the measurands are dissolved in certain aqueous solutions. The physical properties of these solutions can influence the sensor signal in the same order of magnitude than a mass attachment. Therefore, the response due to the environment must be known precisely. In sections 5.3.1 and 5.3.2, it is analyzed how the SMRs behave in contact with water. Blood, saliva and certain bio-chemical solutions can be more viscous, which is why the sensing characteristics have also been analyzed in liquids of higher viscosities, described in section 5.3.3. Finally, section 5.3.4 analyzes the expected sensing characteristics.

5.3.1. Impedance characteristics in pure water

5.3.1.1. Observation: difference between shear and longitudinal modes

Figure 5.4 a) shows a broadband characteristic of the impedance amplitude of a resonator from sample SIIIa in air (dashed line) and in pure water (solid line). The water was applied with a syringe as described in section 5.2.1. Sample SIIIa exhibits high Q-factors in air with average effective coupling coefficients of 0.08 and homogeneous film properties (see section 4.6.1). Its complete impedance characteristic (amplitude and phase) has been given in Figure 4.25. The resonator measured here has an area of $200 \times 200\ \mu m^2$. When

[9] A. Phommahaxay, Diploma Thesis, Siemens/ESIEE (2004).
[10] P. W. Laird, *Nature Reviews* **3**, 253 (2003).

immersed in water, all peaks are damped and their amplitude is reduced. For the longitudinal mode peak (LM) at 1.7 GHz however, the damping is much stronger and the resonance almost disappears. The wide-band characteristic is slightly lowered for the measurement in water because an additional capacitive path exists through the liquid between the top and bottom electrodes of the SMR. Since the total clamped capacitance will therefore be larger, the wide-band impedance will be lower. As seen on Figure 5.4 b), similar observations can be done for sample SIIIb. The fundamental shear and longitudinal mode resonance peaks have been analyzed more closely. Figure 5.4 c) shows the narrow-band characteristic for the shear mode of SIIIa in air and in water. The phase maximum decreases from 0.16 rad to -0.5 rad. A small resonance frequency shift of 630 kHz can be recognized. An effective coupling coefficient of 0.083 and a Q-factor of 442 are observed in air, corresponding to what has been seen in Chapter 4. In water, the Q-factor drops to 235.[11] The Q-factor calculated from the slope of the phase, Q_{SLOPE}, decreases from 227 in air to 123 in water. Three other resonators have been tested on this wafer. In average, the Q-factors drop from 445 to 225 (reduction of 49 %) and the frequency change is 636 kHz. The average Q_{SLOPE} in water is 118 down from 215 in air. The effective coupling coefficient stays constant at 0.08.

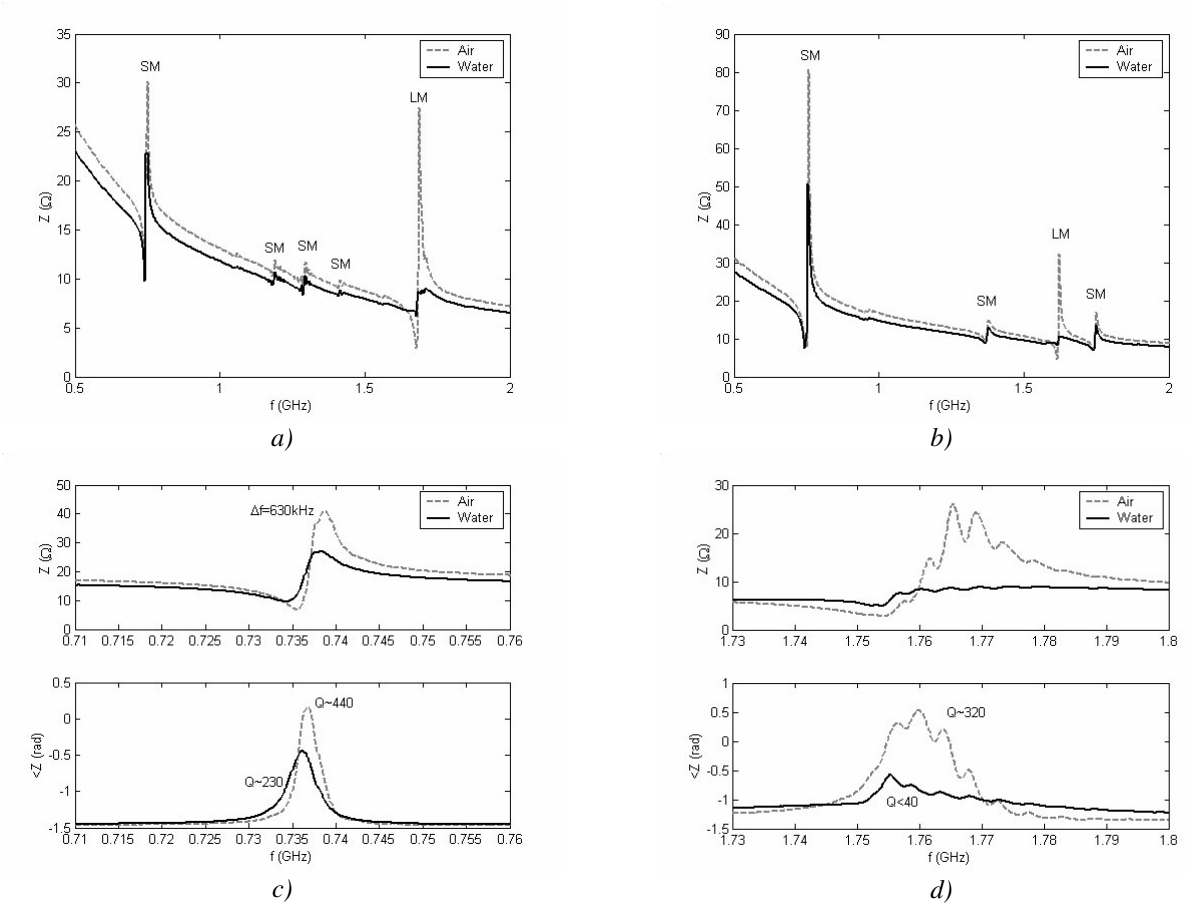

Figure 5.4 : Broadband impedance characteristics of samples SIIIa (a) and SIIIb (b) in air and pure water; and narrowband characteristics of the fundamental shear (c) and longitudinal (d) modes of SIIIa in air and water.

[11] These values can be obtained by fitting of the impedance on a BVD model, which will be shown in section 5.3.2.

For comparison, the longitudinal mode narrow-band characteristics of SIIIa are shown on Figure 5.4 d). The heavy over-modes are due to imperfect reflectivity of the mirror, which is optimized for the shear mode. By fitting a BVD model on the curve, a Q-factor of 321 was obtained in air. As can be seen, the resonance is heavily damped in water and reaches a Q-factor of less than 40. For the 4 tested resonators of sample SIIIa, in average, the longitudinal Q-factors drop from 276 to 58. The corresponding Q_{SLOPE} lie well below 10.

These initial observations clearly show the advantage of the shear mode over the longitudinal mode for measurements in water. For sample SIIIa, **in average, the shear Q-factors are reduced by 49 %, whereas the longitudinal mode Q-factors are reduced by 79 %.** For sample SIIIb the results are similar, however, the reduction is less pronounced. The shear Q-factors are only reduced by 25 % from 248 to 186, but the longitudinal Q-factors decrease heavily by 70 %. The different values for the reduction of Q for samples SIIIa and SIIIb could be due to the fact that the coupling coefficient of SIIIb is much higher at an average of 0.146. The Q-factors in water lie around 200 for both wafers. Due to its high coupling, sample SIIIb features average Q_{SLOPE} in water of 187, which potentially gives high mass resolutions.

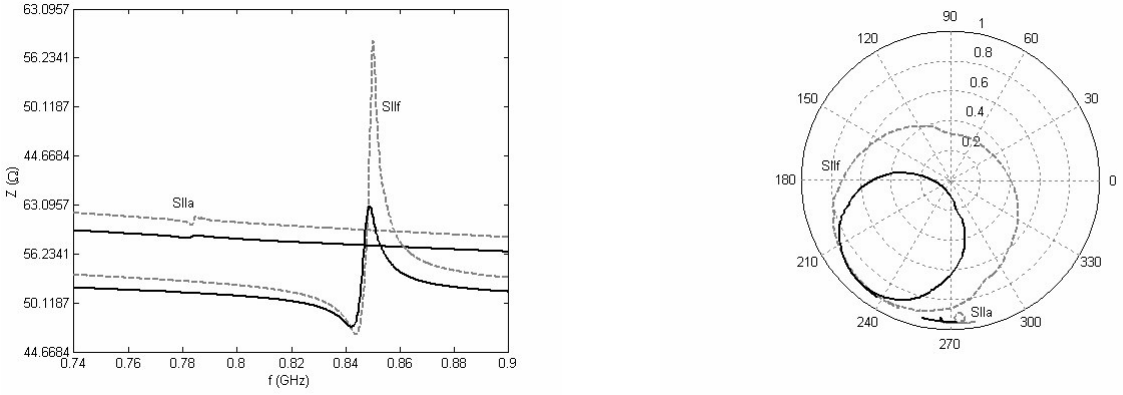

a) *b)*

Figure 5.5 : Comparison between the measured narrowband impedance characteristics of samples SIIa (K_{eff}=0.012) and SIIf (K_{eff}=0.128) in air (solid line) and in pure water (dashed line): a) impedance amplitude, b) Smith-chart representation. Q_{SLOPE} drops from around 350 and 311 in air, to around 200 and 192 in water respectively.

5.3.1.2. Observation: difference between different shear mode samples

Figure 5.5 shows a comparison between the narrowband shear mode impedance characteristics of samples SIIa and SIIf. Both samples have been realized with PROCESS II, but differ by the employed buffer-layer and acoustic mirror. As was shown on Table 4.2, sample SIIa was the very first SMR realized in this work with fitted Q-factors of more than 300 and an effective coupling coefficient of only 0.012. Sample SIIf is one of the latest samples and features a Q-factor in air of 311 at an effective coupling coefficient of 0.128, i.e. 10 times higher than SIIa. Although the Q_{BVD} are very similar, the Q-factors computed from the slope of the phase are different: 25 for sample SIIa (estimated) and 284 for sample SIIf. The situation is worse in water. As can be seen, the resonance of sample SIIa nearly totally disappears bringing the Q-factor Q_{SLOPE} to values as low as those that have been recorded for the longitudinal mode. The fitted Q-factors both stay at around 200. For sample SIIf, Q_{SLOPE} in water is 156. This value permits to have a zero-phase crossing in water, which can be recognized by the crossing of the central horizontal line on the Smith-Chart on Figure 5.5 b).

5.3.1.3. Theoretical explanations for the reduction of Q_{BVD} and f_s

In the previous two sub-sections, it was seen that although the Q_{BVD} in air of samples SIIa, SIIf, SIIIa and SIIIb are different, they are similar in water and all lie around 200. Moreover, the resonance frequency change for the 4 samples of several hundreds of kHz is also similar. In this section, it will be analyzed more closely how Q_{BVD} and the resonance frequency change in contact with water and if the well-established QCM theory can be adapted to SMRs. Figure 5.6 a) and b) illustrate the average Q-factor and resonance frequency change for several SMRs of samples SII d, e and f, and SIII a and b.

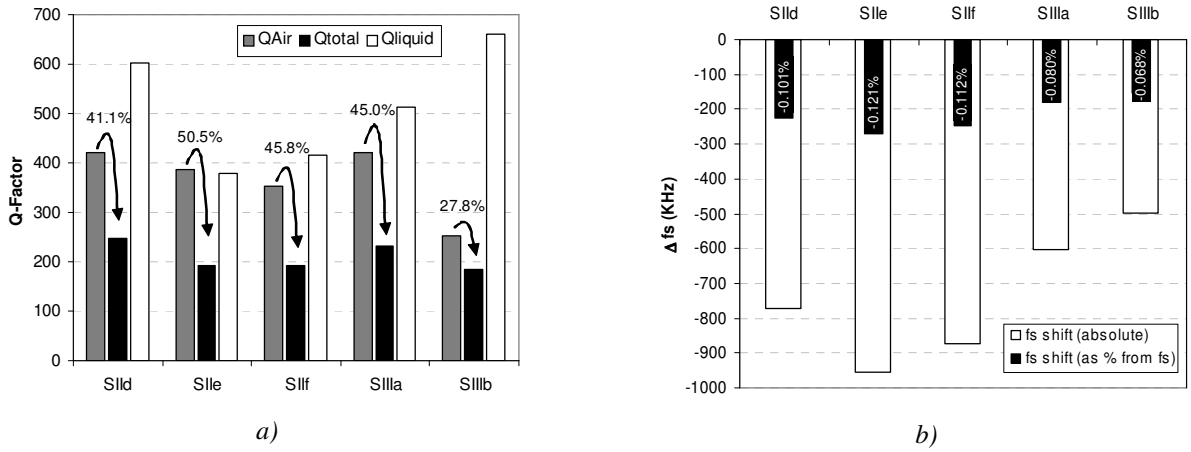

Figure 5.6 : Average change of SMR Q-factors (a) and resonance frequency (b) in water for resonators of different samples. Q_{Total} is the Q-factor in water; Q_{Air} and Q_{Liquid} are the Q-factor contributions from the losses in air and to the liquid respectively.

The total Q-factors in water lie around 200. They depend on the various energy loss mechanisms and a particular quality factor can be attributed to each loss source. When operated in air, the losses (acoustic mirror, wave scattering, material losses) are incorporated in the quality factor obtained by fitting the impedance to the BVD model, Q_{BVD}. When the shear wave mode is coupled into a viscous media such as water, an additional loss source will be added to the device leading to a reduction of the overall Q. **The reciprocal of this additional loss is expressed by the Q-factor Q_{Liquid}**. Using equation (2.99), the resulting Q_{Total} can be written as:

$$\frac{1}{Q_{Total}} = \frac{1}{Q_{Air}} + \frac{1}{Q_{Liquid}} \qquad (5.1)$$

These three quality factors are shown on Figure 5.6 a), where Q_{Air} and Q_{Total} are the quality factors obtained by measurement, and Q_{Liquid} was calculated using equation (5.1). As can be seen, Q_{Liquid} is very much dependent on the sample. At first glance this seems odd, since the losses in liquid are expected to be mainly dependent on the properties of the liquid. It can be understood by considering the theoretical developments done for QCMs when covered by a *semi-infinite* liquid layer.

In section 2.3.4 it was seen that a slight longitudinal mode contribution is also excited at the shear mode resonance frequency, since the polarization direction of the waves is slightly inclined with respect to the surface normal. However, for a c-axis inclination between 0° and 30°, this inclination of the polarization is

less than 5° and the quasi-shear wave can be regarded as a predominantly pure shear mode. One can easily show that in shear resonance, the losses due to the longitudinal contribution are neglectable with respect to the viscosity losses on the shear contribution. This is the reason why the theories developed for a pure shear mode QCM based on AT-quartz crystals can also be considered for the study of the SMR devices of this work. For a simple quartz device operating in a liquid of density ρ_L and viscosity η_L, Q_{Liquid} is:[12]

$$\frac{1}{Q_{Liquid}} = 2\frac{\sqrt{\rho_L \eta_L f_0}}{\sqrt{\pi \rho_Q \mu_Q}} \tag{5.2}$$

Where f_0 is the resonance frequency of the unloaded quartz and ρ_Q and μ_Q are its density and shear elastic modulus respectively. This formula is only valid for Newtonian liquids meaning that the viscosity must be constant for different shear rates or frequencies, which is the case for pure water at 800 MHz. The SMRs of this work are multi-layered devices and based on thin films whose acoustic properties can differ from the bulk properties of the materials. Therefore, no single acoustic velocity or density can be defined. However, the impedance of a quartz resonator is described by the same equation which is valid for a particular resonance for a SMR, equation (2.92). It can therefore be assumed that equation (5.2) is also valid for SMRs where the quartz properties $\rho_Q \cdot \mu_Q$ are replaced by a constant C_{SMR} characteristic for a certain resonator and resonance:

$$\frac{1}{Q_{Liquid}} = 2\frac{\sqrt{\rho_L \eta_L f_0}}{\sqrt{\pi C_{SMR}}} \tag{5.3}$$

For a perfect FBAR consisting of a thin film of 16° inclined ZnO and vibrating in pure shear mode, C_{SMR} is equal to:

$$C_{16°-ZnO} = \bar{c}_{55} \cdot \rho = 4.97 \cdot 10^{10} \cdot 5680 = 2.83 \cdot 10^{14}\,(\mathrm{Pa.kg/m^3}) \tag{5.4}$$

Knowing that $\rho_L \eta_L$ in water is equal to 0.89 Pa.s.kg/m^3, we find a Q_{Liquid} of **559** for a resonator vibrating at 800 MHz. Comparing with Figure 5.6, the measured Q_{Liquid} are of the same order of magnitude. **Since the samples have different stack designs and different ZnO layer properties, the respective C_{SMR} constants, corresponding to effective densities and shear moduli, are slightly different, leading to the differences in Q_{Liquid}.** It is observed that samples SIIe and SIIf have similar $Q_{Liquids}$. Interestingly these two samples have also similar stack designs, both having a 4-fold Pt-ZnO mirror with SiO_2 top layer. The highest Q-liquid of 641 corresponding to the lowest losses into the liquid, is found for sample SIIIb, which has a W-SiO_2 mirror. The constants C_{SMR} can be estimated through formula (5.3) and the measurement results. In average, they vary between $1.29 \cdot 10^{14}$ Pa.kg/m^3 for sample SIIe to $3.59 \cdot 10^{14}$ Pa.kg/m^3 for sample SIIIb. As expected, they are close to the constant $C_{16°-ZnO}$ of a perfect ZnO FBAR.

A similar analysis can be done to explain the resonance frequency change shown in Figure 5.6 b). Kanazawa and Gordon found the expression of the resonance frequency shift of a quartz plate when immersed in a Newtonian liquid:[13]

[12] C. D. Stockbridge, *Vacuum Microbalance Techniques* **5**, Plenum Press, New York, 147 (1966).
[13] K. K. Kanazawa, J. G. Gordon, *Analytica Chimica Acta* **175**, 99 (1985).

$$\Delta f = -f_0^{3/2}\sqrt{\frac{\rho_L \eta_L}{\pi \mu_Q \rho_Q}} \tag{5.5}$$

Again, this expression can be applied to SMRs by using the constant C_{SMR}:

$$\Delta f = -f_0^{3/2}\sqrt{\frac{\rho_L \eta_L}{\pi C_{SMR}}} \tag{5.6}$$

For the same reasons than those mentioned above, C_{SMR} can be very different for the different SMR samples, leading to different resonance frequency shifts. For a perfect FBAR consisting only of a thin film of 16° inclined ZnO and vibrating at 800 MHz, the resonance frequency shift would be **716 kHz**. Again, the average frequency shifts shown in Figure 5.6 are all close to that value. The constants C_{SMR} estimated with formula (5.6) and the measurements results lie between $1.54 \cdot 10^{14}$ Pa.kg/m^3 for sample SIIe and $4.41 \cdot 10^{14}$ Pa.kg/m^3 for sample SIIIb, which is slightly higher to what was found with Q_{Liquid}.

A simple check can be done to see if formulas (5.6) and (5.3) can be applied to SMRs. Combining both formulas, we get:

$$\frac{1}{Q_{Liquid}} = -2\frac{\Delta f_s}{f_s} \tag{5.7}$$

The relation between Q_{Liquid} and Δf_s is independent of the properties of the liquid and the resonator. Figure 5.7 shows this relationship for the individual resonators whose average values are given in Figure 5.6. As can be seen, roughly, the relationship holds. This confirms that the constants C_{SMR} computed through the Q-factors match those computed through the resonance frequency shift. The average values for SIIe, SIIf and SIIIb perfectly match the theoretical prediction. For sample SIId, some points lie below the line and for sample SIIIa, they are above it.

The differences between the values obtained for the different samples can be attributed to several effects. There are inherent measurement and fitting errors. Due to the differences in stack design and ZnO properties, different C_{SMR} could result for the different samples. There are also two effects that make the theory underlying both formulas not absolutely valid in case of SMR devices. First, this theory assumes that there is no **slip** at the interface between the SMR and the water. The coupling of the acoustic wave into the liquid depends on the hydrophobic / hydrophilic properties of the surface layer. In certain cases a considerable part of the energy at the solid-liquid interface is dissipated as heat, which is referred to as molecular or interfacial slip.[14] The effect of slip can decrease Q_{liquid} due to additional energy loss and decrease the frequency shift. Secondly, the theory assumes a zero **roughness** of the surface of the resonator. Since the SMR of this work can have a surface roughness of up to 10 nm, which is of the same order of magnitude than the penetration depth, liquid can be trapped in crevices. This liquid acts like a rigid mass attachment, resulting in a higher frequency shift. Moreover corners and edges can deviate the flow of liquid and increase the viscous

[14] M. Thompson, G. L. Hayward, *Proc. IEEE Int. Freq. Contr. Symp.*, 114 (1997); G. McHale, M. I. Newton, M. K. Banerjee, J. A. Cowen, *Mat. Sci. Eng. C* **12**, 17 (2000).

dissipation.[15] An exact characterization of the surface would be necessary to be able to predict the liquid influence on the measured frequency and damping shifts.

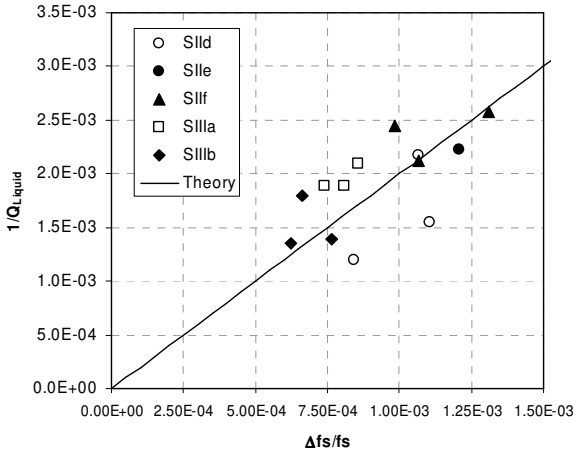

Figure 5.7 : Relation between the normalized resonance frequency shift and the losses into the liquid.

Kanazawa and Gordon mentioned that the frequency shift can be seen as a gravimetric effect on the resonance. In fact, the shear wave is strongly damped when entering the liquid. This damping can be described by the penetration depth, given by:[16]

$$\delta_P = \sqrt{\frac{\eta_L}{\rho_L \pi f}} \tag{5.8}$$

The mass of the liquid within this penetration depth can be considered in the same way than a mass layer on top of the resonator. The corresponding frequency shift can be readily found by using the mass sensitivity of the resonator. For a frequency of 800 MHz in water, the penetration depth is 18.8 nm. This distance is much smaller than the height of the liquids applied to the SMRs (generally more than 1 mm) and justifies the assumption of the developments done above which are only valid in case of a semi-infinite liquid. The corresponding mass/area in water is 940 ng/cm^2.[17] With a sensitivity of -760.8 Hz.cm^2/ng as calculated with the Sauerbrey relation (see formula (4.1)) for a perfect FBAR consisting only of a thin film of 16° inclined ZnO vibrating at 800 MHz, we again obtain a frequency shift of 716 MHz, corresponding to the value directly computed by the Kanazawa formula.[18] As was seen in Chapter 4, the sensitivity of SMRs strongly depends on the acoustic stack design and not only on the resonance frequency. It is influenced by the thickness of the individual layers, their acoustic velocity and their density. Since these values vary for the different SMRs considered above, the obtained frequency shifts varies.

In conclusion, the established QCM theory seems to work for SMRs at 800 MHz in pure water. Instead of the density-modulus product, the formulas can be applied using C_{SMR} valid for a certain resonator and a

[15] D. Johannsmann, *Macromol. Chem. Phys.* **200**, 501 (1999).
[16] K. K. Kanazawa, J. G. Gordon, *Analytica Chimica Acta* **175**, 99 (1985).
[17] Considering a linear decrease of the wave amplitude within the penetration depth, the mass of the entrained liquid is $\frac{1}{2}\delta_P\rho_L$.
[18] This value for the sensitivity is slightly higher than the value calculated in Chapter 4, -807 Hz.cm^2/ng, since in Chapter 4 the inclination of the ZnO was not taken into account, giving a slightly lower acoustic velocity than at 16°.

certain resonance. These formulas are only valid in case of a Newtonian liquid. For higher viscosities, the situation can be different, which is examined in section 5.3.3 for the Q-factors and in section 5.4.1 for the frequency shift. Since the Q-factors due to the liquid are of the same order of magnitude than those in air, the overall Q-factor is determined by both. Whereas the Q-factor due to the liquid cannot greatly be improved, the Q-factor in air can be optimized. It is expected that it can be brought to values over 1000.[19] In that case, the total Q-factor in water would be mainly determined by Q_{liquid}. Other examinations of the interaction between the SMR surface and the liquid are given in the thesis of J. Weber.[20]

5.3.2. Effect on BVD values in pure water

For the design of the integrated read-out circuitry it is important to describe the SMR impedance with equivalent electrical elements.[21] Moreover, fitting an equivalent circuit model to electric measurements allows an extraction of SMR properties. Therefore, the Butterworth-Van Dyke model (BVD) was introduced in section 2.4.5. The values of C_0, C_m, L_m and R_m are given in equations (2.104) to (2.107). Martin *et al.* have shown that the characteristics of a quartz resonator in contact with a semi-infinite liquid can be described by adding some elements to this basic BVD model.[22] Similarly to Kanazawa and Gordon, they assumed no slip at the interface and a perfectly plane surface. The resulting extended BVD model is shown in Figure 5.8.

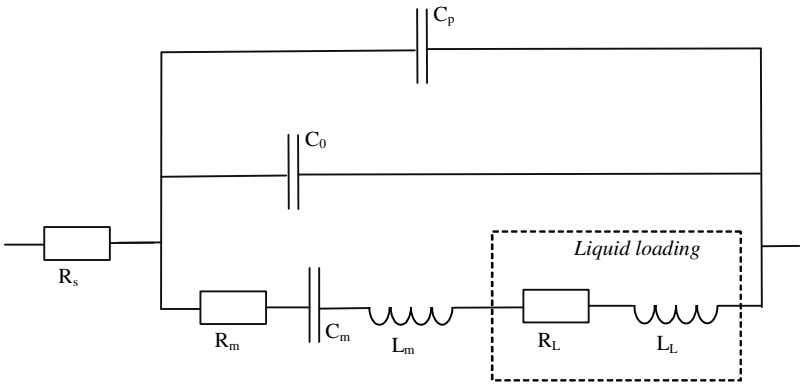

Figure 5.8 : Extended BVD model in liquids. The frequency change and damping of the resonance due to the liquid are represented by R_L and L_L. The additional electrical path through the liquid is represented by C_P.

As for the unperturbed BVD model, this model describes the impedance in a narrow-band frequency region around a particular resonance. The additional dielectric path from signal to ground through the liquid adds a parallel capacitance C_P to the circuit. It depends on the design of the electrodes and the liquid which is used. For conductive liquids, an additional parallel conductance must also be added. In the case of water and glycerol solutions however, the conductivity of the liquid is negligible and the conductance can be considered as an open circuit.

[19] K. M. Lakin, G. R. Kline, K. T. McCarron, *IEEE Trans. Microwave Theo. Techn.*, **41**, 2139 (1993).
[20] J. Weber, PhD Thesis, Universität Augsburg, to be published.
[21] Personal communication from Kari Tukkiniemi, VTT, Finland.
[22] S. J. Martin, V. E. Granstaff, G. C. Frye, *Anal. Chem.* **63**, 2272 (1991).

The liquid loading resulting in a resonance frequency change and a damping of the resonance is represented by R_L and L_L, which are added to the motional arm of the model. For a QCM of resonance frequency f_0, density ρ_Q and shear elastic modulus μ_Q, the values are given by:[23]

$$R_L = 2f_0^{3/2}{}_0 L_m \sqrt{\frac{4\pi\rho_L\eta_L}{\rho_Q\mu_Q}} \tag{5.9}$$

$$L_L = 2f_0^{1/2} L_m \sqrt{\frac{\rho_L\eta_L}{\pi\rho_Q\mu_Q}} \tag{5.10}$$

The elements added to represent the liquid loading of the quartz are related to the unperturbed QCM parameters. Consequently, knowing the parameters of a QCM in air permits to find the response to a given liquid. Since these formulas are based on the same theoretical derivations than the formulas for Δf and Q_{liquid} presented in the previous section, it can be inferred that **this extended BVD model can also be applied to SMRs using C_{SMR} instead of $\rho_Q \cdot \mu_Q$**. In the same way that R_m is related to the losses of the resonator in air, R_L represents the additional losses in liquids. The frequency change is dependent on the additional L_L. This can be interpreted as an addition of additional mass to the resonator surface. As the conductance of the liquid can be neglected, the extended BVD model can be brought back to a standard BVD model by adding R_m and R_L, L_L and L_m, and C_0 and C_P. [24] C_m should not change. This justifies the use of the BVD model to fit impedances recorded in water. The mass loading affects the resonant frequencies equally, but in a sensor measurement, the series resonator frequency is preferred because it is less influenced by the circuit elements that are not intrinsic to the resonator, for example a variation of the clamped capacitance C_0 due to C_P.

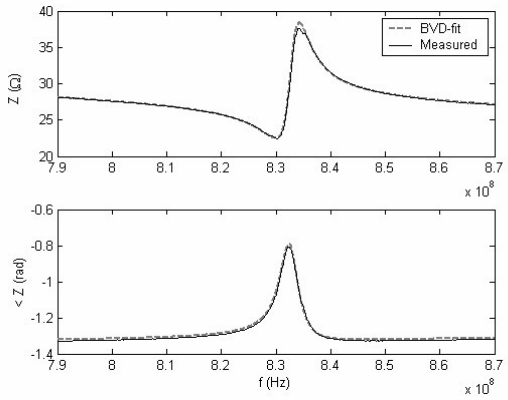

Figure 5.9 : Typical measured and fitted BVD impedance characteristic of an SMR in pure water.

To test the extended BVD model in water and obtain average values for electronic circuit design, 6 wafers each corresponding to sample SIIf were fabricated. On each wafer, there were 8 arrays which had a design for measurement in liquids and which lay in the region of sufficient shear mode excitation. From each array of 20 resonators, one was measured in air and in water at 25°C, and fitted on a BVD circuit. A typical measured characteristic in water with the fitted BVD characteristic is given in Figure 5.9. The good

[23] S. J. Martin, V. E. Granstaff, G. C. Frye, *Anal. Chem.* **63**, 2272 (1991).
[24] J. Auge, P. Hauptmann, J. Hartmann, S. Rösler, R. Lucklum, *Sens. Act. B* **24-25**, 43 (1995).

correspondence of the model with the measurements can be observed. In average, a line resistance R_s of 6.6 Ω had to be placed in series with the BVD model to account for electrical losses from the contact line in our design. This explains that the phase does not reach $-\pi/2$ outside the resonance.

The average results are given in Table 5.1, along with the standard deviation for each parameter. The average values in air have a very low spread. The resonance frequency has a standard deviation of only 1%. Although the ZnO process used here (PIIj) has a very high spread of the values in the utilizable region, the resonators that have been measured in this experiment all lie on the same line parallel to the blind and on the same spots on the wafer. This spread is thus a measure of the reproducibility of the process over different wafers.

TABLE 5.1
AVERAGE AND STANDARD DEVIATION OF DIFFERENT PARAMETERS OF MEASURED SMRS IN AIR AND IN PURE WATER.

Parameter	Air	Water	Change	%-Change
f_s (MHz)	839.38 ± 1%	838.29 ± 1%	-1.09	-0,13%
Q_{BVD}	397 ± 6%	204 ± 3%	-193	-48,57%
K_{eff} (%)	0.047 ± 13%	0.043 ± 13%	-0.004	-9,72%
C_0 (pF)	6.31 ± 4%	7.60 ± 4%	1.29	20,48%
C_m (fF)	11.50 ± 28%	11.23 ± 27%	-0.273	-2,37%
L_m (µH)	3.42 ± 23%	3.48 ± 22%	0.06	1,65%
R_m (Ω)	47.9 ± 20%	90.5 ± 21%	42.6	88,81%

Again, average Q-factors of around 200 have been found in water, corresponding to what was seen in 5.3.1. The frequency change is 1.09 MHz, which is slightly higher than for the resonators examined in sub-section 5.3.1.3. The higher frequency shift is mainly due to the higher resonance frequency of 840 MHz. The effective coupling has slightly dropped. This can be explained through the increase of C_0 from 6.3 pF to 7.6 pF. C_P is therefore 1.29 pF. If C_0 increases, the effective coupling and C_m can decrease, since the three values are related through formula (2.105). In principle C_m should stay constant and the change is probably due to fitting effects. As expected, L_m and R_m have both increased. With formula (5.9), the increase of R_m permits to find a value for C_{SMR} of $1.7 \cdot 10^{14}$ Pa.kg/m^3, which perfectly corresponds to the values found in 5.3.1.3 for sample SIIf. The value for C_{SMR} computed by the change of L_m is slightly lower, which might be attributed to the fact that L_m in liquid is lower than expected, due to the decrease of C_m. R_s does not change when the SMR is immersed in water, staying at 6.7 Ω. This shows that the liquid effectively is non-conductive and R_s is only due to the electrical resistance of the signal lines and the contact probes. In conclusion, the trend of the changes of the BVD values between air and water corresponds to the expected theory. Moreover, the fitting of the impedance on the BVD in water provides good results, which is important for electric circuit design.

5.3.3. Effect on Q-factor in liquids of different viscosities

The experiments described in the previous section were performed in pure water which can be considered as a perfectly Newtonian liquid at 800 MHz. Well-established formulas for the frequency change and damping

could therefore be used. To investigate the SMR behaviour for higher viscosities, a number of measurements in glycerol solutions with different concentrations were performed.

Figure 5.10 shows the impedance characteristic of a SMR from sample SIIf in different glycerol solutions. It has an effective coupling coefficient of 0.086 and a parallel resonance frequency of around 798 MHz. In air, it has a quality factor Q_{BVD} of 336. It was measured at 20°C. The glycerol concentrations varied from 0 to 100 %, which gives estimated viscosities varying from 1.005 cP to 1499 cP. Between the applications of the glycerol solutions, the SMRs were cleaned with isopropanol and distilled water. As can be seen, the phase maximum decreases from -0.56 rad to -1.24 rad with increasing viscosity. At the same time the point of minimum amplitude shifts to lower frequencies.

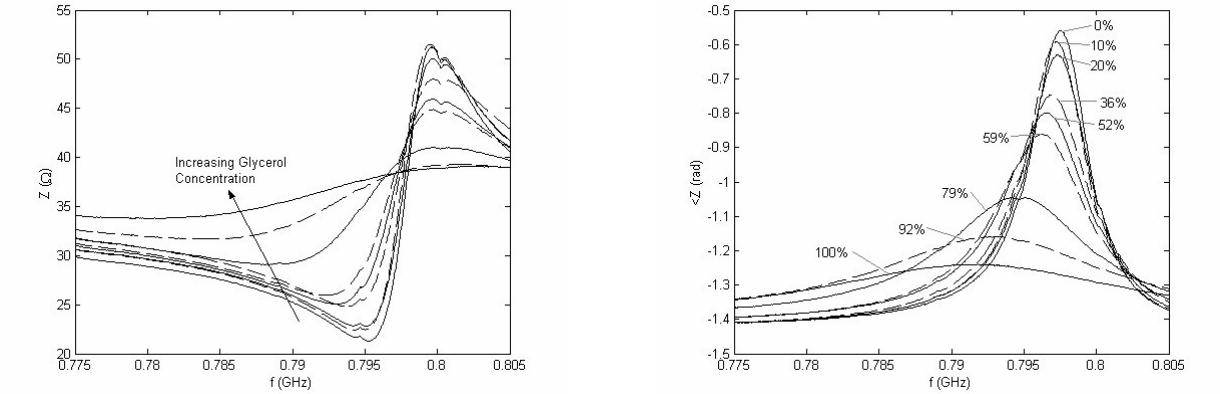

a) *b)*

Figure 5.10 : Impedance characteristics (a: amplitude; b: phase) for an SMR in contact with liquids with glycerol concentrations of 0% to 100% at 20°C (viscosities of 1, 1.76, 3.16, 6.76, 10.25, 55.47, 328.4 and 1499 cP).

Figure 5.11 shows the shear mode apparent Q-factors Q_{SLOPE} and the device Q-factors Q_{BVD} for the impedance characteristics of Figure 5.10 as a function of the viscosity (resonator A). The values for two other resonators from this sample are also shown (resonator B and C). The three curves correspond well. As expected, Q_{BVD} is always higher than Q_{SLOPE}. Q_{BVD} drops from around 200 in air to 30 in 100% glycerol. Q_{SLOPE} drops from 110 to 10. Figure 5.11 also shows the longitudinal mode Q_{BVD}. It constantly stays below 20. The graph clearly shows the **big advantage of the shear mode over the longitudinal mode**.

When immersing this resonator in water, the resonance frequency shift and the Q-factor change permit to find a value for C_{SMR} as has been seen in section 5.3.1. Both values are close: a C_{SMR} of $1.4 \cdot 10^{14}$ Pa.kg/m^3 was found by using the Q-factor change and a C_{SMR} of $1.9 \cdot 10^{14}$ Pa.kg/m^3 by using the frequency shift. The theoretical curve for the Q-factor reduction obtained using equations (5.1) and (5.3) is shown on Figure 5.12. Both values of C_{SMR} give approximately the same curve. Although it is not explicitly shown on the figure, the density change has been taken into account in this theoretical line. As can be seen, the measured Q_{BVD} correspond quite well to the expected values up to a viscosity of 5 cP, corresponding to a glycerol concentration of 44 % at 20°C. Afterwards, the expected Q-values lie below the actually measured ones, meaning that there is less loss than expected. The difference is due to the fact that for higher viscosities, the glycerol solution starts exhibiting a certain elasticity while the effective dynamic viscosity is diminished.

Part of the acoustic energy will then not be dissipated as viscous losses but be transmitted into the liquid. Since the losses are lower than expected, it must be assumed that the loss through elastic transmission is lower than the loss due to viscous friction. The visco-elastic effect is treated in more detail in section 5.4.1.

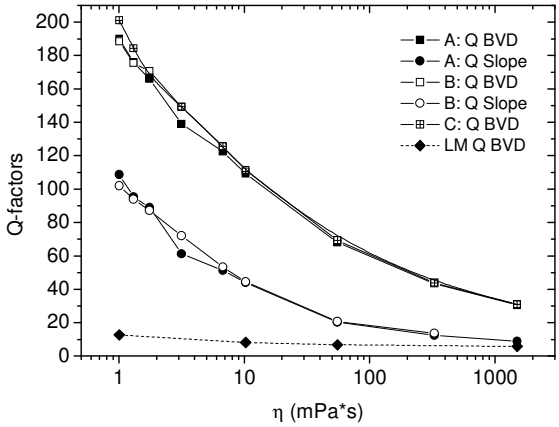

Figure 5.11 : Device and apparent shear mode quality factors Q_{BVD} and Q_{Slope} and longitudinal mode Q_{Slope} factors for three different SMRs vibrating at around 800 MHz in glycerol solutions of different viscosities η.

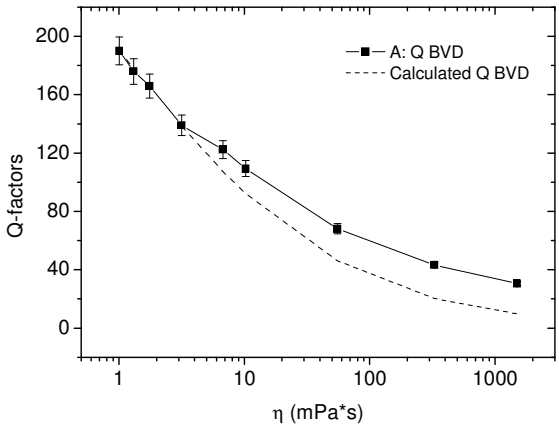

Figure 5.12 : Device quality factors Q_{BVD} compared with the theoretical curve for an SMR vibrating at around 800 MHz in glycerol solutions of different viscosities η.

5.3.4. Calculated gravimetric sensing characteristics

The previous sections have shown that SMRs can be operated in liquids of different viscosities with resonance frequencies of up to 850 MHz and Q-factors of up to 200 in pure water. Since these characteristics are not much different from those in air, it is expected that bio-chemical gravimetric measurements are also possible in liquid, similar to measurements done in air.[25] Moreover, since the resonance frequency changes

[25] R. Gabl, H.-D. Feucht, H. Zeininger, G. Eckstein, M. Schreiter, R. Primig, D. Pitzer, W. Wersing, *Biosens. Bioelectron.* **19**, 615 (2004).

as a function of the liquid viscosity, the SMRs could be used as high-frequency viscosity sensors. The sensing characteristics of the SMR used as sensor are determined by its sensitivity and its mass resolution.

As seen in Chapter 4, the **sensitivity** of the SMRs to mass changes on their surface depends on the stack design. Since the change of the resonance frequency due to a change in viscosity can also be expressed as a mass change, the viscosity sensitivity also depends on this mass sensitivity. It is expected that the mass sensitivity does not considerably change in liquids. A mass addition and a liquid addition add inductances L_M and L_L respectively to the motional arm of the BVD model. This changes the effective L_m, thereby changing the resonance frequency. The sensitivity of the SMR thus depends on the magnitude of L_L and L_M with respect to L_m. L_L and L_M are both much smaller than L_m, which explains that the mass sensitivity should stay the same in liquids as in vacuum. This was shown by Bruckenstein and Shay with QCMs by analyzing frequency changes resulting from metal deposition and from oxide formation.[26] Although the viscosity and mass sensitivities do stay constant, it is important to know both in case of gravimetric measurements, since the employed bio-chemical solutions can have different viscosities and both effects can overlap. Protein films for example have a thickness of about 20 nm, which is in the same order of magnitude than the penetration depth.[27] One can also solve this problem by measuring the resonance frequency prior to and after the bio-chemical binding in the same buffer-solution, thereby removing the viscosity effect. In short, the expected relative mass sensitivity in liquids stays at around -1000 cm^2/g.

The **mass resolution** of the SMR depends on Q_{SLOPE} and the frequency or phase resolution. The quality factors in liquids are much lower than those in air, bringing a considerable reduction of the mass resolution. Assuming a three-fold standard deviation of the frequency fluctuation of less than 3000 Hz for measurements with the Network Analyzer,[28] a mass resolution of less than 4 ng/cm^2 could be reached in water with sample SIIf having a Q_{SLOPE} of 110. If the Q_{BVD} values of around 200 can be reached by increasing the effective coupling coefficient, for example with sample SIIIb, values about 2 ng/cm^2 are expected to be reached since the frequency fluctuation would drop to 1650 Hz. Similarly, a mass resolution of about 10 ng/cm^2 would be feasible in a liquid having a viscosity of 10 cPa with an apparent Q-factor of only 40 for the SMR, which is still a very good value. In blood, with a viscosity of approximately 3 to 5 times that of water,[29] the sensors would therefore still be able to function. The mass resolutions obtainable with longitudinal mode are much worse. Even if the maximum Q_{BVD} of 20 in water can be reached by Q_{SLOPE}, the mass resolution would not be larger than 20 ng/cm^2, which is much worse than comparable QCM values. Therefore longitudinal SMRs do not need to be considered for practical bio-chemical sensing applications directly in liquid.

In conclusion, the obtained SMR characteristics in liquid should be adequate for bio-chemical gravimetric sensing applications in liquids (at 800 MHz), with the advantage of possible integration with CMOS circuitry and miniaturization.

---

[26] S. Bruckenstein, M. Shay, *Proc. Pittsburgh Conf. and Expos.*, Atlantic City, NJ 81983).
[27] C. Kößlinger, E. Uttenthaler, S. Drost, F. Aberl, H. Wolf, G. Brink, A. Stanglmaier, E. Sackmann, *Sens. Act. B* **24-25**, 107 (1995).
[28] This value was determined by frequency measurements in water.
[29] Viscosity for whole blood: 3.3 to 5.5 cP; R. S. Rosenson, A. McCormick, E.F. Uretz, *Clin. Chem.* **42**, 1189 (1996).

5.4. Sensing applications

5.4.1. Viscosity sensing

5.4.1.1. Sensing of the viscosity in the Newtonian range

As has been seen in paragraph 5.3, the immersion in liquids produces a resonance frequency shift which depends on the viscosity and the density of the liquid. The SMRs can therefore also be used to measure the viscosity. The change of resonance frequency for a simple quartz resonator and for Newtonian liquids was derived by Kanazawa and was given in equation (5.5). This relationship seems to hold for SMRs when immersed in water. Here, we will examine the frequency shifts in liquids of varying viscosity. The resonators from sample SIIf, used for the variation of the Q-factor as explained in section 5.3.3, can also be used for the resonance frequency change. They were measured in liquids of glycerol concentrations varying from 0 to 100% at 20°C, which gives estimated viscosities varying from 1 cP to 1500 cP. Figure 5.13 shows the series resonance frequency shift relative to air of three different resonators as a function of the square root of the viscosity density product of the different glycerol solutions. The three curves are very similar. The dashed line on the figure represents the expected shift from the Kanazawa formula calculated with the C_{SMR} extracted from the shift between water and air. For viscosity values below 5 cP, corresponding to glycerol concentrations of 44%, a linear dependence can be observed similar to what was expected. In that case, if density changes are smaller than viscosity changes, the SMR can serve as convenient, economical and highly sensitive viscometer. For higher viscosity values however, the points diverge from a linear dependence and the glycerol can not be referred to as a Newtonian liquid. This is analyzed in the next sub-section.

In the linear region, the viscosity sensitivity, i.e. the frequency change dependence on $\sqrt{\rho_L \eta_L}$ was evaluated to around **-10 MHz·cm^2·s$^{0.5}$/g**. The higher operating frequency of the SMR results in an enhanced sensitivity to viscosity changes compared to previously reported QCMs. Lin *et al.* found a sensitivity of -0.1057 MHz·cm^2·s$^{0.5}$/g for a 30 MHz QCM.[30] Rabe *et al.* found a value of -0.2465 MHz·cm^2·s$^{0.5}$/g for a 49.2 MHz QCM.[31] The SMRs vibrating at around 800 MHz have thus absolute sensitivities 50 to 100 times higher than that of typical QCMs. Regarding the relative viscosity sensitivity, the SMRs have values about 3.5 times that of a 30 MHz QCM. Lin *et al.* assumed a 10 Hz frequency stability for the 30 MHz quartz. Assuming a constant density, they detected a minimum relative viscosity change of $\Delta\eta_L/\eta_{L,Water}=2\cdot10^{-3}$, i.e. a minimum absolute change of $2\cdot10^{-3}$cP. In our case, assuming a frequency fluctuation (standard deviation) of less than 1000 Hz, which has been determined by frequency measurement in water and can still be improved, a **minimum viscosity change of 9.10^{-4} cP** can be detected (with a three-fold standard deviation of the frequency), which is about half the value found by Lin *et al.* for a 30 MHz QCM. These values show that the SMRs can be used as viscosity sensors with better performance than typical QCMs.

It is important to remember this sensitivity to viscosity when performing gravimetric bio-chemical measurements. Indeed, depending on which bio-chemical solution is used, the viscosity can change. One way to solve this problem is to measure the resonance frequency prior to and after the bio-chemical binding

[30] Z. Lin, C. M. Yip, I. S. Joseph, M. D. Ward, *Anal. Chem.* **65**, 1546 (1993).
[31] J. Rabe, S. Büttgenbach, B. Zimmermann, P. Hauptmann, *Proc. IEEE/EIA Int. Freq. Contr. Symp.*, 106 (2000).

in the same **buffer-solution**. Another is to do measurements at **different frequencies**. Since the resonance frequency change due to the viscosity and due to the mass attachment vary differently with respect to the resonance frequency, simple linear equations permit to differentiate both effects. Further results about measuring with viscosity and more detailed measurements at low concentrations of glycerol were done with the devices of this work.[32] They confirm what was observed in this experiment.

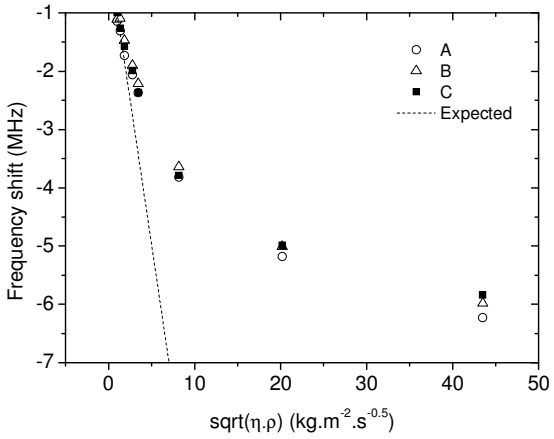

Figure 5.13 : Series resonance frequency shift relative to air for three shear mode FBARs (A,B,C) vibrating at 800 MHz in glycerol solutions with different sqrt(ρ.η) products.

5.4.1.2. Visco-elasticity

If a liquid is in its non-Newtonian range, its viscosity is not constant for different shear rates or frequencies. Maxwell derived a simple model to characterize a visco-elastic liquid. In general visco-elastic materials require complex models,[33] but in an idealized case of liquids consisting of small molecules the Maxwell model is sufficient. It describes the liquid as a serial connection of a dashpot and a spring corresponding to the viscous and the elastic properties. Similar to what was done in section 2.4.4 for the elasticity constant, a complex frequency dependent viscosity can be defined by:[34]

$$\eta_L(\omega) = \frac{\eta_{L,0}}{1 + j \cdot \omega \cdot \tau} \tag{5.11}$$

Where ω represents the angular frequency and $\eta_{L,0}$ is the static viscosity at $\omega = 0$. τ is the relaxation time given by:

$$\tau = \frac{\eta_{L,0}}{\mu^{\infty}} \tag{5.12}$$

Where μ^{∞} is the shear rigidity modulus, defined as the liquid shear modulus when it becomes frequency independent (infinite frequency). Water has a μ^{∞} of around $6.6 \cdot 10^9$ Pa. Recently, a value of $2.5 \cdot 10^9$ Pa has

[32] J. Weber, M. Link, R. Primig, D. Pitzer, M.Schreiter, *Proc. IEEE Frequ. Contr. Symp.*, Miami, ID 6169 (2006).
[33] G. Schramm, "Einführung in Rheologie und Rheometrie", Gebrüder Haake GmbH, 2000.
[34] B. Jakoby, M. Vellekoop, *Sens. Act. A* **68**, 275 (1998).

been obtained for pure glycerol. But various values can be found, ranging from $3.1 \cdot 10^7$ Pa to $2.56 \cdot 10^9$ Pa.[35] The product of the relaxation time and the applied angular frequency specifies how a material behaves. At $\omega \cdot \tau$ products below 1, it will have purely viscous properties with a viscosity equal to $\eta_{L,0}$ (Newtonian range). At very high $\omega \cdot \tau$ products it will have purely elastic properties and behave like a solid with an elasticity modulus μ^{∞}.

Plotting the change in the resistance R_m of the BVD model against the frequency shift, the point of deviation from Newtonian behaviour can be specified (see Figure 5.14).[36] Two lines with different slopes can be observed for resonators A and B, and C respectively. Resonator B has a slightly lower area, and surface effects might be bigger, leading to higher frequency shifts. **For all three measurements, a small deviation from a linear line is observed from the point corresponding to 44% glycerol or a viscosity of 5cP. Distinct deviations are visible at a glycerol concentration of 79% or a viscosity of 55cP**. These points correspond to the deviation of the theoretical line for the measured frequency shift and the Q-factors shown on Figure 5.12 and Figure 5.13 respectively. Teston *et al.* found a visco-elastic behaviour starting at 1000 cP with a SH-APM device of 18 MHz.[35] Jakoby *et al.* found this point at viscosities of 30cP for a Love-wave device at 116 MHz.[37] Winqvist *et al.* found good agreement with Newtonian theory up to 70% glycerol, i.e. a viscosity of around 50cP, at a frequency of 1.2 GHz, but their measurement was not very precise.[38] The different values are due to the fact that the start of visco-elastic behaviour can not really be quantified.

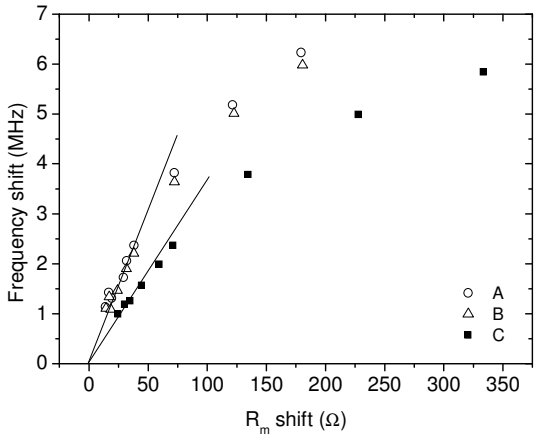

Figure 5.14 : Change of motional resistance R_m versus resonance frequency shift for three shear mode FBARs (A,B,C) vibrating at 800 MHz in glycerol solutions with varying viscosity. The straight line illustrates the behaviour for the first two points.

[35] F. Teston, G. Feuillard, L. Tessier, L.P. Tran Hu Hue, M. Lethiecq, *J. Appl. Phys.* **87**, 689 (2000).
[36] J. Kuntner, G. Stangl, B. Jakoby, *Proc. IEEE Int. Conf. Sens.*, 956 (2003).
[37] B. Jakoby, M. Vellekoop, *Sens. Act. A* **68**, 275 (1998).
[38] G. Wingqvist, J. Bjurström, I. Katardjiev, *Proc. IEEE Ultrason. Symp.*, 50 (2005).

5.4.2. Bio-chemical sensing

Bio-chemical measurements have been performed in collaboration with partners from the European projects to assess the suitability of the SMRs as bio-chemical sensors. In the following, an example of an immunological reaction is described. Sub-section 5.4.2.1 describes the measurement procedure, 5.4.2.2 shows the time-dependent measurement result and 5.4.2.3 gives the obtained sensitivity and mass resolution. An overview of these experiments has been published by Weber *et al.*[39]

5.4.2.1. Bio-chemical solutions and procedure

For the bio-chemical solutions, resonators from sample SIIf with DESIGN 2 have been used. They have an area of $200 \times 200\ \mu m^2$ and resonance frequencies of around 780 MHz. Figure 5.16 a) shows an impedance characteristic of a typical resonator in water. It has an effective coupling coefficient of 0.08 and a Q_{BVD} in water of 205. Q_{SLOPE} is 130. The bio-chemical solutions were flushed over the sensor active area using the closed flow cell described in section 5.2.1. The reagent samples of 200 µl for each injection were pumped through the flow-cell at a flow-rate of 36 µl/min.

An **immunological reaction** was chosen to demonstrate the bio-chemical sensing capability. In an immunological experiment the **binding of an antibody to an antigen** is typically monitored. An antibody is a protein used by the immune system to identify and neutralize foreign objects like bacteria and viruses. Each antibody recognizes a specific antigen. The antigen is usually first fixed on the electrode. After that, sites for non-specific binding (which remain after the binding of the antigen), must be saturated with a non-specific protein. Only then the antibody can be detected specifically by the antigen. In this work, a well-known antigen-antibody pair, Avidin-Antiavidin, has been used. Another typical example from literature is the monitoring of HIV-specific antibodies in rabbit sera.[40] In that case, a recombinant fragment of the protein gp41 of HIV can be used as receptor (antigen). For both reactions bovine serum albumin (BSA) can be used to fill in the non-specific sites.

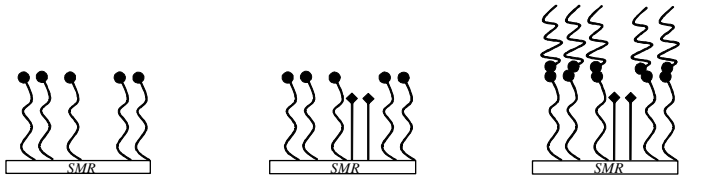

Figure 5.15 : Picture showing the different steps of the bio-chemical experiment.

First, avidin (the antigen) was flushed over the wafer at a concentration of 100 mg/l. As shown schematically on Figure 5.15 a), the protein molecules attach directly to the Au surface of the SMR by hydrophobic and thiol-gold interactions. Avidin is a relatively big molecule and there can be spots between attached molecules that stay free. On these spots, Antiavidin could attach leading to non-specific attachment. For this reason, the second step was to flush the surface with BSA at a concentration of 1 g/l to fill in gaps between avidin

[39] J. Weber, W. M. Albers, J. Tuppurainen, M. Link, R. Gabl, W. Wersing, M. Schreiter, *Sens. Act. A* **128**, 84 (2006).
[40] C. Kößlinger, E. Uttenthaler, S. Drost, F. Aberl, H. Wolf, G. Brink, A. Stanglmaier, E. Sackmann, *Sens. Act. B* **24-25**, 107 (1995).

molecules. BSA is a rather small molecule and can easily fill these empty spots as shown on Figure 5.15 b). Finally, antiavidin at a concentration of 105 mg/l was flushed over the wafer, which binds to the avidin as shown on Figure 5.15 c). These different reagents were dissolved in a buffer-solution containing 150 mM NaCl and 10 mM HEPES at a pH of 7.46. This solution also served as a reference solution before and after the injection of the bio-chemical solutions to eliminate the influence of the viscosity as seen in section 5.4.1.

5.4.2.2. Time-dependent measurement

A complete time evolution for the consecutive bindings of avidin, BSA and antiavidin is shown on Figure 5.16 b) for the parallel resonance frequency. Every injection caused a resonance frequency shift. The beginning of each injection is marked by a dashed line. In general, an injection induced a period of declining resonance frequency when the reagent is binding and the mass on the sensor surface was progressively increasing. This period was followed by a period of stabilization when the reference solution was flushed over the sensor. During this stabilization the resonance frequency slightly increases, which can be due to the partial removal of loosely attached molecules.

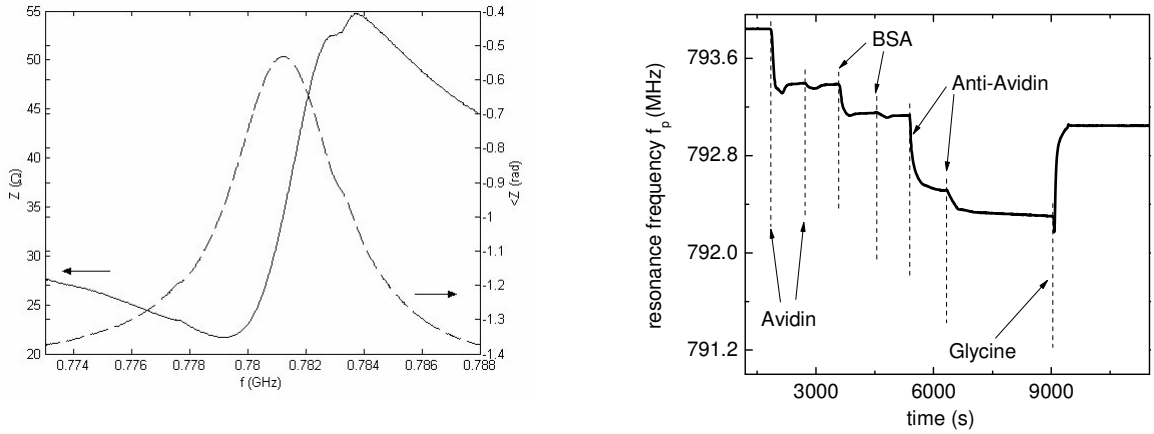

Figure 5.16 : a) Impedance characteristic in water of the resonator from sample SIIf used for the time-dependent bio-chemical measurement shown in b). (courtesy of Jan Weber)

Avidin was injected twice, the second injection permitting to fill in spots that were blocked during the first injection by loosely bound molecules. The first avidin injection brought a large resonance frequency shift of 530 kHz. The second injection, where only a couple of spots are filled, shows a frequency shift of only 10 kHz. The frequency shift due to the subsequent BSA injections was about 250 kHz. During the stabilization phase, the resonance frequency did not change much, showing that detachment processes were much less pronounced. Finally, the antiavidin injections caused frequency shifts of about 620 kHz and 190 kHz for the first and second injections respectively. After the injection of glycine, which is a small non-polar amino-acid ($C_2H_5NO_2$) capable of breaking the avidin-antiavidin connections, the frequency jumps back to the level before the antiavidin injection. The frequency shifts lie in the range of what is being expected for this type of bio-chemical bindings. An excellent frequency stability of less than 1 kHz was obtained. The sensitivities and mass resolutions that have been extracted are given in the next section.

Reference measurements were also performed with a 10 MHz QCM with the same bio-chemical bindings and solutions of same concentrations. It was shown that the avidin-binding has qualitatively the same dynamic response for the SMR and the QCM measurement. This means that the relative speed of frequency change and mass adsorption was the same. In both cases, the resonance frequency declined sharply at the beginning of the injection and flattened afterwards. The maximum reaction speed at the beginning of the injection could be determined to 2.9 Hz/s for the QCM and 4.4 kHz/s for the SMR, which corresponds to mass adsorption speeds of 5.4 ng/cm^2.s and 7.6 ng/cm^2.s respectively. This shows that the observed binding processes are similar for SMR and QCM.

5.4.2.3. Sensitivity and mass resolution

The observed frequency shifts permit to find practical values of the sensitivity and mass resolution of the SMR used as bio-chemical sensor. In fact, reference measurements with a surface plasmon resonance (SPR) technique (Biacore 3000) permitted to find the attached mass. For the avidin-binding, the attached mass was about 420 ng/cm^2 for an experiment where the measured resonance frequency shift was 310 kHz. Thereby, an absolute **sensitivity** of **-738 Hz·cm^2/ng** was derived, corresponding to a relative sensitivity of -946 cm^2/g. These values are slightly lower to the expected sensitivities for a 800 MHz device, which in Chapter 4 were shown to ideally be -807 Hz·cm^2/ng. This can be due to slight differences in stack design, lower frequency, differences of top layer properties and additional elastic bio-chemical layers that can affect the sensitivity of such multi-layered devices. Yet the main difference is probably due to the fact that the bio-chemical attachments were not yet well-controlled, and thus the corresponding frequency shifts vary slightly. However the extracted sensitivities all vary around the mentioned value.

With a 10 MHz QCM using the same experiment, an absolute sensitivity of only 0.54 Hz·cm^2/ng was found, which shows that the obtained absolute mass sensitivity of the SMR is about 1000 times higher than for a typical QCM. Lin *et al.* found a sensitivity of 2.17 Hz·cm^2/ng for a 30 MHz QCM,[41] determined through copper electrodeposition in 0.1 M $CuSO_4$ solution, in exact agreement with the values obtained by the Sauerbrey equation. This value is also easily surpassed by the SMRs of this work. Moreover, since it is very easy to deposit thin films, resonance frequencies of SMR devices can reach 3 to 4 GHz. Provided the characteristics of the thin films are not degraded at lower thicknesses and the electrical resistance of thinner electrodes can be tackled, relative sensitivities of several 3000 to 4000 cm^2/g are reachable.

The **mass resolution** for this particular experiment can be estimated by looking at the frequency fluctuation in a stable state, i.e. in buffer-solution. As explained in section 1.2.4 of Chapter 1, the **three-fold standard deviation of the frequency is defined as the minimum frequency shift** that can be measured. It was determined to be **2580 Hz** for the SMR. Knowing the sensitivity, a mass resolution about **3.5 ng/cm^2** was derived. Lin *et al.* obtain a mass resolution of 9.2 ng/cm^2 assuming a minimum frequency shift of ±10 Hz.[41] Auge *et al.* mention stabilities of down to 3 Hz in water for 10 to 20 MHz QCMs, i.e. minimum frequency shifts of 9 Hz.[42] For a 10 MHz QCM as the one used as a reference in this work, this corresponds to a mass resolution of 16.6 ng/cm^2. Even with a frequency stability of 1 Hz, the mass resolution would only be

[41] Z. Lin, C. M. Yip, I. S. Joseph, M. D. Ward, *Anal. Chem.* **65**, 1546 (1993).
[42] J. Auge, P. Hauptmann, J. Hartmann, S. Rösler, R. Lucklum, *Sens. Act. B* **24-25**, 43 (1995).

5.5 ng/cm^2. In consequence, although the minimum detectable frequency shift is very high, the mass resolution determined for the SMRs of this work is at least twice as good as the resolution of typical QCM systems, which is mainly due to its high sensitivity.

The frequency stability of 2580 Hz was found for a Q_{SLOPE} in water of 130. With sample SIIIb having a coupling coefficient of 0.144, it is expected to reach a Q_{SLOPE} in water of around 200. By making the assumption that the phase resolution of the Network Analyzer stays constant, such a Q-factor would allow a minimum frequency shift of 1680 Hz.[43] Assuming that the ideal absolute mass sensitivity of -807 Hz·cm^2/ng is reached, a mass resolution of 2 ng/cm^2 would be possible, which is at least three times better than for typical QCM. Bio-chemical measurements with these latest samples were being planned at the end of this work. Furthermore, by optimizing the Q-factors of the SMRs and the electronic read-out circuitry, extending the mass resolution into the 1 ng/cm^2 regime seems possible. For comparison, the longitudinal mode minimum frequency shift in water was determined to be 46200 Hz, giving a mass resolution of 21 ng/cm^2.

Other bio-chemical measurements with these devices (e.g. vesicle adsorption on SiO_2 surfaces) are described in the thesis of Jan Weber.[44] They give similar results to the ones mentioned above. The bio-chemical experiments have shown the suitability of shear mode SMRs for gravimetric sensing applications in liquids. The sensing performance in terms of mass sensitivity and mass resolution is better than that of typical QCM devices. Compared with other sensing principles, a gravimetric sensor, where no labelling is required, has the advantage that the bio-chemical (protein) activity is not compromised and that real-time binding (kinetics) information can be extracted. These first results constitute a solid base for future work on integrated biosensors. The performance is expected to improve further through SMR design (e.g. ZnO deposition, stack design, resonator shapes, resonance frequency) and read-out optimization.

5.5. Chapter conclusion

In this chapter, the SMR samples that were described in Chapter 4 have been tested in pure water and glycerol solutions of different concentrations in view of their application as bio-chemical gravimetric sensors or viscosity sensors. The changes of the Q-factors and resonance frequencies have been analyzed in order to assess the SMR performance in liquid environment. Considering the results presented in this chapter, the prediction of effects caused by liquids in gravimetric sensing applications is possible for low viscosity values. In this Newtonian range, the SMRs behave in accordance with well-known formulas developed for QCM devices. In pure water, quality factors Q_{BVD} of around 200 were found for most samples. With sample SIIf, used for most of the bio-chemical experiments, Q_{BVD} was at 205 and Q_{SLOPE} was evaluated at 130. With sample SIIIb, exhibiting an effective coupling coefficient of 0.14, Q_{BVD} was 250 and Q_{SLOPE} 190. These Q-factors allow mass resolutions in the range of those achieved with QCM sensors. For the same viscosity ranges, measured longitudinal mode Q-factors lie well below 20, which demonstrates the superiority of the shear mode over the longitudinal mode. An extended BVD model known for QCM devices, which can be

[43] Simple calculation : $\Delta f_2=\Delta f_1.Q_1/Q_2$.
[44] J. Weber, PhD Thesis, Universität Augsburg, to be published.

brought back to the standard one in case of liquids with low conductance, was also fitted on the measured SMRs. The fitting was very accurate and the elements of the equivalent circuit changed as expected.

It was observed that both the resonance frequency change and the losses expressed by Q_{Liquid} diverge from simple Newtonian behaviour for glycerol concentrations above 44%, i.e. viscosities higher than 5cP. At this point the visco-elastic behaviour of the solution becomes evident. In the linear region below a viscosity of 5cP, the sensors can be used as viscosity sensors with sensitivities of -10 MHz·cm^2·s$^{0.5}$/g, which is 50 to 100 times that of conventional QCM devices.

Experiments with an immunological reaction (Avidin-Antiavidin bindings) have proven the applicability of these SMRs for highly sensitive bio-chemical measurements. Table 5.2 shows a comparison of the measured characteristics with sample SIIf and the expected characteristics with sample SIIIb, compared with a conventional 30 MHz QCM. The obtained mass sensitivity of 738 Hz·cm^2/ng is around 340 times higher than that of the QCM, while the mass resolution of 3.5 ng/cm^2 is 3 times better. With sample SIIIb, the mass resolution is expected to decrease further to only 2 ng/cm^2. Since higher resonance frequencies can easily be obtained, it is expected that the sensitivity can be increased to several kHz·cm^2/ng. These first results constitute a solid base for future work on integrated bio-chemical sensors. Their performance is expected to improve further through SMR design and read-out optimization.

The results of this chapter indicate that high frequency SMRs can be operated successfully in liquids, providing enhanced sensitivity for gravimetric detection and viscosity measurements while keeping similar mass and viscosity resolution than established QCM devices. SMRs thus constitute an attractive device for cheap, disposable and highly integrated sensor arrays for the growing diagnostic market with the advantage of very high sensitivities and excellent mass resolutions.

TABLE 5.2
COMPARISON BETWEEN SM-SMR AND QCM SENSING PROPERTIES

Parameter	Units	SMR SIIf (measured)	SMR SIIIb (calculated)	QCM*** (literature)
Resonance frequency	[MHz]	780	840	30
Q_{SLOPE} in pure water	-	130	190	1180
K_{eff}	-	0.08	0.14	0.05
Absolute mass sensitivity	[Hz·cm^2/ng]	738	807	2.17
Relative mass sensitivity	[cm^2/g]	946	1010	72.3
Absolute viscosity sensitivity ($\Delta f/\sqrt{\rho_L \eta_L}$)	[MHz·cm^2·s$^{0.5}$/g]	-10	n.a.	-0.1057
Relative viscosity sensitivity	[cm^2·s$^{0.5}$/g]	-0.013	n.a.	-0.0035
Three-fold standard deviation of frequency	[Hz]	2580	1680	6.7
Mass resolution *	[ng/cm^2]	3.5	2	9.2
Viscosity resolution *, **	[cP]	$9 \cdot 10^{-4}$	n.a.	$2 \cdot 10^{-3}$

* As determined from the three-fold frequency noise.
** Assuming a constant density of 1 g/cm^3.
*** Z. Lin, C. M. Yip, I. S. Joseph, M. D. Ward, *Anal. Chem.* **65**, 1546 (1993).

General conclusion and perspectives

The best way to predict the future is to invent it.
[Alan Kay]

Amongst the requirements of future health-care are the improvement and better cost-efficiency of medical diagnostics, and the decentralization of the point of care. Easy-to-use, fast, reliable, miniaturized and inexpensive diagnostic devices are required. In this regard, the objective of this thesis was to realize shear mode solidly mounted film bulk acoustic resonators (SMR) and demonstrate their ability to function as bio-chemical sensors in liquid environments. This objective has been reached. The simulation, realization and characterization in air and in liquid of these SMRs, vibrating at around 800 MHz, have been shown in detail. To our knowledge, such shear mode solidly mounted devices have been realized for the first time. This was possible after the successful development of deposition processes for c-axis inclined ZnO thin films. The application of the SMRs in liquids has shown that they are suitable as viscosity and bio-chemical sensors, reaching sensitivities up to 1000 times higher than those of established quartz crystal microbalances (QCM) devices and mass resolutions equal or better than those of QCMs. At the end of this work, the first real-time measurements of antibody-antigen bindings in liquid using the SMRs have been demonstrated. The SMRs are expected to form the core of a new bio-chemical sensing device developed at Siemens CT in the framework of two European Projects, integrating electronic read-out circuits, fluidic systems and bio-chemical components, thereby obtaining a portable and inexpensive system to serve the growing point-of-care medical diagnostic market.

In the following, a short summary of the principal results and achievements is given for each of the main parts of the thesis, namely the SMR modelling and simulation, the development of deposition processes for c-axis inclined ZnO thin films, the realization and characterization of SMRs in air, and the characterization and sensing applications in liquid. An outlook on future improvements and possible research directions related to the each part is also presented.

Resonator modelling, simulation and characterization methods

Summary: This work started with the modelling and simulation of film bulk acoustic resonators (FBAR) in Chapter 2. Based on the equations of the propagation of acoustic waves in piezoelectric materials, an expression for the electrical impedance of a simple FBAR consisting of only a ZnO layer was derived, permitting to define basic resonator parameters such as the series and parallel frequencies, the coupling

coefficient and the Q-factor. It was shown that in general both the longitudinal and shear wave modes are excited depending on the c-axis inclination with respect to the surface normal. At some inclinations, only one mode is excited and at 13.6°, both modes are excited with equal coupling coefficients. Composite FBARs with multiple layers were examined and models like the transmission line model, the Mason Model and the Butterworth-Van Dyke (BVD) Model were introduced. These models were implemented in MATLAB and served reliably throughout this work: prior to SMR realization, to calculate the correct layer thicknesses for a specified target resonance frequency, and after SMR realization, to obtain its characteristics by comparing with simulations and fitting on the BVD model. A method of characterizing thin piezoelectric films with the help of highly over-moded FBARs was also established and implemented in MATLAB, permitting to rapidly derive the coupling coefficient of the film by combining measurement, fittings and simulations.

Perspectives: The modelling and characterization tools developed in this work were sufficient to reach the planned objectives. In future, it could be useful to model the SMRs in a more accurate way, by incorporating both wave modes into the Mason Model and introduce different loss mechanisms (scattering, material loss, …) into the simulations. A further step could be the simulation of the SMRs with finite element methods (e.g. ANSYS), in 2 or even 3 dimensions, to analyze spurious modes.

Deposition of c-axis inclined ZnO thin films

Summary: Three deposition processes for c-axis inclined ZnO films have been developed using reactive DC-pulsed magnetron sputtering (Chapter 3). All three processes build on each other and yield films suitable for shear wave mode excitation. The requirements were a) to obtain inclined ZnO films as fast as possible in order to fabricate SMRs, b) to use the existing planar wafer charging system, c) to use at least 4” wafers, and d) to deposit the ZnO on polycrystalline or amorphous films. These aims have been reached with each of the three processes. For the first process, with no modification of the sputtering equipment, the obtained inclinations varied from zero at the centre of the wafer up to a recorded maximum of 9° at the border, and only 19 % of the wafer surface could be used. For the second process, a rectangular blind was positioned between the target and the substrates. The inclinations were found to depend strongly on the distance to this blind. The maximum recorded inclination was 16° on Al_2O_3 buffer-layers and the inclination decreased with increasing distance to the blind, yielding a 30 % use of the surface. Coupling coefficients up to 0.105 were extracted, which is half of the theoretical maximum that can be obtained at this inclination. The differences were attributed to a relatively broad distribution of the inclination angle and a partially opposite polarity in the different grains. The last process also used blinds positioned between the target and the substrate. The blind permitted to cover the whole 4” wafer surface and by moving the wafer during sputtering, homogeneous films, both in thickness and inclination, were obtained on the whole wafer surface. The inclination was around 10° and coupling coefficients of up to 0.136 were determined. To my knowledge, it is the first process permitting to sputter inclined ZnO films homogeneously on such large surfaces with good reproducibility. For all three processes, simulations in MATLAB have shown that the inclined film growth is a consequence of oblique incidence of the particles.

Perspectives: During this thesis, the sputtering processes have continuously been improved concerning deposition rate, c-axis inclination and coupling coefficient. This progress should be continued in the future. Most importantly, the inclination and dispersion of the films should be further improved in order to obtain higher coupling coefficients. Ways of achieving the same polarity in the different grains could be explored. This could be done by optimizing the buffer-layer, the blind geometry and the sputtering parameters (e.g. substrate holder polarization). The microstructure of the buffer-layer is expected to play a crucial role. Other points of possible research directions are the reduction of the film roughness to decrease the acoustic losses via scattering, and the reduction of the film stress to eliminate delaminating even for complex stack designs.

SMR realization and characterization in air

Summary: The simulation, realization and characterization of SMRs vibrating at around 800 MHz and based on the c-axis inclined ZnO thin films have been shown (Chapter 4). The influence of the acoustic mirror, the buffer-layer and the electrodes on the performance of the SMR has been analyzed. Using simulations with the Mason Model, it was found that the sensitivity of the SMR to mass changes at its surface, can be maximized for a 100 nm Au or Pt top electrode, and a quarter-wavelength Pt bottom electrode (528 nm) while keeping electrical losses low. In this frequency range a relative sensitivity of around -1000 cm^2/g was predicted, which is much better than typical values for QCMs. Different acoustic mirror combinations (Pt-ZnO, W-SiO_2 …) and their respective reflections have been simulated. During the course of this work, the effective coupling coefficient of the SMRs was continuously improved, jumping from 0.012 to 0.149 (K^2 of 2.2 %). Very homogeneous properties have been obtained with SMRs based on the third ZnO deposition process. The apparent Q factors increased from around 3.5 at the beginning of the work to around 230 at the end, which has positive consequences for the obtainable mass resolution.

Perspectives: Consideration of both the various layer materials and thicknesses might further improve the performance of the SMRs. Additional optimization of the shape of the active area could reduce the appearance of spurious modes. The Q-factors are expected to have scope for improvement through lowering of the film roughness to decrease scattering losses. An important concern will also be the integration of SMR with electronic CMOS circuitry and micro-fluidic systems. Here cross-talk problems and additional losses to the environment will have to be dealt with.

SMR characterization in liquids and sensing applications

Summary: The SMRs have been tested in pure water and glycerol solutions of different concentrations in view of their application as sensors in liquid environments. The changes of the Q-factors and resonance frequencies have been analyzed in order to assess the performance of the SMRs. The prediction of effects caused by liquids in gravimetric sensing applications is possible for low viscosity values. In Newtonian range, the SMRs behave in accordance with well-known formulas developed for QCM devices. In pure water and 59 % glycerol, having a ten times higher viscosity, quality factors of around 200 and 140 were respectively found. This allows mass resolutions in the range of those achieved with QCM sensors. For the

same viscosity ranges, measured longitudinal mode Q-factors lay well below 20, which demonstrates the superiority of the shear mode over the longitudinal mode. An extended BVD model known for QCM devices, which can be brought back to the standard one in case of liquids with low conductance, was fitted on the measured SMRs. The fitting was very accurate and the elements of the equivalent circuit changed as expected. It was observed that both the resonance frequency and the Q-factor changes diverged from simple Newtonian behaviour for glycerol concentrations above 44 %, i.e. viscosities higher than 5 cP. At this point the visco-elastic behaviour of the solution becomes evident. In the linear region below a viscosity of 5 cP, the sensors can be used as viscosity sensors with sensitivities of -10 MHz·cm^2·s$^{0.5}$/g, which is 50 to 100 times that of conventional QCM devices. Experiments with an immunological reaction (Avidin-Antiavidin bindings) have proven the applicability of these SMRs for highly sensitive bio-chemical measurements. The obtained mass sensitivity of 738 Hz·cm^2/ng is around 340 times higher than that of a 30 MHz QCM, while the mass resolution of 3.5 ng/cm^2 is 3 times better. Compared with standard commercially available 10 MHz QCMs on which the same measurements were performed, the sensitivity is 1000 times higher and the mass resolution 4 times better. Since higher resonance frequencies can easily be obtained, it is expected that the sensitivity can be increased to several kHz·cm^2/ng.

Perspectives: These first results constitute a solid base for future work on integrated bio-chemical sensors. Yet, to establish the SMRs as a serious alternative to existing sensing principles, more bio-chemical measurements are needed. For this, numerous problems with the fluidic system and the electronic read-out system have to be faced, in order to assure constant measurements conditions. As mentioned above, the performance of the SMR is expected to be further improved (e.g. ZnO deposition, stack design, resonator shapes, resonance frequency, read-out optimization). It is particularly important to improve the Q-factor of the device, in order to come close to the theoretical limit given by Q_{liquid} and ameliorate the mass resolution as far as possible. Moreover the influence of the visco-elasticity of the liquids on the resonator properties merits further investigation.

Global outlook

This work has demonstrated the enormous advantage of shear mode solidly mounted film bulk acoustic resonators for gravimetric sensing applications. They are highly sensitive, can easily be combined with electronics and integrated into arrays, and allow quantitative time-dependent measurements with very good mass resolutions. Compared with the established QCM principle, they feature much higher sensitivities, both to mass and viscosity. They also compare well to other sensing principles used for bio-chemical measurements, especially since no labels are needed to recognize the presence of the measurands and time-dependent measurements with low volumes are possible. They can be expected to make a considerable impact on the growing point-of-care diagnostic market. To conclude, since their areas and thicknesses are several orders of magnitudes lower than that of typical QCMs, and considering their numerous advantages over other sensing principles, it will hopefully only be a matter of time before the ultrasonic, bio-chemical and medical communities, accustomed to the *quartz crystal microbalances*, become familiar with a new device: the *piezoelectric film nanobalance* (PFN).

Conclusion générale et perspectives

Le meilleur moyen de prédire le futur est de l'inventer.
[Alan Kay]

Parmi les exigences que pose le système de la santé publique dans le futur se trouvent l'amélioration et une meilleure gestion des coûts du diagnostic médical, ainsi qu'une décentralisation du point de traitement. Des systèmes de diagnostic d'une utilisation simple, rapides, fiables, miniaturisés et bon marché sont alors nécessaires. Dans ce contexte, l'objectif de cette thèse était d'une part la réalisation de résonateurs à ondes acoustiques de volume à base de couches minces, vibrant en mode de cisaillement et montés sur miroir acoustique (SMR), et d'autre part la démonstration de leur capacité à fonctionner comme capteurs biochimiques en milieux liquides. Cet objectif a été atteint. La simulation, la réalisation et la caractérisation de ces SMRs, résonants à 800 MHz, ont été montrées en détail. A notre connaissance, c'est la première fois que de tels systèmes ont été réalisés. Ceci n'a été possible qu'après le développement de procédés de dépôt de couches minces de ZnO à axe c incliné. L'application de ces SMRs en milieux liquides a montré qu'ils pouvaient être utilisés comme capteurs biochimiques et viscosimètres, avec des sensibilités jusqu'à 1000 fois plus élevées que celles de microbalances à quartz (QCM) conventionnelles, et avec des résolutions égales ou meilleures. Vers la fin de ce travail, les premières mesures en temps réel de réactions biochimiques d'anticorps et d'antigènes ont été effectuées en utilisant ces SMRs. Leur utilisation est prévue pour un nouveau système de détection biochimique développé chez Siemens CT dans le cadre de deux projets européens, intégrant des circuits électroniques, des systèmes fluidiques et des composants biochimiques. On obtiendrait ainsi un système portable et bon marché pour le marché du diagnostic médical.

Dans la suite de cette conclusion, un bref résumé des principaux résultats, suivi de propositions d'améliorations et de perspectives, sont donné pour chaque partie de la thèse : la modélisation et la simulation des SMRs, le développement de procédés de dépôt de couches minces de ZnO à axe c incliné, la réalisation et caractérisation des SMRs à l'air, et la caractérisation et détection en milieux liquides.

Modélisation, simulation et méthodes de caractérisation de résonateurs

Résumé: Ce travail a débuté par la modélisation et la simulation de résonateurs à ondes acoustiques de volume à base de couches minces (FBAR) (Chapitre 2). En se basant sur les équations de propagation d'ondes acoustiques dans les solides piézoélectriques, une expression de l'impédance électrique d'un FBAR simple constitué uniquement d'une couche de ZnO a été établie, permettant de définir les paramètres

fondamentaux du résonateur tels que les fréquences de série et parallèle, le coefficient de couplage et le facteur de qualité. Il a été montré qu'en général les modes longitudinal et de cisaillement peuvent être excités simultanément selon l'inclinaison de l'axe c. Ensuite, des FBAR composés de multiples couches ont été examinés et des concepts tels que le modèle de la ligne de transmission, le modèle de Mason et le modèle de Butterworth-Van Dyke (BVD) ont été introduits. Une fois implémentés dans MATLAB, ces modèles ont servi d'une manière fiable tout au long de ce travail. Avant la réalisation des SMRs, ils ont permis de calculer les épaisseurs des différentes couches pour une certaine fréquence de résonance. Après leur réalisation, ils ont permis d'obtenir les caractéristiques des SMRs. Une méthode de caractérisation de couches minces utilisant des FBARs à modes supérieurs a été établie et implémentée dans MATLAB, permettant la détermination rapide du coefficient de couplage de couches en combinant mesures, adaptation et simulations.

Perspectives: Les outils de modélisation et de caractérisation développés ont suffi pour atteindre les objectifs de ce travail. A l'avenir, les SMRs pourraient être modélisés d'une façon plus précise, en incorporant les deux modes d'ondes dans le modèle de Mason et en introduisant les différents mécanismes de pertes (dispersion, friction) dans les simulations. De plus les modes parasitaires devraient être analysés en utilisant p.ex. des méthodes d'éléments finis dans 2 ou 3 dimensions.

Dépôt de couches minces de ZnO à axe c incliné

Résumé: Trois procédés de dépôt de couches minces de ZnO à axe c incliné ont été développés en utilisant la pulvérisation réactive magnétron (Chapitre 3). Les trois procédés sont basés l'un sur l'autre et ont permis d'obtenir des couches minces permettant d'exciter le mode de cisaillement. Le cahier de charge était a) d'obtenir rapidement des couches minces de ZnO incliné afin de pouvoir réaliser des SMRs, b) d'utiliser le système de chargement planaire existant, c) d'utiliser au moins des wafers 4 pouces, et d) de pouvoir déposer le ZnO sur des couches amorphes ou polycristallines. Ces objectifs ont été atteints avec chacun des trois procédés. Pour le premier procédé, aucune modification de l'équipement de pulvérisation n'a été effectuée. Les inclinaisons obtenues ont varié de 0° au centre du wafer à un maximum de 9° au bord et seulement 19 % de la surface pouvaient être utilisés. Pour le deuxième procédé, un cache rectangulaire a été positionné entre la cible et le substrat. Une inclinaison maximale de 16° a été obtenue avec des couches intermédiaires (buffer) d'Al_2O_3 et nous n'avons pu observer que l'inclinaison décroît en fonction de la distance au cache, ce qui donne une utilisation de 30 % de la surface. Des coefficients de couplage jusqu'à 0.105 ont été extraits, ce qui correspond à la moitié du maximum théorique à cette inclinaison. La différence a été attribuée à une distribution relativement large de l'inclinaison dans les différents grains, ainsi qu'à une polarité des grains partiellement opposée. Pour le dernier procédé, plusieurs caches ont été positionnés entre la cible et le substrat. Les caches ont permis de couvrir toute la surface du wafer 4". En faisant bouger le wafer durant la pulvérisation, des couches minces, homogènes en épaisseur et en inclinaison, ont été obtenues sur la surface entière du wafer. L'inclinaison est de 10° et des coefficients de couplage jusqu'à 0.136 ont été déterminés. A ma connaissance, il s'agit du premier procédé permettant d'obtenir des couches de ZnO incliné homogènes sur de larges surfaces avec une très bonne reproductibilité. Des simulations dans MATLAB ont permis de montrer que la croissance de la couche inclinée est due à une incidence oblique des particules.

Perspectives: Les procédés de pulvérisation ont été améliorés continuellement du point de vue de la vitesse de dépôt, de l'inclinaison de l'axe c et du coefficient de couplage. Cette progression doit être continuée dans le futur. Le plus important est d'améliorer le degré et de réduire la dispersion de l'inclinaison des grains afin d'obtenir des coefficients de couplage plus élevés. Des moyens permettant d'obtenir la même polarité des grains doivent être explorés. On pourrait également optimiser la géométrie du cache, les paramètres de pulvérisation et la couche intermédiaire. La microstructure de celle-ci joue un rôle crucial. D'autres perspectives de recherche pourraient être la réduction de la rugosité afin de diminuer les pertes acoustiques dues à la dispersion et la réduction des contraintes afin d'éliminer le risque de craquelures.

Réalisation et caractérisation de SMRs à l'air

Résumé: La simulation, la réalisation et la caractérisation de SMRs vibrant à 800 MHz et basés sur des couches minces de ZnO à axe c incliné ont été montrées (Chapitre 4). Les influences du miroir acoustique, de la couche intermédiaire et des électrodes sur la performance du SMR ont été analysées. Des simulations avec le modèle de Mason ont montré que la sensibilité gravimétrique du SMR peut être maximisée pour une électrode supérieure en Au ou Pt de 100 nm et une électrode inférieure en Pt de 528 nm, avec seulement de faibles pertes électriques. Avec des fréquences de 800 MHz, une sensibilité relative de -1000 cm^2/g a été calculée, ce qui est meilleur que les valeurs typiques des QCMs. Différentes combinaisons de matériaux ont été testées pour le miroir acoustique (Pt-ZnO, W-SiO_2), et leurs réflexions respectives ont été simulées. Le coefficient de couplage effectif des SMRs a été continuellement amélioré, de 0.012 au début à 0.149 vers la fin (K^2 de 2.2 %). Des propriétés très homogènes ont été obtenues avec des SMRs basés sur le troisième procédé de dépôt de ZnO. Le facteur de qualité apparent est passé de 3.5 au début de ce travail à 230 vers la fin, ce qui a des conséquences très positives pour la résolution massique.

Perspectives: Un choix judicieux des matériaux et des épaisseurs des différentes couches permettrait une poursuite de l'amélioration de la performance des SMRs. Une optimisation de la surface active pourrait réduire l'apparence de modes parasites. Les facteurs de qualité pourraient être augmentés en optimisant la rugosité des couches pour réduire les pertes par diffusion. Une préoccupation majeure sera également l'intégration des SMRs dans l'électronique CMOS et dans les systèmes microfluidiques. Les interférences électroniques possibles et les pertes vers l'environnement devraient être minimisées.

Caractérisation des SMRs en milieu liquide et applications comme capteurs

Résumé: Les SMRs ont été testés dans de l'eau pure et dans des solutions de glycérol en vue de leur application comme capteurs en milieu liquide (Chapitre 5). Les changements du facteur de qualité et des fréquences de résonance ont été analysés pour évaluer la performance des SMRs. Les effets causés par le liquide lors d'une détection gravimétrique peuvent être estimés pour de faibles viscosités. Dans le domaine Newtonien, les SMRs se comportent selon les formules bien établies des QCMs. Dans de l'eau pure et dans 59 % de glycérol, qui a une viscosité 10 fois plus élevée, les facteurs de qualité s'élevaient à 200 et à 140 respectivement. Ceci permet d'obtenir des résolutions dans le même ordre de grandeur que celles des QCMs.

Les facteurs de qualité du mode longitudinal sont inférieurs à 20, ce qui démontre la supériorité du mode de cisaillement. Le modèle BVD, également valable pour des SMRs dans les liquides d'une faible conductance, a été utilisé pour l'adaptation des valeurs mesurées. Les changements de la fréquence de résonance et du facteur de qualité ne correspondent plus au comportement Newtonien simple pour des concentrations de glycérol au-delà de 44 %, c.-à.-d. des viscosités plus grandes que 5 cP. A ce moment-là, le comportement viscoélastique de la solution devient évident. Dans la région linéaire en-dessous d'une viscosité de 5 cP, les SMRs peuvent être utilisés comme viscosimètres avec une sensibilité de -10 MHz·cm^2·s$^{0.5}$/g, ce qui est 50 à 100 fois plus que celle des QCM conventionnels. Des expériences avec une réaction immunologique (liaison Avidin-Antiavidin) ont démontré que ces SMRs peuvent être utilisés comme capteurs biochimiques hautement sensibles. La sensibilité obtenue de 738 Hz·cm^2/ng est environ 340 fois plus grande que celle d'un QCM de 30 MHz et la résolution de 3.5 ng/cm^2 est 3 fois meilleure. Comparé à un QCM standard de 10 MHz sur lequel les mêmes mesures ont été effectuées, la sensibilité est 1000 fois plus grande et la résolution 4 fois meilleure. Comme des fréquences beaucoup plus grandes peuvent aisément être obtenues, il est probable que la sensibilité pourra être augmentée à plusieurs kHz·cm^2/ng.

Perspectives: Ces premiers résultats constituent une base solide pour de futurs travaux de capteurs biochimiques intégrés. Toutefois, pour établir les SMRs comme alternative sérieuse aux principes de détection existants, d'autres expériences biochimiques seront nécessaires. Pour cela, de nombreux problèmes avec le système fluidique et le système électronique de détection doivent être résolus afin de garantir des conditions de mesure stables. Comme mentionné, la performance des SMRs peut encore être améliorée (p.ex. dépôt du ZnO, design du résonateur, fréquence de résonance, optimisation de l'électronique). Il est particulièrement important d'accroître le facteur de qualité des SMRs, afin de s'approcher de la limite théorique donnée par Q_{liquid} et d'améliorer la résolution autant que possible. De plus, l'influence de la viscoélasticité des liquides sur les propriétés des résonateurs doit être analysée plus en détail.

Perspectives globales

Ce travail a permis de démontrer les énormes avantages des résonateurs à ondes acoustiques de volume à base de couches minces pour des applications comme capteurs gravimétriques. Ils peuvent aisément être combinés avec de l'électronique et intégrés en matrices, et permettent des mesures quantitatives avec de très bonnes résolutions. Ils ont des sensibilités beaucoup plus élevées que les QCMs, aussi bien par rapport à un changement de masse que de viscosité. Ils ont également des avantages par rapport à d'autres principes physiques puisqu'ils peuvent reconnaître la présence de molécules sans marquage physique supplémentaire et que des mesures en fonction du temps sont possibles avec des volumes très faibles. On peut donc s'attendre à ce que ces systèmes aient un impact considérable sur le marché du diagnostic médical. Pour terminer, comme la surface et l'épaisseur des SMRs sont inférieures de plusieurs ordres de grandeur à celles des QCMs typiques, et en considérant les avantages par rapport à d'autres principes de détection, il est à espérer que les communautés ultrasonique, biochimique et médicale, habituées aux *microbalances à quartz piézoélectrique*, se familiarisent très vite avec un nouveau système : la *nanobalance à couche piézoélectrique* (PFN).

Related publications and patents

A. Articles in refereed journals

° **M. Link**, M. Schreiter, J. Weber, R. Primig, D. Pitzer, R. Gabl, Solidly mounted ZnO Shear Mode Film Bulk Acoustic Resonators for Sensing Applications in Liquids, *IEEE Transactions on Ultrasonics, Ferroelectrics, and Frequency Control*, Vol. **53**, No. 2, pp. 492-496, February 2006.

° **M. Link**, M. Schreiter, J. Weber, R. Gabl, D. Pitzer, R. Primig, W. Wersing, M.B. Assouar, O. Elmazria, C-axis inclined ZnO films for shear-wave transducers deposited by reactive sputtering using an additional blind, *Journal of Vacuum Science & Technology A*, Vol. **24**, Issue 2, pp. 218-222, March 2006.

° **M. Link**, J. Weber, M. Schreiter, W. Wersing, O. Elmazria, P. Alnot, Sensing characteristics of high-frequency shear mode resonators in glycerol solutions, *Sensors and Actuators B*, in press, available online, May 2006.

° J. Weber, W. M. Albers, J. Tuppurainen, **M. Link**, R. Gabl, W. Wersing, M. Schreiter, "Shear Mode FBARs as Highly Sensitive Liquid Biosensors", *Sensors and Actuators A*, Vol. **128**, pp. 84-88, 2006.

° J. Weber, **M. Link**, R. Primig, D. Pitzer, W. Wersing, M. Schreiter, "Investigation of the scaling rules determining the performance of Film Bulk Acoustic Resonators operating as Mass-Sensors", *IEEE Transactions on Ultrasonics, Ferroelectrics, and Frequency Control*, in press, 2006.

° E. Aubert, E. Wenger, **M. Link**, B. Assouar, C. Didierjean, C. Lecomte, "Thin film disorientation measurement using the single crystal Nonius Kappa CCD diffractometer", *Journal of Applied Crystallography*, Vol. **39,** 2006.

° R. Gabl, H.-D. Feucht, H. Zeininger, G. Eckstein, M. Schreiter, R. Primig, D. Pitzer, W. Wersing, "First results on label-free detection of DNA and protein molecules using a novel integrated sensor technology based on gravimetric sensor principles", *Biosensors and Bioelectronics* **19**, pp. 615-620, 2004.

B. Patent applications

° **M. Link**, M. Schreiter, R. Gabl, Kondensatorstruktur mit dielektrischer Zwischenschicht, Verfahren zum Herstellen der Kondensatorstruktur und Verwendung der Kondensatorstruktur, Deutsche Patentanmeldung 10 2004 047 023.5 (2004), Patent granted on 13.7.2006, number 10 2004 047 023.

° **M. Link**, M. Schreiter, R. Gabl, Verfahren zum Herstellen eines polykristallinen Keramikfilms auf einem Substrat, Kondensatorstruktur mit dem Keramikfilm und Verwendung der Kondensatorstruktur, Deutsche Patentanmeldung 10 2005 014 160.9 (2005).

° **M. Link**, M. Schreiter, J. Weber, Vorrichtung und Verfahren zur Bewegung einer Flüssigkeit, Deutsche Patentanmeldung 10 2005 043 034.1 (2005).

° **M. Link**, M. Schreiter, J. Weber, Vorrichtung und Verfahren zur Detektion einer Substanz in einer Flüssigkeit, Deutsche Patentanmeldung 10 2005 062 945.8 (2005).

° **M. Link**, M. Schreiter, D. Pitzer, W. Wersing, Dünnfilmkondensator mit strukturierter Bodenelektrode, Verfahren zum Herstellen des Dünnfilmkondensators und Verwendung des Dünnfilmkondensators, Deutsche Patentanmeldung 10 2006 004 448.7 (2006).

° **M. Link**, M. Schreiter, Verfahren und Vorrichtung zum Herstellen eines polykristallinen Keramikfilms auf einem Substrat, Kondensatorstruktur mit dem Keramikfilm und Verwendung der Kondensatorstruktur, Deutsche Patentanmeldung 10 2006 003 847.9 (2006).

C. Conference proceedings

° **M. Link**, M. Schreiter, J. Weber, D. Pitzer, R. Primig et R. Gabl, Microstructures FBAR montées sur miroir acoustique exploitant le mode de cisaillement dans des films minces de ZnO et opérant en milieu liquide, *Journées Nationales du Réseau Doctoral de Microélectronique*, 10th – 12th May 2005, Paris, pp. 114-116.

° **M. Link**, M. Schmidt, J. Weber, R. Primig, D. Pitzer, R. Gabl, M. Schreiter, Film Bulk Acoustic Resonators for Sensing Applications in Liquid Environments, *Eurosensors XIX*, *Barcelona*, 11th -14th September 2005, Proceeding N° TB10.

° **M. Link**, M. Schreiter, J. Weber, D. Pitzer, R. Primig, M.B. Assouar, O. Elmazria, C-axis inclined ZnO films deposited by reactive sputtering using an additional blind for shear BAW devices, *Proceedings IEEE Ultrasonics Symposium, Rotterdam*, 18th – 21st September 2005, pp. 202-205.

° **M. Link**, M. Schreiter, M.B. Assouar, J. Weber, D. Pitzer, R. Primig, O. Elmazria, Dépôt de couches minces de ZnO avec axe c incliné par pulvérisation réactive modifiée et application pour résonateurs vibrant en mode de cisaillement, IEACM-2, 22nd – 24th November 2005, Nancy, Volume des résumés, page 8.

° J. Weber, **M. Link**, R. Primig, D. Pitzer, M.Schreiter, Sensor for Ambient Pressure and Material Strains using a Thin Film Bulk Acoustic Resonator, *IEEE Ultrasonics Symposium, Rotterdam*, 18th – 21st September 2005, pp. 1258-1261.

° J. Weber, **M. Link**, R. Primig, D. Pitzer, M.Schreiter, High Frequency Viscosity Sensing with FBARs, *IEEE Frequency Control Symposium, Miami*, ID 6169, 5th-6th June 2006.

° R. Gabl, M. Schreiter, E. Green, H.-D. Feucht, H. Zeininger, J. Runck, W. Reichl, R. Primig, D. Pitzer, G. Eckstein, W. Wersing, Novel integrated FBAR sensors: a universal technology platform for bio- and gas-detection, *Sensors 2003, Toronto*, 21st – 24th October 2003, pp. 1184-1188.

D. Communications (oral presentation or poster)

° **M. Link**, M. Schreiter, J. Weber, D. Pitzer, R. Primig and R. Gabl, C-Axis Inclined ZnO Films by Modified Reactive Sputtering for Shear Mode FBARs, *European Marie Curie Training Course "Low Temperature Plasma Physics: Basics and Applications" and "Master Class: Biotechnical and Medical Applications"*, Physikzentrum Bad Honnef, 26th September -8th October 2004 (Poster).

° **M. Link**, M. Schreiter, J. Weber, D. Pitzer, R. Primig, O. Elmzria, P. Alnot, Capteurs en milieu liquide à base de microstructures FBAR exploitant le mode de cisaillement dans les films minces de ZnO, *Journées Nationales du Réseau Doctoral de Microélectronique*, 10th – 12th May 2005, Paris (Poster).

° **M. Link**, M. Schmidt, J. Weber, R. Primig, D. Pitzer, R. Gabl, M. Schreiter, Film Bulk Acoustic Resonators for Sensing Applications in Liquid Environments, *Eurosensors XIX*, *Barcelona*, 11th -14th September 2005 (Oral Presentation N° TB10).

° **M. Link**, M. Schreiter, J. Weber, D. Pitzer, R. Primig, M.B. Assouar, O. Elmazria, C-axis inclined ZnO films deposited by reactive sputtering using an additional blind for shear BAW devices, *IEEE Ultrasonics Symposium, Rotterdam*, 18th – 21st September 2005 (Oral Presentation N° 5B-2).

° **M. Link**, M. Schreiter, J. Weber, D. Pitzer, R. Primig, M.B. Assouar, O. Elmazria, P. Alnot, Microstructures FBAR vibrant en cisaillement pour applications comme capteurs en milieu liquide, *Doctoriales de Lorraine 2005*, 17th – 21st October 2005, La Bresse (Poster).

° **M. Link**, M. Schreiter, M.B. Assouar, J. Weber, D. Pitzer, R. Primig, O. Elmazria, Dépôt de couches minces de ZnO avec axe c incliné par pulvérisation réactive modifiée et application pour résonateurs vibrant en mode de cisaillement, IEACM-2, 22nd – 24th November 2005, Nancy (Oral presentation).

° J. Weber, **M. Link**, R. Primig, D. Pitzer, M.Schreiter, Sensor for Ambient Pressure and Material Strains using a Thin Film Bulk Acoustic Resonator, *IEEE Ultrasonics Symposium, Rotterdam*, 18th – 21st September 2005 (Oral Presentation N° 3K-3).

° J. Weber, **M. Link**, R. Primig, D. Pitzer, M.Schreiter, High Frequency Viscosity Sensing with FBARs, *Proc. IEEE Frequency Control Symposium, Miami*, ID 6169, 5th-6th June 2006 (Oral presentation).

List of figures

List of tables

CV

Mathias LINK (ing.microtechn.dipl.EPF)

French and German, raised in Luxembourg

Born on February 4th 1979, Frankfurt/Main (D)

Email: mathias.link@a3.epfl.ch

Professional Experience

10/2003	- 10/2006	SIEMENS Corporate Technology (Materials and Microsystems)	Munich, D
10/2003	- 1/2005	INWENT (International Human Resources Development)	Munich, D
4/2003	- 6/2003	IEE (International Electronics & Engineering)	Findel, L
10/2002	- 3/2003	PHILIPS Research Laboratories	Eindhoven, NL
7/2001	- 9/2001	BMW Engineering and Research Centre	Munich, D
8/1997	- 9/1997	HUSKY Injection Moulding Systems	Dudelange, L

Education

10/2003	- 9/2006	UNIVERSITE HENRI POINCARE, NANCY I, LPMIA	Nancy, F
10/1998	- 3/2003	SWISS FEDERAL INSTITUTE OF TECHNOLOGY (EPFL)	Lausanne, CH
9/1991	- 6/1998	LYCEE MICHEL RODANGE	Luxembourg, L

Languages

French, German, English, Luxembourgish

Monsieur **LINK Mathias**

DOCTORAT DE L'UNIVERSITE HENRI POINCARE, NANCY 1

en PLASMAS, OPTIQUE, OPTO-ELECTRONIQUE & MICRO-NANOSYSTEMES

VU, APPROUVÉ ET PERMIS D'IMPRIMER H°1238

Nancy, le 6 octobre 2006

Le Président de l'Université

UNIVERSITÉ HENRI POINCARÉ NANCY LE PRÉSIDENT

J.P. FINANCE

Université Henri Poincaré, Nancy I
24-30 rue Lionnois - B.P. 3069 - 54013 NANCY Cédex
Tél. : 03 83 68 20 00 - Fax : 03 83 68 21 00